THE UNIVERSITY OF QUEENSLAND

AUSTRALIA

Lattice Boltzmann Modelling of Nonlinear Coupled Pore Scale Processes in Porous Media Systems and the Applications in Geological Engineering

Jinfang GAO

Master of Engineering (Computer Science)

Bachelor of Science (Mathematics and Computational Technology)

A thesis submitted for the degree of Doctor of Philosophy at

The University of Queensland in 2014

School of Earth Sciences

Centre for Geoscience Computing

Abstract

The coupled subsurface flow involving heat transfer (**T**), hydraulic flow (**H**) and chemical reactions (**C**) in highly heterogeneous geomaterials are essential but also challenging to model in geosciences and geological engineering. To study such complex subsurface processes, multiple scales spanning from the nanoscale to basin scales are required regarding diverse applications. The pore scale is the dominant physical mediator of the above coupled fluid dynamics; hence many scientific and practical engineering decisions for the basin, reservoir and near-wellbore models have been driven by the averages of the pore scale physical processes governing fluid flow.

With respect to the pore scale studies, the following key issues still remain as problems:

1) How to appropriately describe and model the transport phenomena at the physically important scales, and provide a unifying framework to deal with a range of such multi-physics (**T**, **H**, **C**) coupled issues, rather than typical models tailored to address a single problem?
2) How to fundamentally describe and investigate the resultant effect of pore scale coupled (**T**, **H**, **C**) processes on the representative parameter - permeability? Is it size dependent and how to define it if yes?

The thesis aims to study the **System** (**T**, **H**, **C**) as a whole coupled problem. A general numerical framework has been proposed by applying and extending multi-disciplinary technologies for the solutions, which is capable of simulating coupled processes in seemingly different geological problems. The contributions are summarized as:

1) *Measuring porous media tortuosity and mineral distributions regarding different micro-CT scan resolutions.*

   The advanced modern imaging (as revealed by the *micro-CT* scanning and *QEMSCAN* mineralogy mapping) is used to derive the *3D* digital sample including materials analysis. The relative results provide the pore scale characterisation of complex real-world materials (e.g. sedimentary rocks), definition of the conductive pore network, properties of complex materials, and geometry heterogeneity. This serves as the first step for the whole thesis study, for building a pore scale heterogeneous geomaterials map with diverse intersecting pores and minerals for further fluid transport simulations;

2) *Describing the coupled transport phenomena of the **System** (**T**, **H**, **C**) at the pore scale for heterogeneous sedimentary rocks.*

A lattice Boltzmann method (*LBM*) based multi-physics computational model is developed and implemented here as an effective algorithm to address these three fully coupled geological parameters. The model extends the conventional lattice Boltzmann model, and provides simulations including: fluid transport through a combination of different matrix structures with disparate permeability, heat transfer in bulk fluids and solid matrix, and the simultaneous presence of chemical reactions with reactive minerals. Through benchmarks and experimental validation, the model enables coupled **System (T, H, C)** modelling with the temporal evolution at the pore scale, subjected to thermal and chemical reaction (dissolution/precipitation) effects in ways that honor subsurface petrophysical conditions;

3) *Effective parallel computing for massive data sets generated from high resolution micro-CT scans.*

   A parallel supercomputing algorithm is developed to address massive data sets and the large scale simulations on supercomputers. Through various benchmarks and practical applications, the effective implementation of the parallel computational *XLBM* (extended *LBM*) platform has achieved a nearly-linear speedup and nearly-orthogonal extensibility, and it is effective to handle massive data sets from Gigabytes to Terabytes as an initial input in high-resolution or large scale computational analysis. The computing efficiency still reaches around 93.8% when 512 processors are used, which confirms the high scalability of the custom *XLBM* and provides capability for massive data sets analysis;

4) *Evaluating the 4D permeability and the sensitivity of sample size (scale).*

   A reliable *4D* permeability evaluation model is introduced with respect to the modelling of the general coupled problem **System** (**T**, **H**, **C**) and the resultant effect on the pore scale geo-structures (dynamic porosity change). Through the available experiments, the developed computational software provides reliable prediction for specific carbonic acid reactions: the *4D* permeability approaches a constant value when the whole system reaches the reactive transport equilibrium status over a long period of time (e.g. three years); and the sensitivity analysis of sample size (scale) on the representative parameter – permeability, shows that the permeability can be determined as the average parameter from the pore scale, when the size is large enough to reach the representative size.

The thesis presents a coordinated and extended multidisciplinary approach to coupled **System** (**T**, **H**, **C**) in fractured porous media. The methods and the algorithm developed in this study are general and can be extended to deal with a wide range of nonlinear coupled flow problems in porous media.

Declaration by author

This thesis is composed of my original work, and contains no material previously published or written by another person except where due reference has been made in the text. I have clearly stated the contribution by others to jointly-authored works that I have included in my thesis.

I have clearly stated the contribution of others to my thesis as a whole, including statistical assistance, survey design, data analysis, significant technical procedures, professional editorial advice, and any other original research work used or reported in my thesis. The content of my thesis is the result of work I have carried out since the commencement of my research higher degree candidature and does not include a substantial part of work that has been submitted to qualify for the award of any other degree or diploma in any university or other tertiary institution. I have clearly stated which parts of my thesis, if any, have been submitted to qualify for another award.

I acknowledge that an electronic copy of my thesis must be lodged with the University Library and, subject to the policy and procedures of The University of Queensland, the thesis be made available for research and study in accordance with the Copyright Act 1968 unless a period of embargo has been approved by the Dean of the Graduate School.

I acknowledge that copyright of all material contained in my thesis resides with the copyright holder(s) of that material. Where appropriate I have obtained copyright permission from the copyright holder to reproduce material in this thesis.

Publications during candidature

Journal Papers (published and under review)

1) Gao, J., Xing, H., Rudolph, V., Li, Q., & Golding, S. D. 2014. Parallel Lattice Boltzmann Computing and Applications in Core Sample Feature Evaluation. *Transport in Porous Media*, 107: 65-77. http://dx.doi.org/10.1007/s11242-014-0425-1
2) Gao, J., Xing, H. L., Tian, Z., Muhlhaus, H., 2014. Lattice Boltzmann modelling and evaluation of fluid flow in heterogeneous porous media involving multiple matrix constituents. *Computers & Geosciences*, 62, 198-297.
3) Tian, Z., Xing, H., Tan, Y., & Gao, J., 2014. A coupled lattice Boltzmann model for simulating reactive transport in CO_2 injection. *Physica A: Statistical Mechanics and its Applications*, 403, 155-164.
4) Gao, J., Xing, H. L., 2012. LBM simulation of fluid flow in fractured porous media with permeable matrix. *Theor. Appl. Mech. Lett*. 2, 032001.

Peer-reviewed Conference Full Papers and Oral Presentations

5) Gao, J., Xing, H. L., Li, Q., Rudolph, V., Golding, S. D., Scale Effect of 3D Heterogeneous Porous Media on Geo-Fluid Characteristics: Insight from Massively Parallel Lattice Boltzmann Computing (SPE-167043-MS). *2013 Unconventional Resources Conference and Exhibition - Asia Pacific*. Brisbane, Queensland, Australia. 11-13 November, 2013. http://dx.doi.org/10.2118/167043-MS
6) Gao, J., Xing, H. L., 2013. High performance simulation of complicated fluid flow in 3D fractured porous media using LBM. In: M. Daydè, O. Marques, and K. Nakajima (Eds.), High Performance Computing for Computational Science - VECPAR 2012 Proceedings, LNCS, Springer, Heidelberg, 7851, 93-104. http://dx.doi.org/10.1007/978-3-642-38718-0_12
7) Xing, H. L., Gao, J., Unconventional Gas Mining: Insights from Pore to Mine Scale Simulations. In: T. Mares, Eastern Australasian Basins Symposium IV. *Fourth Eastern Australasian Basins Symposium and Exhibition (EABS IV)*, Brisbane, Australia, (1-9). 11-14 September 2012.
8) Xing, H. L., Gao, J., Zhang, J., Liu, Y., 2011. Towards an Integrated Simulator for Enhanced Geothermal Reservoirs. ICS UNIDO, paper 3224 (10 pages).
9) Xing, H. L., Zhang, J., Gao, J., and Liu, Y. PANDAS and its New Applications in Geothermal Modelling. Australian Geothermal Energy Conference 2011, Melbourne, Australia.

Conference Abstracts and Posters

10) Gao, J., Xing, H. L., Pore Scale Investigation of Interaction between Fluid Flow and Fracturing along Faults for Earthquake Studies. *10th Annual Meeting of the Asia Oceania Geosciences Society (AOGS 2013)*. Brisbane, Queensland, Australia. 24-28 June, 2013.
11) Gao, J., Xing, H. L., Li, Q., Golding, S. D., Numerical Modelling and Evaluation of Pore Scale Geo-Fluid Behaviour in the CO_2 Geosequestration System (Poster). *CO2CRC Research Symposium 2012*. Sunshine Coast, Queensland, Australia. 27-29 November, 2012.

ANLEC* (*Australian National Low Emissions Coal Research and Development*) *Project reports

12) Dawson, G. K. W., Biddle, D., Farquhar, S. M., Gao, J., Golding, S. D., Jiang, X., Keck, R., Khan, C., Law, A. C. K., Li, Q., Pearce, J. K. , Rudolph, V., Watson, A., Xing, H. L., 2014. ANLEC Project 7-1110-0101: Achieving Risk and Cost Reductions in CO_2 Geosequestration through 4D Characterisation of Host Formations. Final Report. ANLEC R&D, Manuka, ACT, Australia, p. 140. (Peer reviewed research report).
13) Dawson, G. K. W., Sidiq, H., Pearce, J., Gao, J., Golding, S. D., Rudolph, V., Li, Q. and Xing, H. L., 2013. ANLEC Project 3-1110-0101: Review of laboratory-scale geochemical and geomechanical experiments simulating geosequestration of CO_2 in sandstone, and associated modelling studies Manuka, ACT, Australia: Australian National Low Emissions Coal Research and Development.

Publications included in this thesis

Gao, J., Xing, H. L., Tian, Z., Muhlhaus, H., 2014. Lattice Boltzmann modelling and evaluation of fluid flow in heterogeneous porous media involving multiple matrix constituents. *Computers & Geosciences*, 62, 198-297. - incorporated as parts of Chapter 3.

Contributor	*Statement of contribution*
Jinfang Gao (Candidate)	Wrote programs and ran simulations (100%) Wrote and edited the manuscript (65%) Provided analysis and interpretation (50%)
Huilin Xing	Gave comments and edited the manuscript (15%) Provided analysis and interpretation (30%)
Zhiwei Tian	Gave comments and edited the manuscript (15%) Provided analysis and interpretation (20%)
Hans Muhlhaus	Gave comments and edited the manuscript (5%)

Gao, J., Xing, H. L., 2012. LBM simulation of fluid flow in fractured porous media with permeable matrix. *Theor. Appl. Mech. Lett*. 2, 032001. - incorporated as parts of Chapter 3.

Contributor	*Statement of contribution*
Jinfang Gao (Candidate)	Designed conception (60%) Wrote programs and ran simulations (100%) Wrote and edited the manuscript (70%) Provided analysis and interpretation (50%)
Huilin Xing	Designed conception (40%) Gave comments and edited the manuscript (30%) Provided analysis and interpretation (50%)

Gao. J., Xing. H. L., Rudolph, V., Li, Q., Golding, S.D., 2014. Parallel Lattice Boltzmann Computing and Applications in Core Sample Features Evaluation. *Transport in Porous Media*, 107: 65-77. http://dx.doi.org/10.1007/s11242-014-0425-1. - incorporated as parts of Chapter 4 & 7.

Contributor	*Statement of contribution*
Jinfang Gao (Candidate)	Wrote programs and ran simulations (100%) Wrote and edited the manuscript (50%) Provided analysis and interpretation (40%)
Huilin Xing	Gave comments and edited the manuscript (15%) Provided analysis and interpretation (20%)
Victor Rudolph	Gave comments and edited the manuscript (15%) Provided analysis and interpretation (20%)
Sue Golding	Gave comments and edited the manuscript (15%) Provided analysis and interpretation (20%)
Qin Li	Gave comments and edited the manuscript (5%)

Contributions by others to the thesis

My advisors, Associate Professor Huilin Xing and Professor Sue Golding of the School of Earth Sciences, the University of Queensland, each contributed to editing the thesis prior to submission.

Professor Victor Rudolph of the School of Chemical Engineering, the University of Queensland, contributed to editing of Chapter 1 and 2.

Dr. Grant Dowson of the School of Earth Sciences, the University of Queensland contributed to editing of Appendix-A and Dr. Qin Li of the Environmental Engineering & Queensland Micro- and Nanotechnology Centre, Griffith University contributed to editing of Appendix-B.

Dr. Alexandra Golab and FEI Lithicon for provision of the micro-CT data sets of sandstone samples from Chinchilla 4 well that were used in Chapter 4, 6 and 7 for flow and chemical reaction analysis.

Professor Victor Rudolph and Mr. Luc Turner of the School of Chemical Engineering for provision of the coal sample micro-CT images used in Chapter 7 for chemical reactions and 4D permeability analysis.

Professor Jian Hou of China University of Petroleum (Huadong) for provision of the micro-CT images for digital sandstone sample reconstruction and flow analysis in the early stages of my PhD candidature.

Statement of parts of the thesis submitted to qualify for the award of another degree

None.

Acknowledgements

I wish to express my great gratitude to all these people who have supported and inspired me to have made this thesis possible.

First and foremost, I would like to express the deepest appreciation to my supervisors, Associate Professor Huilin Xing, Professor Sue Golding, and Dr. Qin Li for their guidance and great support during my research. As my principle supervisor, A/Prof. Huilin Xing introduced me to this interesting field of research on geodynamics and modelling in the early stages of my PhD candidature, and to learn how to properly work in a scientific way. He helped me to see the big plan of my work, and also led me into a great source of knowledge spinning from many scientific disciplines. This has significantly broadened my view. Without his sustained guidance, great support and encouragement, I would not have finished this PhD study.

I must acknowledge and thank my associate supervisor, Professor Sue Golding. She, with great patience and indeed enthusiasm, inspired me to take an adventure in the 'geology world'. Having followed her advices, I have started to understand more geology knowledge related to my research, especially in CO_2 sequestration. She also helped me a lot in obtaining micro-CT images of sandstone samples from the Chinchilla 4 well (Queensland, Australia), which greatly has supported my research study. I am also amazed by her abilities as an excellent project manager with great planning skills that make her an impressive and reliable supervisor.

I am also very grateful to Dr. Qin Li. She was quite supportive and helpful in many questions regarding my thesis research. Besides, she cares more about my personal life and also gave me lots of suggestions including overseas lives and personal development, which was pretty impressive.

I would also like to express my deepest appreciation to Prof. Victor Rudolph for his generous assistance, encouragements and advices during my study, which were greatly appreciated. Especially, he helped me a lot in conceptualizing the outline of Chapter one when I was struggling to sort it out. I am also quite grateful to Victor for his suggestions and enlightening discussions throughout my candidature. Thank you very much, Victor.

I would also give my special gratitude to Dr. Zhiwei Tian from the China University of Geosciences (Wuhan). Being an expert in lattice Boltzmann modelling, he helped me a lot in understanding the basic theory of lattice Boltzmann method when he had a one-year visiting at the Centre for Geoscience Computing. He also gave me lots of suggestions and comments on my first journal paper. Without his assistance on my research project, I would not have made rapid progress on my research in a short time.

I am also grateful to Dr. Alexandra Golab and FEI Lithicon, Prof. Victor Rudolph and Mr. Luc Turner, Prof. Jian Hou of China University of Petroleum (Huadong), for provision of the micro-CT data sets, and our ANLEC project members Dr. Grant Dawson, Dr. Julie Pearce, Ms Susan Farquhar for their discussions and useful suggestions during my candidature.

I would also thank Prof. Joan Esterle particularly, for her generous advices and consideration on both my study and personal life all the time, and also Prof. Gregg Webb for his support on my confirmation, and also warm suggestions on my research and career development. Special thanks to Prof. Steve Tyson, A/Prof. Gideon Rosenbaum, Prof. Hans Muhlhaus for their advices about how to do research. I am also thankful to Ms Tracy Paroz and Ashleigh Paroz for their great support during my candidature, which was quite impressive.

I would express my gratitude to Dr. Kevin Welsh. I have taken his course 'Sedimentary Petrology and stratigraphy' as recommended by Prof. Sue Golding and was shocked by his great teaching skill. He is very nice with great patience to the students, and he also took us to interesting field trips and lab experiments. Thanks to Kevin, I got a full mark seven at this course. More importantly, He inspired me in learning geology knowledge, which was found quite essential in my later research.

Great thanks to Prof. Xuebin Chi from the Chinese Academy of Sciences for his sustained support and encouragement so that I am always brave and confident enough to challenge myself, and to be a better person. Thanks to Prof. Hongwu Zhang from Dalian University of Technology, his generosity, foresight and great leadership has significantly impressed me and inspired me in the future life.

I would thank A/Prof. Lutz Gross, Dr. Louise Olsen-Kettle, Dr Jingyu Shi, Mr. Ziping Fang, Dr. Joel Fenwick, Mr. Cihan Altinay for their assistance during my stay at Centre for Geoscience Computing. I would also thank my friends Dr. Vince Boros, Dr. Stephanie Hamilton, Dr. Lin Gao, Yan Liu, Xiangchong Liu, Nianchao Zhang, Zhiting Han, Quanshu Li, Wei Zhou and Qin Li for their help during my life in Brisbane.

I wish to acknowledge financial assistance provided through ARC Discovery Project (DP110103024), Australian National Low Emissions Coal Research and Development (ANLEC R&D) and Virtual Near Wellbore Project of CCSG. I also gratefully acknowledge the financial support by the International Postgraduate Research Scholarships and the Australia Postgraduate Award scholarship.

Last but not the least; I would like to thank my family for being a constant source of emotional and moral support during my candidature and my life. They encourage me to pursue my dreams and to be a persistent, optimistic and compassionate person to face all challenges. The thesis could not have been done without their endless and selfless love.

Keywords

Lattice Boltzmann method, nonlinear coupled flow dynamics, heat transfer, chemical reactions, heterogeneous porous media, digital core, *micro-CT* and *QEMSCAN*, Representative Elementary Volume (*REV*), *4D* permeability, parallel computing

Australian and New Zealand Standard Research Classifications (ANZSRC)

ANZSRC code: 040403 Geophysical Fluid Dynamics (80%)

ANZSRC code: 091406 Petroleum and Reservoir Engineering (20%)

Fields of Research (FoR) Classification

FoR code: 0404 Geophysics (100%)

Be Humble to the World.

Be Passionate to our Dreams.

我们 来于尘土 归于尘土

却永远拥有 星空般高远的 梦想

Table of Contents

List of Figures

List of Tables

List of Abbreviations

LBM	Lattice Boltzmann method
XLBM	Extended lattice Boltzmann method
REV	Representative Elementary Volume
BGK	Bhatnagar-Gross-Krook model
MRT	Multiple-relaxation-time model
N-S	Navier–Stokes equations
K-C	Kozeny- Carman
Re	Reynolds number
Pr	Prandtl number
Ra	Rayleigh number
Da	Darcy number
I/O	Input/Output
MPI	Message Passing Interface
CBM	Coal bed methane
micro-CT	Micro-computed tomography
QEMSCAN	Quantitative evaluation of materials by the Scanning Electron Microscopy
BSE	Backscattered electron
SEM	Scanning electron microscope
EDS	Energy dispersive X-ray spectroscopy
SIP	Standard identification protocol
MD	Molecular Dynamics
DDF	Double-distribution function models
MC	Monte Carlo method
PD	Pore Network method
DPD	Dissipative Particle Dynamics

Chapter 1 Introduction

1.1 Introduction and Overview

Fluid transport processes in the natural subsurface environment are commonly exploited for material recovery, for example of potable water or valuable brines (Kaufman and Orlob, 1956; Patrick et al., 1987; Keating et al., 2012; Vengosh et al., 2014), or for energy, e.g. geothermal heating or cooling (Palmer et al., 1992; Bedrikovetski et al., 2005; Zhao et al., 2009; Koh et al., 2011). The recovery of hydrocarbons in the form of crude oil or natural gas (Graue, 2001; Michael et al., 2010; Mokhatab and Poe, 2012) represents one of the single largest classes of human industrial activity, and underpins modern civilization.

For modelling subsurface transport processes, multiple dimensional scales are required. For example, in coal and shale, and for CO_2 geosequestration in these reservoirs, which is the main focus of this work, the base physical processes operate in geometric terms at ~ *nm* scales, where surface sorption and diffusion through nano-porosity operate (Loucks et al., 2009); ~ *mm* scales for transport in cleats and cracks (Han et al., 2010); ~ *cm* scales for typical laboratory measurements and characterisation of core samples (Pearce, 2012; Farquhar et al., 2013; Farquhar et al., 2014); ~ *m* scales relevant to near well environments (Gaus, 2010); tens of meters for typical reservoir models (Vasco et al., 1999), and ~ *km* for basin scale models (Juanes et al., 2010). In temporal terms, the dynamics may change from microseconds or less for surface equilibration, to decades for reservoir depletion.

Nanoscale study deals primarily with surface area effects on materials, and refers to structures with a length scale applicable to nanotechnology, whereas fluid viscous transport is governed significantly by diffusion at the pore scale, and by viscous flow at the cleat or crack network scale. These small scales are the dominant physical mediator of transport. Hence, many scientific and practical engineering decisions for the basin, reservoir and near-wellbore models, which dictate resource and field development at larger scales, are generally represented by properties obtained from core scale measurements (Golab et al., 2010; Perrin and Benson, 2010; Knackstedt et al., 2012), which are themselves already averages of the nanoscale physical processes governing fluid flow.

Providing appropriate averages as reliable and representative parameters at any given scale raises a number of key issues that still remain as problems: (1) appropriate modelling of the transport phenomena at the physically important scales, importantly, multi-physics coupling of ‘fluid flow (**H**)

– thermal effect (**T**) - geochemical interactions (**C**)' at the pore and fracture flow scales; and (2) suitable averaging methods for upscaling the flow physics from ~*mm* to ~*km* scales.

This thesis is directed at the former problem: modelling fluid flow in ways that honor subsurface petrophysical conditions, at the micron to centimeter scales. It considers realistic fluid transport networks, and coupled flow processes with solid interactions in non-absorbing, single phase transport. Physically, the work considers sedimentary rocks and coals as the reservoir rocks, and water, gas (methane) and CO_2 as the fluids, representing important stages in coal bed methane (CBM) recovery and CO_2 enhanced CBM and CO_2 geosequestration operations. To accomplish this requires:

1) actual pore scale networks for flow, as revealed by *micro-CT* scanning with *QEMSCAN* mineral analysis;
2) methods to handle massive data sets in a parallel processing and computing environment;
3) a fluid transport model for fluid flow in heterogeneous geomaterials, implemented here through the lattice Boltzmann method with a nearly-linear speedup and nearly-orthogonal extensibility; and
4) a coupling model for describing interactions of fluid flow, thermal effect and geochemical reactions, together with resultant effect on the pore scale geo-structures (e.g. porosity change).

Secondly, the work also provides a discussion on upscaling research from ~*mm* scale to larger scales, by providing reliable and representative parameter, most importantly, for permeability. This integrates the former study of 'fluid flow-thermal effect-chemical reactions' modelling and resultant effect on porosity and flow dynamics through pore networks.

1.2 Interdisciplinary Approaches Required

1.2.1 Modern imaging technology: pores and geomaterials

1.2.1.1 *Micro-CT* and microstructures

The micro-computed tomography (*micro-CT*) technology, also known as *high-resolution X-ray tomography* or μCT, is an advanced method for measuring pore scale features: grain size, sorting degree, pore-filling clay, distribution of heavy minerals, and particularly pore connectivity important for flow networks (Wellington and Vinegar, 1987; Knackstedt et al., 2012; Golab et al., 2013a; Golab et al., 2013c). Besides, it provides a non-destructive and efficient way to characterize features of microstructures.

The *micro-CT* uses the absorption intensity of *X-ray* through different materials or object textures. In the process, the primary entity measured is the *X-ray* absorption defined as the attenuation coefficient. The measured attenuation coefficient is then correlated to the mass density of a special segment, due to their disparate mass contents. Thus, the *X-ray* intensity of penetration and non-penetration through these structures can be compiled into density marked gray-scale (black/white color) maps (Wellington and Vinegar, 1987; Kalender, 2006).

In the *micro-CT* scanning, the scanning resolution represents the spacing of adjacent elements of the scanned volume. The resolution is commonly dictated by users on the basis of different scanning cases, for obtaining sufficient microscale information. In general, it trades off time to acquire the image against the detail that makes up scanned images (usually in the form of a rectangular array of equal-sized elements, known as picture pixels). High resolution scanned images carry much more information and consequently require more storage space, memory size and computational processing to transform raw attenuation to density maps and visual images. These steps often represent the practical limits of the tomography. As a result of *micro-CT,* pores, fractures and frame skeletons can be observed on these scanned images.

1.2.1.2 *QEMSCAN* and geomaterials mapping

Quantitative evaluation of materials by the Scanning Electron Microscopy *(QEMSCAN*) technique allows quantitative mineralogical analysis of complex grain mineral types and inter-granular materials, including carbonates cement and lithic fragments (Corcoran, 1989; Pirrie et al., 2004; French et al., 2008; Field and Atkins, 2012). It integrates backscattered electron (*BSE*) information from a scanning electron microscope (*SEM* for imaging) and energy dispersive *X-ray* spectroscopy (*EDS* for elemental analysis) to characterize the petrophysical information of the samples.

The *QEMSCAN* method identifies mineral information within a thin section using the beam and provides repeatable rock texture analysis. For example, the point measured by the beam on the sample is assigned to the appropriate mineral by comparing with the standard identification protocol (*SIP*) (Goodall, 2008); it is then marked with the corresponding color and name of the mineral. A mineralogical map is thus generated step by step by rastering the beam over the sample. Similar to the *micro-CT* technique, the spacing between adjacent beam points can be controlled, and a small spacing provides more detailed mineralogy of fine-grained lithic fragments (but at the cost of beam time and computational complexity).

In geomaterials mapping, overlaying the *QEMSCAN* image on the corresponding photomicrograph enables the differentiation of rock fragments or complex grains, and also mitigates mismatched

grains (Allen et al., 2012). Both plain light and cross polarized photomicrographs are used to provide identification of rock fragments (plain light) and distinguish between polycrystalline and monocrystalline quartz (cross polar), amongst other techniques.

1.2.2 Parallel processing and computing: massive data sets

3D micro-CT scans with *QEMSCAN* mapping deliver a high level of detail for samples at higher resolutions. This also generates enormous initial digital data sets, which in turn require much more processing in later computational simulations. For example, a 1 *cm* scale cubic sample is likely to generate around 125 *Gigabytes* of initial digital data at a 4 μm voxel size (resolution of 2500 × 2500 × 2500). Conventional personal computers or small local work stations are unsuitable for such computational duties, providing insufficient computational resources by way of processor performance, memory demands, and disk storage. Moreover, massive data sets in this work require special Input/Output (*I*/*O*) access and effective data communication among multiple processors. Effective parallel computing is essential for this task.

In parallel computing, scalability and computational efficiency (Amdahl, 1967; Rodgers, 1985; Gustafson, 1988) are used to evaluate the modelling performance. Scalability is measured by speedup, describing the correlation between the problem size and the number of processors. The best speedup is an upward linear line, representing orthogonal design of algorithms and computing modules. Here, orthogonality guarantees the size of the problem is proportional to the number of processors used. Computational efficiency relates to the proportion of time consumed on data communication among different processors compared with actual computation. A specialized parallel algorithm with high scalability and computing performance is essential for implementing massive data sets processing and computing in this thesis work.

1.2.3 Multi-physicochemical coupled processes: System (T, H, C)

The underground reservoir rocks possess many inherently heterogeneous mineral components distributed in complex and often disturbed patterns, which complicates the description of individual processes and their inter-connection and -dependence. Multi-physicochemical coupled processes commonly occur in these natural subsurface systems, involving coupling and interactions of thermal effect (**T**), hydraulic flow (**H**) and chemical reactions (**C**) in highly heterogeneous geomaterials. Such a coupled **System (T, H, C)** determines alteration of pore scale petrophysical structures and resultant parameters at representative scales, which dominates the subsurface flow behaviour.

In general, fluid flow in heterogeneous geomaterials is dictated by the pore connectivity, grain contacts and material properties at the pore scale. Meanwhile, geothermal process such as heat

transfer can affect flow dynamics because of the convection through pore networks, and the conduction through pores, frame grains or other lithic fragments. This leads to dynamic alterations in flow behaviour. Besides, the heat transfer influences disparate potential chemical reactivity rates in the acid environment, which is associated with the solubility of acid fluids. Moreover, geochemical reactions result in dissolution or precipitation of reactive phases (e.g. carbonates), changing the petrophysical structures (porosity) and consequently the flow dynamics (Kissinger, 1957; Hahn and Shiu, 1986; Gupta et al., 1990; Park et al., 1991; Cansell et al., 1993; Hobbs et al., 2000; Valo et al., 2004; Li et al., 2008; Yin et al., 2011). Chemical fluid-rock interactions add to the dynamic complexity of fluid transport through geomaterials. With respect to the coupled **System (T, H, C)**, micro-changes have great influence on the fluid dynamics at the pore scale, and further evaluation of representative parameters at larger scales.

1.2.4 Modelling framework: coupled System (T, H, C) dynamics at the pore scale

There are commonly two types of modelling approaches: empirical modelling and mathematical functional relationship modelling. Empirical modelling involves observation, dependency and agency (Nesić et al., 1997; Saptoro et al., 2006). The first step is to get observation data of the target system; and the second step is to organize the data through scatterplots of the data, which are regressed to generate linear, logarithmic or more complex functions for providing dependency relationships. Finally, the empirical methods use agency to try and clarify the dependencies by matching changes and outcomes. These methods focus on the observation of a system, and try to find dependent and statistically relevant relationships within the data. It depends extensively on the observation data, which usually brings strong evaluation bias; furthermore, these relationships produced by the empirical modelling are not necessarily mechanistically-relevant for forecasting or describing trends.

In most cases, mathematical modelling is superseding empirical modelling. Mathematical modelling focuses on mechanisms that relate to the system physics, as such better captures the quantitative principles that underlie a process or system. Mathematical models based on fundamental theory can be verified by observations or experience from empirical models, and provide means for forecasting and predicting trends. They have the very distinct advantage in revealing processes that are important, but cannot be accessed by physical measurement.

Within the mathematical modelling, there are mainly three sub-approaches operating modelling at appropriate length scales: microscale modelling (~ *nm* to ~ *mm*), pore scale modelling (~ μm to ~ *cm*) and macroscale modelling (~ *m* to ~ *km*). These three approaches have their respective

strengths at different Knudsen numbers (*Kn*), where *Kn* is the ratio between the mean free molecule path and a characteristic length scale representing the system heterogeneity (e.g. the obstacle size).

The macroscale modelling approaches depend on finite difference, finite volume and finite element methods (Joseph et al., 1981; Nithiarasu et al., 1997) amongst many variants, which are commonly considered as 'classical' modelling methods (or Navier-Stokes methods). Those approaches solve continuum-based partial differential conservation equations (e.g. of mass, momentum and energy) using some form of specific numerical discretization (Connor and Brebbia, 1976; Huyakorn and Pinder, 1986; Ferziger and Perić, 1999; Lewis et al., 2004; Reddy and Gartling, 2010), and have been applied broadly in the macroscale simulation of subsurface flow (~ *m* to ~ *km* scale). From the perspective of a macroscale view, representative parameters characterized from smaller scales are used as 'static' and 'statistical' characters; in reality, however, changes of these features tend to happen in many cases. For instance, rock texture and mineral distribution, grain sorting and contacts, pore or fracture networks, and fluid mixtures amongst many others, all have simultaneous interrelated influences on petrophysical structures and flow profiles. Those often lead to significant variations of resultant representative parameters that are used as input parameters at macroscopic scales. Macroscale modelling is generally weak in its consideration and treatment of these issues.

In contrast, the microscale modelling takes its perspective at the level of atoms, molecules or micro-particles, and seeks to investigate information at microscales. This involves modelling methods from ~ *nm* to ~ *mm* scales. For instance, the focus of Molecular Dynamics (*MD*) (Koplik et al., 1988; Hirshfeld and Rapaport, 1998) is on fluid dynamics simulations at ~ *nm* scales, by modelling the movement of large numbers of atomic and molecular scale 'particles' on the basis of an intermolecular potential; and these particles move freely at any direction and interact with other particles according to the classical Newton's laws of motion. Other microscale modelling approaches such as Dissipative Particle Dynamics (*DPD*) (Hoogerbrugge and Koelman, 1992; Dzwinel and Yuen, 2000) and the direct simulation Monte Carlo (*MC*) (Wagner, 1992; Degond and Dimarco, 2012) are off-lattice pseudo-particle methods in conjunction with the Newtonian dynamics. Although those microscale approaches have the ability for theoretically simulating continuum hydrodynamics, it is significantly restricted in molecular scale applications due to the limitation of intrinsic nanoscale modelling of particle-particle interactions.

The pore scale modelling is aimed at providing the exchange, aggregation and disaggregation of information between the microscale and the macroscale. There are broad applications of pore scale methods, such as the pore network (*PD*) (Fatt, 1956; Sugita et al., 1995; Blunt, 2001; Blunt et al.,

2002) and the lattice Boltzmann (*LB*) (Succi, 2001; Sukop and Thorne Jr, 2007)., enabling investigations from ~ μm to ~ cm scales.

Pore network modelling operates a pore-volume network from a target object, by describing pore volumes, pore throats and connecting channels. The fluid flow in the connecting pores is governed by hydraulic potential, the resistance in pore volumes and some other external forces. It simplifies objects as pore structure (tortuosity) and ignores material interactions. The weakness of the method is lack of understanding in the fundamental multi-physicochemistry, and operates only as a 'static' model without providing description of dynamical geo-structures alterations regarding thermal and chemical reaction effect. These oversimplified approximations limit its usefulness to reasonably describe complex flow transport.

Regarding real geological systems, the main challenge for computational analysis is to account for the heterogeneity of geomaterials (including geometry, topology and the presence of multiple diverse physical and chemical components). This heterogeneity occurs at all scales, but fluid is most affected by variations at the pore scale. A major issue is how to construct an appropriate model to describe pore scale flow dynamics in sufficient detail to reflect reality. Characterisation of a real geomaterial by advance imaging like high-resolution X-ray micro-CT/QEMSCAN enables the quantification of pore scale features, including microstructural information such as grain sizes and sorting, pores, and tortausity, as well as the distribution of multiple different geomaterial compositions. This therefore permits the construction of "digital reservoir" rocks. The lattice Boltzmann method (*LBM*) applied here is capable of simulating fluid flow through such complex pore networks.

The *LBM*, also known as lattice gas automata, has applications across scales, but in the present context is applied at the pore scale flow dynamics. As with *MD* and *DPD* methods, *LBM* describes fluid dynamics using small cells containing fictive particles interacting through consecutive propagation and collision processes with their neighbors over discrete lattice grids, instead of solving the Navier-Stokes equations or its simplified form from the macroscale view. *LBM* uses the kinetics mechanism derived from the microscale, incorporates detailed information at the microstructure level, occupies a position between the full molecular dynamics and macroscopic descriptions, and therefore provides true mesoscale modelling; it is partway between full molecular dynamics simulations and conventional macroscopic depictions of reservoirs, and provides a means to examine viscous flow behaviours in elements with arbitrary mass (in this work, larger than single molecules, but much smaller than the global flow field) to provide a reference base for representative parameters to then be used in macroscale models.

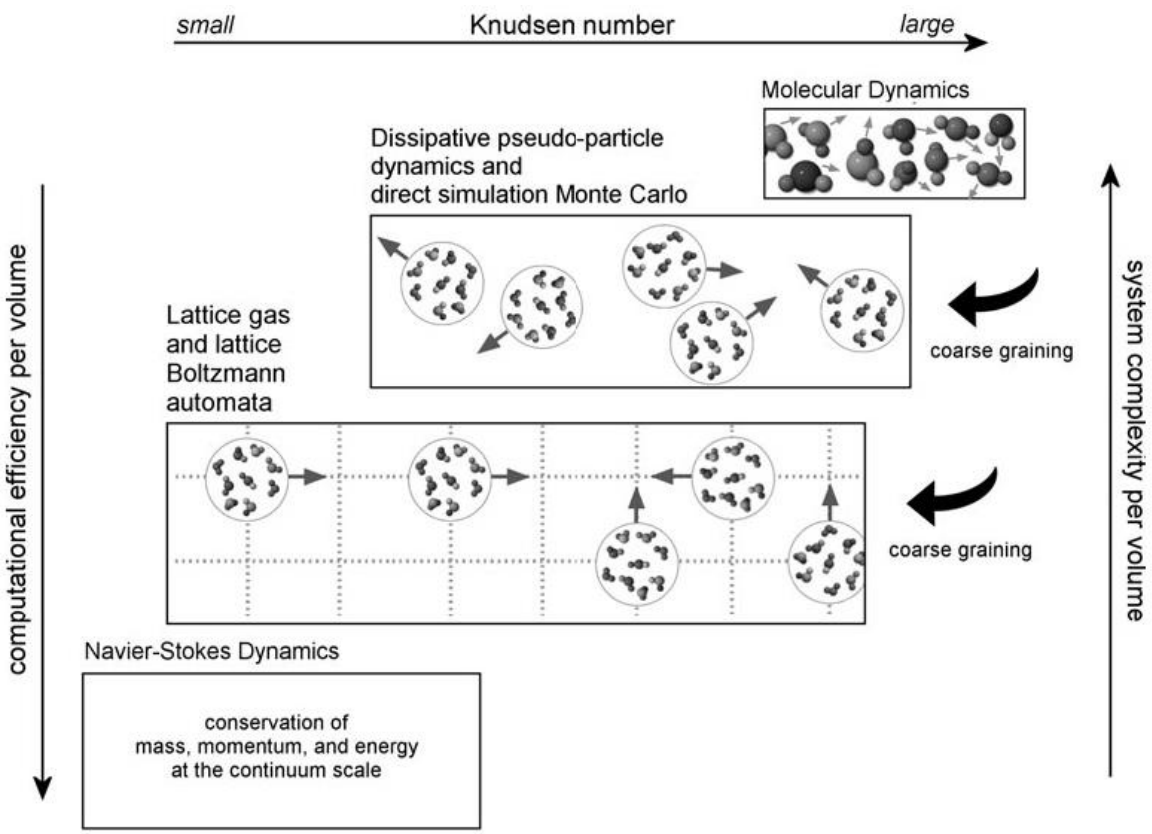

Fig. 1-1 Multiple approaches for computational fluid dynamics with their preferred range of applicability (Raabe, 2004).

Fig. 1-1 has shown relationships between the pore scale *LBM* and the other two kinds of modelling (the microscale *MD* or *DPD* and the conventional macroscale approaches). The *LBM* discretizes the macroscale continuous space and time with countable directions, and simulates the fluid as coarse-grained fictive particles. As the direct generalization of so-called "particles-in-cell", a lot of properties can be assigned to each particle population, modelling exchange of mass, momentum, energy, spin, etc. It does not guarantee the convergence of the ensample to any continuous system. Therefore, a lot of publications are devoted to mathematical convergence of the modelled ensample to stochastic system of *PDEs*; by using the Chapman-Enskog procedure, the Navier–Stokes equations can be derived from the *LBM* equations in the incompressible limit that density variation is small (slightly compressible fluid)(Aharonov and Rothman, 1993; Succi, 2001; Guo et al., 2002; Kang et al., 2002a; Sukop and Or, 2004; Aaltosalmi, 2005; Gao et al., 2014a; Tian et al., 2014). Those methods gain extreme importance during the last decade, with high rise of the computational capacities, when a lot of particles can be handled.

The *LBM* operates a pore scale study of both flow dynamics and geomaterials detail, and incorporates many essential characteristics of realistic microscopic processes. It examines flow dynamics and geomaterials at the mesoscale incorporating many essential characteristics of the real

processes, including accounting for fundamental flow mechanisms in real fluid transport networks having pore scale heterogeneous structures. It also provides averaging methods for upscaling the flow physics from pore scale to macroscale. Moreover, it permits coupling of multiple physical processes, such as thermal interactions, chemistry changes, solute transport, fluid interactions with complex geomaterial surfaces, and alterations of pore scale petrophysical structures related to those coupled processes. Furthermore, utilization of the particle description or the kinetic equations in the *LBM* over discrete lattice grids also provides advantages in fully parallel algorithms for massive data sets cases, thereby making it amenable to supercomputer processing. These issues are all elaborated later in this dissertation.

1.3 Thesis Structure and Summary

The thesis documents the numerical investigation of appropriate modelling of the nonlinear coupled pore scale **System (T, H, C)** problems in heterogeneous geomaterials and resultant impacts. An interdisciplinary approach spanning fluid transport, thermal effect, chemical reactions, modern imaging technology, numerical computing and advanced computational science is applied. The thesis has eight chapters, and correlations of main Chapters 3-7 are shown as Fig. 1-2.

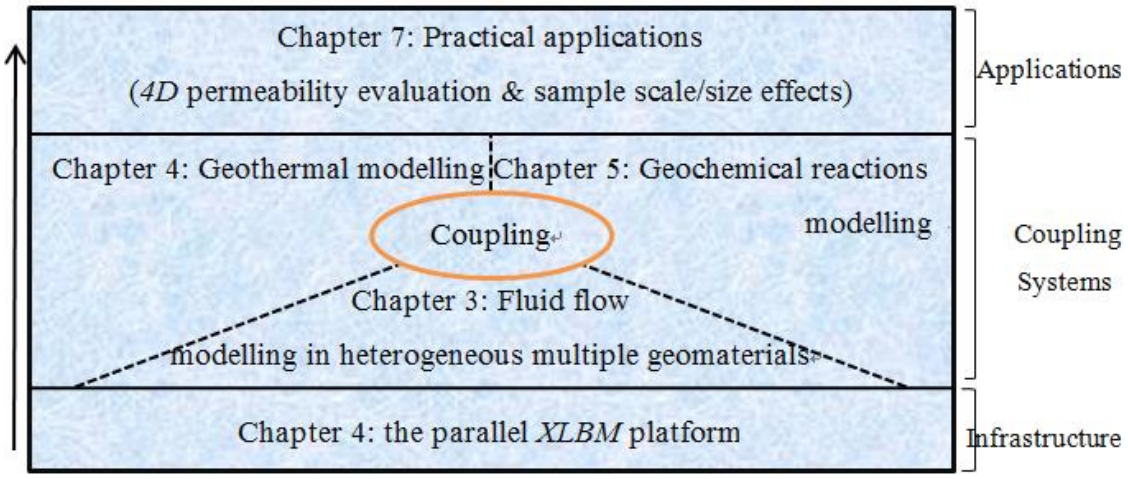

Fig. 1-2 Correlations of main Chapters 3 to 7 (arrow indicates the inter-connection and -dependence).

Chapter 1: an introduction and an overview of this research.

Chapter 2: a literature review, providing background and current state of knowledge.

Chapter 3: an eXtended *LBM* (*XLBM*) based model for modelling fundamental fluid transport (**H**) in pore scale heterogeneous geomaterials. This includes description of heterogeneity and

geomaterials with different permeability, pore scale flow dynamics on each *2D* pixel (or *3D* voxel) by furthering the conventional *LBM* together with material localization method, multiple contact boundaries and the statistics theory; it also includes the reconstruction of digital samples from *micro-CT*/*QEMSCAN* images. The model is implemented as a custom *XLBM* platform, serving as the basis for study of **System (T, H, C)** issues.

Chapter 4: a parallel solution for massive *3D* data sets processing and computing (from high-resolution digital samples), and its implementation into the custom *XLBM* for running on supercomputers (parallel *XLBM*). It includes: a special Input Preparation module as pre-processing, designed for reconstructing and re-decomposing massive data sets into required blocks; an effective parallel computing and data communication scheme as Run-time Control, introduced with ideal nearly-linear speedup (scalability); a memory-saving scheme for effective data management and visualization. A pore scale study is conducted for the sensitivity analysis of a digital core sample regarding massive data sets, including sensitivity of: *micro-CT* voxel size on sample composition, geomaterial properties on pore scale fluid dynamics. Through practical applications, the parallel *XLBM* is effective to handle massive data sets from *Gigabytes* to *Terabytes* as an initial input; and the computing efficiency still reaches around 93.8% when 512 processors are used.

Chapter 5: modelling of the coupled **System (T, H)** problem, including: pore scale geothermal process (conduction and convection) through pores and solids (or minerals) in heterogeneous porous media, and interactions between the fluid transport and thermal effect. The thermal module focuses on the evolution of heat transfer through multiple geomaterials involving pore structures and materials with respective intrinsic permeability. Similar to that in the fluid flow (**H**) field, each lattice node also has its own thermal property comprising the whole heat transfer (**T**) field due to the description of material localization. The thermal module is planted into the custom parallel *XLBM* providing a compatible coding interface for fluid flow and thermal effect coupling. Through benchmarking and verifying, the model is further used for two applications. The results have shown: evolution of temperature inside multiple geomaterials occurs significantly different because of the influence of different intrinsic geometry and geomaterial distributions. Specially, the evolution of temperature inside the impermeable solid is slower than that in geomaterials with higher permeability; and the heat evolution in porous media is far behind the fluid transport before reaching their respective equilibrium status.

Chapter 6: modelling of the coupled **System (T, H, C)** problem, including: acid fluid interactions on reactive and non-reactive mineral surfaces, solid-phase dissolution and mass transfer, and resultant porosity change. A general geochemical reaction model is deduced and implemented in the

parallel *XLBM* code, and then specified as a CO_2-water-rock system (involving reactive calcite, and non-reactive quartz, feldspars or other lithic fragments), which was verified against results from a laboratory experiment for CO_2 sequestration study (carried out by the University of Queensland). According to the results, the following conclusions can be drawn: the reaction concentrates in the region at contact surfaces with the acid fluid (carbonic acid), and some carbonic acid penetrates towards the centre of sample along the dissolved cleavages between the main aggregate and other non-reactive matrix; the calcite has been dissolved very quickly in the first few weeks and then experiences a gentle dissolution stage, which significantly relates to the reaction front meeting numerous small calcite-cemented areas or narrow cleavages that has slowed down the dissolution progress; the modelling system reaches the reaction equilibrium status in around 1440 days, and creates a porosity enhancement from 1.1% to 10.7%; whereas around 7.4% of the calcite is un-affected due to the lack of connectivity with the open pores or other dissolved calcite structures, where the acid fluid cannot access. The proposed model can be extended to study multiple reactive minerals with disparate reactivity rates, and can provide predictive simulations beyond the time range of experiments.

Chapter 7: a permeability study based on the pore scale coupled **System (T, H, C)**, including: practical applications of the developed computational model in *4D* permeability measurement for acid stimulation of a coal sample (in situ carbonates distribution determined by the *micro-CT*/*QEMSCAN*), and analysis about the sample scale (size) effects on the evaluation of representative parameter – permeability. The work in this chapter confirms the assumption that the measured permeability gradually approaches a constant value when the sample size reaches the *REV* scale or larger. Here, the critical sample size that provides the *REV* scale permeability is defined as the corresponding *REV* sample size. This study also confirms the capability of the proposed model in describing the coupled processes and resultant impact on the porosity and permeability changes, which builds a link between the pore scale and the *REV* scale for further reference for typical laboratory measurements on core samples at centimeter scales, near-well environments at meter scales, or typical reservoir models at tens of meters scales and basin models at kilometer scales.

Chapter 8: a summary of conclusions from previous chapters, and suggestions for future directions regarding this research work.

1.4 Contributions of This Work

The thesis presents a coordinated and extended multidisciplinary approach to coupled fluid flow-thermal effect-chemical transport in natural, fractured sedimentary rocks and/or coals. To accomplish this, it combines advanced modern imaging to derive the pore scale petrophysical structures, and the lattice Boltzmann (*LB*) computational method to implement spatial and temporal evolution of the fluid transport within this structure, including under the influence of geothermal and geochemical conditions. The massive data sets that need to be handled for this require specialized supercomputing techniques that form part of the development. The final result is the implementation of an effective custom parallel *XLBM* computational and modelling platform.

Significant and time consuming aspects of this work have included the thorough and meticulous effort required to implement the computer coding, entailing detailed familiarity and understanding of every aspect of the physics and chemistry within the simulation, followed by mathematical rendering and then coding. Whereas many parts of this do not represent new discovery or knowledge, the synthesis of all the parts into a working simulation represents a substantial outcome and assembly of diverse knowledge.

The work also contains novel aspects, which are further elaborated below.

1.4.1 Parallel *XLBM* and implementation on supercomputers

The whole thesis work is implemented within a custom computing platform, parallel *XLBM*. The platform incorporates functional extensions and statistics description into the conventional *LBM*, and provides effective coding interfaces for more complex and easily extended multi-physicochemical studies.

It briefly includes three functional modules: (1) an Input Preparation scheme, for automatically re-decomposing and reconstructing massive initial structural data sets from high-resolution *micro-CT*/*QEMSCAN* images; (2) an efficient Run-time Control scheme including parallel computing algorithm and its implementation on supercomputers with an overlapped data communication module, for effectively coupling ‘fluid flow-thermal effect-geochemical reaction’ simulations with ideal nearly-linear speedup and nearly-orthogonal extensibility; and (3) a memory-saving scheme for effectively reducing memory consumption in run-time and visualizing significantly computing outputs.

1.4.2 *4D* permeability evaluation

For engineering purposes, many practical engineering decisions and analysis are done at much larger scales using a representative parameter, most importantly, permeability. Permeability is functionally dependent on pore connectivity and tortuosity in the pore networks. In general, reservoir rocks have strong *3D* anisotropy, which can be evaluated by directional permeability defined as *3D* permeability. Moreover, coupled **System (T, H, C)** processes affect the porosity changes and flow dynamics through pore networks, and have a dynamic effect on directional permeability over the time scale (the fourth scale). All of these factors may result in dynamical permeability changes at a *4D* scale (*4D* permeability).

With an insight gained from a range of nonlinear coupled pore scale processes in heterogeneous geomaterial structures, it is feasible to model the trend of *4D* permeability variation to a condition where the whole system involving coupled processes reaches a relatively equilibrium status through an 'unsteady' dynamic phase. Analysis and evaluation of the *4D* permeability is conducted as a contribution of the thesis work to fluid flow modelling in ways that honor subsurface petrophysical conditions, at the micron to centimeter scales, where even small changes of the pore scale structures are likely to trigger significant permeability variation at larger scales.

1.4.3 Sample scale (size) effects and massive data sets computing

There is currently limited capacity for upscaling from pore scale (which is physically where changes occur) to laboratory scale (where measurements of properties are typically done), and to field scale (simulations that are operationally important).

This work is primarily focused on the pore scale, where *micro-CT* provides the flow path information at resolutions in the micron scale. An important question is what minimum sample scale (size) is necessary to retain physical structure fidelity (e.g. pore size and tortuosity) and provide reliable and representative transport calculations (e.g. directional permeability) for upscaling to be useful for comparison and validation against laboratory characterizations. At the micron scale resolution, the data size for *micro-CT* scans and the computational load for flow simulation become unwieldy, even impossible, when the overall sample size exceeds the ~ *cm* scale. This then needs to be further upscaled.

The permeability is sensitive to the sample scale (size). As the sample size increases, the measured permeability gradually approaches a constant value until the sample size reaches a certain scale or larger. Then this critical sample size is defined as the corresponding representative sample size, also known as the Representative Elementary Volume (*REV*); it can provide reference for typical

laboratory measurements on core samples (~ *cm* scales), near-well environments (~ *m* scales), or typical reservoir models (~ 10 *m* scales) and basin scales (~ *km*).

In this work, the sample scale effect on flow modelling examines *4D* permeability at different sample scales and voxel resolutions, with the objective to establish a representative minimum scale, by computing massive data sets using the custom parallel *XLBM*. The study builds a link from pore scale to larger scales, where the link term across different scales is the *4D* permeability. The permeability can be determined as the average parameter from the pore scale, when the size is large enough to reach the *REV* size; whereas samples with rather smaller sizes than this corresponding *REV* scale significantly lead to an unreliable permeability measurement.

Chapter 2 Literature Review

2.1 Introduction

The thesis aims to study the pore scale coupled **System (T, H, C)** in natural, fractured reservoir rocks and the resultant impact on the *4D* permeability evaluation. Following Chapter 1 Introduction, it is essential to apply a coordinated and extended interdisciplinary approach spanning fluid transport, thermal effect, chemical reactions, modern imaging technology, numerical modelling and high performance computing science for the study. To accomplish this, this chapter provides a literature review on the above issues firstly and then briefly lists the relevant scientific challenges and how the thesis work addresses them.

2.2 Coupled System (T, H, C)

In the subsurface, there is always fluid flow (**H**) in fractures or permeable geomaterial structures, for instance oil or gas flow in energy reservoirs (Dake, 1983; Sloan, 2003; Gerritsen and Durlofsky, 2005), potable water or valuable brines and groundwater infiltration and movement (Kaufman and Orlob, 1956; Patrick et al., 1987; Keating et al., 2012; Vengosh et al., 2014). Besides, the heat transfer process (**T**) is common in pumping and injection of water in geothermal energy engineering (Palmer et al., 1992; Bedrikovetski et al., 2005; Zhao et al., 2009; Koh et al., 2011), heat conduction and convection in natural gas storage (Zalba et al., 2003; Sáez and Toledo, 2009), and geothermal gradients (Bickle, 1978; Hitchon, 1984; Bedrikovetski et al., 2004; Gorman and Senger, 2010). Moreover, reactive or solute transport (**C**) often occurs in near wellbore environments including carbon sequestration (Gherardi et al., 2012; Huerta et al., 2012; Pearce et al., 2013) and oil or gas recovery and extraction (Emery et al., 1992; Molero Gómez et al., 1996; Rahman, 2000; Bedrikovetski, 2006; Karaj and Müller, 2011), and contaminant transport (Yong et al., 1992; Bedient et al., 1994; Pearce et al., 2014).

The coupled nonlinear processes in these subsurface systems represent one of the single largest classes of human industrial activity, and underpin modern civilization. Experiments and applications of coupled or partly coupled processes have been conducted in many fields such as mineral exploration (Hobbs et al., 2000), geothermal energy (Birkholzer and Tsang, 2000; Shaik et al., 2011) and magma movement (Spera et al., 1982; Ogawa, 1994; Jackson et al., 2005; Zhang, 2008), CO_2 injection (André et al., 2010; Farquhar et al., 2013), soils (Van Genuchten, 1980; Seetharam et al., 2007), groundwater (Edmunds et al., 1984; Chilakapati et al., 2000) and petroleum

geomechanics (Dusseault, 2004a; b). According to these studies, one process can significantly affect or initiate other processes in such coupled multi-physicochemical systems.

The interactions among different processes in the **System (T, H, C)** can be summarized as:

1) *Fluid flow and thermal effect coupling*: this two-way interaction mainly involves heat transfer (thermal convection and conduction), and fluid movement induced by temperature gradient and difference (Lapwood, 1948; Hart, 1981; Eckert and Drake Jr, 1987; Burmeister, 1993; Domenico and Schwartz, 1998; Wang et al., 1999; Ingham and Pop, 2005; Vafai, 2010; Incropera, 2011; Shaik et al., 2011).
2) *Fluid flow and chemical reactions coupling*: this involves the transport of the dissolved or precipitated reactive solid-phase inclusions along with the in-situ fluids such as brine or water. This has been studied well from the macroscale view in both geochemistry theories and experimental studies (Levenspiel, 1972; Lerman, 1979; Domenico and Schwartz, 1998; Levenspiel, 1999; Kaszuba et al., 2003; Gaus et al., 2008; Andreani et al., 2009; Pearce et al., 2012; Farquhar et al., 2013; Farquhar et al., 2014; Pearce et al., 2014), and geochemical modelling and experimental-modelling studies at reservoir scales by *TOUGHREACT* (Xu et al., 2004a; Xu et al., 2004b; Xu et al., 2005; Juanes et al., 2006; Gherardi et al., 2007; Xu, 2008; Alexander and Bryant, 2009).
3) *Thermal effect and chemical reactions coupling*: this coupling mainly relates to the thermal effect on the pH value and chemical reaction rates. Arrhenius (Arrhenius, 1896) has introduced a general equation for describing the relationship between the temperature and the effective reaction rates. Beside, some studies have also conducted relevant research (Kissinger, 1957; Hahn and Shiu, 1986; Gupta et al., 1990; Park et al., 1991; Cansell et al., 1993; Hobbs et al., 2000; Valo et al., 2004; Li et al., 2008; Yin et al., 2011).
4) *Interactions of coupled flow dynamics with multiple geomaterials*: the coupled fluid systems interact with the geomaterials, including fluid penetration through permeable geomaterial surfaces or being blocked by the impermeable solids at the surfaces, and reactions on the reactive geomaterial surfaces at very small scales (~ μm) that then result in porosity and fluid dynamics changes (Lerman, 1979; Danesi et al., 1981; Domenico and Schwartz, 1998; Scherer et al., 2000; Luhmann et al., 2011; Farquhar et al., 2014), which significantly relates to the generation of new pore throats at the pore scale.

Notwithstanding these studies, understanding of the multi-physicochemical **System (T, H, C)** in geology is still challenging for multiple geological phenomena including CO_2 geosequestration,

near wellbore environments, typical reservoir conditions such as coal and shale, material recovery of potable water or valuable brines, and the energy field such as geothermal heating or cooling.

2.3 Permeability and the Coupled System (T, H, C)

Permeability evaluation of sedimentary rocks and coals has long been a hot topic in studies of reservoir rocks and formations (Lishman, 1970; Rose, 1982; Al-Hadrami and Teufel, 2000; Rasolofosaon and Zinszner, 2002; Teimoori et al., 2005; Clavaud et al., 2008; Aghighi and Rahman, 2010), fractured or fault zones (Snow, 1969; Zhang et al., 1999; Mühneust and Schmittbuhl, 2001; Zhang et al., 2001), seismicity (Khan and Teufel, 2000; Parra, 2000; Ali, 2011), coal beds (Wei et al., 2007; Fu et al., 2009) and coal bed methane (Chaianansutcharit et al., 2001; Zulkarnain, 2005; Massarotto et al., 2009b), CO_2 sequestration (Spiteri et al., 2005; Juanes et al., 2006; Bennion and Bachu, 2008; Cinar et al., 2008; Armitage et al., 2011; Dubos-Sallée and Rasolofosaon, 2011; Cheng et al., 2012; Bielicki et al., 2013), and near-wellbore environments (Agarwal et al., 1979; Gatens et al., 1991; Ameri et al., 1993; Ayan et al., 1994; Barton et al., 1997; Cline and Tiab, 2001; Yetkin et al., 2009) etc.

Permeability is usually measured in *1D* for homogenous porous media, but in *3D* (at the three orthogonal orientations) for anisotropic ones. Recent studies about *3D* permeability include applications at different scales, mainly:

1) At the macroscale (e.g. near wellbore, reservoir or basin scales) (Karacan, 2009; Syed et al., 2011; Ahmed et al., 2012; Gasda et al., 2013), where the permeability is an average value from laboratory experiments of drill cores and the practical well tests (e.g. drawdown pressure test);
2) At the pore scale, on one hand, the research have focused on the digital core analysis of pore scale petrophysical structures and thereby relative porosity-permeability relationship regarding different reservoir rocks (Arns et al., 2003; Bauget et al., 2005; Andersson et al., 2011; Desbois et al., 2011; Khalili et al., 2012). For instance, the Kozeny-Carman (*K-C*) equation is widely used for generally representing these intrinsic features (Carman, 1956). Here, the permeability K relates to the porosity ϕ of the reservoir rocks:

$$K = \frac{\phi^3 {d_p}^2}{150(1-\phi)^2} \qquad \text{Eq. 2-1}$$

Here, d_p is the solid particle diameter. For a given porous medium, the parameters in those equations can be specialized as required.

On the other hand, the research have focused on *3D* dynamical simulations using some pore scale numerical methods (Ghassemi and Pak, 2011; Ghezzehei, 2012; Sugita et al., 2012; Cao et al., 2014). The directional permeability *K* is calculated according to the *Darcy's* law (Whitaker, 1986; Pant et al., 2012):

$$K = \frac{\nu_e \bar{u}}{\nabla P} \qquad \text{Eq. 2-2}$$

Here, $\bar{u}$ is the average velocity of the fluid flow through the reservoir rocks; ν_e is the viscosity of the fluid and ∇P is the pressure gradient applied on the fluid flow.

Notwithstanding, much research and many field trials have shown the permeability of sedimentary rocks or coals varies with effective petrophysical and chemical impacting factors. For instance, Lingard et al. (Lingard et al., 1984) have used the laboratory data to indicate that the directional, anisotropic stress increase can affect the measured permeability in other than an exponential decline. Besides, Close (Close, 1993) has reported that further coalification imparted by more rapid methane desorption can result in further cleat aperture. Gary (Gray, 1987) has studied the desorption-induced matrix shrinkage effect on the permeability increase of coal bed methane, and Massarotto et al. (Massarotto et al., 2001; Massarotto et al., 2003b; Massarotto et al., 2009b) have discussed the dynamic permeability increases due to the depletion of the coal bed methane and directional net stress, and the coal permeability change experimentally through the dynamic permeability measurement of in-situ coal samples (at ~ *cm* scale). These studies are also used for evaluating the coalbed methane recovery process (Wang et al., 2007b; Wei et al., 2007; Massarotto et al., 2009a; Massarotto et al., 2014), anisotropic permeability characterisation of coals (Massarotto et al., 2003a), constant volume coalbed methane reservoirs (Massarotto et al., 2009a), and even carbon geosequestration and the resultant permeability influence (Wang et al., 2007a; Wang et al., 2009; Massarotto et al., 2010; Wei et al., 2010). Meanwhile, Pan et al. have conducted laboratory characterisation of coal reservoir permeability (Pan et al., 2010) and also theoretical research for the permeability modelling for the coal reservoir (Pan and Connell, 2012), gas sorption-induced or adsorption-induced coal swelling (Pan and Connell, 2007; Clarkson et al., 2010; Pan and Connell, 2011b) and CO_2 sequestration in coal (Pan and Connell, 2009; 2011a; Qu et al., 2012). Furthermore, Dawson et al. (Dawson et al., 2011) have experimentally proven the effect of the chemical impacting factor, such as the supercritical CO_2 and water interactions with coals under simulated in situ conditions, on the anisotropic permeability evaluation.

According to these studies, the in situ permeability of the reservoir rocks is very dynamic, varying with time as internal pore structures are changed due to the reservoir fluid production (e.g. brine, water, methane and carbon dioxide). This combination of fundamental physical *3D* anisotropic permeability with dynamic variations over the temporal scale yields a term - *4D* permeability for the in situ permeability of reservoir rocks. The *4D* permeability is essential for reservoir or basin scale modelling and engineering such as during the wells drilling, injection of carbon dioxide, and oil or gas production, in particular around the near wellbore areas. For instance, the *4D* permeability change can induce break out of overburden in such as mining or coalbed methane (Barton and Zoback, 2002; Robertson, 2005; Dawson and Esterle, 2010; Palmer, 2010; Wei et al., 2010) or leakage of sequestrated CO_2 (Shipton et al., 2004; Benson and Cole, 2008; Viswanathan et al., 2008; Liu et al., 2010). Regarding that the transport of fluids through reservoir rocks significantly affect the *4D* permeability evaluation, the petrophysical mechanism between the pore scale fluid dynamics especially the coupled **System (T, H, C)** and induced *4D* permeability change, however, still remains challenging, hence requiring further fundamental research at the pore scale.

2.4 Numerical Modelling of Coupled System at the Pore Scale

With the development of modern computing resources and technologies, numerical modelling techniques have become an indispensable tool in geological and resources engineering; it has become one of the most promising techniques to provide reliable analysis and prediction in an efficient and non-destructive way (Zhao et al., 1994; Jing, 2003; Jiang, 2011).

It is common knowledge that macroscale qualities derive from and depend on variables at microscales. In geological systems, interrelated pore scale features such as rock texture, mineral distribution, grain sorting and contacts, pore or fracture networks, and fluid mixtures all affect the simultaneously interrelated processes of flow profiles, heat transfer, mineral dissolution and precipitation, and mass transfer etc. These often lead to significant resultant variations of macroscopic phenomenon such as change of permeability and fluid plume transport behaviour. For example, the possible creation of permeability in the near wellbore area in CO_2 injection correlates with the porosity increase due to dissolution of carbonates at the pore scale (André et al., 2010; Gherardi et al., 2012; Huerta et al., 2012; Farquhar et al., 2013; Pearce et al., 2013). In addition, reaction kinetics can significantly affect the integrated results of such coupled processes in CO_2 sequestration (Danesi et al., 1981; Witten Jr and Sander, 1981; Gupta et al., 1990; Yoshino et al., 2009). In order to appropriately describe and model the transport phenomena at the physically important scales, it is essential to provide an effective computational approach, advanced for pore

scale modelling and analysis, to deal with a range of such multi-physicochemical coupled (**T**, **H**, **C**) issues.

2.4.1 Conventional computational approaches

Numerical methods such as the finite difference, finite volume and finite element methods (Joseph et al., 1981; Nithiarasu et al., 1997) are widely applied to solving the macroscale governing partial differential equations (e.g. mass, momentum and energy conservation equations) through different numerical discretization (Connor and Brebbia, 1976; Peyret and Taylor, 1985; Huyakorn and Pinder, 1986; Ferziger and Perić, 1999; Lewis et al., 2004; Reddy and Gartling, 2010). These methods are described as the conventional computational approaches here. In general, conventional approaches are used for macroscale simulations where parameters are averages from *REV* scales that originally derive from pore scale structures. Here, the *REV* scale refers to the smallest size providing reliable and representative transport calculations (e.g. directional permeability) for upscaling reference, which is larger than the pore scale but much smaller than the field or reservoir scales. Conventionally, geomaterial parameters (e.g. porosity and permeability) at the *REV* scale are defined based on the experiments as well as statistical correlations, and then averaged and upscaled to the grid blocks used in field scale or reservoir scale simulations.

The conventional approaches for solving nonlinear multiscale processes employ the explicit introduction of different coordinate systems into the governing continuum equations (Cohen and Rosenblat, 1979). The characteristic scale parameters of the coordinate systems under different scales are applied to deriving the governing equations for each scale (Yu and Fish, 2002; Kouznetsova et al., 2004; Pasternak and Mühlhaus, 2005). However, for pore scale applications, conventional approaches are only applicable for periodic microstructures, but not suitable for problems with random coefficients (Chen et al., 2003) where strong connections exist across different scales (e.g. heterogeneity or anisotropy). The same condition applies for asymptotic homogenization theory-based multiscale models (Morandi Cecchi and Fornasier, 2005; Zhang et al., 2007) that are widely employed to analyse composite materials and poroelastic materials with periodic structures. Therefore, the conventional macroscale approaches are more suitable for simulations or analysis at the reservoir scale engineering but not suitable for describing the detailed characteristics and variation of heterogeneous structures and multiple geomaterial properties (minerals) at the pore scale, where coupled nonlinear fluid dynamics take effects on the evaluation of the *REV* scale or even further macroscale parameters. This requires pore scale modelling.

2.4.2 Pore scale modelling approaches

In order to conduct pore scale investigation of the coupled **System (T, H, C),** and aggregation and disaggregation of information between the pore scale multi-physicochemical processes and macroscale observations, there are typically two effective pore scale numerical methods, the Pore Network method and the lattice Boltzmann method.

2.4.2.1 Pore Network method

In pore network models, a pore volume network connected by channels allows for description of the complex pore space geometry of heterogeneous structures (e.g. rocks, soils and other solid components), and simplified geometries are applied to describing pore volumes and connecting channels (Fatt, 1956; Sugita et al., 1995; Blunt, 2001; Blunt et al., 2002). Basically, regular lattices are employed to retain pore volumes at different nodes (Blunt and King, 1990; Fenwick and Blunt, 1998), whereas other irregular lattices are used in some cases (Fenwick and Blunt, 1998; Oren et al., 1998; Prat, 2002). Such characteristic values as pore volumes, channel radius, and other pore and channel geometric characteristics, and even pore positions can be selected arbitrarily (Wilkinson and Willemsen, 1983), or according to possible experimentally determined pore space geometries based on dissimilar simulation requirements (Oren et al., 1998; Patzek, 2001).

Movement of fluid flow in the connecting pores of pore network models is governed by hydraulic potential, the resistance in the pore volumes and some other external forces. Take the single-component/single-phase simulations as an example, the description equation is defined as below:

$$Q_{ij} = G_{ij}\left(\Phi_i - \Phi_j\right) \qquad \text{Eq. 2-3}$$

Here, Q_{ij} means the fluid flow rate, G_{ij} is the fluid conductance of the channel, and Φ_i and Φ_j are the hydraulic potential of pore *i* and pore *j* respectively.

Generally, physical processes in the idealized-geometry porous media are simply assumed, and the capillary and viscous forces associated with the pore volumes are always assumed to be negligible in these models. Relevant models have been even further simplified in some cases, such as drainage and imbibition (Joekar Niasar et al., 2009), the invasion percolation displacement of a wetting fluid component by a non-wetting fluid component (Wilkinson and Willemsen, 1983), fluid-fluid displacement process (Witten Jr and Sander, 1981; Paterson, 1984; Vedvik et al., 1998; Ferer et al., 2003), water transport and gas diffusion (Sinha and Wang, 2007) and vapor phase diffusion in drying models (Yiotis et al., 2006).

The Pore Network method is used to extract the pore information inside the porous media by describing pore volumes, and builds a pore volume network connected by channels. This method is advanced for using less memory usage and hard-drive storage; however, it oversimplifies the porous medium as a pore network and cannot feasibly distinguish multiple geomaterials (minerals) or handle the interactions between fluid dynamics and different geomaterials (e.g. multiple fluid-solid interactions, potential chemical reactions and relevant induced outcomes). This exhibits a constraint to reasonably and efficiently dealing with fluid transport, thermal effect and chemical reactions (especially on the surfaces of reactive matrices) in complex geometries, due to the lack of description of the main aggregate and other matrix (both reactive and non-reactive). Moreover, in some low permeability cases, it is beyond the capability of the Pore Network method to extract effective pore networks due to the poor pore connectivity in these cases. Thus, it is hard to reasonably and accurately describe realistic fluid dynamics in the heterogeneous porous media using the Pore Network method. Additionally, the Pore Network method is not well suited for the simulations of complex fluid flow in fractured porous media or other systems with complex macro-pores according to Meakin et al. (Meakin and Tartakovsky, 2009). This limitation of these models requires a substantial effort to develop and validate more complex models for the coupled **System (T, H, C)** instead of such oversimplified approximations.

2.4.2.2 Lattice Boltzmann method

Instead of solving the conventional Navier-Stokes equations or its simplified form with macroscopic properties, the common feature of the lattice Boltzmann method (*LBM*) is the discretization of space and time with countable orientations; it incorporates many of the essential characteristics of the realistic microscopic processes so that the macroscopic averaged properties obey the macroscopic equations. In detail, the *LBM* discretizes the Boltzmann equation as a lattice, and fictive particles with different values are used to describe each lattice node as fluid or solid. Such particles perform consecutive propagation and collision with their neighbors over discrete regular or irregular lattice grids for describing fluid dynamics. A variety of collision models have been proposed in the past two decades for conducting reasonable and effective simulations in the relevant fields. For executing rational collision and propagation, both the single-relaxation-time model (also known as Bhatnagar-Gross-Krook model (*BGK*)) (Chen et al., 1992; Swift et al., 1996; Nithiarasu et al., 1997; Ansumali and Karlin, 2002; Guo and Zhao, 2002) and the multiple-relaxation-time model (*MRT*) (d'Humières, 2002; Yu et al., 2003; McCracken and Abraham, 2005; Pan et al., 2006; Premnath and Abraham, 2007; Li et al., 2011; Luo et al., 2011) have been broadly used.

The lattice Boltzmann method focuses on the particle-particle interaction based on a dimensionless lattice grid and has the character of molecular dynamics that each particle on the grid conducts collision interaction with its neighbors. This provides a strong capacity for modelling laminar to turbulent flow of complex fluids (Sahimi, 2011) and porous media flow with complex pore networks (Benzi et al., 1992; Qian et al., 1992; Chen and Doolen, 1998; Succi, 2001; d'Humières, 2002; Brownlee et al., 2007; Sukop and Thorne, 2007; Aidun and Clausen, 2010).

Compared with the other numerical methods, the lattice Boltzmann method has shown extensive potential applicability to the pore scale simulation of complex nonlinear coupled processes, such as thermal porous media flow (He et al., 1998; Guo and Zhao, 2005; Tian et al., 2006; Wang et al., 2007c; Wang et al., 2007d), and simple diffusion and buoyant mixing of dense solutions (Perea-Reeves and Stockman, 1997; Stockman, 1997). In this context, a set of reaction diffusion equations plus a solvent described by the Navier-Stokes equation were discussed by Dawson et al. regarding a homogeneous case (Dawson et al., 1993b), which was then used to study the effective diffusivity of a heterogeneous porous medium when the geomaterials were impermeable or permeable with a different diffusivity (Alvarez-Ramírez et al., 1996; Chen and Doolen, 1998).

Kang et al. developed a pore-scale *LBM* model for simulating chemical reactions on solid surfaces among the porous medium (Kang et al., 2002b). Recently, they further applied the model in the simulations of the injection of CO_2-saturated brine into structured porous media, and focused on the study of the fundamental physics occurring at the pore scale for reactions involved in geologic CO_2 sequestration (Kang et al., 2010a). However, these methods disregarded realistic heterogeneous porous media (multiple geomaterials involving reactive and non-reactive minerals) and rather used arbitrary geometries consisting of only one reactive mineral, which is relevant only to the acidulation process in carbonate reservoirs.

In addition, the utilization of the particle description or the kinetic equation also provides some of the advantages of molecular dynamics, easy implementation of boundaries and fully parallel algorithms. A number of studies have also focused on the parallel computing research and performance analysis due to the strong potential computing scalability in *LBM* (Kandhai et al., 1998; Desplat et al., 2001; Pan et al., 2004; Wang et al., 2005; Mazzeo and Coveney, 2008; Clausen et al., 2010; Vidal et al., 2010). Besides, some studies have also been conducted on applications of *LBM* in parallel *GPU* computing (Bernaschi et al., 2010; Myre et al., 2011). However, the implementation of fast-speed parallel computation for large initial architectural input cases (e.g. initial input of digital core data sets $\geq$ 100GB) remains challenging, including the processing of large initial architectural data sets, large data sets run-time control (e.g. memory consumption and

data communication), as well as visualization of massive output data sets, which requires further exploration and improvement in both algorithms and codes.

2.5 Modern Imaging Technology

In order to provide reasonable modelling for pore scale coupled **System (T, H, C)**, the internal structure detail of reservoir rocks is essential and forms the basis of this thesis work, with further model verification through laboratory results.

The *X-ray computed Tomography*, a widely accepted imaging technology, uses the absorption intensity of *X-ray* through different materials or object textures to create cross-sections of a physical object that can be used to recreate a virtual *3D* structure without destroying the original one (Wellington and Vinegar, 1987; Kalender, 2006). In particular, the *Micro-Computed Tomography (micro-CT)*, also known as the *High-resolution X-ray Computed Tomography*, *X-ray Micro-Computed Tomography* or *μCT*, is further advanced for yielding high-resolution three dimensional *X-ray* images of solid opaque objects quickly (Carlson et al., 2003; Latham et al., 2008; Golab et al., 2013c). Besides, the most comprehensive solution for accurate mineralogical analysis is to use *QEMSCAN* (Quantitative evaluation of materials by the Scanning Electron Microscopy) for extending the mineral identification capacity of *micro-CT* scanning for geomaterials. The *QEMSCAN* is capable of identifying most ore- and rock-forming minerals on a micro-scale in just milliseconds, and provides an integrated automated mineralogy and petrography solutions for mineralogy studies of core samples in a non-destroyable and repeatable way (Corcoran, 1989; Pirrie et al., 2004; French et al., 2008; Field and Atkins, 2012).

The modern imaging technology has made rapid progress with applications in many fields, such as geomaterials and geomechanics study in engineering geology for industrial and research purposes. It includes the examination and analysis of clastics (Itoi et al., 2003; Golab et al., 2010) and carbonates (Arns et al., 2005b; Sok et al., 2010), coal (Van Geet and Swennen, 2001; Mazumder et al., 2006; Wolf et al., 2008; Yao et al., 2009; Golab et al., 2013c), soil science (Taina et al., 2008; Tracy et al., 2010; Mooney et al., 2012), formation structures (Golab et al., 2010; Bera et al., 2011), reservoir rocks, seal rocks and sediments (Berner, 1970; Raynaud et al., 1989; Hirono et al., 2003; Bornert, 2010; Hall et al., 2010; Knackstedt et al., 2012), petro-physics (Arns et al., 2005a), and quantitative description of grain-scale structures (Larson et al., 2002; Okabe and Blunt, 2005; Li et al., 2006; Wildenschild and Sheppard, 2013). Besides, applications of the modern imaging technology have been conducted in flow transport in porous media (Turner et al., 2004; Sinha et al., 2006), gas and oil exploration and production (Dong et al., 2007; Desrues et al., 2010; Feali et al.,

2012), single- or multi-phase flow properties (Knackstedt et al., 2006; Knackstedt et al., 2009), CO_2 injection and sequestration (Karacan, 2007; Pone et al., 2009; Pone et al., 2010; Pearce et al., 2012; Pearce, 2012; Farquhar et al., 2013; Golab et al., 2013a; Farquhar et al., 2014).

The advanced imaging technology is essential for the thesis work in providing the pore scale information of the heterogeneous porous media, which serves as the first step for further dynamical coupled **System (T, H, C)** modelling.

2.6 Parallel Processing and Computing

High resolution *micro-CT*/*QEMSCAN* scans of reservoir rock samples can deliver a high level of pore scale detail. This also generates enormous initial digital data sets, at least hundreds of *Gigabytes* to *Terabytes*, which in turn require much more processing for further dynamical coupled **System (T, H, C)** modelling in later computational simulations. This dynamical modelling requires higher processor performance, large memory and huge disk storage, and special Input/Output (*I*/*O*) access that are beyond the capacity of conventional personal computers or small local work stations.

Parallel computing (also known as supercomputing or high performance computing) is the opposite of the serial or sequential computing that uses only one processor for data processing or computation on conventional personal computers. Parallelism aims to use less computer time or solve problems with larger sizes that are impossible for these conventional personal computers and has been broadly used since its appearance (Fox et al., 1994; Kumar et al., 1994; Barney, 2010).

In parallel computing, multiple computing processors, large memory and hard-disk storage are integrated using high speed connecting networks, where large problems are feasible to be divided into smaller ones and assigned onto multiple processors for calculations in parallel or concurrently (Almasi and Gottlieb, 1989; Kumar et al., 1994).

2.6.1 Computing performance

Efficient parallel algorithms (and programs) are meant to increase the computing speed or the size of target problems by optimizing the sequential algorithm for running on a particular parallel computing infrastructure. Parallel computing algorithms (and programs) are more difficult to write than sequential ones, because concurrency creates potential software bugs and problems that are new compared with the conventional sequential algorithms (and programs). The most common issue is that the race condition, and communication and synchronization between different sub-tasks greatly hinder the high parallel algorithms (and programs) performance (Gropp et al., 1999; Grama, 2003).

The performance of parallel computing is usually described by two terms, speedup and computing efficiency. The maximum possible speedup for the parallelization of a sequential algorithm (and program) is known as the *Amdahl's law* (Amdahl, 1967; Rodgers, 1985; Gustafson, 1988) :

$$\text{Speedup} = p/(p \times \alpha + 1 - \alpha) \qquad \text{Eq. 2-4}$$

Where α is the time consumption of the sequential running fraction in the whole parallel algorithm (and program), and p is the number of processors used in the parallelization.

The speedup describes the scalability of the parallel algorithm (and program) on multiple supercomputing infrastructures. The best speedup is an upward linear line, representing orthogonal computing structures or complete sub-tasks independency. The orthogonality guarantees the size of the problem is proportional to the number of processors used (the slope of the straight line is 1). However, the actual speedup cannot reach a straight slope as 1 due to fixed memory size, inter-processor communication and synchronization delays etc.

The other term, computing efficiency, is to evaluate the proportion of time consumed on data communication among different processors compared with the total computing time. It is defined by (Ferziger and Perić, 1996; Dongarra et al., 2003):

$$E = t_s/(p \times t_p) \qquad \text{Eq. 2-5}$$

Here, E is the computing efficiency, and t_s is the total time consumed in the sequential program condition for the target problem, and t_p is the total computing time consumed in the parallel program condition for the target problem; p is the number of processors used in the parallel computing case.

Both the speedup and the computing efficiency are used to analyse the performance of the parallel algorithms, either theoretically using asymptotic run-time complexity or in practice by measuring the time of program execution. Given a certain number of p, the speedup and the computing efficiency are equivalent measurements.

In addition, the implementation of the parallel coding requires consideration of supercomputing infrastructures for less synchronization time of data communication and high computing efficiency and scalability; thus it is essential to design compatible codes for migration in multi-platform infrastructures. Parallel coding is based on multiple operating systems such as GNU/Linux, Mac OS X, Solaris, AIX, HP-UX, and Windows platforms; hence it also refers to the usage of compiler directives, library routines, and settings of environment variables. Besides, extra cost of time will be induced as the computational node numbers increase, and the efficiency of parallel computing is

then reduced if the parallel algorithms and coding are not well designed.

2.6.2 Status of parallel computing applications

According to the famous *Moore's Law* (Moore, 1965; Schaller, 1997) that the transistor density in a microprocessor doubles every 18 to 24 months, the hardware has been experiencing a high-speed development in the past 60 years. The *Moore's Law* is still effective but there are predictions about its end due to the power consumption issues (Schaller, 1997; Mann, 2000; Kish, 2002; Tuomi, 2002; Esmaeilzadeh et al., 2011); however, the development of the supercomputing infrastructures has still experienced great advances until the year of 2014.

The performance of the supercomputing machines is calculated by the capability of processors conducting the frequency of float computations. According to the highest computing ability on the international top 500 list in November 2013 (Top 500 website), the highest one is about 100 *Petaflops* per second. Such high-efficiency supercomputers are usually used in fields with computing intensity such as geoscience, bio-information technology, meteorological science, and pressure engineering.

Numerous studies about the parallel computing have been conducted such as compiler optimization (Bomans et al., 1990; Hiranandani et al., 1991; Koelbel and Mehrotra, 1991; Bugnion et al., 1996; Bennett, 2003; Karlsson and Brorsson, 2004), parallel algorithms design (Hockney and Jesshope, 1988; Leighton, 1992; Olson, 1995; Plimpton, 1995; Nakajima, 2002; Darriba et al., 2012; Kirk and Wen-mei, 2012; Migdalas et al., 2012), high performance analysis (Cochocki and Unbehauen, 1993; Asanovic et al., 2009; Ekanayake and Fox, 2010; Fuller and Millett, 2011; Bekkerman et al., 2012), and parallel software development (Li, 1988; Grimshaw, 1993; Nakajima, 2003; Bielak et al., 2010; Cui et al., 2010; Christen et al., 2011; Vetter et al., 2011; Ayres et al., 2012). In geoscience, applications of parallel computing have been used in multiple fields such as studies about earthquakes (Yin et al., 1995; Bao et al., 1996; Yu et al., 2004; Cui et al., 2009; Cui et al., 2010) and fluid flow (Galperin and Orszag, 1993; Marshall et al., 1997; Xing et al., 2013).

In particular, parallel lattice Boltzmann computing has also been studied since the past few decades. These studies include code development (Desplat et al., 2001; Axner et al., 2008; Mazzeo and Coveney, 2008), implantation on multiple supercomputing platforms (Carter and Oliker, 2006; Donath et al., 2008; Clausen et al., 2010), and performance optimization (Pohl et al., 2003; Wilke et al., 2003; Pohl et al., 2004; Velivelli and Bryden, 2006; Vidal et al., 2010). However, compared with hardware development, software and applications of parallel computing in geoscience are far behind; high extensibility of the parallel algorithms and coding is also a bottleneck of further

applications of parallel computing in problems with larger sizes, such as processing of massive initial architectural data sets, effective run-time computing, data communication and synchronization, and outputs visualization in the parallel lattice Boltzmann computing.

2.7 Summary and Knowledge Gaps

As mentioned in Section 2.3, there have been several approaches for the permeability studies. Notwithstanding, numerical methods have shown strengths for various reasons, such as the short time taken to achieve long-term modelling prediction over a range of spatial and temporal scale, non-destructive and repeatable way, and low capital and operating cost.

The current literature has shown the knowledge gaps with respect to the permeability study from the pore scale to the *REV* scale in coupled **System (T, H, C)**. Some of the questions are:

- ✧ How to effectively measure the micro-structure of the reservoir rocks, importantly at the pore scale and process the massive initial architectural data sets?
- ✧ How to describe actual pore scale networks for flow, and multiple geomaterials for further coupled **System (T, H, C)** modelling?
- ✧ How to propose an effective fluid transport model for flow through heterogeneous porous media with multiple geomaterials and permeability?
- ✧ How to reasonably describe coupled interactions of fluid flow, thermal effect, and geochemical reactions, and resultant induced impact on pore scale geo-structures (e.g. porosity change)?
- ✧ How to handle enormous numerical data sets and associated computational processing loads for flow simulation on supercomputing environment?
- ✧ How to correlate the coupled System (T, H, C) effect at the pore scale and the *4D* permeability evaluation over a range of spatial and temporal scale?
- ✧ How to study the sample scale (size) effect on permeability evaluation, to yield permeability at the *REV* scale for different rank reservoir rocks?

The interdisciplinary knowledge is required to address the above issues to provide an intermediate solution for a better understanding of every aspect. The following section lists what the challenges are and how the thesis work has addressed them.

2.7.1 Parallel processing of high resolution *3D* digital samples

The modern imaging technology provides a powerful tool to measure and analyse the microstructures and components of natural and artificial materials at the pore scale that can be applied in a wide range of research topics.

The *micro-CT/QEMSCAN* is carried out at ~ *mm* to ~ *cm* scales and generates scans with small pixel size (down to ~ μm) to reveal sufficient pore scale information. These high resolution (small pixel size) images carry much more information and consequently require more storage space, memory size and computational processing resources to transform the density images to *3D* digital reservoir rock samples; these steps often represent the practical limits of the tomography. For instance, a 1 *cm* scale cubic sample can generate around 125 *Gigabytes* of digital raw data sets under a voxel size of 4 μm, and this is merely the initial architectural input for the dynamical simulations. In later dynamical simulations, around 2 *Terabytes* memory and 400 *Gigabytes* output data are required at each time step (Gao and Xing, 2013).

Regarding these issues, the thesis work has implemented parallel processing of the high-resolution scans of reservoir rock samples as an effective tool. An Input preparation module is proposed for *3D* digital sample reconstruction (at least hundreds of *Gigabytes*), by automatically splitting, combing and resizing the raw initial data sets into required sub-blocks for multiple processors processing. This fills the gap between the massive pore scale initial architectural data sets and the efficient inputs for applications of these outcomes in the later dynamical modelling.

2.7.2 Parallel *XLBM* for coupled System (T, H, C) modelling

The current *LBM* has been developed and studied as numerical schemes for porous media flow with irregular solid boundary conditions (e.g. grain contacts). This shows more potential advantages in dealing with pore scale fluid-solid interactions (e.g. reactions on the reactive mineral surfaces, penetration through permeable geomaterial sections) than the Pore Network method.

This provides a feasible and basic study for the thesis work. However, there still remain many challenges:

1) The *LBM* has been widely used for representative homogeneous cases or heterogeneous porous media with a single geomaterial at the pore scale. In particular, in the latter pore scale cases, 0/1 *LBM* model (0 for pores, and 1 for impermeable solids) has been broadly used. However, multiple geomaterials with respective permeability or reactive character have not been

considered but are essential for modelling coupled multiple-physicochemical **System (T, H, C)** in heterogeneous porous media;

2) Further exploration about the appropriate modelling of the coupled multiple-physicochemical processes in **System (T, H, C)** at the pore scale are required. Guo et al. (Guo and Zhao, 2005) have studied thermal conduction in pores and solids, whereas heat transfer and interactions with fluid transport and chemical reactions in porous geomaterials still require further consideration. Although Kang et al. (Kang et al., 2002b; Kang et al., 2007; Kang et al., 2010a) have proposed a model for studies of chemical reactions at the pore scale, however it is still less understood how the reactions occur in the pore scale multiple geomaterials involving both reactive and non-reactive mineral grains. Moreover, the existing research are still in *2D* and focused on the corresponding numerical algorithm itself, rather than the scientific issues in the coupled system;
3) Although the conventional *LBM* itself has potential advantages over the conventional approaches in high performance computing on supercomputers, the bottle neck for the thesis work is in special Input/Output (*I*/*O*) access for massive data sets inputs, large memory and huge disk storage, time consumption in data communication and synchronization, higher processor performance, and results visualization.

In order to solve these issues, a parallel *XLBM* (eXtended *LBM*) is proposed in this thesis for providing high-performance parallel algorithm and coding interfaces for more complex and easily extended multi-physicochemical processes studies, by incorporating functional extensions, statistics theory, and advanced computational science into the conventional *LBM*.

2.7.3 *4D* permeability and representative parameters

The thesis has focused on the modelling of coupled **System (T, H, C)**. However, what are the outcomes for studying pore scale processes?

With an insight from a range of nonlinear coupled pore scale processes using the parallel *XLBM*, the thesis work measures the *4D* permeability variation over the temporal scale, through a dynamic or 'unsteady' phase to a relatively 'stable' equilibrium status. This significantly relates to the coupled **System (T, H, C)** and resultant effect on the change of porosity and fluid dynamics. The work is first verified by laboratory experiments and elaborated on further for long-time prediction, which is beyond the time range of the experiments. Analysis and evaluation of the *4D* permeability is conducted as a contribution of the thesis work to fluid flow modelling in ways that honor subsurface petrophysical conditions, at the micron to centimeter scales, where even small changes at the pore scale are likely to trigger significant permeability variation at larger scales.

Regarding analysis of sample size effect, the pore scale study contributes to the measurement of the effective representative parameter, permeability, as inputs for macroscale simulations. In detail, the permeability is sensitive to the sample scale or size such that the measured permeability gradually approaches a constant value when the sample size reaches a certain scale or larger. Thus, the critical sample size is defined as the corresponding *REV* scale sample size, and the permeability measured at this sample size is used as the representative parameter for macroscale references.

Chapter 3 The eXtended *LBM* for Pore Scale Fluid Flow (H) in Heterogeneous Geomaterials

3.1 Introduction

In the pore scale **System (T, H, C)**, the appropriate modelling of fluid transport (**H**) is fundamental and essential for coupling of multiple processes. Generally, the subsurface systems possess high *3D* anisotropy with multiple heterogeneous reservoir rocks such as sedimentary rocks or coals across a multitude of mechanically significant scales, which dominate the subsurface fluid flow.

In heterogeneous geomaterials, different materials (minerals) exhibit different individual porosity and permeability characteristics. In a system of reservoir engineering, for instance, individual quartz grains are essentially impermeable as known in sedimentology (Nedkvitne et al., 1993; Boggs, 1995; Worden and Morad, 2000), whereas partly altered feldspar grains commonly show some permeability due to the presence of cleavages or other internal cracks within them and consequently may allow some internal fluid flow to occur. Lithic fragments are pieces of preexisting rock reduced to sand size grains in a sedimentary rock, and are recognizable parts of older rocks that have been eroded, transported, deposited and Incorporated into new rocks; such lithics typically have some degree of internal porosity and potentially permeability regarding different sorting and sizes of fragments. Clays commonly have numerous small pore spaces between very small platelets or grains; moreover, clays sometimes have very low hydraulic conductivity due to their small pore throat radiuses that can hold a large volume of water without releasing it easily and rapidly (Neuzil, 1994). Nevertheless, clays are somewhat permeable due to the large volume of pore spaces (Mitchell et al., 1900; Green et al., 1981; Tavenas et al., 1983). Hence, it is not only the pore networks and fluids (e.g., viscosity or multi-fluid mixtures), but also properties of geomaterials (e.g. quartz, feldspars, clays and lithic fragments) that can affect the fluid transport in the coupled **System (T, H, C)**. General grain sorting variation, diverse sizes of fragments, discreet layering and cementation may occur and all impact upon the pore-perm characteristics of a sample. Although studies about these former two impacting factors have been considerable, less consideration is yet conducted about the geomaterials impact on the flow dynamics.

Regarding real geological systems, the main challenge for computational analysis is to account for the heterogeneity of geomaterials (including geometry, topology and the presence of multiple diverse physical and chemical components) at the pore scale, and propose appropriate modelling method to describe pore scale flow dynamics in such porous media systems. For the former issue, high-resolution *micro-CT*/*QEMSCAN* enables the characterisation of pore scale features to quantify microstructures including grain size and sorting, pores and tortuosity, and distribution of multiple

geomaterials, hence reconstructing digital reservoir rocks. For the latter issue, the lattice Boltzmann method (*LBM*) that is capable of simulating fluid flow through complex pore networks is first employed.

For further modelling fluid flow transport (**H**) in pore scale heterogeneous porous media involving multiple geomaterial components, an *eXtended LBM* model (*XLBM*) is proposed in this chapter by furthering the conventional *LBM* (e.g. *Guo and Zhao* (*2002*)) by adding material localization, multiple contact boundaries, and the statistics theory (Section 3.2) for modelling fluid flow through multiple heterogeneous geomaterials. In the *XLBM*, each lattice node representing an individual geomaterial has its own hydraulic property regarding its nature, which is also advanced for further coupling with **System (T, C)** issues in later chapters. The technique for reconstruction of digital reservoir rocks using *micro-CT*/*QEMSCAN* images is also introduced in Section 3.2, and the scans have been translated into a high-resolution corresponding lattice for *XLBM* simulations. Based on the theory, a custom *XLBM* code is developed for implementing *2D*/*3D* numerical simulations. After being validated by various benchmarks (Section 3.3), the impact of heterogeneous geomaterials on fluid flow dynamics at pore scale has been carefully studied and discussed through two application cases (Section 3.4).

3.2 Methodology and Modelling Approach

3.2.1 Generalized Navier–Stokes (N–S) equations for porous media flow

Generalized Navier–Stokes equations for isothermal incompressible fluid flow in porous media are (Bell et al., 1989; Guo and Zhao, 2002; Bear, 2013):

$$\nabla \cdot \mathbf{u} = 0 \qquad \text{Eq. 3-1}$$

$$\frac{\partial \mathbf{u}}{\partial t} + (\mathbf{u} \cdot \nabla)\left(\frac{\mathbf{u}}{\phi}\right) = -\frac{1}{\rho}\nabla(\phi p) + \nu_e \nabla^2 \mathbf{u} + \mathbf{F} \qquad \text{Eq. 3-2}$$

Here, ρ is the fluid density; **u** is the volume-averaged velocity; v_e is an effective viscosity and ϕ means the average porosity of a porous medium. **F** stands for the total body force on the fluid flow due to the effect of the porous medium and other external force fields, which can be described as (Carman, 1956; Guo and Zhao, 2002):

$$\mathbf{F} = -\frac{\phi \nu}{K}\mathbf{u} - \frac{\phi F_\varepsilon}{\sqrt{K}}|\mathbf{u}|\mathbf{u} + \phi \mathbf{G} \qquad \text{Eq. 3-3}$$

here, v is the kinematic viscosity of the fluid; **G** is the external body force (e.g. gravity or buoyancy); F_ε is the geometric function and K is the permeability of the porous medium. These formulas relate to the porosity ϕ, whereas the correlation of porosity and permeability varies regarding different porous media. In practice, the Kozeny-Carman (*K-C*) equation is widely used for generally representing those intrinsic features (Carman, 1956). Both F_ε and K are described by:

$$F_\varepsilon{}^2 = \frac{1.75^2}{150\phi^3} \qquad \text{Eq. 3-4}$$

$$K = \frac{\phi^3 d_p{}^2}{150(1-\phi)^2} \qquad \text{Eq. 3-5}$$

Here, d_p is the solid particle diameter. For a given porous medium, the parameters in those equations may be specialized as required.

As the porosity approaches 1.0, the generalized momentum equation (Eq. 3-2) reduces to the Navier–Stokes equation for free fluid flows (absence of porous geomaterials). In Eq. 3-3 , the first term on the right side is the linear (*Darcy*) drag, whereas the second term is the nonlinear (*Forchheimer*) drag due to inertial effects. Without this nonlinear term, Eq. 3-2 becomes the *Brinkman-extended Darcy* equation (low-speed flows) (Martys et al., 1994; Spaid and Phelan Jr, 1997; Ginzburg, 2008). However, for high-speed flows, the nonlinear term cannot be neglected.

3.2.2 Lattice Boltzmann method for generalized N-S equations

The lattice Boltzmann method works differently from the conventional macroscopic approaches (e.g. *FEM*, *FDM* or FVM) (Duguid and Lee, 1977; Huyakorn, 1983; Or and Tuller, 2000; Reichenberger et al., 2006). Instead of solving the Navier-Stokes (*N-S*) equations or its simplified form with macroscopic properties, the *LBM* discretizes the space and time, and simulates the fluids and geomaterials as fictive particles. These particles perform consecutive propagation and collision processes (with countable neighbors) over a lattice grid, which can be viewed as a discrete scheme for the Boltzmann equation with discrete velocities. By simulating streaming and collision behaviour across a limited number of particles in countable directions, the intrinsic particle interactions evince a microcosm of viscous flow behaviour applicable across the greater mass (Joseph et al., 1982; Diodato, 1994). Since the *LBM* focuses on the particle-particle interaction based on a dimensionless lattice grid, it has shown great advantages in dealing with complex and diverse material boundary situations. A group of studies have shown the capacity of *LBM* in modelling porous media flow with complex pore networks (Aharonov and Rothman, 1993; Kang et

al., 2002a; Sukop and Or, 2004; Aaltosalmi, 2005). The framework of the generalized Bhatnagar-Gross-Krook (*BGK*) *LBM* equation is summarized as (Succi, 2001):

$$f_i\left(\mathbf{x}+\mathbf{e_i}\Delta t, t+\Delta t\right)- f_i\left(\mathbf{x},t\right)=-\frac{1}{\tau}\left[f_i\left(\mathbf{x},t\right)- f_i^{eq}\left(\mathbf{x},t\right)\right]+\Delta t F_i \qquad \text{Eq. 3-6}$$

It reveals the evolution of fluid flow over the lattice grid. Here, the left term of Eq. 3-6 is the propagation part, and the right side is the collision part. Δt is the time increment and τ is the dimensionless relaxation time, which is related to the numerical computing stability. $\mathbf{e_i}$ is discrete velocity unit vector at the *ith* direction; *i* ranges from 0 to 8 in the classical two dimensional *D2Q9* model, and ranges from 0 to 18 in the classical three dimensional *D3Q19* model (Fig. 3-1). $f_i(\mathbf{x},t)$ and $f_i(\mathbf{x}+\mathbf{e_i}\Delta t, t+\Delta t)$ are the distribution function of the particle with velocity $\mathbf{e_i}$ at position *x* at the time step *t* and $t+\Delta t$, respectively. The equilibrium distribution function $f_i^{eq}(\mathbf{x},t)$ is determined by:

$$f_i^{eq}\left(\mathbf{x},t\right)=\omega_i\rho\left[1+\frac{\mathbf{e_i}\cdot\mathbf{u}}{c_s^2}+\frac{\left(\mathbf{e_i}\cdot\mathbf{u}\right)}{2\phi c_s^4}-\frac{\mathbf{u}^2}{2\phi c_s^2}\right] \qquad \text{Eq. 3-7}$$

Here, c_s is 1/3 speed of sound running over the lattice grid, and ω_i is the weight coefficient at the *ith* direction. For two dimensional cases (Fig. 3-1 (a), *D2Q9* model), ω_i = 4/9 (for *i* = 0), 1/9 (for *i* = 1, 2, 3, 4), and 1/36 (for *i* = 5, 6, 7, 8); For three dimensional cases (Fig. 3-1 (b), *D3Q19* model), ω_i = 1/3 (for *i* = 0), 1/18 (for *i* = 1, 2, … , 6), and 1/36 (for *i* = 7, 8, …, 18).

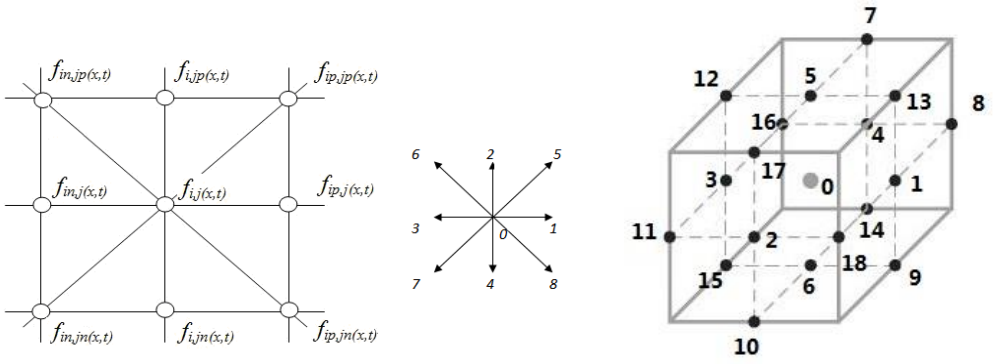

(a) (b)

Fig. 3-1 Lattice grid and nodes relationship (a) in the classical *2D LBM* lattice structure (*D2Q9*): one particle node in the center and its 8 neighbors, (b) in the classical *3D LBM* lattice structure (*D3Q19*): one resting particle (gray point in the cubic center) and its 18 neighbors (black points).

To build the correlation between the force term F_i in Eq. 3-6 and the force term **F** in Eq. 3-2, Guo et al. (Guo and Zhao, 2002) have introduced an equation:

$$F_i = \omega_i \rho \left(1 - 1/2\tau\right)\left[\frac{\mathbf{e_i}\cdot\mathbf{F}}{c_s^2} + \frac{\left(\mathbf{uF}+\mathbf{Fu}\right):\left(\mathbf{e_i e_i} - c_s^2\mathbf{I}\right)}{2\phi \mathbf{c}_s^4}\right] \quad \text{Eq. 3-8}$$

Accordingly, the density and velocity are:

$$\rho = \sum_i f_i, \qquad \rho\mathbf{u} = \sum_i \mathbf{e_i} f_i + \frac{\Delta t}{2}\rho\mathbf{F} \quad \text{Eq. 3-9}$$

The macro velocity can be expressed as Eq. 3-10 and Eq. 3-11 by combining Eq. 3-3, Eq. 3-4, Eq. 3-5, Eq. 3-8 and Eq. 3-9:

$$\mathbf{u} = \frac{\mathbf{v}}{c_0 + \sqrt{c_0^2 + c_1|\mathbf{v}|}} \quad \text{Eq. 3-10}$$

$$\mathbf{v} = \frac{1}{\rho}\sum_i \mathbf{e}_i f_i + \frac{\Delta t}{2}\phi\mathbf{G} \quad \text{Eq. 3-11}$$

Where c_0 and c_1 are described as:

$$c_0 = \frac{1}{2}\left(1 + \phi\frac{\Delta t}{2}\frac{\nu_e}{K}\right), \quad c_1 = \phi\frac{\Delta t}{2}\frac{F_\varepsilon}{\sqrt{K}} \quad \text{Eq. 3-12}$$

Here, ν_e is defined as $\Delta t\ (\tau - 0.5)\ c_s^2$. Following the similar procedure by Guo and Zhao (Guo and Zhao, 2002), Eq. 3-6 to Eq. 3-12 for incompressible fluid flow can be derived as the generalized Navier–Stokes equations for isothermal incompressible fluid flow in porous media.

3.2.3 The *eXtended LBM* for flow through multiple materials

A custom *eXtended LBM* (*XLBM*) model extending the conventional lattice Boltzmann method with material localization, multiple contact boundaries, and the statistics theory, is introduced for modelling fluid flow through multiple heterogeneous geomaterials.

3.2.3.1 Material localization

A variable $\phi_\alpha\ (0 \le \alpha \le N)$ for specifying the individual material component at each lattice node is introduced and applied as material localization. N is the number of different material components, thus the total number of components including pore apertures (α = 0) is N+1. The equilibrium distribution function $f_i^{eq}(\mathbf{x},t)$ is further accordingly revised as:

$$f_i^{eq}(\mathbf{x},t) = \omega_i\rho\left[1 + \frac{\mathbf{e_i}\cdot\mathbf{u}}{c_s^2} + \frac{\left(\mathbf{e_i}\cdot\mathbf{u}\right)}{2\phi_\alpha c_s^4} - \frac{\mathbf{u}^2}{2\phi_\alpha c_s^2}\right] \quad \text{Eq. 3-13}$$

The force term equations based on the above theory are further modified as:

$$F_i = \omega_i \rho\left(1-1/2\tau\right)\left[\frac{\mathbf{e_i}\cdot\mathbf{F}}{c_s^2}+\frac{\left(\mathbf{uF}+\mathbf{Fu}\right):\left(\mathbf{e_i e_i}-c_s^2\mathbf{I}\right)}{2\phi_\alpha c_s^4}\right] \quad \text{Eq. 3-14}$$

$$\rho=\sum_i f_i, \qquad \rho\mathbf{u}=\sum_i \mathbf{e_i} f_i+\frac{\Delta t}{2}\rho\mathbf{F} \quad \text{Eq. 3-15}$$

F stands for the total body force on the fluid flow involving external force fields and the resistance effect by the main aggregate or other materials, which is described as a whole as:

$$\mathbf{F}=-\frac{\phi_\alpha \nu_s}{K_\alpha}\mathbf{u}-\frac{\phi_\alpha F_{\varepsilon\alpha}}{\sqrt{K_\alpha}}|\mathbf{u}|\mathbf{u}+\phi_\alpha\mathbf{G} \quad \text{Eq. 3-16}$$

The first two terms on the right side of the equation are the resistance forces on the fluid derived from the main aggregate or other materials. ν_s is the kinematic viscosity of the fluid; $F_{\varepsilon\alpha}$ is the geometric function related to the αth component and K_α is the intrinsic permeability of the αth component within the porous medium. Both $F_{\varepsilon\alpha}$ and K_α are described by the Kozeny-Carman (*K*-*C*) equations (Carman, 1956). These formulas were originally developed for sphere or grain packs (Ergun, 1955), and are employed here for describing geomaterial properties with a simplified definition that all geomaterials are analogized as groups of spheres or grain packs.

$$F_{\varepsilon\alpha}{}^2=\frac{1.75^2}{150\phi_\alpha{}^3} \quad \text{Eq. 3-17}$$

$$K_\alpha=\frac{\phi_\alpha{}^3 d_{p\alpha}{}^2}{150\left(1-\phi_\alpha\right)^2} \quad \text{Eq. 3-18}$$

Each lattice node within the porous medium has its own hydraulic property referring to the localized geomaterial porosity ϕ_α. For pores, ϕ_α (α = 0) is 1.0 and resistance force reduces to zero; whereas ϕ_α ($1 \le \alpha \le N$-1) is commonly less than 1.0 for other geomaterial components with low intrinsic permeability. As an extreme condition, the porosity ϕ_α and the intrinsic permeability K_α (α = *N*) of an impermeable aggregate are both zero without considering the fluid flow effect. Regarding the effective diameter d_p of each particle within the heterogeneous porous geomaterial aggregate, this correlates with the nature of each geomaterial component. For example, microscale clay particles tend to have very small effective diameters around ~ μm. In particular, soil scientists usually consider the size as 2 μm, sedimentologists often use 4-5 μm as the average clay particle

size, and colloid chemists tend to use 1 μm (Guggenheim and Martin, 1995). Hence, the clay permeability typically ranges from ~ nD to ~ mD when its porosity is less than 0.5.

The macro velocity can be expressed as shown in Eq. 3-19 by combining Eq. 3-14 to Eq. 3-18:

$$\mathbf{u} = \frac{\mathbf{v}}{c_0 + \sqrt{c_0^2 + c_1|\mathbf{v}|}} \qquad \text{Eq. 3-19}$$

Where the temporary velocity **v,** and variables c_0 and c_1 are described as:

$$\mathbf{v} = \frac{1}{\rho}\sum_i \mathbf{e}_i f_i + \frac{\Delta t}{2}\phi_\alpha \mathbf{G} \qquad \text{Eq. 3-20}$$

$$c_0 = \frac{1}{2}\left(1 + \phi_\alpha \frac{\Delta t}{2}\frac{\nu_e}{K_\alpha}\right), \quad c_1 = \phi_\alpha \frac{\Delta t}{2}\frac{F_{\varepsilon\alpha}}{\sqrt{K_\alpha}} \qquad \text{Eq. 3-21}$$

Here, v_e is defined as $\Delta t\ (\tau - 0.5)\ c_s^2$.

Following the similar procedure by Guo and Zhao (2002), Eq. 3-6, and Eq. 3-13 to Eq. 3-21 for incompressible fluid flow can be described as:

$$\nabla \cdot \mathbf{u} = 0 \qquad \text{Eq. 3-22}$$

$$\frac{\partial \mathbf{u}}{\partial t} + (\mathbf{u}\cdot\nabla)\left(\frac{\mathbf{u}}{\phi_\alpha}\right) = -\frac{1}{\rho}\nabla(\phi_\alpha p) + \nu_e \nabla^2 \mathbf{u} + \mathbf{F} \qquad \text{Eq. 3-23}$$

This is a specific form of the generalized *N–S* equation for isothermal incompressible fluid flow in porous media according to the Chapman-Enskog expansion for heterogeneous cases, which reduces to the Eq. 3-1 and Eq. 3-2 for homogenous cases.

3.2.3.2 Multiple contact boundaries

Fluid flow on multiple geomaterial contact boundaries is demonstrated in a schematic diagram (Fig. 3-2): (a) boundary between pores and permeable materials; (b) boundary between different permeable materials; (c) boundary between pores and the impermeable aggregate; and (d) boundary between permeable materials and the impermeable aggregate.

Based on Eq. 3-6, Eq. 3-13 to Eq. 3-21, pores can be idealized as an extreme geomaterial with an average porosity of 1.0 (where the resistance force is zero). Therefore, when the fluid flows through multiple geomaterials and/or pore structures (Fig. 3-2 (a) and (b)), the resistance force can be

generally described using Eq. 3-16 to Eq. 3-18. It relates to the geomaterial localization properties (individual porosity and permeability). For instance, the resistance force term on the fluid flow is approaching to when the geomaterial has very low porosity (e.g. close to zero), which can be regarded as the impermeable aggregate. When the fluid flow accesses the impermeable aggregate (Fig. 3-2 (c) and (d)), it cannot pass through these aggregate boundaries. More research work have been conducted to model this geomaterial boundaries, and some schemes have been developed (Aidun and Lu, 1995; He et al., 1997; Zou and He, 1997; Chen and Doolen, 1998; Aidun and Clausen, 2010). Among these studies, the bounce-back scheme implements the extreme resistance force case with a fully bounce-back velocity distribution. It describes the fluid particle dynamics on impermeable aggregate surfaces with simplicity and numerical accuracy. We combine this bounce-back scheme into the conventional lattice Boltzmann method as an extension.

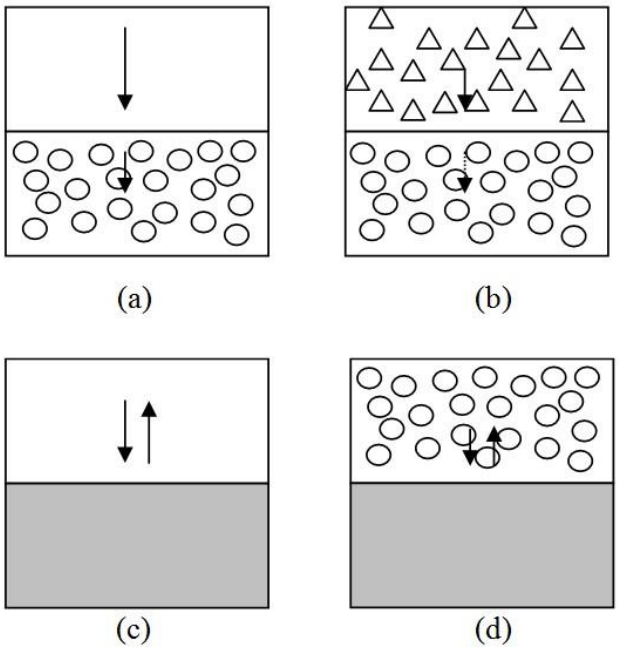

Fig. 3-2 Schematic diagram for fluid flow experiencing multiple material boundaries.

For *2D* cases:

$$f_{(i,j),1} = f_{(ip,j),3} \quad f_{(i,j),2} = f_{(i,jp),4} \quad f_{(i,j),3} = f_{(in,j),1} \quad f_{(i,j),4} = f_{(i,jn),2}$$

$$f_{(i,j),5} = f_{(ip,jp),7} \quad f_{(i,j),6} = f_{(in,jp),8} \quad f_{(i,j),7} = f_{(in,jn),5} \quad f_{(i,j),8} = f_{(ip,jn),6}$$

Eq. 3-24

For *3D* cases:

$$f_{(i,j,k),1} = f_{(ip,j,k),3} \quad f_{(i,j,k),2} = f_{(i,jn,k),4} \quad f_{(i,j,k),3} = f_{(in,j,k),1} \quad f_{(i,j,k),4} = f_{(i,jp,k),2}$$

$$f_{(i,j,k),5} = f_{(i,j,kp),6} \quad f_{(i,j,k),6} = f_{(i,j,kn),5} \quad f_{(i,j,k),7} = f_{(i,jp,kp),10} \quad f_{(i,j,k),8} = f_{(ip,jp,k),11}$$

$$f_{(i,j,k),9} = f_{(ip,j,kn),12} \quad f_{(i,j,k),10} = f_{(i,jn,kn),7} \quad f_{(i,j,k),11} = f_{(in,jn,k),8} \quad f_{(i,j,k),12} = f_{(in,j,kp),9}$$

$$f_{(i,j,k),13} = f_{(ip,j,kp),15} \quad f_{(i,j,k),14} = f_{(i,jp,kn),17} \quad f_{(i,j,k),15} = f_{(in,j,kn),13} \quad f_{(i,j,k),16} = f_{(in,jp,k),18}$$

$$f_{(i,j,k),17} = f_{(i,jn,kp),14} \quad f_{(i,j,k),18} = f_{(ip,jn,k),16}$$

Eq. 3-25

3.2.3.3 Statistics description

Natural geomaterials typically have impurities, which is also known as mineral noise. Regarding one certain geomaterial constituent (porosity as ϕ_α, $1 \le \alpha \le N$-1), a variable $\phi_{\alpha p}$ (p as position) for specifying the impurity level of individual geomaterial at each lattice node is introduced into the *XLBM* model. Given an impure geomaterial α (average porosity ϕ_α), the porosity probability distribution $\phi_{\alpha p}$ at each node of geomaterial α meets the statistics Weibull distribution:

$$f\left(\phi_{\alpha p}\right) = \frac{A}{\phi_\alpha}\left(\frac{\phi_{\alpha p}}{\phi_\alpha}\right)^{A-1} \exp\left[-\left(\frac{\phi_{\alpha p}}{\phi_\alpha}\right)^{A}\right] \qquad \text{Eq. 3-26}$$

According to the Weibull distribution, the porosity probability distribution $\phi_{\alpha p}$ can be described as:

$$\phi_{\alpha p} = \phi_\alpha\left(\ln\frac{1}{1-U}\right)^{\frac{1}{A}} \qquad \text{Eq. 3-27}$$

In Eq. 3-26 and Eq. 3-27, A (>0) controls the shape of the distribution, and U is the uniform random number ranging from 0 to 1. Commonly, when A is larger than 2, the distribution describes the Gaussian distribution, which is reasonable for generating the statistic distribution of the localized porosity of geomaterial α at each lattice node.

In the *XLBM*, it describes the flow mechanism through cavities and multiple geomaterials with some permeability, and discusses the flow behaviour on the impermeable aggregate surfaces by analysing corresponding force conditions, where each constituent (at each lattice grid) has its own hydraulic properties. It reasonably describes the complex distribution of resistance forces occurring within different mineral components (e.g. the main aggregate or permeable geomaterials), and simulates fluid flow in heterogeneous porous media with various permeable geomaterials at the same time.

3.2.4 Reconstruction of digital porous media from *micro-CT*/*QEMSCAN* images

The *micro-CT*/*QEMSCAN* data provide insight into the inherently complex heterogeneous topology and geomaterials properties. There is still a gap between those scanned images and the digital input data for numerical modelling. For filling this gap and processing high-resolution scanned images and converting such images into *2D* or *3D* digital structures, a pre-processing coding module employing modern imaging technology (Hou et al., 2009; Golab et al., 2013c) is implemented into the custom *XLBM* platform in three steps:

1) Adjusting dull and low-contrast images into high-quality;
2) Conducting image segmentation for clear grain contacts; and
3) Extracting pixel data to distinguish geometric information.

After these steps, the noise generated during the scanning process can be significantly removed using this imaging quality refinement. Then a fourth step is added based on the *XLBM* theory:

4) Describing material localization with impurities for further simulations using the *QEMSCAN* information.

The reconstructed digital porous media (reservoir rock samples) have preserved the porous media character such that each lattice node (*2D* pixel or *3D* voxel) remains its geomaterial information, applicable for simulating localized hydraulic property over the discrete *XLBM* lattice grid.

3.3 Benchmarks

To validate the *XLBM* approach, two benchmarked test cases are carried out in this section. Both cases have studied the fluid flow through a porous medium (porosity $\phi = 0.1$) filled infinite plate channel (vertical width as H). The grid size is 80×80, the relaxation time is 0.8, and the *Reynolds* number (*Re*) is $u_0 H/v$, where v is the fluid viscosity and u_0 is the peak velocity along the flow direction. The *Darcy* number (*Da*) is described as K/H^2, where K means the permeability defined by Eq. 3-18.

3.3.1 Couette flow through a porous medium filled channel

In the Couette flow case (Chepurniy, 1984; He et al., 1998; Kuznetsov, 1998; Taheri et al., 2009; Vafai, 2010), the flow is driven by a constant velocity u_0 along the positive horizontal orientation at the top plate ($y = H$); the bottom plate ($y = 0$) is set as zero velocity. Both the left and right sides are free boundaries (infinite).

In Fig. 3-3, it shows the profile of velocity (horizontal orientation) between the top wall and the bottom wall under different *Da* numbers when *Re* = 10. The simulation results are compared with analytical solutions (Kuznetsov, 1998). The simulation results under different *Da* conditions are marked with symbols, with their corresponding analytical solutions shown in solid lines. In this case, the modelling results of *XLBM* fit the analytical solutions well.

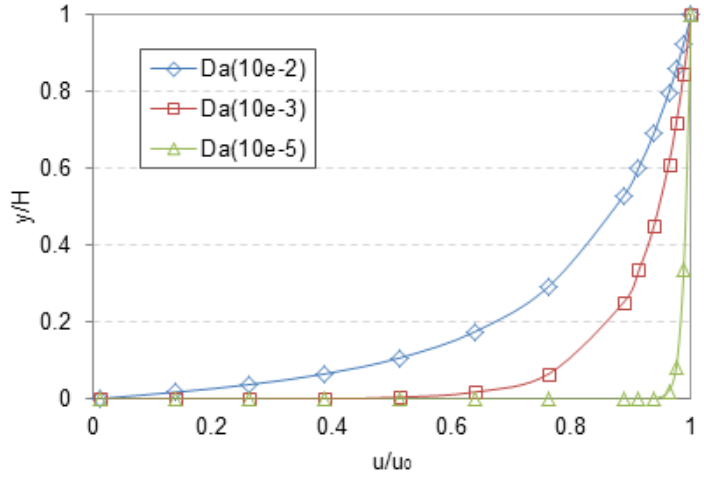

Fig. 3-3 Velocity profile (horizontal orientation) between the top wall (y = *H*) and the bottom wall (y = 0) under different *Da* numbers when *Re* = 10 (simulation results using *XLBM* marked with symbols, and analytical solutions shown in solid lines).

3.3.2 Poiseuille flow through a porous medium filled channel

The Poiseuille (Chen and Doolen, 1998; Chandesris and Jamet, 2006; Taheri et al., 2009) flow is driven by a constant force **G** along the channel orientation (horizontal axis) from the left side through a porous material filled channel. Periodic boundary conditions (infinite) are applied to the left entrance and the exit on the right, and the top and bottom walls are set as zero velocity at both horizontal and vertical orientations.

Fig. 3-4 compares the simulation results (marked with symbols) and the finite-difference solutions (solid lines) as the flow reaches the steady status. In Fig. 3-4 (a), the dashed line is an extreme condition when the porous medium has an average porosity of 1.0, which means no material but rather a cavity. The curved line shows the variation of the peak velocity of fluid flow in the porous medium right at the middle along the vertical orientation (where $y = H/2$) under different *Da* numbers, and the nonlinear inertial effect due to the porous medium (Forchheimer term) confirms the validity of the *XLBM* approach. The capacity of *XLBM* in modelling porous media flow is also proven in Fig. 3-4 (b) as the velocity distribution (marked in symbols) at the cross-section of fluid

flow direction under different *Da* numbers when *Re* = 0.1 has been verified by finite-difference solutions (solid lines).

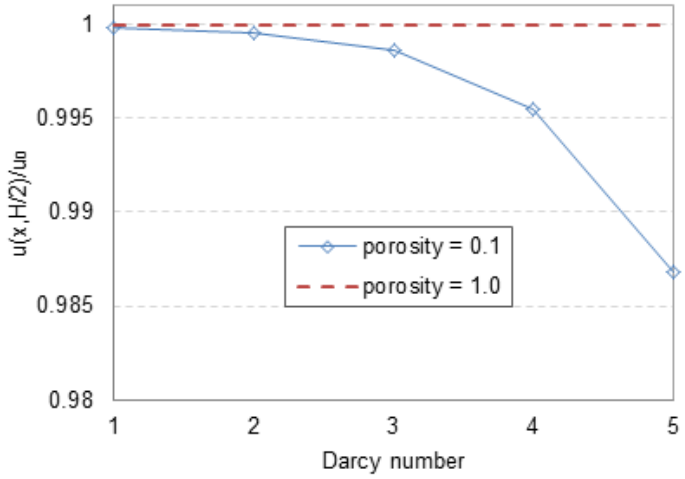

(a)

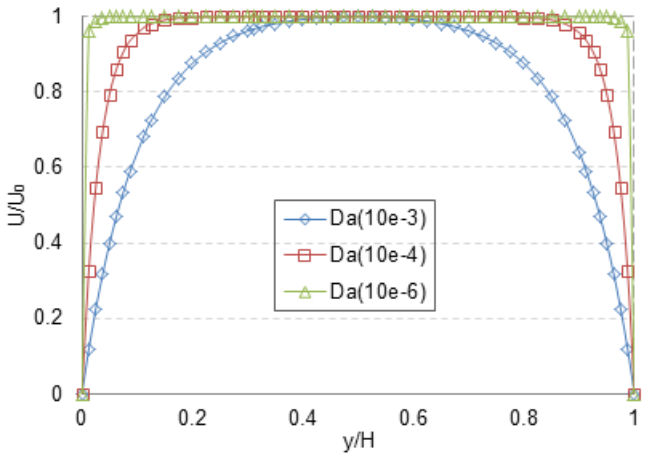

(b)

Fig. 3-4 (a) Variation of the peak velocity of fluid flow at the middle of the vertical orientation (where $y = H/2$) under different *Da* numbers; (b) Profile of velocity (horizontal orientation) between the top wall and the bottom wall under conditions of different *Da* numbers when *Re* = 0.1 (simulation results using *XLBM* marked with symbols and the finite-difference solutions shown in solid lines).

3.4 Preliminary Tests and Discussions

Two application cases are illustrated here to demonstrate the capacity of the *XLBM* in simulating fluid flow in heterogeneous porous media with complex geometry topology and disparate geomaterials.

3.4.1 Impact of geomaterial properties on flow behaviour

The *2D* porous medium includes pore spaces (in black color) and a material (in white color), which is 315 pixels in length and 295 pixels in width (Fig. 3-5 (a)). The original scan is in dull and low-contrast condition, the high-quality image used for modelling after the digital reconstruction through the pre-processing coding module has shown the clearly polished pore structures and material boundaries (Fig. 3-5 (b)).

In this application, we have compared two cases with the same topology but different material properties (case 1: the material is impermeable; case 2: the material has an average porosity ϕ of 0.23 with impurity), for studying the impact of material property on the flow dynamics. In both cases, the initial and boundary conditions are: the fluid flow is driven by the buoyancy from the bottom to the top (Eq. 3-28), and both the left and right side walls are closed without fluid in or out (Eq. 3-29)

$$\mathbf{G} = -F_{buoyancy} \qquad \text{Eq. 3-28}$$

$$\mathbf{u}(x, y) = 0 \quad (x = 0)$$
$$\mathbf{u}(x, y) = 0 \quad (x = L) \qquad \text{Eq. 3-29}$$

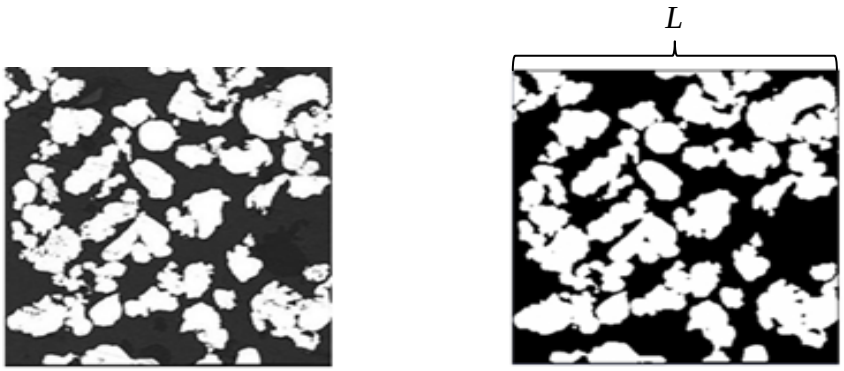

(a) (b)

Fig. 3-5 (a) Scan of an original porous medium section (315 × 295), and (b) the polished porous media structure after the reconstruction using the pre-processing coding module.

Flow flux features illustrated inside the porous medium are significantly different in two cases, although they share the same geometry structure (topology). Fluid flow route, velocity profile of fluid flow, and detached velocity profile in both cases are compared in Fig. 3-6 after computing convergence (flow reaching the steady status). In case 1, the velocity distribution differs at pores and the aggregate (Fig. 3-6 (a), (c) and (e)), and fluid only flows through the pore networks and is

obstructed against impermeable aggregate surfaces. In contrast, there is a seepage (Fig. 3-7 (b), (d) and (f)) through the permeable matrix material and the overall resultant fluid velocity of the model is much reduce (by orders of magnitude), where the highest velocity value is less than 1/100 of that in the impermeable aggregate case. This clearly demonstrates that is it is not only the major pore topology that governs fluid transport; if permeability of the matrix material and hence fluid flux through this material is not considered, the overall fluid flux through the modeled sample may be overestimated by the model.

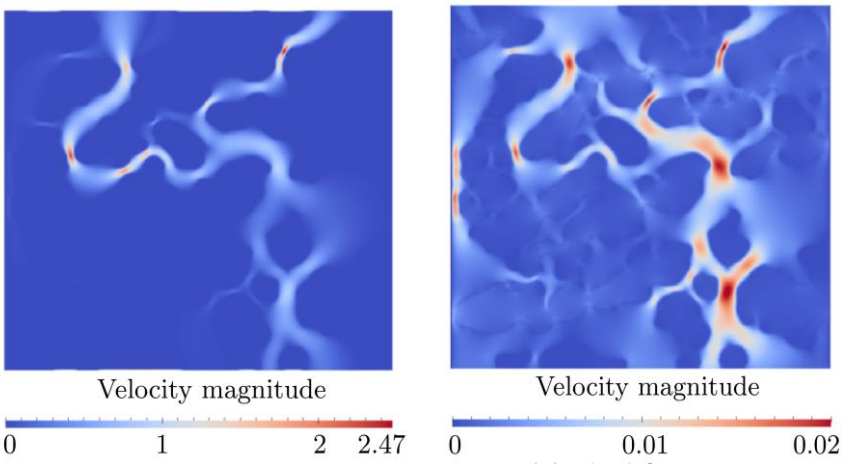

(a) (b)

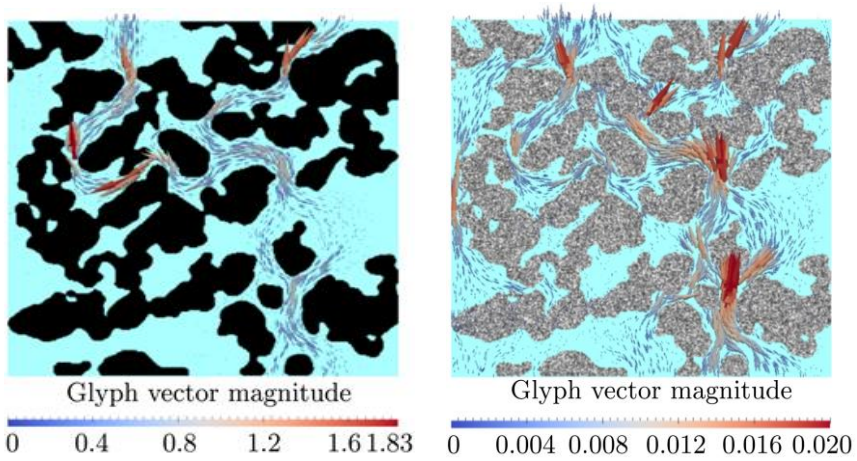

(c) (d)

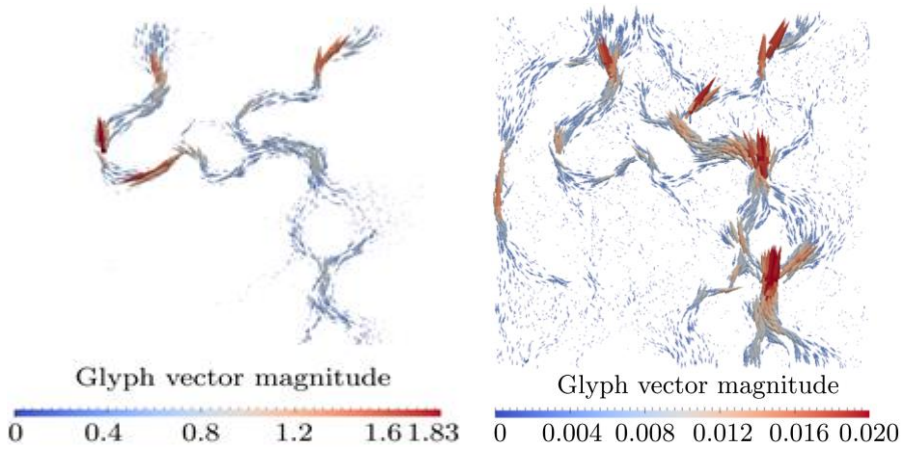

(e) (f)

Fig. 3-6 Fluid flow route with (a) the impermeable aggregate and (b) permeable geomaterials; velocity profile of fluid flow with (c) the impermeable aggregate and (d) permeable geomaterials; velocity profile (e) detached from (c), and velocity profile (f) detached from (d).

3.4.2 Effect of material property on the fluid transport

This case seeks to illustrate the effect of material properties and geometric topology on pore scale fluid flow using the custom *XLBM* code. The *2D* porous thin section (Fig. 3-7) is a square consisting of quartz sections (impermeable), lithic fragments (relatively high permeable in this that has a significant impact upon the outcome of this model), highly altered feldspar grains (relatively low permeable here) and pore structures. The lattice grid of the whole domain is 201 × 201 (L = 201) and the relaxation time τ is defined as 0.8 for computing stability. The lithic fragments are given an an average porosity of ϕ_1 (ϕ_1 = 0.5), and the sections containing highly altered feldspar grains have an average porosity of ϕ_2 (ϕ_2 = 0.1). The porosity ϕ_0 for pores is 1.0, thus the resistance force in pores is reduced to zero according to Eq. 3-16 until Eq. 3-18. The porosity ϕ_3 of impermeable quartz is reasonably zero based on the previous introduction. The fluid enters from the left side and exits at the right side driven by a constant external body force $\mathbf{G}$ = 0.1 (along the x-axis in Fig. 3-7) with a set *Reynolds* number (Re = 0.1). Both the top and bottom walls are zero velocity closed boundaries (Eq. 3-30).

$$\mathbf{u}(x, y) = 0 \quad (y = 0)$$
$$\mathbf{u}(x, y) = 0 \quad (y = L) \qquad \text{Eq. 3-30}$$

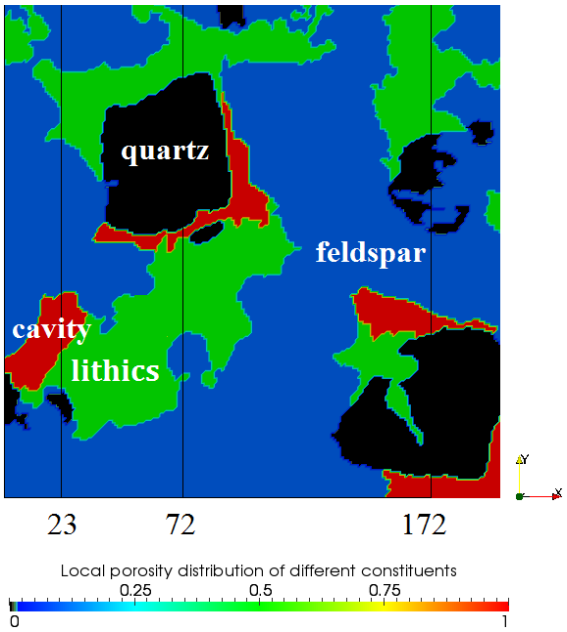

Fig. 3-7 A thin section of porous medium involving multiple geomaterials in different colors (pore - red, lithic fragments - green, highly altered feldspar grains - blue, quartz - black). The vertical black lines at x = 23, 72 and 172 indicate cross-sections to be studied.

The velocity field of the fluid flow in the whole porous medium domain is illustrated at steady state in Fig. 3-8. Generally, the fluid flow is blocked by the impermeable aggregate (quartz sections), and flows faster in pores. Besides, it flows more slowly when passing through the permeable geomaterial sections (feldspar fragments and lithics) than the pores.

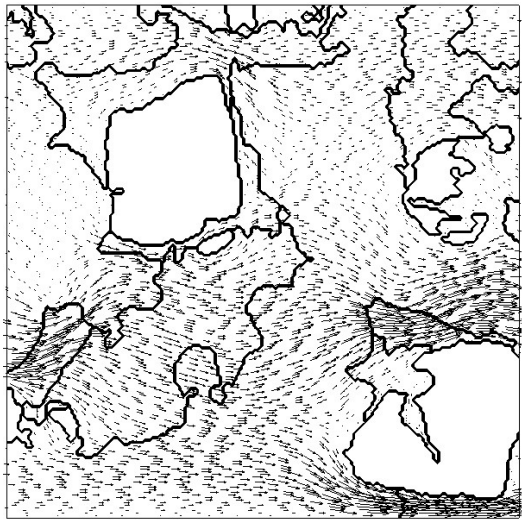

Fig. 3-8 Distribution of multiple geomaterials (thick black lines indicate surfaces of geomaterials), and velocity distribution of the fluid flow (arrows and length indicate the velocity direction and size, respectively).

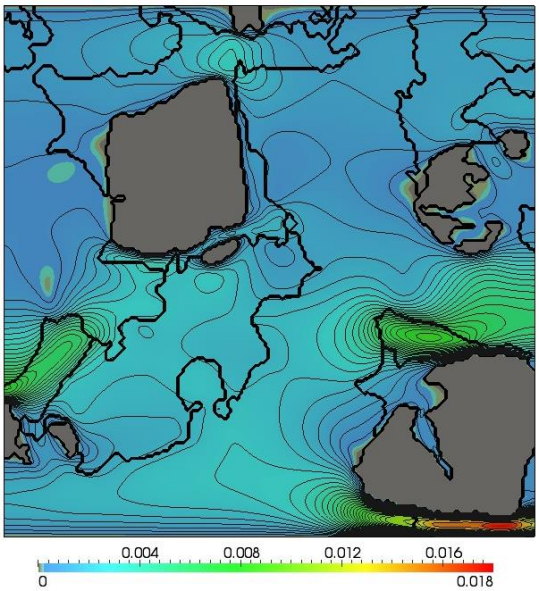

Fig. 3-9 Distribution of multiple geomaterials (thick black lines indicate surfaces of geomaterials), and velocity magnitude field with contours (contour step = 50).

Furthermore, Fig. 3-9 illustrates the velocity magnitude distribution (contour step = 50). Intuitively, the flow dynamics are mainly dominated by the geometric topology of the impermeable aggregate, but pore structures also greatly affect the velocity distribution. All the flow here results through matrix seepage as the pores are disconnected in the section modeled here. At a more detailed level, closure of some contours appears on the surfaces among pores, feldspar fragments, lithics and quartz, due to the disparate porosity distribution and irregular geometric boundaries. These material-flow effects deserve more detailed analysis, but still (as presented) serve here to illustrate how the *XLBM* can analyse permeable seepage phenomena in heterogeneous porous media involving multiple geomaterials.

Three vertical cross-sections (along x = 23, 72 and 172 in Fig. 3-7) are chosen for comparing general flow character under different geomaterial properties, including: the distribution of detailed local geomaterial porosity, velocity at the horizontal (x-axis) and vertical orientation (y-axis), and the total velocity magnitude. The related results are shown in Fig. 3-10, Fig. 3-11 and Fig. 3-12 respectively.

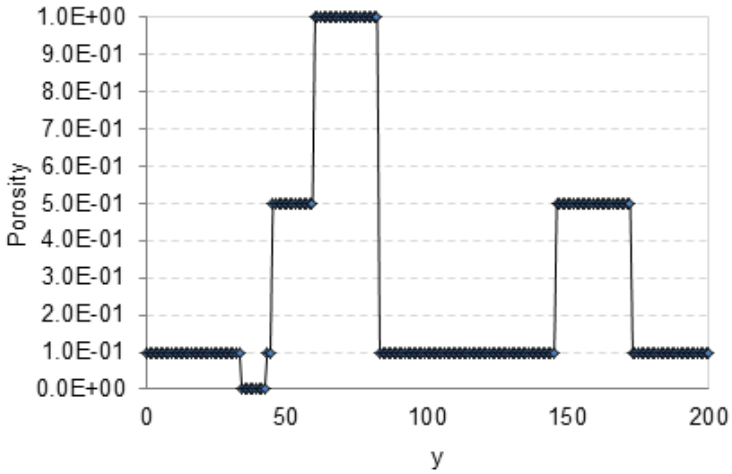
1.0E+00
9.0E-01
8.0E-01
7.0E-01
6.0E-01
5.0E-01
4.0E-01
3.0E-01
2.0E-01
1.0E-01
0.0E+00
Porosity
0
50
100
150
200
y

(a)

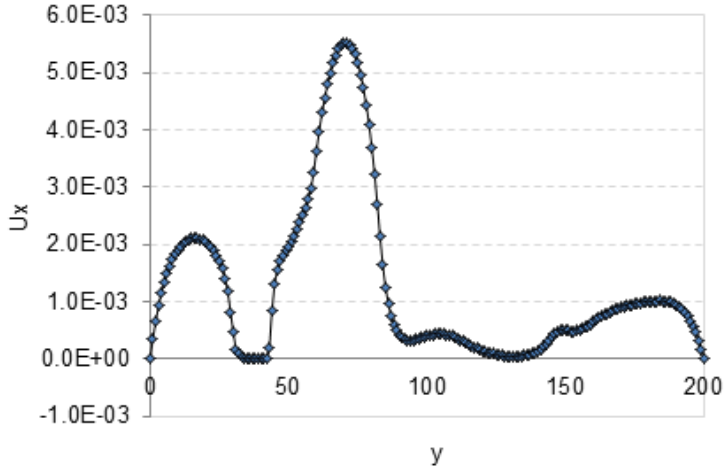
6.0E-03
5.0E-03
4.0E-03
3.0E-03
2.0E-03
1.0E-03
0.0E+00
-1.0E-03
Ux
0
50
100
150
200
y

(b)

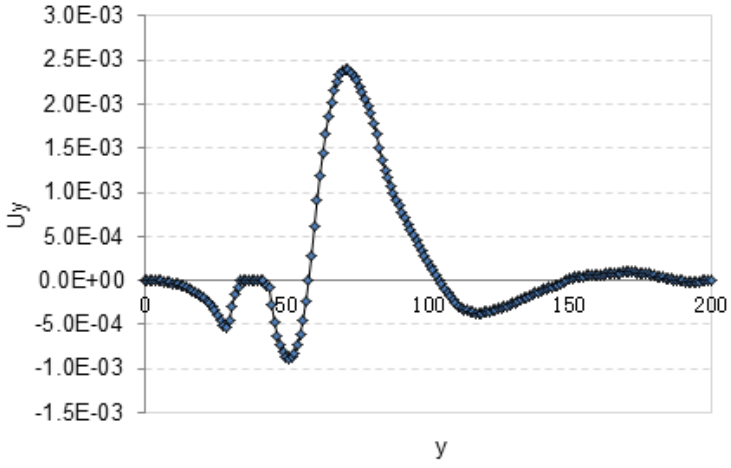
3.0E-03
2.5E-03
2.0E-03
1.5E-03
1.0E-03
5.0E-04
0.0E+00
-5.0E-04
-1.0E-03
-1.5E-03
Uy
0
50
100
150
200
y

(c)

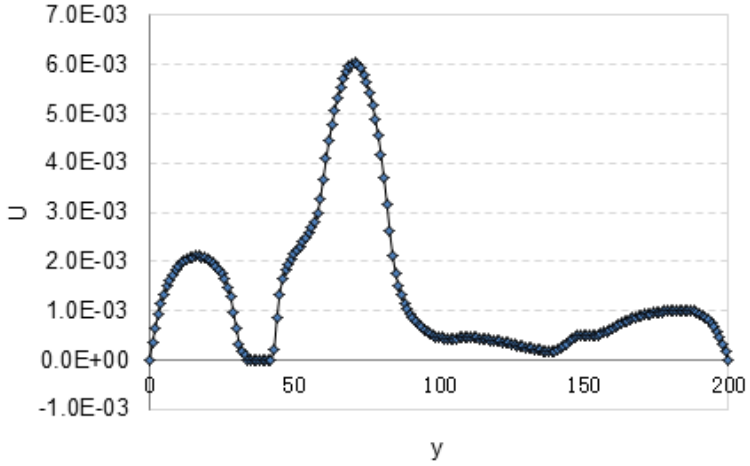

(d)

Fig. 3-10 Porosity distribution and velocity distribution at the cross-section x = 23: (a) distribution of local geomaterial porosity; (b) velocity profile along the horizontal orientation; (c) velocity profile along the vertical orientation; (d) and total velocity magnitude distribution.

The detailed porosity distribution at the vertical cross-section x = 23 are shown in in Fig. 3-10 (a): quartz (ϕ_3 = 0.0) is observed in $34 \leq y \leq 42$, a pore (ϕ_0 = 1.0) in $60 \leq y \leq 82$, and lithics (ϕ_1 = 0.5) in $45 \leq y \leq 59$ and $146 \leq y \leq 172$, whereas feldspar fragments (ϕ_2 = 0.1) fill the others. The horizontal velocity of fluid flow along this cross-section varies according to the local porosity distribution (Fig. 3-10 (b)):

1) The fluid flows faster in the pore space ($60 \leq y \leq 82$), and reaches the highest value of 0.00552 at y = 70;
2) From y = 0 to y = 34, the velocity of flow through feldspar fragments between two impermeable walls behaves as a pseudo-Poiseuille type due to the constant driving force **G.** Then the velocity decreases to zero due to the quartz block around $34 \leq y \leq 42$;
3) Horizontal velocity distribution from y = 45 to y = 59 increases due to the relatively higher lithic fragment porosity in this area. Similar phenomena can be seen in $146 \leq y \leq 172$ with a slight velocity hump; and
4) The flow has a relatively higher speed around y = 180 to y = 200 while preparing to flow through a narrow feldspar fragments filled slit (Fig. 3-7).

A similar vertical velocity character can be observed along this cross-section (Fig. 3-10 (c)):

1) The fluid flows with a higher speed along the positive y-axis in the pore space ($60 \leq y \leq 82$), due to the pore structure slanting upward to the right;

2) Since the fluid flow bypasses a big quartz at the right side of this cross-section, the velocity distribution from y = 105 to y = 148 is in the negative y-axis, but that from y = 149 to y = 188 is in the positive y-axis. A similar impedance effect of a small quartz grain ($34 \leq y \leq 42$) on the fluid flow can be found; and
3) Inside such quartz sections, there is no fluid flow observed.

Fig. 3-10 (d) shows that the horizontal velocity component has the dominant influence on the total velocity magnitude because of the x-axis driving force. The flow character is primarily determined by the geometric topology of the porous medium, especially the quartz and pore structures. Moreover, different geomaterial properties have also affected the flow character, which is illustrated along each orientation in Fig. 3-10 (b) and (c).

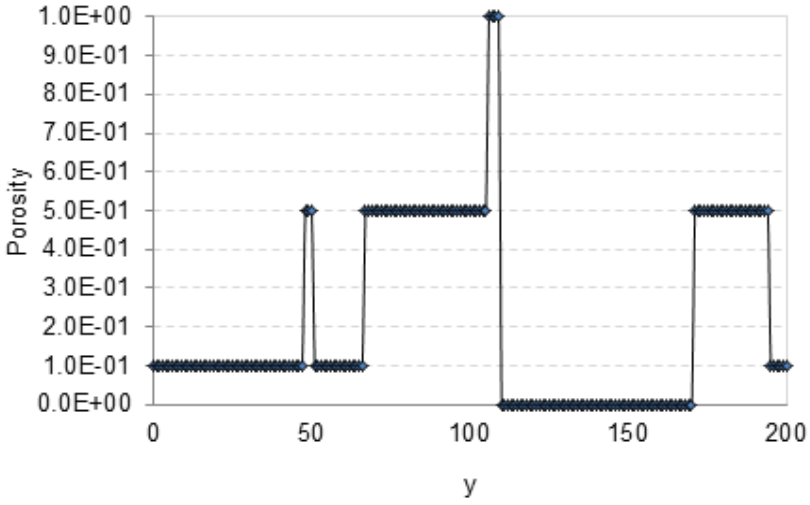

(a)

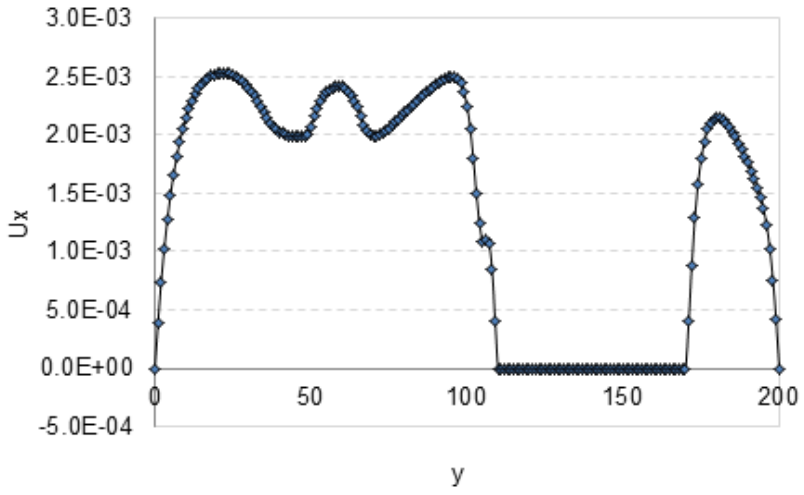

(b)

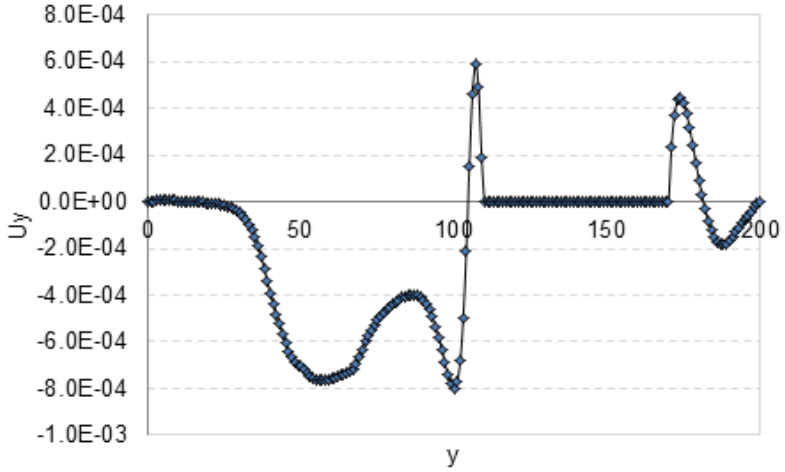

(c)

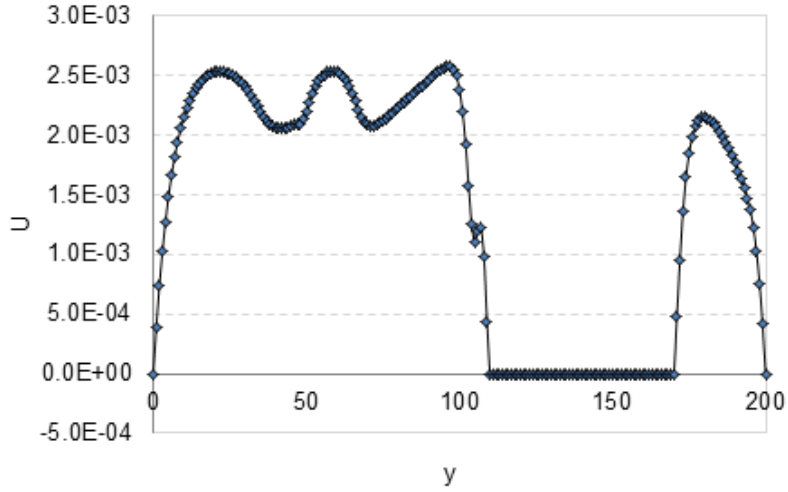

(d)

Fig. 3-11 Porosity distribution and velocity distribution at the cross-section x = 72: (a) distribution of local geomaterial porosity; (b) velocity profile along the horizontal orientation; (c) velocity profile along the vertical orientation; (d) and total velocity magnitude distribution.

A similar comparison is made for the cross-section x = 72 (Fig. 3-7) where four constituents are identified (Fig. 3-11 (a)): a pore space exists from y = 106 to y = 109, and a quartz section appears from y = 110 to y = 170, lithic fragments take up areas $48 \leq y \leq 50$, $67 \leq y \leq 105$ and $171 \leq y \leq 194$, and feldspar fragments fill the other areas left.

In Fig. 3-11 (b), there is a peak in the velocity distribution around y = 180, which occurs because that point is around the center of a narrow slit filled with low permeable feldspar fragments. Furthermore, there is a "ω" type velocity profile in $0 \leq y \leq 100$. This is because of the irregular contact boundaries between feldspar fragments and lithics from y = 51 to y = 66, which form a "delta" type feldspar fragment filled area. This configuration slows down the outlet velocity of fluid

flow in lithics and speeds up the flow in feldspar fragments. The big quartz ($110 \leq y \leq 170$) blocks the fluid totally, so that there is no fluid flow observed inside this area (Fig. 3-11 (b) and (c)).

The vertical velocity distribution varies according to the complex geometric topology:

1) The slanting upward to the right pore ($106 \leq y \leq 109$) allows higher flow speed in the positive y-axis;
2) Due to the bypassing effect of the big quartz section, vertical velocity of the flow from $y = 0$ to $y = 100$ is in the negative y-axis; and
3) There is chuting flow through a narrow lithics filled slit around $171 \leq y \leq 194$.

From Fig. 3-11 (d), we can see that the impact of vertical velocity on the total velocity magnitude is relatively smaller than that at the horizontal orientation. However, the vertical velocity distribution (Fig. 3-11 (c)) of fluid is clearly different from that in a homogeneous porous medium (no velocity distribution in the y-axis) due to the effect of multiple geomaterials on fluid flow in the heterogeneous porous medium.

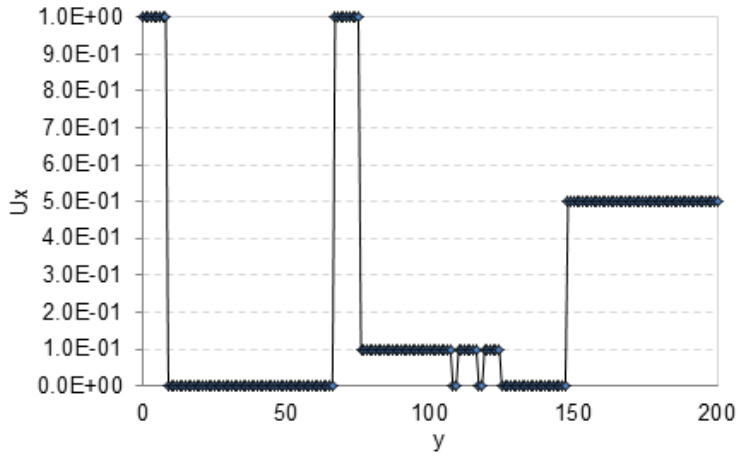

(a)

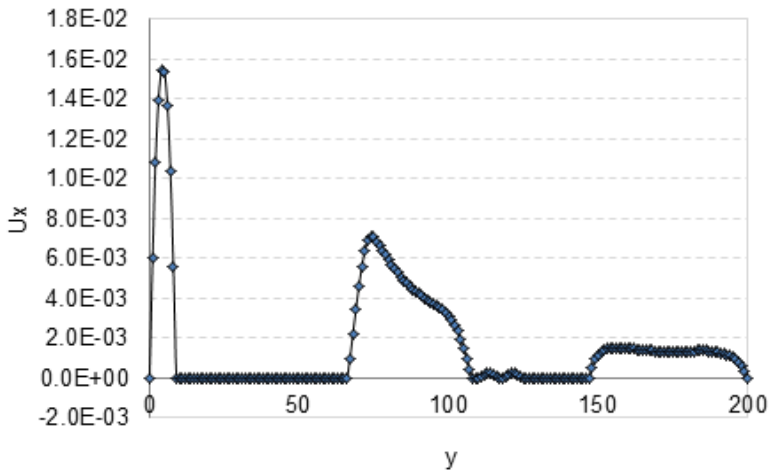

(b)

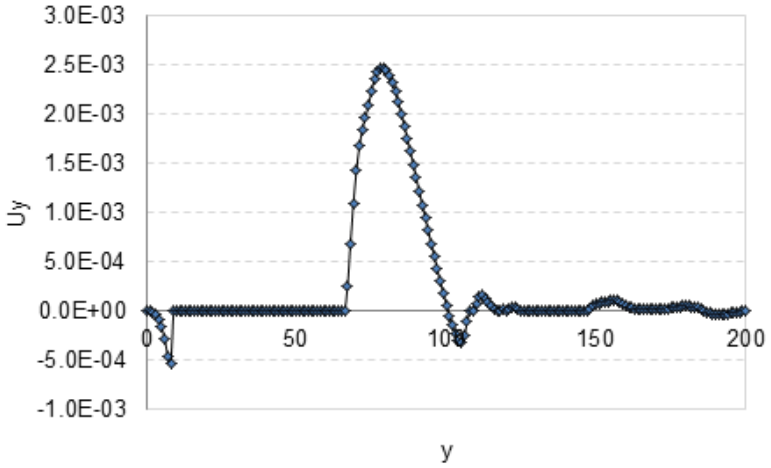

(c)

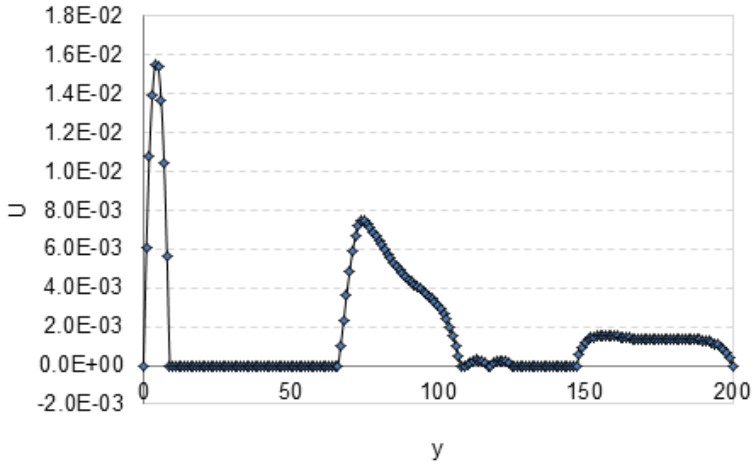

(d)

Fig. 3-12 Porosity distribution and velocity distribution at the cross-section x = 172: (a) distribution of local geomaterial porosity; (b) velocity profile along the horizontal orientation; (c) velocity profile along the vertical orientation; (d) and total velocity magnitude distribution.

The geomaterials distribution at the cross-section x = 172 (Fig. 3-7) is more complex (Fig. 3-12 (a)): pores occur from y = 0 to y = 8, and from y = 67 to 75. There is also a distribution of lithic fragments at $148 \leq y \leq 200$, and quartz occupies the space along the way ($9 \leq y \leq 66$, $108 \leq y \leq 109$, $117 \leq y \leq 118$, and $125 \leq y \leq 147$). The other areas are filled with feldspar fragments.

In the pores ($0 \leq y \leq 8$, and $67 \leq y \leq 75$), the horizontal velocity has a big hump distribution, whereas there is no fluid flow through the quartz. The feldspar fragments ($110 \leq y \leq 116$, and $119 \leq y \leq 124$) allow a slower flow through this area, whereas the fluid flows faster in feldspar fragments ($76 \leq y \leq 107$) due to the higher speed fluid flow in the nearby pores (Fig. 3-12 (b)). Compared with

the velocity profile in feldspar fragments ($110 \leq y \leq 116$, $119 \leq y \leq 124$), fluid flow is faster in the lithic fragments ($148 \leq y \leq 200$).

Similar to the above description, there is no fluid through the quartz grains ($9 \leq y \leq 66$, $108 \leq y \leq 109$, $117 \leq y \leq 118$, and $125 \leq y \leq 147$). A negative y-axis velocity is observed at $0 \leq y \leq 8$, and this detour of flow is induced by the adjacent quartz section (Fig. 3-7). The speed of fluid flow is highest in the big pore due to less resistance in this area. Both the effect of the pore space ($67 \leq y \leq 75$) and the quartz ($9 \leq y \leq 66$) guiding the flow to the right and upwards leads to a higher vertical velocity around $76 \leq y \leq 107$. In the lithic fragments area ($148 \leq y \leq 200$), the flow is more horizontally steady, so the vertical velocity shows less fluctuations. The impact of vertical velocity on the total velocity magnitude at this cross-section is relatively smaller than that at the horizontal orientation (Fig. 3-12 (d)).

Through the above numerical analysis at three cross-sections (Fig. 3-7, Fig. 3-10, Fig. 3-11 and Fig. 3-12), obvious effects of multiple geomaterials and geometric topology on the fluid flow in heterogeneous porous media can be summarized as:

1) There is no fluid flow observed through the quartz grains that are assumed to be impermeable, which is marked as a local porosity value as 0.0 in Fig. 3-10 (a), Fig. 3-11 (a) and Fig. 3-12 (a);
2) Fluid flows faster through pores (marked as a local porosity value as 1.0 in Fig. 3-10 (a), Fig. 3-11 (a) and Fig. 3-12 (a)) because of the zero resistance force in these areas according to the Eq. 3-16. Meanwhile, a lower-speed fluid flow is observed in the permeable geomaterial sections compared with that in pores;
3) The total velocity magnitude is dominated by the horizontal velocity of the flow as it is driven under an x-axis constant force (due to the numerical experiment settings), but the flow patterns are significantly different from the Poiseuille flow observed in homogenous porous media; and
4) The vertical velocity of flow is complex and different from that in conventional homogenous porous media applications, where the vertical velocity commonly remains close to zero (Guo and Zhao, 2002).

The *XLBM* can analyse permeable seepage phenomena in heterogeneous porous media involving multiple geomaterials (e.g. low local intrinsic permeability). In contrast, there will be no fluid pass through the whole domain (Fig. 3-7) if the conventional pore-solid *LBM* is employed to investigate such kinds of issues without the *XLBM* as it hardly describes the connecting pores.

3.5 Conclusions

The conventional *LBM* is first introduced for modelling fundamental fluid flow dynamics in pore scale porous media with complex geometry topology. It is then extended by adding the statistics theory, material localization, and multiple contact boundaries to describe the heterogeneous porous media with permeable geomaterials (denoted as *XLBM* for simplification); it also includes the reconstruction of digital samples from *micro-CT*/*QEMSCAN* images. The model is implemented as a custom *XLBM* code, and benchmarked through comparison with the existing analytical solutions. By using the *micro-CT/QEMSCAN* images, digital *2D*/*3D* reservoir rock samples are reconstructed and integrated for providing microstructure detail for *XLBM* simulations.

Application examples demonstrate the capacity and usefulness of the *XLBM* model in studying the effect of geometric information and geomaterial properties on the pore fluid flow detail: no fluid flow is observed through the impermeable aggregate, whereas fluid flows faster through pores due to the zero resistance force in these areas. External force is the main reason for leading flow profiles, and those flow profiles are also significantly affected by geomaterial properties. In addition, a lower-speed fluid flow is observed in permeable geomaterials compared with that in pores, which may significantly change the flow pattern in the whole domain (e.g. Fig. 3-6 (c)-(f)), and is beyond the capability of the conventional *LBM*.

The *XLBM* describes the flow mechanism through cavities and multiple geomaterials containing at least some permeability, and shows the flow behaviours on the surfaces of impermeable aggregates by providing each constituent (on each lattice grid) with its own hydraulic properties. This provides a reasonable reproduction of the complex distribution of resistance forces within different mineral components (e.g., the main aggregates or permeable geomaterials), and simulates fluid flow in heterogeneous porous media having a variety of permeable and impermeable geomaterials. The *XLBM* model strengthens the capability of determining reliable permeability values in later studies by integrating geomaterials as an impacting factor and serves as the basis for more advanced study of the coupled **System (T, H, C)** issues.

Chapter 4 Parallel *XLBM* for Pore Scale Flows with Massive Data Sets Processing in *3D* Cases

4.1 Introduction

In order to model coupled **System (T, H, C)** in heterogeneous porous media, it is essential to characterize the detail of pore scale information including geometry, tortuosity and distribution of multiple minerals. This is an essential step for further studying and verifying porous media flow, heat transfer and chemical reactions through the benchmarks and experiments.

As introduced in previous chapters, *micro-CT* scanning with *QEMSCAN* mineral analysis is used for characterisation of pore scale detail of reservoir rocks in a non-destroyable and repeatable way. These imaging technologies have provided capability in quantifying internal microstructures and distribution of multiple geomaterials, hence delivering a high level of sample detail. Meanwhile, there are also a few issues related to the processing of massive data sets due to:

1) High resolution scans

The *micro-CT* scanning is carried out on a small scale (~ *mm* to ~ *cm*) and generates scans with small pixel sizes (down to ~ μm) to reveal sufficient pore scale information. This enables the description of pore scale geometry and mineral information detail, which is essential for the dynamical modelling process elaborated on further. High resolution (small pixel size) scanned images carry much more information but with large data sets, hence requiring more storage space, memory size and computational processing to transform raw attenuation to density maps and visual images; For instance, a 1 *cm* scale cubic sample (with a voxel size of 4 μm) can generate around 125 *Gigabytes* of digital raw data sets, and this is merely the initial architectural input for the dynamical simulations.

2) Dynamical modelling

The numerous initial architectural inputs consequently imply associated enormous computational processing loads in dynamical **System (T, H, C)** modelling. With respect to high-resolution digital core samples (size of data sets ≥ 100 *Gigabytes*), the main challenges for implementing fast-speed modelling are processing of large initial architectural data sets, large run-time memory and data management, and visualization of massive data outputs. Conventional personal computers or small local work stations are unsuitable for such computational duties, providing insufficient computational resources by way of processor performance, memory demands, and disk storage. Thus, massive data sets in this thesis work require special Input/Output (*I*/*O*) access and effective

data communication among multiple processors. Effective parallel computing algorithm and codes are essential for this task.

As introduced in Chapter 3, *XLBM* is advanced for simulations of fluid transport in porous media with heterogeneity and multiple geomaterials. The character of molecular dynamics that each particle on the grid conducts collision interaction with its neighbors enables its strong potential capacity in parallel computing (Kandhai et al., 1998; Desplat et al., 2001; Pan et al., 2004; Wang et al., 2005; Clausen et al., 2010; Vidal et al., 2010). However, it still requires substantial efforts to achieve a more efficient algorithm with high computing performance, for dealing with issues such as large Input/Output (*I*/*O*) access and numerous data communication among multiple processors on supercomputers.

This chapter focuses on the issue of massive data sets processing and computing, and corresponding solutions including parallelism algorithm, code implementation, and computing performance analysis. A parallel *XLBM* platform including the Input Preparation, Run-time Control, and Data Management and Visualization, has been introduced in Section 4.2, for providing end-to-end service for modelling fluid dynamics in massive *3D* heterogeneous reservoir rocks. Techniques to develop and install the platform on supercomputers (e.g. *Savanna* and *Raijin*) are also discussed.

As an application example, a pore scale study of a heterogeneous sandstone sample from the Chinchilla 4 borehole in the Surat Basin (Queensland, Australia) has been conducted in Section 4.3. The sample is a cuboid of 10.14 $mm \times 9.636\ mm \times 12.276\ mm$, and the *X-ray* computed *micro-CT* scans have a voxel size of 6.6 μm with 4.17 billion grid elements generated as an initial architectural input, after being reconstructed as a *3D* digital sample; the digital sample by capturing microscopic physical structure using high-resolution scans has been translated into a corresponding lattice for simulations using the custom parallel *XLBM*. The following factors essential for the evaluation of fluid flow features are studied regarding the high heterogeneity and anisotropy of this microstructure: (1) the sensitivity of voxel size of *micro-CT* scans on the sample composition, for retaining physical structure fidelity (e.g. geomaterial composition, pore size and throats, and porosity and tortuosity) and (2) the sensitivity of individual geomaterial component property on pore scale fluid dynamics (e.g. fluid flux fields). Computing performance analysis in Section 4.4 has shown that a nearly-linear speedup has been achieved as the CPU (or processor) number increases using the custom parallel *XLBM*. This has confirmed the parallel *XLBM* in providing high performance modelling for even larger initial data sets (e.g. *Terabytes*).

4.2 Parallelism Algorithm and Implementation

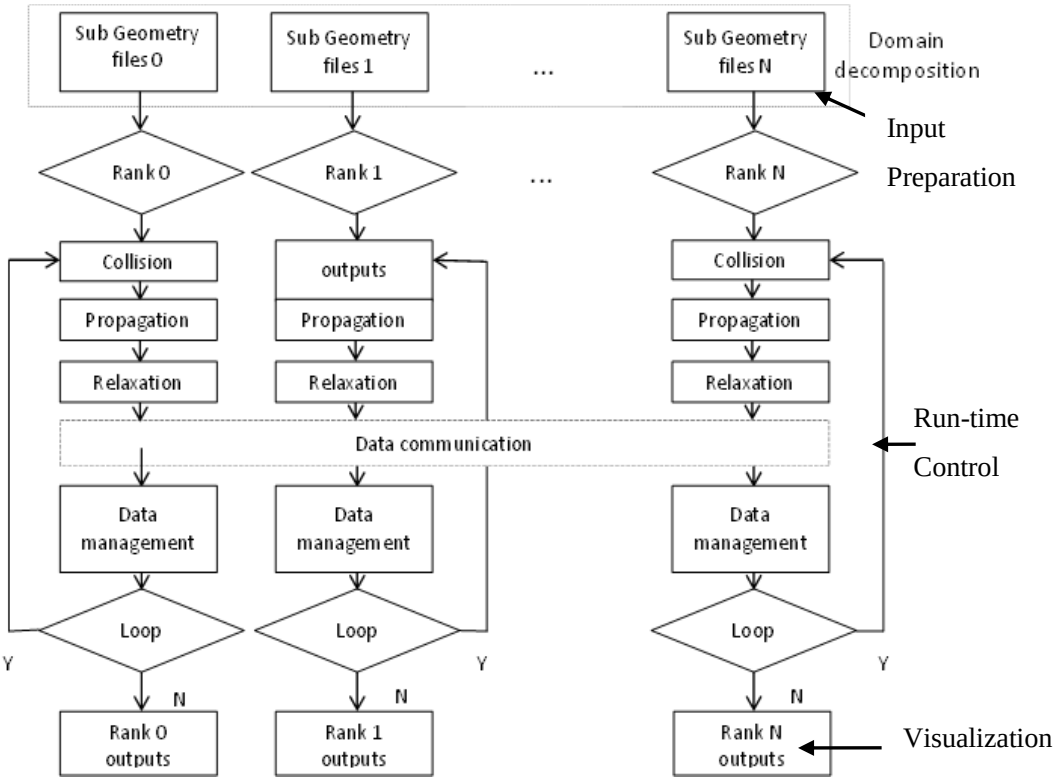

Fig. 4-1 Flow chart of the custom *XLBM* parallelism implementation.

In traditional *master-slave* parallel algorithms (Kumar et al., 1994), the master processor (rank 0) conducts Input/Output (*I*/*O*) instructions, including: reading all data in, domain decomposition and subset data (geometry information) broadcasting to all the other processors for later computing, and data collection for outputs. This traditional *master-slave* method is no longer appropriate for modelling massive initial architectural inputs in this thesis work, since the numerous initial architectural inputs are far beyond the Input/Output limitation of a single processor processing. A *LBM* based parallel algorithm is proposed in this section to solve these problems with an effective parallel scheme implemented in the custom *XLBM* code. Fig. 4-1 shows the code structure, including Input Preparation, Run-time Control, Data Management and Visualization.

4.2.1 Input preparation

In Chapter 3, we have discussed the reconstruction technique of *3D* heterogeneous reservoir rock samples by using *micro-CT*/*QEMSCAN* images. For massive initial architectural data sets processing, the reconstruction technique upgrades the sequential reconstruction algorithm (Section 3.2.4) as a parallel version by processing a set of scans in groups on different processors. In most cases, huge raw data sets are stored in separated files, for example, as a group of a few slices along the vertical orientation (block files, Fig. 4-2 (a)), which means each file represents a few sample

layers along the vertical orientation (*z*-orientation). These files require further re-decomposition for efficient data inputs for later parallel computing.

The function of the Input Preparation module is to automatically re-process the huge raw data sets to new storage files as required for further effective run-time computing; and an approach (as shown in Fig. 4-2 (b)-(d)) is introduced here in this section for re-decomposing these raw digital data set files as required forms and sizes.

In Fig. 4-2 (a), the huge raw data sets are originally stored in separated files (*File.0* to *File.N*, from the bottom to the top) due to the limitation of file storage, and the scale (domain size at different orientations) of each file is described as *PreScaleX* (*x*-orientation), *PreScaleY* (*y*-orientation) and *PreScaleZ* (*z*-orientation). Besides, the scale of each re-decomposed file is defined as *ReScaleX* (*x*-orientation), *ReScaleY* (*y*-orientation) and *ReScaleZ* (*z*-orientation) as required for further parallel computing, and the number of re-decomposed files (sub-domain) along each orientation is described as *dimX* (*x*-orientation), *dimY* (*y*-orientation) and *dimZ* (*z*-orientation). Thus $dimX = PreScaleX/ReScaleX$, $dimY = PreScaleY/ReScaleY$ and $dimZ = \sum PreScaleZ/ReScaleZ$ ($\sum PreScaleZ$ stands for the total number of vertical layers in all N+1 files).

Given a computing size (*dimX*, *dimY*, *dimZ*), any preliminary massive raw data sets can be automatically re-decomposed into the required blocks for later parallel modelling, after execution of the Splitting, Combing, and Resizing modules.

Splitting

Given the number of preliminary massive raw data files as $N+1$, each file is assigned to one or more processors for decomposing the file into $dimX \times dimY$ sub-files along the *XoY* (horizontal) flat. The number of data files after the horizontal splitting reaches $(N+1) \times dimX \times dimY$ (as shown in Fig. 4-2 (b)).

Combing

The sub-files are recombined along the vertical orientation as a group of transit-files (column), and the number of these data files reduces to $dimX \times dimY$. The processors used in this module are $dimX \times dimY$ (as shown in Fig. 4-2 (c)).

Resizing

The data files are processed along the vertical orientation (column), and each column is assigned to one or more processors and re-decomposed into *dimZ* files for final run-time simulations. The

number of data files increases to *dimX*×*dimY*×*dimZ* after the Resizing execution (as shown in Fig. 4-2 (c)).

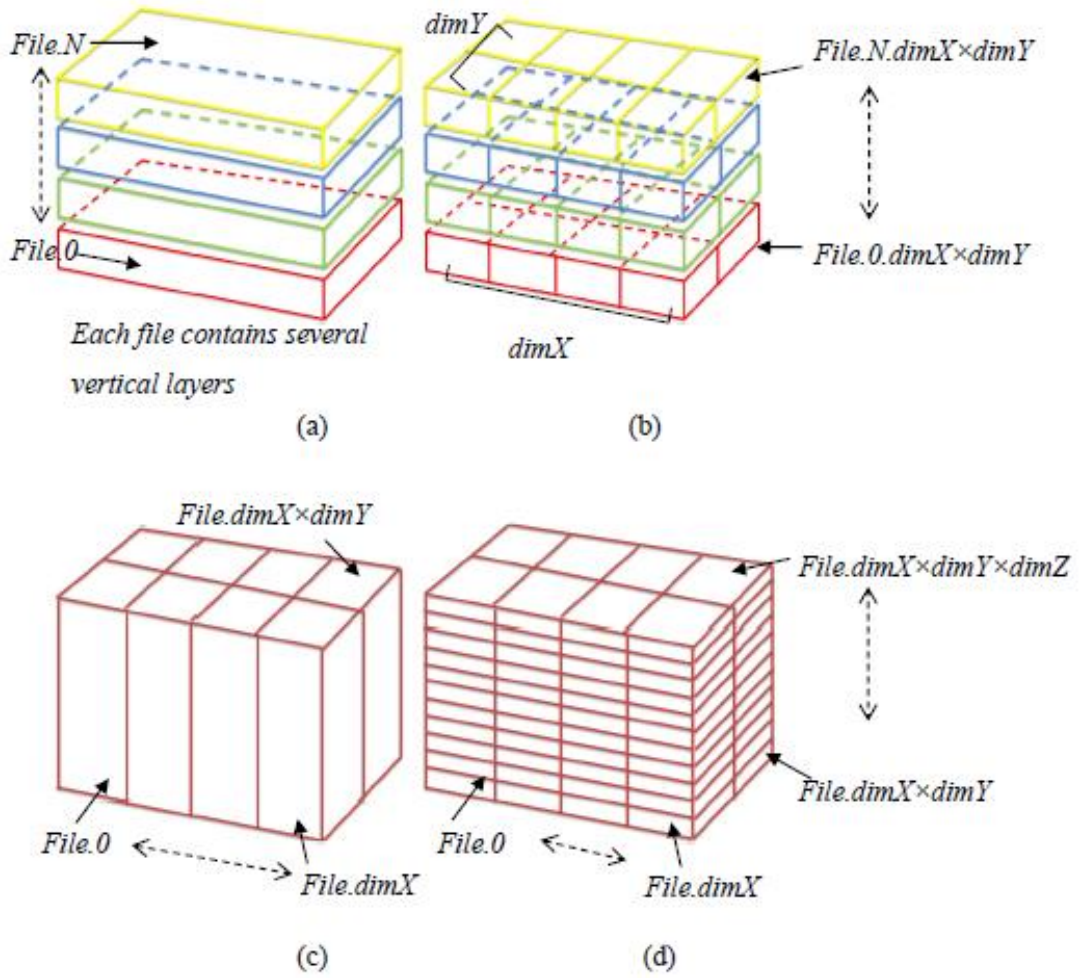

Fig. 4-2 Schematic diagram of the Input Preparation function: storage of huge raw data sets (a) after the *3D* reconstruction from *micro-CT*/*QEMSCAN* images, (b) after the Splitting module, (c) after the Combining module, and (d) after the Resizing module.

4.2.2 Run-time control

According to the re-decomposed data files generated from Input preparation module, each processor in Run-time control conducts the parallel Input/Output (*I/O*) and reads in its corresponding sub-file only; each processor is responsible for performing calculations for its portion of the simulation volume grid, as well as dealing with boundary conditions at the external edges of each volume. This is advanced for effective parallel *I/O*.

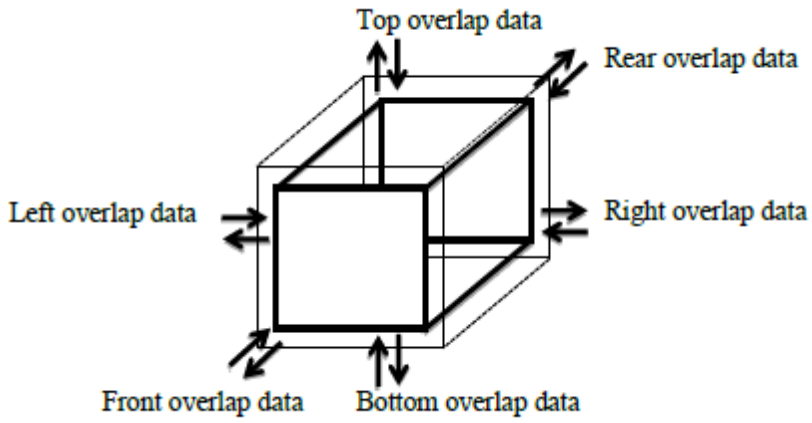

Fig. 4-3 Schematic diagram of one-layer overlap scheme for data swapping and updating between neighboring subgrids at each time step.

In the Run-time Control, data exchange and communication (swapping and updating) among different processors is vital and significantly dominates the parallel computing efficiency. Considering the character of *LBM*, a one-layer overlap (padding layer) scheme is chosen for data swapping and updating exchanged from the edge of the neighboring subgrid (Fig. 4-3).

Due to the large data swapping at each time step, the bottleneck is the time consumption in data communication. We have optimized the neighbor-locating module and package communication scheme by sending and receiving compacted data package among subgrid neighbors hence reducing total computing time by up to 58%.

The neighbor-locating module

Here, *current* means the current processor rank, *source* is the rank number sending the overlap data to the *current* rank and *dest* is the rank number receiving the overlap data from the *current* rank. All these *current*, *source*, and *dest* ranks conduct local computations for high performance modelling, and swap overlapped boundary data at each time step for data updating.

neighbors (int *current*, int &*source*, int &*dest*)

The neighbor at the negative *x*-horizontal orientation

dest = *current* - dimY*dimZ;

source = *current* + dimY*dimZ;

if (*dest* < 0) *dest* += dimX*dimY*dimZ;

if (*source* > numCores-1) *source* -= dimX*dimY*dimZ;

The neighbor at the positive *x*-horizontal orientation

```
dest = current + dimY*dimZ;
source = current - dimY*dimZ;
if (dest > numCores-1)   dest -= dimX*dimY*dimZ;
if (source < 0)   source += dimX*dimY*dimZ;
```

The neighbor at the negative *y*-horizontal orientation

```
dest = current - dimZ;
source = current + dimZ;
if (dest < 0)
    dest += dimY*dimZ;
else
    if (dimY*dimZ- dest %(dimY*dimZ)-1 < dimZ)
        dest += dimY*dimZ;
if (source %(dimY*dimZ) < dimZ)
    source -= dimY*dimZ;
```

The neighbor at the positive *y*-horizontal orientation

```
dest = current + dimZ;
source = current - dimZ;
if (dest %(dimY*dimZ) < dimZ)
    dest -= dimY*dimZ;
if (source < 0)
    source += dimY*dimZ;
else
    if (dimY*dimZ- source %(dimY*dimZ)-1 < dimZ)
        source += dimY*dimZ;
```

The neighbor at the negative vertical (*z*) orientation

```
dest = current -1;
source = current +1;
if (dest < 0)
    dest += dimZ;
else
    if (dest %dimZ == dimZ -1)
```

```
            dest += dimZ;
    if (source %dimZ == 0)
        source -= dimZ;
```

The neighbor at the positive vertical (*z*) orientation

```
    dest = current +1;
    source = current -1;
    if (dest %dimZ == 0)
        dest -= dimZ;
    if (source < 0)
        source += dimZ;
    else
        if (source %dimZ == dimZ -1)
            source += dimZ;
```

Packaging communication

Each processor uses Message Passing Interface (*MPI*) scheme to implement data communication, such as *MPI_Pack*() to pack the overlapped data into different buffers, and then uses the *MPI_Sendrecv*() to send/receive corresponding packages to/from all its neighbors once at a time step.

4.2.3 Data management and visualization

Reservoir rock samples commonly contain a high percentage of solids as matrix. In simulations of heterogeneous porous media flow, a function of memory-saving scheme for run-time calculations and outputs visualization is proposed by only storing information of fluid grid. The detailed memory-saving scheme is shown in Fig. 4-4; it only records grid data involving the fluid points (marked in blue circles) and the fluid-solid boundary points (marked in yellow circles), but ignores the inside solid matrix that is not involved in fluid dynamics (marked in red circles). This data set extraction effectively reduces the memory and hard-disk consumption in both run-time computing and outputs visualization. At last, the computational output files are stored in the standard *vtk* format and can be visualized by a variety of visualization software (e.g. *Paraview*).

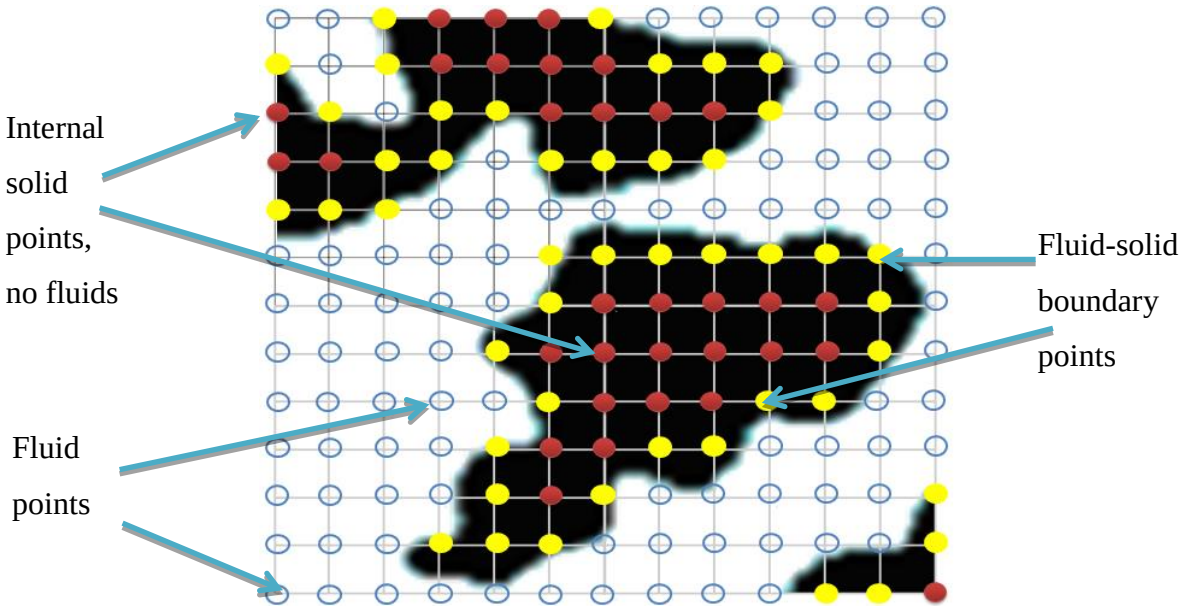

Fig. 4-4 Schematic diagram of memory-saving scheme and its usage in a reservoir rock sample slice (solid matrix in black and pores in void).

4.2.4 Supercomputing facilities

The scalable parallel *XLBM* code has been designed to maintain portability on different computing architectures, compilers, and *MPI* libraries. A portable *Makefile* is programmed to enable easy compilation across different multicore platforms. We have employed two supercomputing infrastructures for running simulations, the earth systems simulator (*Savanna*) at the University of Queensland and a Fujitsu Primergy high-performance cluster (*Raijin*) in the National Computational Infrastructure (NCI).

Savanna is first used for the program testing, debugging and calculation. It is a 64-bit *SGI ICE* 8200 *EX* Parallel Computer, with 128 Intel Xeon quad-core processors (512 cores at 2.8 *GHz* each), 2 *Terabytes* of memories, 14.4 *Terabytes* of disk on a Nexis 8000 *NAS*, and with peak speed reaching 5.7 *Terabytes* (ESSCC). Based on *Savanna*, the custom *XLBM* parallelization has been implemented with the message-passing paradigm of *MPI* library (v4.1.1.036) for running programs on the distributed-memory computing infrastructures, with the Intel *C++* compiler employed.

Raijin is a distributed-memory cluster under the EIF Climate HPC Centre Funding Agreement between the Commonwealth of Australia and the Australian National University. It has 57,472 cores (Intel Xeon Sandy Bridge technology, 2.6 *GHz*) in 3592 compute nodes, approximately 160 *Terabytes* of main memory, infiniband FDR interconnect; and approximately 10 *Petabytes* of usable fast file system for short-term scratch space. It provides a peak performance of approximately 1.2 *Petaflops* and the unit of shared memory parallelism is the node, which comprises dual 8-core Intel

Xeon (Sandy Bridge 2.6 *GHz*) processors, i.e., 16 cores. The memory specification across the nodes is heterogeneous in order to provide a configuration that is capable of accommodating the requirements of most applications, and providing also for large-memory jobs. Two-thirds of the nodes have 32 *Gigabytes*, almost one-third of the nodes have 64 *Gigabytes*, and two per cent of the nodes have 128 *Gigabytes.*, i.e., 8 *Gigabytes*/core (NCI).

4.3 Applications and Discussions

4.3.1 A reservoir rock sample and *3D* digital reconstruction

The Precipice Sandstone analysed here from the Chinchilla 4 well in the Surat Basin (Queensland, Australia) is taken as an example of a pore scale study on a massive core data set. The cuboid sample has a size of 10.14 *mm* × 9.636 *mm* × 12.276 *mm*, which was deliberately chosen from a zone that crosses from coarse grained to medium grained. The difference in grain sizes has resulted in a distinct anisotropy between the horizontal and vertical permeability. Fig. 4-5 visually shows the sample structure (Fig. 4-5 (a)) and a cross-section along the horizontal orientation (Fig. 4-5 (b)) and a cross-section illustrating a view of the highly anisotropic structure along the vertical orientation (Fig. 4-5 (c)).

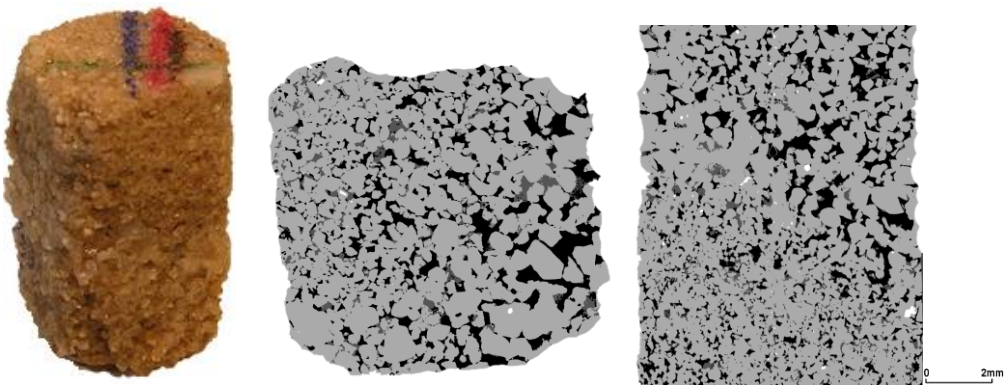

(a) (b) (c)

Fig. 4-5 (a) The Precipice Sandstone sample (10.14 *mm* × 9.636 *mm* × 12.276 *mm*); a cross-section of the sample along (b) the horizontal orientation and (c) the vertical orientation demonstrating its anisotropy (cavity – black, quartz – light gray, clay – dark gray) (Golab, 2012; Farquhar et al., 2013; Gao et al., 2014b).

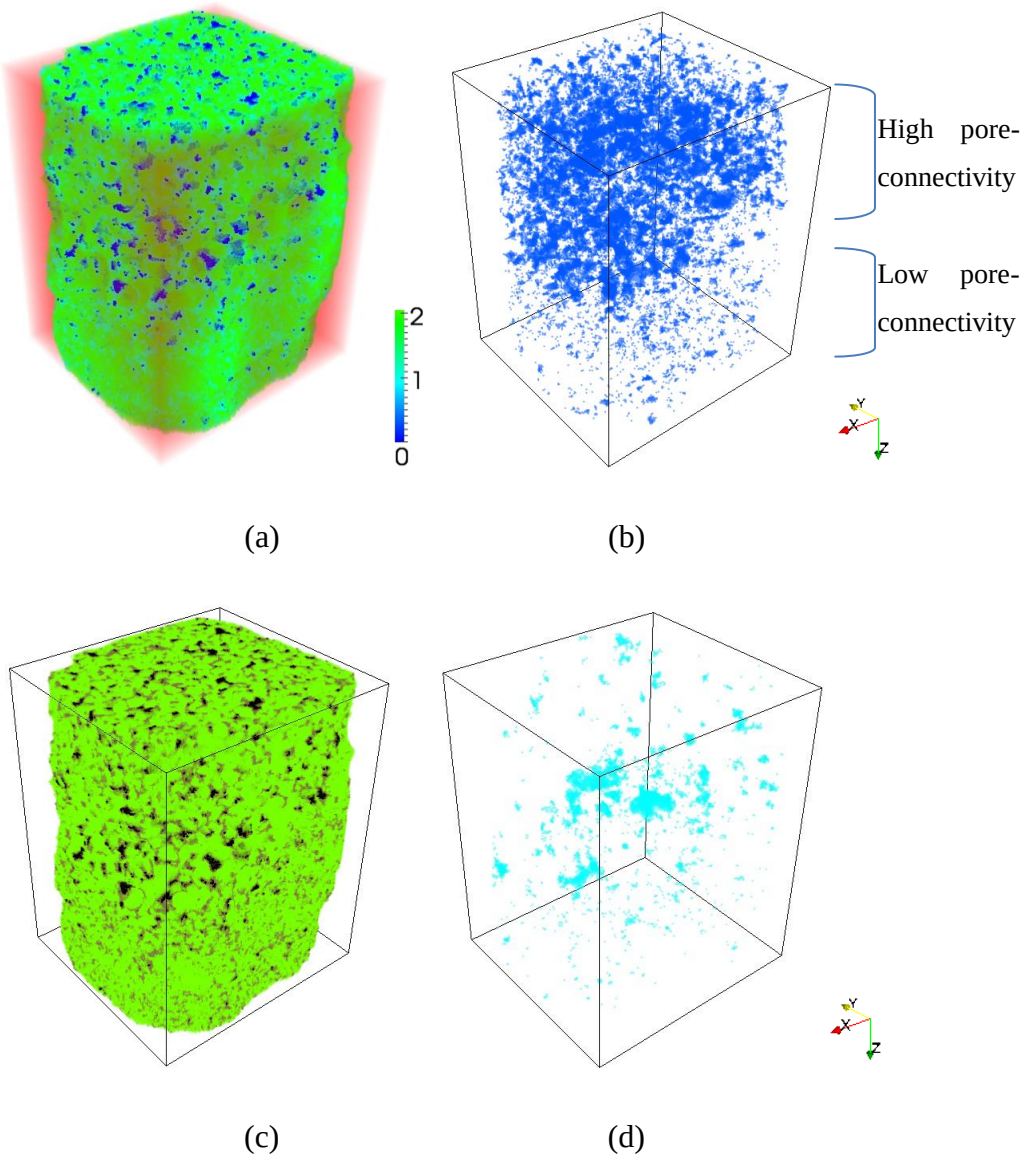

Fig. 4-6 (a) Digital sample with a lattice resolution of 1536 × 1460 × 1860 (> 4.17 billion grid elements) reconstructed from the 10.14 *mm* × 9.636 *mm* × 12.276 *mm* sandstone core (quartz – green, clays – light blue, and pores – dark blue); (b) pore structures; (c) quartz structures; and (d) clays.

As observed in *micro-CT* images, most of the rock minerals (around 77%) are quartz (the main aggregate), and a small portion (around 5%) is kaolinite (one of the clay minerals) and the clay-infilling is evident in this sample. Pore sizes and pore throats of the sandstone sample tested are around 40.5 ± 22.6 *μm* and 25.3 ± 20.7 *μm*, respectively, and 97.7% of the pore spaces are connected within the sample. The *X-ray* computed tomography *micro-CT* scans have a voxel size of 6.6 *μm*. Accurate numerical reconstruction of *3D* porous media involving multiple components with complex grain contacts is implemented using these images. The digital structure has a lattice resolution of 1536 × 1460 × 1860 based on the sample, and consists of more than 4.17 billion grid

elements. Fig. 4-6 (a) shows the *3D* digital sample structure reconstructed from the *micro-CT* images (the main aggregate quartz marked as 2, clays marked as 1 and pores as 0), and Fig. 4-6 (b)-(d) show pore, quartz and clay structures, respectively. Note that large pore throats and high pore connectivity are observed in the half top of the sample, and relatively smaller pore throats and low pore connectivity are found in the half bottom section, which confirms the observation of anisotropy along the vertical orientation.

4.3.2 Sensitivity analysis of digital cores

The sandstone sample (Fig. 4-6) has a complex tortuosity structure with two kinds of geomaterials (quartz and clay). The sensitivity of (1) *micro-CT* voxel size on the sample composition (e.g. relative composition ratio η_α), and (2) properties of geomaterial components on fluid dynamics have been numerically investigated in the following sections.

1) Effect of voxel size on evaluation of sample composition

For simplification, the composition ratio of different geomaterial components is described as:

$$\eta_\alpha = \frac{\Psi_\alpha}{\sum_{\alpha=0}^{N} \Psi_\alpha} \qquad \text{Eq. 4-1}$$

Here, α means the αth component (e.g. pores, clay or quartz) in the porous medium; ψ_α is the total volume of the αth component in the porous medium; $\sum\psi_\alpha$ is the total volume of all N+1 kinds of components in the porous medium including pore apertures.

The cuboid sandstone generates a digital sample with a lattice resolution of 1536 (L_x) × 1460 (L_y) × 1860 (L_z) at the 6.6 μm voxel size. Considering the sample anisotropy, we compare the voxel size effects on the physical structure fidelity (e.g. each composition volume ratio) by coarsening the voxel size from 6.6 μm to 13.2 μm and 33 μm (Fig. 4-7). The corresponding sample lattice resolution then becomes 500 × 500 × 930 at the 13.2 μm voxel size and 200 × 200 × 372 at the 33 μm voxel size.

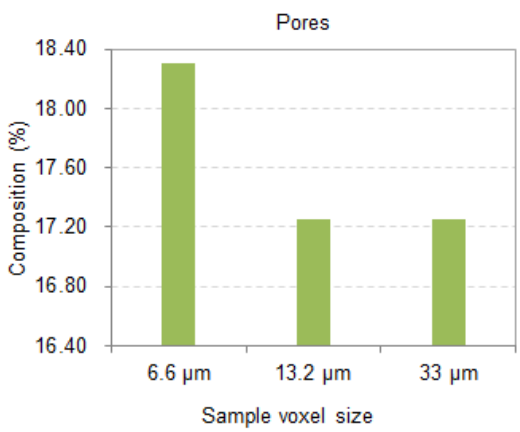

(a)

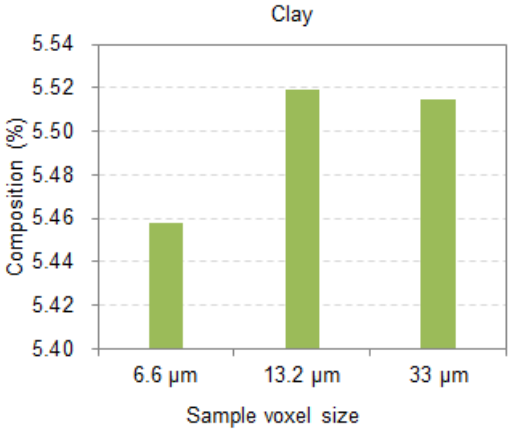

(b)

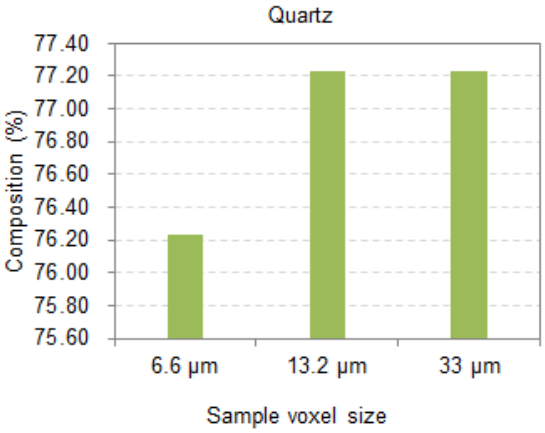

(c)

Fig. 4-7 Composition analysis of the core sample (10.14 *mm* × 9.636 *mm* × 12.276 *mm*) with different voxel sizes (6.6 *μm*, 13.2 *μm* and 33 *μm*): volume ratio of pores (a), clays (b) and quartz grains (c).

Fig. 4-7 shows the variation of each composition volume ratio under different voxel size conditions. In all 6.6 *μm*, 13.2 *μm* and 33 *μm* cases, quartz takes up more than 75% of the whole sample volume (Fig. 4-7 (c)), pore volumes are less than 20% (Fig. 4-7 (a)) and clays are around 5% (Fig. 4-7 (b)). Clear differences of each composition ratio are observed as the voxel size is coarsened from 6.6 *μm* to 13.2 *μm*. For instance, the pore volume ratio shrinks from more than 18.2% to around 17.2%, which occurs because of the loss of small pores, whereas both clay and quartz show a volume ratio increase. The results have shown that around 1.0 % of pores (larger than 6.6 *μm* but smaller than 13.2 *μm*) exist between sections of clays or quartz grains. When comparing the 13.2 *μm* and 33 *μm* voxel size cases, there is no clear difference for each composition ratio due to the highly coarsened process, which also shows most of the pores (99%) have a size larger than 33 *μm*.

Similarly to these investigations of the sensitivity of pore space geometry at the coarser-scaled simulations, *X-ray micro-CT* scans with large voxel size (lattice resolution, larger than 6.6 μm) could also result in loss of the detailed internal structure information (especially some narrow pore throats) of the porous media.

2) Effect of voxel size on pore scale fluid dynamics

Grid independence is a basic consideration for the LBM simulations. Since the sample tortuosity is quite complex, it is not feasible to define the accurate ratio of lattice nodes versus pore apertures for grid independence. In order to analyse the sensitivity of voxel size on fluid dynamics, three cases are compared, namely 6.6 μm, 13.2 μm and 33 μm. Both quartz and clay are set as impermeable and the fluid is driven under a pressure gradient of 0.1 (unitless) along the positive *z*-axis (vertical orientation). All the side walls are set as free-slip boundaries (Eq. 4-2). For *XLBM* calculation parameters, the relaxation time τ is defined as 1.25 and the Reynolds number (*Re*) is defined as 0.1 in this case for computing stability.

$$
\begin{aligned}
&\mathbf{u}_i(x,y,z)=0, \mathbf{u}_j(x,y,z)=0 \quad (x=0, L_x)\\
&\mathbf{u}_i(x,y,z)=0, \mathbf{u}_j(x,y,z)=0 \quad (y=0, L_y)\\
&\mathbf{u}_k(x,y,z)=\mathbf{u}_k(x+1,y,z)=0 \quad (x=0)\\
&\mathbf{u}_k(x,y,z)=\mathbf{u}_k(x-1,y,z) \quad (x=L_y)\\
&\mathbf{u}_k(x,y,z)=\mathbf{u}_k(x,y+1,z)=0 \quad (y=0)\\
&\mathbf{u}_k(x,y,z)=\mathbf{u}_k(x,y-1,z) \quad (y=L_y)
\end{aligned}
\qquad \text{Eq. 4-2}
$$

Here, *i, j, k* stand for the three orthogonal dimensions along the *x*-, *y*- and *z*-axis.

Fig. 4-8 shows the whole isometric view of the fluid dynamics (velocity magnitude) with different voxel size conditions. As observed in all three cases, more fluid distributes through the half top of the sample due to the larger pore throats and high pore connectivity in this area. In the 6.6 μm case, more fluid flow has been found inside the sample as the porosity is relatively higher compared with other two cases. For clarity, the fluid flux fields are shown for a small part representing only 1.2 *mm* × 1.2 *mm* × 0.24 *mm* of the block. Fig. 4-9 (a), Fig. 4-10 (a) and Fig. 4-11 (a) have shown the selected geometric structure and topology for three cases, where the difference of mineral composition can hardly be visually observed. However, the fluid flux field for each case is observed differently in Fig. 4-9 (b), Fig. 4-10 (b) and Fig. 4-11 (b), respectively: the fluid flow is enhanced in

Fig. 4-10 (b) due to the greater porosity and higher pore connectivity, hence contributing to larger fluid flow distribution through the core sample.

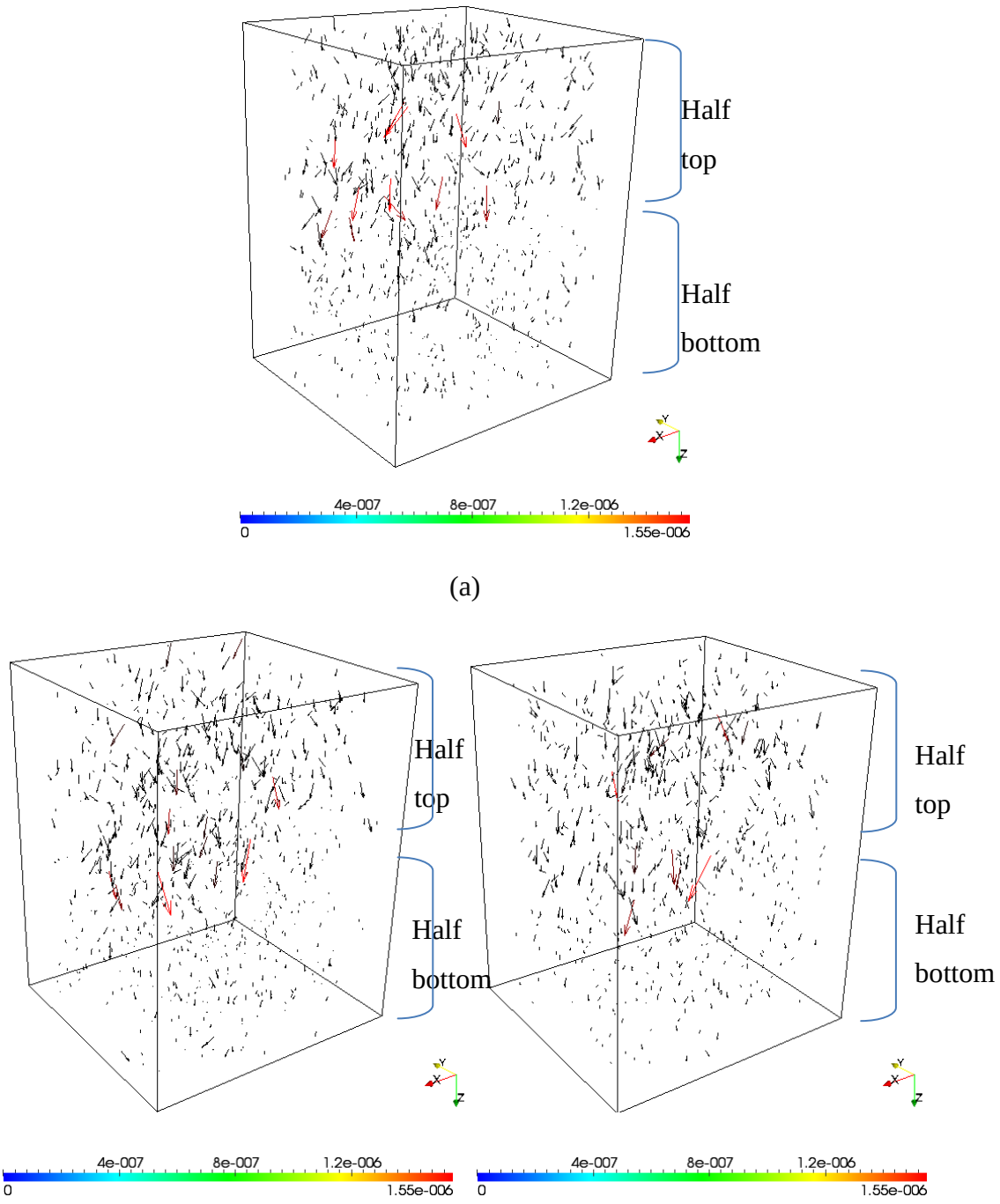

Fig. 4-8 The isometric view of the fluid dynamics inside the porous medium regarding different voxel size cases: (a) 6.6 μm, (b) 13.2 μm and (c) 33 μm.

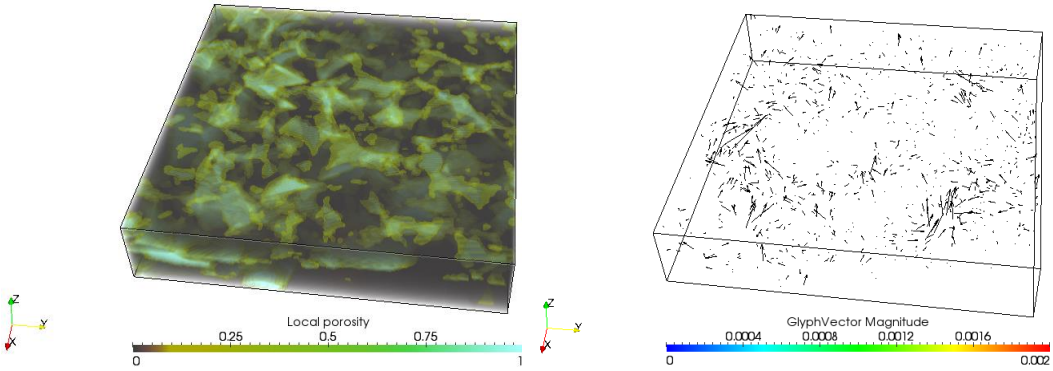

(a) (b)

Fig. 4-9 (a) Digital sub block of the sample at voxel size of 6.6 μm (cavity - light blue, clay - light yellow and quartz – black), and (b) flow flux field distribution.

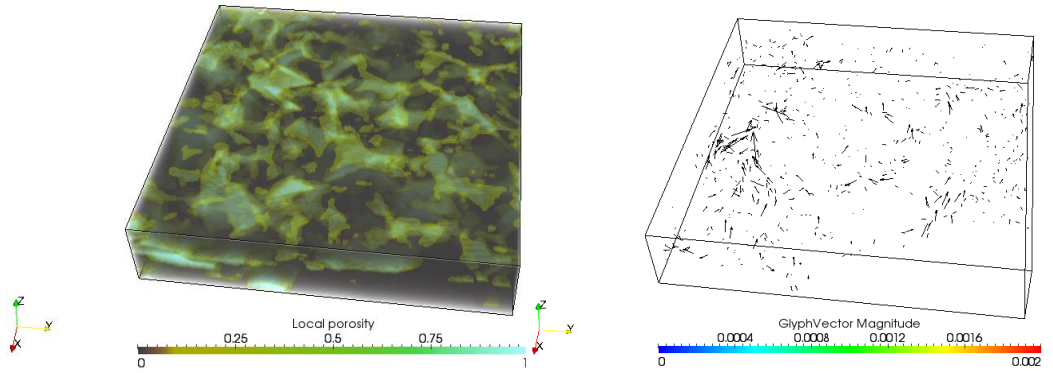

(a) (b)

Fig. 4-10 (a) Digital sub block of the sample at voxel size of 13.2 μm (cavity - light blue, clay - light yellow and quartz – black), and (b) flow flux field distribution.

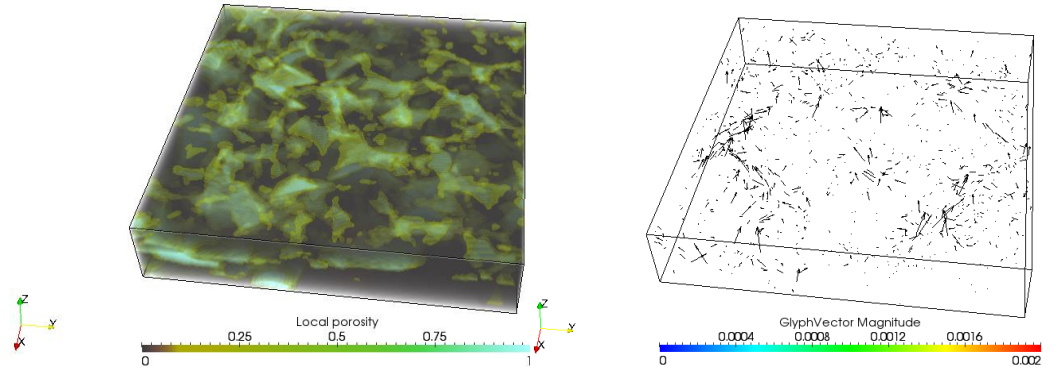

(a) (b)

Fig. 4-11 (a) Digital sub block of the sample at voxel size of 33 μm (cavity - light blue, clay - light yellow and quartz – black), and (b) flow flux field distribution.

4.4 Parallel Computing Performance Evaluation

This section illustrates the computing performance of the parallel *XLBM* in providing effective simulations of massive initial architectural data sets cases. According to the definition of parallel computing performance (Section 2.6.1), the improved speedup with the parallel *XLBM* (marked in red, Fig. 4-12 (a)) is close to the ideal linear speedup (dashed line, the proportional constant *k* is 1) that is achieved by reducing the data communication and memory consumption. Compared with the original speedup (blue line), it shows highly nearly-linear speedup and scalability for even larger initial massive data sets cases. Fig. 4-12 (b) shows the computing efficiency reaching around 93.8% even using 512 processors; this confirms the effective computing performance of the custom parallel *XLBM*. Moreover, the parallel code is available for transplantation on even larger supercomputing infrastructures in future studies.

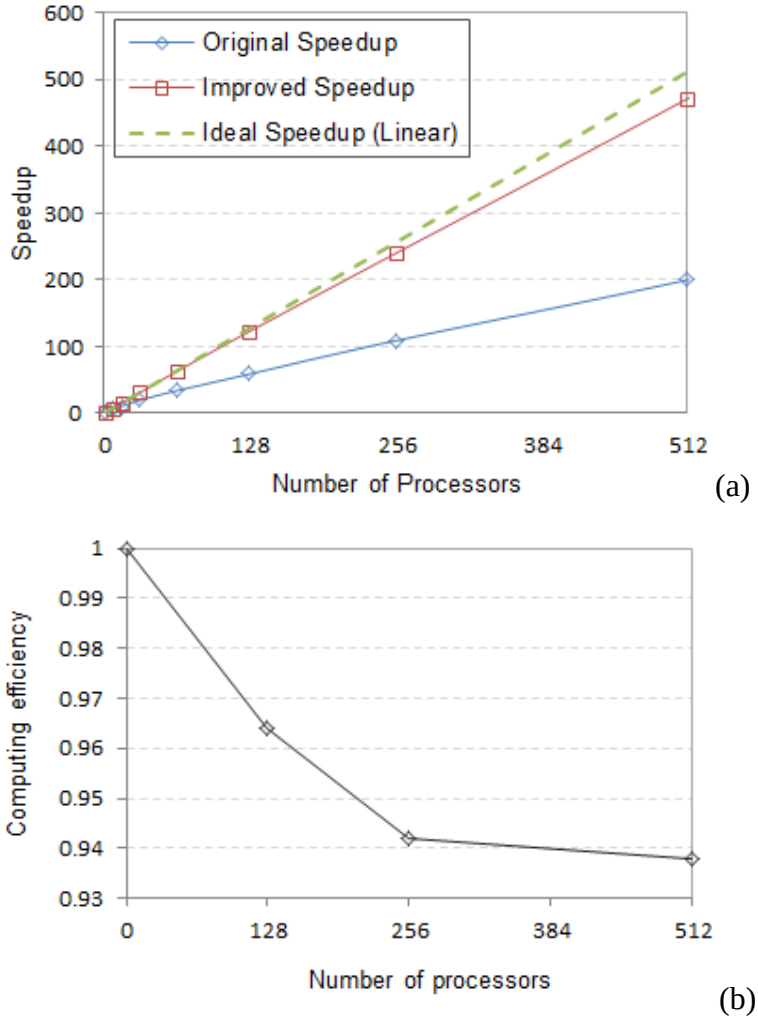

Fig. 4-12 (a) Scale-up testing of parallel efficiency (speedup) on the supercomputer *Raijin*. The dashed line represents the theoretical linear performance (the proportional constant *k* is 1), the red solid line is the improved speedup by the parallel *XLBM* and the blue solid line is the previous computing speedup; (b) Computing efficiency regarding different numbers of processors used.

4.5 Conclusions

This chapter develops a computationally demanding parallel *LBM* platform for: (1) processing massive initial architectural data sets generated from high resolution *micro-CT*/*QEMSCAN* images based on reservoir rock samples; and (2) conducting high-performance dynamical simulations for the coupled **System (T, H, C)** on supercomputing infrastructures, which is impossible for conventional personal computers or small working stations. The platform provides high-efficiency end-to-end service, including: (1) the Input Preparation module, for automatically re-decomposing and processing huge initial architectural data set files into required sub-block sizes; (2) the Run-time Control module and an effective parallel *LBM* code, for simulating complex fluid dynamics in *3D* heterogeneous porous media at the pore scale; and (3) the Data Management module, for memory saving as well as data extraction for run-time computation and outputs visualization. The custom parallel *LBM* platform has been implemented and installed on the supercomputing infrastructures, *Savanna* and *Raijin*.

A pore scale study of a heterogeneous sandstone sample (cuboid of 10.14 $mm \times 9.636\ mm \times 12.276\ mm$) from the Chinchilla 4 borehole in the Surat Basin has been conducted. The digital sample has a lattice size of 1536 × 1460 × 1860 with 4.17 billion grid elements after *3D* reconstruction. Regarding the Chinchilla sample, we established that (1) the composition ratio is relatively sensitive to voxel resolution: higher resolution imaging is required to retain narrow pore throats and excessively coarsened voxel resolutions result in severe loss of internal microstructures information (particularly some narrow pore throats); (2) voxel size effect on pore scale fluid dynamics: fluid flow dynamics are sensitive to the composition ratios and individual geomaterial property, and this requires higher resolution imaging to identify detailed microstructures and retain narrow pore throats inside the dense geomaterials; (3) it is not feasible to define the accurate ratio of lattice nodes versus pore apertures for meeting the grid independence due to the complex sample tortuosity.

Providing massive data sets processing and computing, the custom parallel *LBM* has shown nearly-linear improved speedup and scalability (close to the ideal linear speedup line) that is achieved by reducing the data communication and memory consumption. The computing efficiency reaches around 93.8% even in 512 processors cases; this demonstrates the effective computing performance of the custom parallel *LBM* for ever larger data sets problems and also high scalability for implementation of further coupled **System (T, H, C)**.

Chapter 5 Parallel *XLBM* Modelling of Pore Scale Thermal Effect in Heterogeneous Geomaterials

5.1 Introduction

Heat transfer (**T**) is common in subsurface systems, and has become an increasingly important topic in areas such as hydrodynamics and geothermal energy (Bickle, 1978; Hitchon, 1984; Palmer et al., 1992; Birkholzer and Tsang, 2000; Zalba et al., 2003; Bedrikovetski et al., 2004; Zhao et al., 2009; Shaik et al., 2011), reservoir engineering (Park et al., 1991; Uysal et al., 2000; Sáez and Toledo, 2009; Zhao et al., 2009; Gorman and Senger, 2010; Koh et al., 2011; Yin et al., 2011) and geochemistry (Kissinger, 1957; Hahn and Shiu, 1986; Gupta et al., 1990; Cansell et al., 1993; Hobbs et al., 2000; Li et al., 2008; Uysal et al., 2011; Yin et al., 2011). As introduced in Chapters 1 and 2, heat transfer at the pore scale significantly affects fluid transport (**H**) and chemical reactivity (**C**) in the whole coupled **System (T, H, C)**, which requires more relevant studies.

A significant body of research has investigated heat transfer, and the interactions between heat transfer (thermal convection and conduction) and fluid transport in porous media due to the temperature gradient and difference (Lapwood, 1948; Hart, 1981; Hart and St John, 1986; Eckert and Drake Jr, 1987; Burmeister, 1993; Ingham and Pop, 2005; Nield and Bejan, 2006; Vafai, 2010; Incropera, 2011; Shaik et al., 2011; Roshan and Rahman, 2013). In particular, some research has focused on the heat transfer in nano-fluids (Keblinski et al., 2002; Daungthongsuk and Wongwises, 2007; Wang and Mujumdar, 2007) and unsteady pore scale flow (Magnico, 2009; Kopanidis et al., 2010). Fluid transport largely depends on the pore tortuosity, geometric heterogeneity and mineral characters (introduced in Chapter 3), whereas the heat may transfer through any structures including pores, fractures and geomaterials. This leads to heat conduction and convection in three types of porous media (Fig. 5-1) and may influence the fluid transport. Besides, the heat transfer may also affect chemical reaction rate, hence the dissolution of acid inclusions under different temperature conditions may be changed (to be discussed in Chapter 6). It is still essential to study the physics of the thermal effect and interactions with other coupled processes at the pore scale.

This chapter focuses on the pore scale geothermal process (both conduction and convection) and its interactions and coupling with fluid transport, which is through pores and solids (or minerals) in heterogeneous porous media with multiple geomaterials. A geothermal model is extended and updated through the double-distribution function models (*DDF*) for modelling of the pore scale geothermal phenomena, and discussing the resultant impact on the whole porous media system (Section 5.2). The geothermal model has been implemented into the custom parallel *XLBM* and provides a compatible coding interface to achieve the coupling of the fluid flow (**H**) model (Chapter

3) and the geochemical reactions (**C**) model (Chapter 6) at the pore scale. The model is first validated by a benchmarked test (natural convection in a square cavity) in Section 5.3.1, and then studies two pore scale application examples (Section 5.3.2 and 5.3.3).

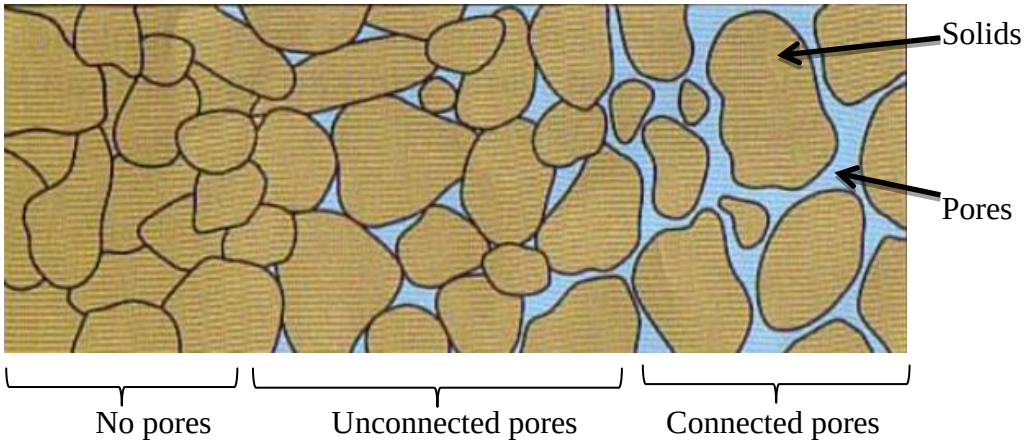

Fig. 5-1 Heat transfer occurs in different porous media geometries (Meinzer, 1923).

5.2 *XLBM* Modelling of Heat Transfer in Heterogeneous Geomaterials at the Pore Scale

As introduced in Chapter 3, the generalized Navier–Stokes equations for isothermal incompressible fluid flows in porous media with multiple geomaterials are:

$$\nabla \cdot \mathbf{u} = 0 \qquad \text{Eq. 5-1}$$

$$\frac{\partial \mathbf{u}}{\partial t} + (\mathbf{u} \cdot \nabla)\left(\frac{\mathbf{u}}{\phi_\alpha}\right) = -\frac{1}{\rho}\nabla(\phi_\alpha p) + \nu_e \nabla^2 \mathbf{u} + \mathbf{F} \qquad \text{Eq. 5-2}$$

It is well known that in the assumption that the viscous heat dissipation and compression induced by the pressure are negligible, the generalized macroscopic governing equation for the heat transfer in incompressible fluids and solids is described by a simpler passive-scalar equation (Nithiarasu et al., 1997):

$$(\rho c_p)\frac{\partial T}{\partial t} + \mathbf{u} \cdot \nabla T = \nabla \cdot (\alpha_m \nabla T) + \dot{Q} \qquad \text{Eq. 5-3}$$

T is the macroscale temperature; $\dot{Q}$ stands for the heat source from fluids or solids (the heat generation per unit volume); and $\mathbf{u}$ is the fluid flow velocity. Here, the heat capacity c_p and the

effective thermal diffusivity α_m depend on the intrinsic geometry of the porous media. These parameters are generally described as (Whitaker, 1977; Vafai and Tien, 1981):

$$\rho c_p = (1-\phi)\rho_s c_{ps} + \phi\rho_f c_{pf} \quad \text{Eq. 5-4}$$

$$\alpha_m = (1-\phi)\alpha_{ms} + \phi\alpha_{mf} \quad \text{Eq. 5-5}$$

ρ_f is the fluids density, and ρ_s is the solids density; c_{pf} is the specific heat capacity of the fluids, and c_{ps} stands for the specific heat capacity of solids; α_{mf} is the specific thermal diffusivity through fluids, and α_{ms} is the specific thermal diffusivity through solids.

In addition, there are also two dimensionless terms that describe the relationship between the fluid transport (momentum transport) and the heat transport - Prandtl number (*Pr*) and Rayleigh number (*Ra*):

$$\mathrm{Pr} = \frac{\nu}{\alpha_m} \quad \text{Eq. 5-6}$$

$$Ra = \frac{\mathbf{g}\beta\Delta T L^3}{\nu\alpha_m} \quad \text{Eq. 5-7}$$

Here, the Prandtl number represents the ratio between momentum transport and heat transport; and the Rayleigh number is associated with buoyancy driven flow, which is also known as free convection or natural convection. When the Rayleigh number is smaller than the critical value for a certain fluid, the heat transfer is mainly through conduction; when it is larger than the critical value, the heat transfer is mainly through convection.

*LBM*s have been classified into two categories for the fluid flow with heat transfer in a plain medium: multispeed models (*MS*) and double-distribution function models (*DDF*). The multispeed models extend the basic isothermal *LBM* model by introducing an even larger set of discrete velocities. In addition, even higher order terms for velocities are employed into the equilibrium distribution functions. The double-distribution function models solve the convection-diffusion equation together with the velocity field, and couple those two processes together as a whole by using coupling terms. Similar models for studying plain medium flow and the associated heat transfer have been proposed by many researchers (Guo and Zhao, 2005; Wang et al., 2007c; Shokouhmand et al., 2009).

In the *XLBM*, each lattice node has its own hydraulic property due to the description of material localization. Here, the *DDF LBM* is employed and extended into the proposed *XLBM* model where the temperature distribution function is described as:

$$T_i\left(\mathbf{x}+\mathbf{e_i}\Delta t, t+\Delta t\right)-T_i\left(\mathbf{x},t\right)=-\frac{1}{\tau_T}\left[T_i\left(\mathbf{x},t\right)-T_i^{eq}\left(\mathbf{x},t\right)\right]+\omega_{Ti}\left(1-\frac{1}{2\tau_T}\right)\frac{\dot{Q}}{\rho c_p} \qquad \text{Eq. 5-8}$$

It reveals the evolution of heat transfer over the lattice grid in porous media. Here, T_i is the temperature distribution function, and τ_T is the dimensionless relaxation time. In the *XLBM*, τ_T depends on the material character (e.g. heat capacity c_p) at each lattice node due to the presence of multiple solids (or minerals):

$$\tau_T=\frac{\alpha_m}{\rho c_p c_s^2 \Delta t}+0.5 \qquad \text{Eq. 5-9}$$

Here, the heat capacity c_p and the effective thermal diffusivity α_m are specified as:

$$\rho c_p=\left(1-\phi_\alpha\right)\rho_s c_{ps}+\phi_\alpha \rho_f c_{pf} \qquad \text{Eq. 5-10}$$

$$\alpha_m=\left(1-\phi_\alpha\right)\alpha_{ms}+\phi_\alpha \alpha_{mf} \qquad \text{Eq. 5-11}$$

This equation is capable of determining the evolution of heat transfer through multiple geomaterials involving pore structures, and materials with respective intrinsic permeability. As an extreme condition, particularly for pores (ϕ_α = 1.0), the former terms on the right side of Eq. 5-10 and Eq. 5-11 reduce to zero, whereas for the impermeable aggregate (ϕ_α = 0.0), the latter terms on the right side of Eq. 5-10 and Eq. 5-11 reduce to zero.

The equilibrium temperature distribution function T_i^{eq} is:

D2Q9 cases:

$$T_i^{eq}=\begin{cases} -\dfrac{2\mathbf{u}^2}{3c_s^{\,2}}T & \left(i=0\right) \\ \dfrac{1}{9}T\left[\dfrac{3}{2}+\dfrac{3\mathbf{e_i}\cdot\mathbf{u}}{2c_s^{\,2}}+\dfrac{9\mathbf{e_i}\cdot\mathbf{u}}{2c_s^{\,2}}-\dfrac{3\mathbf{u}^2}{2c_s^{\,2}}\right] & \left(i=1,2,3,4\right) \\ \dfrac{1}{36}T\left[3+\dfrac{6\mathbf{e_i}\cdot\mathbf{u}}{c_s^{\,2}}+\dfrac{9\mathbf{e_i}\cdot\mathbf{u}}{2c_s^{\,2}}-\dfrac{3\mathbf{u}^2}{2c_s^{\,2}}\right] & \left(i=5,6,7,8\right) \end{cases} \qquad \text{Eq. 5-12}$$

D3Q19 cases:

$$T_i^{eq} = \begin{cases} -\dfrac{\mathbf{u}^2}{2c_s^{\,2}}T & (i=0) \\ \dfrac{1}{18}T\left[1+\dfrac{\mathbf{e_i}\cdot\mathbf{u}}{c_s^{\,2}}+\dfrac{9\mathbf{e_i}\cdot\mathbf{u}}{2c_s^{\,4}}-\dfrac{3\mathbf{u}^2}{2c_s^{\,2}}\right] & (i=1,2,...,6) \\ \dfrac{1}{36}T\left[2+\dfrac{4\mathbf{e_i}\cdot\mathbf{u}}{c_s^{\,2}}+\dfrac{9\mathbf{e_i}\cdot\mathbf{u}}{2c_s^{\,4}}-\dfrac{3\mathbf{u}^2}{2c_s^{\,2}}\right] & (i=7,8...,18) \end{cases} \quad \text{Eq. 5-13}$$

These equations (Eq. 5-12 and Eq. 5-13) imply the effect of fluid transport on the temperature distribution field. The macroscopic temperature in the *XLBM* is calculated by:

$$T = \sum_i T_i + \frac{\dot{Q}}{2\rho c_p}\Delta t \quad \text{Eq. 5-14}$$

Compared with Eq. 3-3, the force term **F** in Eq. 5-2 needs to reconsider the thermal effect on the fluid transport:

$$\mathbf{F} = -\frac{\phi_\alpha \nu}{K_\alpha}\mathbf{u} - \frac{\phi_\alpha F_{\varepsilon\alpha}}{\sqrt{K_\alpha}}|\mathbf{u}|\mathbf{u} + \phi_\alpha \mathbf{G} \quad \text{Eq. 5-15}$$

Here, the external force **G** can be further described as:

$$\mathbf{G} = -\mathbf{g}\beta(T - T_0) + \mathbf{a} \quad \text{Eq. 5-16}$$

g is the gravitational acceleration, and β is the thermal expansion coefficient. T_0 is the reference (or initial) temperature; and **a** stands for the external force term. Eq. 5-12 and Eq. 5-13 represent the influence of the heat transfer on the fluid transport.

In the geothermal *XLBM* model, the capacity of heat transfer among different geomaterials correlates to its intrinsic geometry. Specially, for fluids in fractures or pores (ϕ_α = 1), the above energy equation (Eq. 5-3) is:

$$(\rho_f c_{pf})\frac{\partial T}{\partial t} + \mathbf{u}\cdot\nabla T = \nabla\cdot(\alpha_{mf}\nabla T) + \dot{Q}_f \quad \text{Eq. 5-17}$$

For solids only (or mineral sections) with ϕ_α = 0, the above energy equation (Eq. 5-3) is derived as:

$$(\rho_s c_{ps})\frac{\partial T}{\partial t} = \nabla\cdot(\alpha_{ms}\nabla T) + \dot{Q}_s \quad \text{Eq. 5-18}$$

Where, $\dot{Q}_f$ and $\dot{Q}_s$ are heat source from fluids and solids, respectively.

5.3 Benchmark

To validate the geothermal *XLBM* model, natural convection in a square cavity is carried out in this section as a benchmarked test. Here, the *XLBM* is specified as a case of an average porosity of ϕ_α = 1.0 for the verification by available analytical results. The natural convection flow in a square cavity has been studied in some research work (de Vahl Davis, 1983; Hortmann et al., 1990). The benchmark solution here is set as a lattice grid size of 350 × 350. The Reynolds number (*Re*) is 10^{-1}, the Darcy number (*Da*) is 10^{-4}, and the Prandtl number (*Pr*) is set as 0.75. The Rayleigh numbers (*Ra*) are set as 10^3, 10^4, 10^5 and 10^6 for four cases, where the relaxation time τ is set as 2.0, 1.25, 0.8 and 0.55, respectively. The τ_T is defined as $\tau_T = (2\times\tau\text{-}1)/(2\times Pr)+0.5$. All the boundary walls are set as zero velocity. Moreover, the left wall is at a higher temperature T_2 = 1.0, and the right wall is set as a lower temperature T_1 = 0.0. The initial field is set as a reference temperature $T_0 = (T_2 + T_1)/2$.

A cross-section along the middle of *y*-axis is selected for comparison of the *XLBM* simulation results with the analytical solutions in Fig. 5-2 (velocity) and Fig. 5-3 (temperature), where the analytical solutions are marked with solid lines, and the simulation results are shown in symbols. It is observed in Fig. 5-2 that (a) the peak of the vertical velocity becomes larger when the *Ra* value increases. Besides, the fluid close to the left and right walls moves faster along the vertical direction, whereas the vertical velocity of the fluid around the centre of the square gets smaller when the *Ra* value increases. In Fig. 5-3, the temperature distribution close to the left and right walls becomes denser as the *Ra* increases, hence driving the fluid transport (Fig. 5-2) and forming vortices (Fig. 5-4). All the simulation results fit the analytical solutions well, which demonstrated the correctness of the developed model and code.

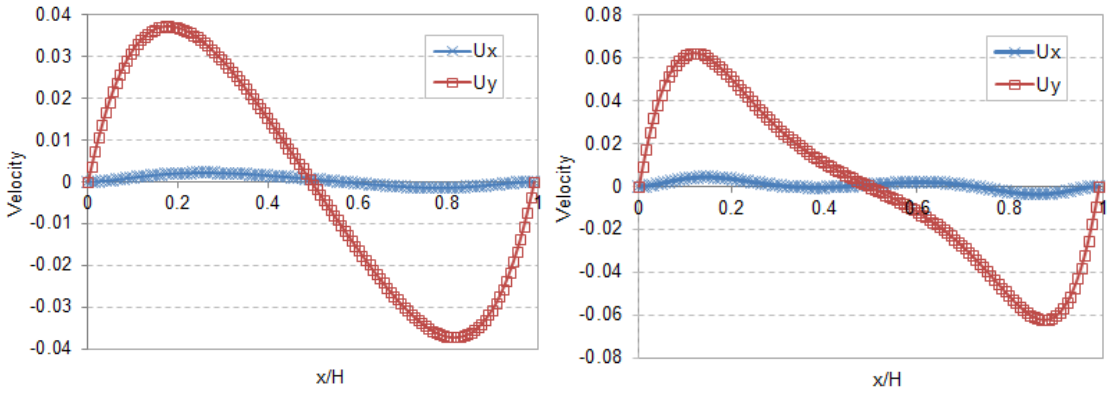

(a) (b)

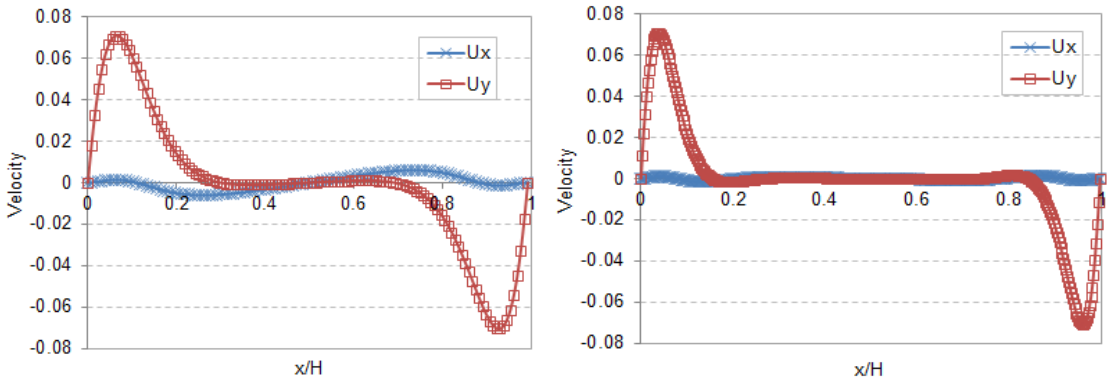

(c) (d)

Fig. 5-2 Comparison results of velocity distribution along the middle of *y*-axis at different *Ra* conditions between *XLBM* simulation (shown in symbols) and the analytical solution (shown in solid lines) (de Vahl Davis, 1983; Hortmann et al., 1990): (a) $Ra = 10^3$, (b) $Ra = 10^4$, (c) $Ra = 10^5$ and (d) $Ra = 10^6$.

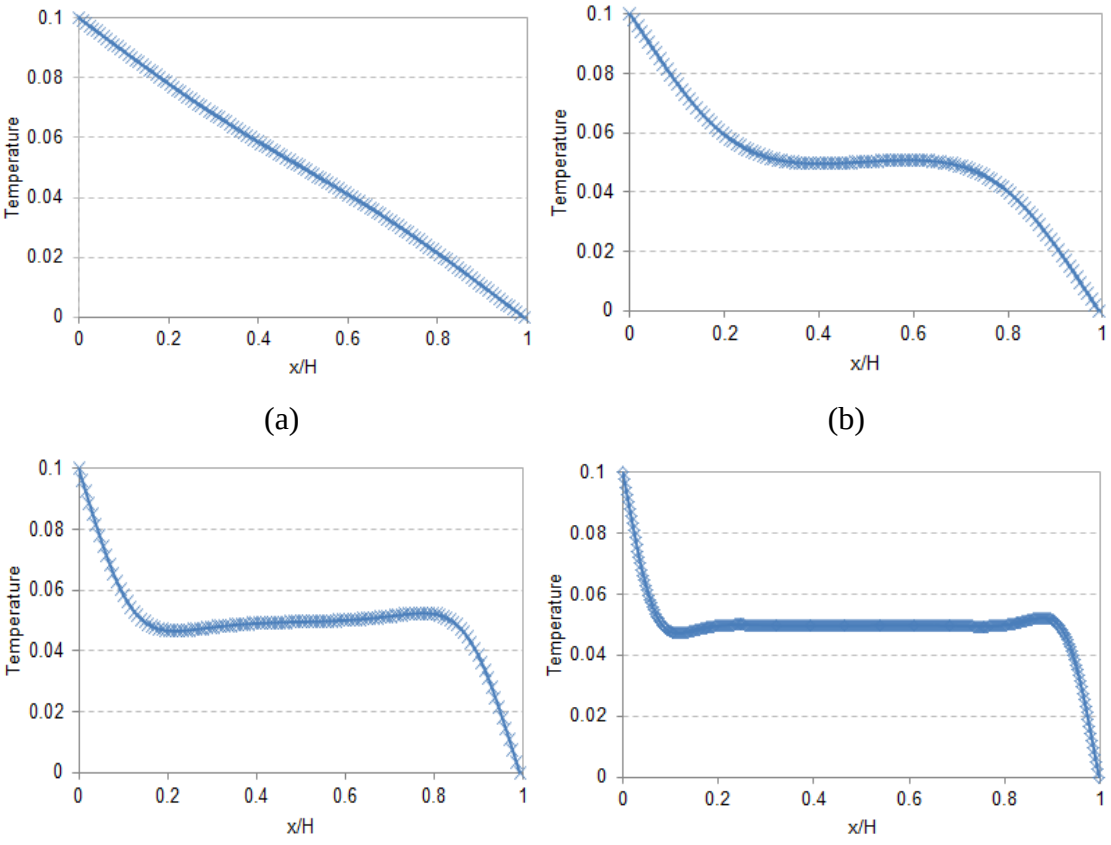

(a) (b)

(c) (d)

Fig. 5-3 Comparison results of temperature distribution along the middle of *y*-axis at different *Ra* conditions between *XLBM* simulation (shown in symbols) and the analytical solution (shown in solid lines) (de Vahl Davis, 1983; Hortmann et al., 1990; Barakos et al., 1994): (a) $Ra = 10^3$, (b) $Ra = 10^4$, (c) $Ra = 10^5$ and (d) $Ra = 10^6$.

The distributions of fluid movement at different *Ra* conditions are illustrated in Fig. 5-4. From Fig. 5-4 (a) to (d), the central vortex tends to become elliptic as *Ra* number increases from 10^3 to 10^4; the ellipse then breaks into two vortices in Fig. 5-4 (c) when the *Ra* number reaches 10^5, and the vortices moved towards the side walls and a third vortex appears in the centre of the square cavity when the *Ra* number is 10^6.

The distributions of isotherms at different *Ra* conditions are also illustrated in Fig. 5-5. From Fig. 5-5 (a) to (d), the heat transfer changes from conduction to convection between the left hot wall and right cold wall, and the isotherms are from almost vertical to horizontal in the centre of the square cavity.

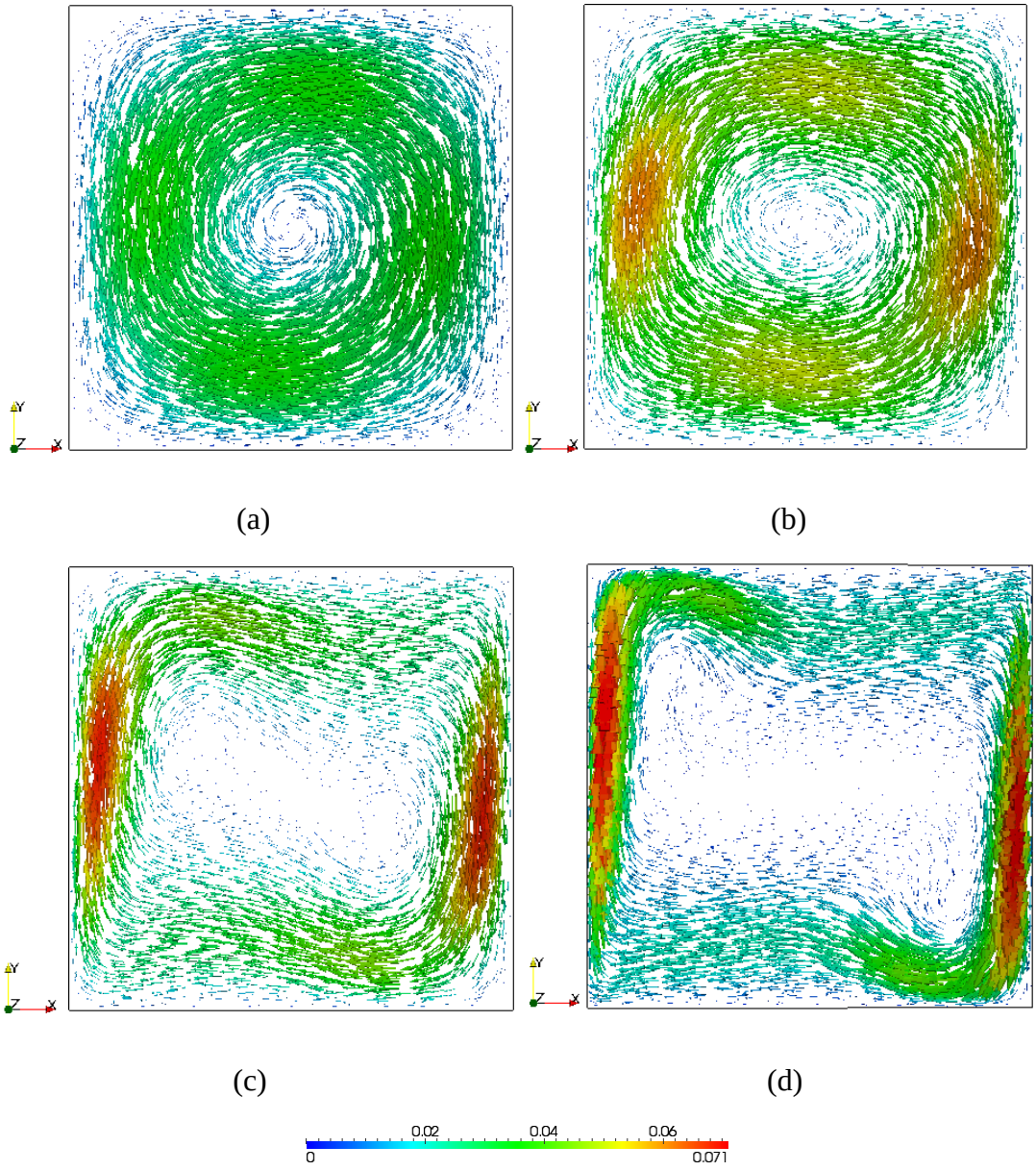

Fig. 5-4 Distributions of streamlines at different *Ra* conditions: (a) *Ra* = 10^3, (b) *Ra* = 10^4, (c) *Ra* = 10^5, and (d) *Ra* = 10^6.

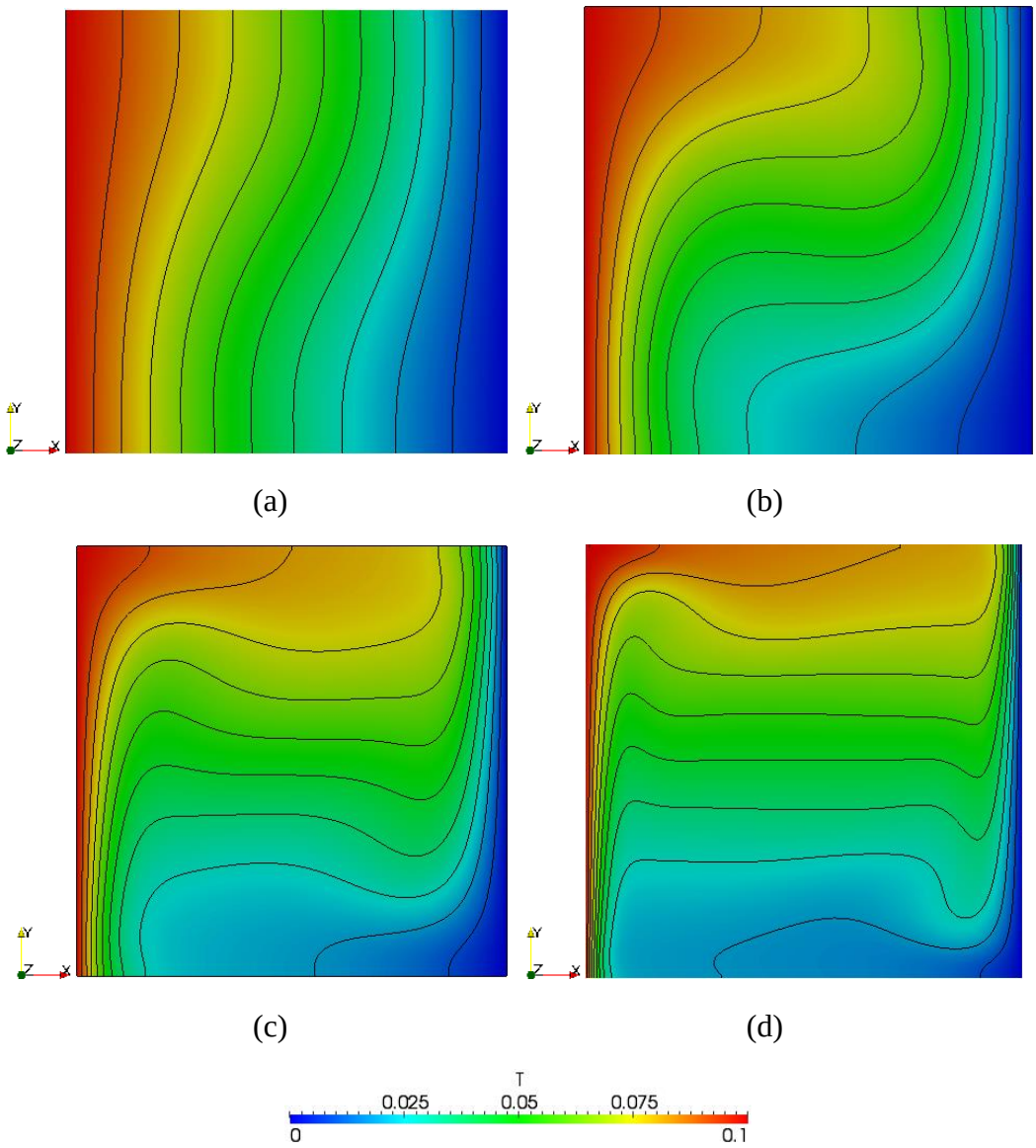

Fig. 5-5 Simulation results of isotherm at different *Ra* conditions: (a) $Ra = 10^3$, (b) $Ra = 10^4$, (c) $Ra = 10^5$ and (d) $Ra = 10^6$.

5.4 Simulation Results and Discussion

Two applications are set up for studies in: (1) the effect of intrinsic pore scale geometry and geomaterials on the heat distribution; and (2) heat transfer and fluid transport interactions with each other at the pore scale.

5.4.1 Intrinsic geometry/geomaterials and the heat distribution

In this case, a unitless square (lattice grid size of 700 × 700) is studied for the thermal conduction and convection through a cavity with a solid (at a pixel radius of 200) in the centre (Fig. 5-6). The setting of parameters is dimensionless and similar to those used in Section 5.3.1: *Re* is 10^{-1}, *Da* is 10^{-4}, and *Pr* is 0.71; both the top and bottom walls are set as zero velocity; the left wall is at a higher

temperature T_2 = 1.0, and the right wall is at a lower temperature T_1 = 0.0. The initial field is set as an average temperature $T_0 = (T_2 + T_1)/2$. To study the geometrical and geomaterial effect on heat transfer, we compared the distributions of velocities and isotherms in different solid permeability and heat capacity conditions: an impermeable solid and a permeable solid.

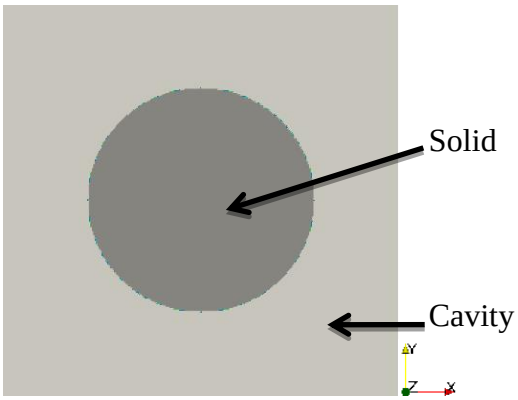

Fig. 5-6 A solid (radius as 200) inside a cavity (lattice size as 700×700).

In the impermeable solid case, the distributions of velocity field are shown in Fig. 5-7 (two *Ra* conditions) when the whole field reaches its velocity equilibrium status. In Fig. 5-7 (a), the shape of streamlines is nearly round around the impermeable solid: as the *Ra* value increases to 10^5, the streamlines move clockwise and slant towards the top right corner as well as the down left corner (Fig. 5-7 (b)). This occurs because of the effect of temperature difference and the presence of the impermeable solid on the fluid flow field.

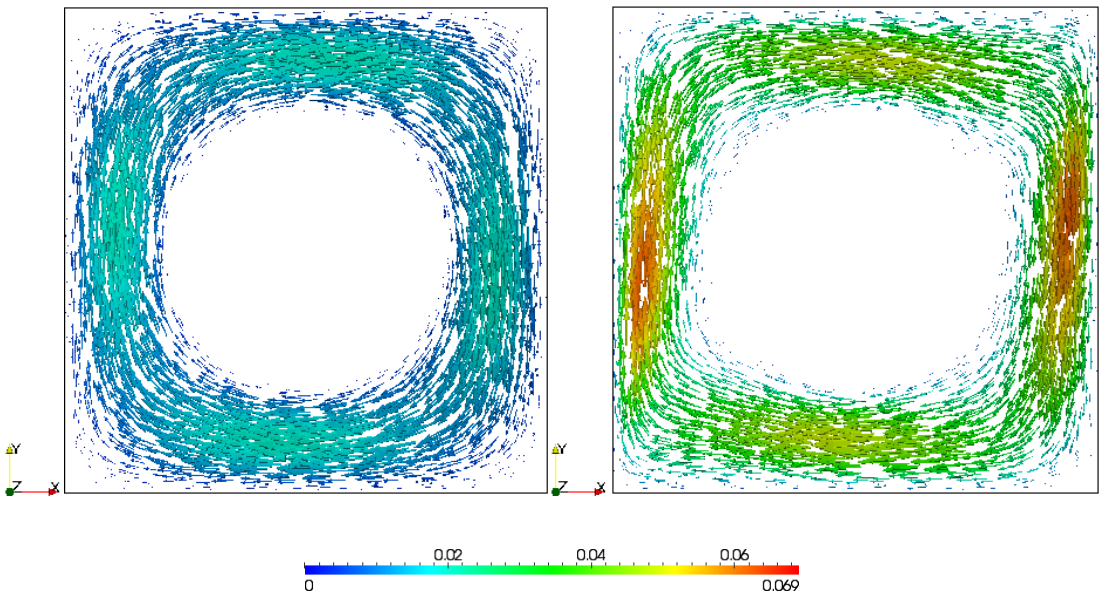

(a) (b)

Fig. 5-7 Distributions of velocity at the velocity equilibrium status with an impermeable solid (conventional *LBM* and *XLBM* with zero porosity): (a) $Ra = 10^3$, and (b) $Ra = 10^5$.

Fig. 5-8 shows the distributions of isotherms in the impermeable solid case. Similar to the natural convection in a square cavity in Section 5.3.1, the heat transfer changes from conduction to convection between the left hot wall and right cold wall as the *Ra* number increases from 10^3 to 10^5. The impermeable solid has resulted in a bending of the isothermals close to the solid surface, and appears as though the solid has attracted the temperature as a 'magnet'. Besides, the distributions of isotherms in the solid are not as large as that in the cavity, and the value of temperature varies a little and is close to the initial temperature T_0 = 0.5 due to the initial settings. This occurs because the evolution of heat transfer inside the impermeable solid is slower than the heat transfer in the cavity fluids. Therefore, it requires an even longer time for the temperature distribution inside the impermeable solid to diverge from the initial settings (initial average temperature as 0.5) and reach the temperature equilibrium status.

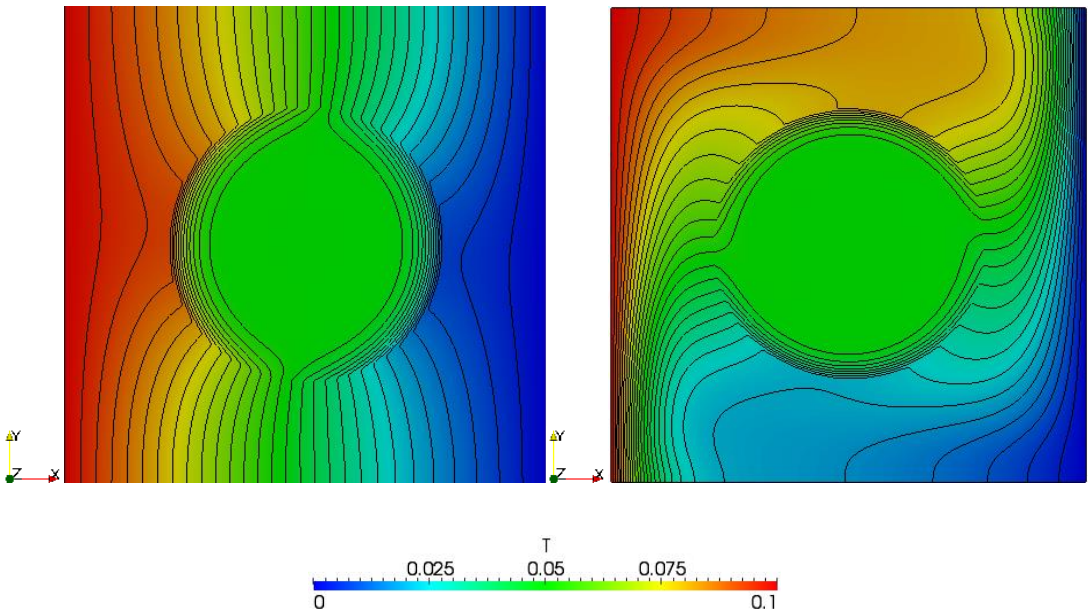

(a) (b)

Fig. 5-8 Distributions of temperature with isotherms at the velocity equilibrium status with impermeable solid (conventional *LBM* and *XLBM* with zero porosity): (a) *Ra* = 10^3, and (b) *Ra* = 10^5.

In comparison, the permeable solid case with porosity of 0.1 is calculated with the same conditions as the above. Fig. 5-9 (a) and (b) show the distributions of velocity field (at two *Ra* conditions) when the whole field reaches its velocity equilibrium status respectively. The distribution of the fluid velocity is similar to the cavity flow, but with a relatively small velocity inside the permeable solid. This penetration of fluid into the permeable solid results in a difference of the temperature distribution (Fig. 5-10) compared with the impermeable solid case: the heat conducts quickly into

the permeable solid in both *Ra* cases. Specially, the heat transfer inside the permeable solid evolves to reach the horizontal equilibrium distribution as the cavity flow case, due to the permeable solid's higher heat capacity than that in the impermeable solid case.

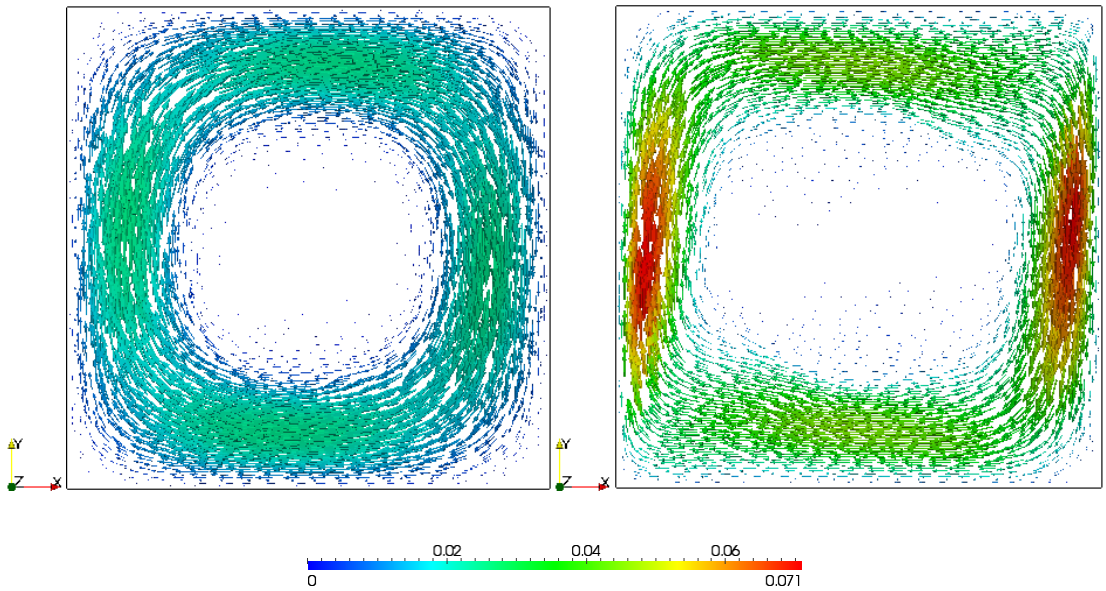

(a) (b)

Fig. 5-9 Distributions of velocity when it reaches the steady field at different *Ra* conditions for the permeable solid case (*XLBM* with porosity of 0.1): (a) $Ra = 10^3$, and (b) $Ra = 10^5$.

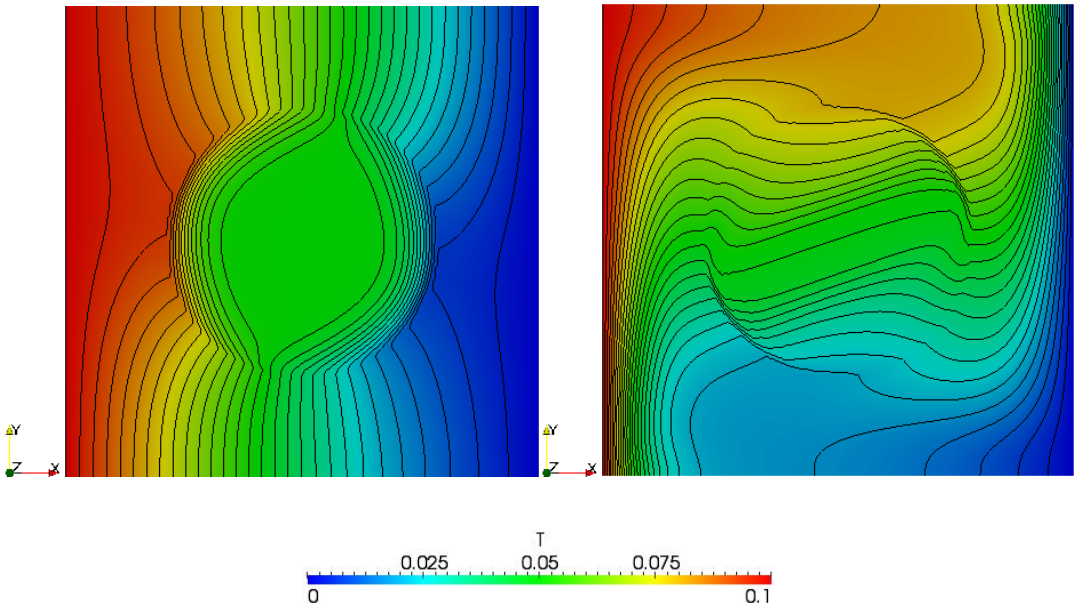

(a) (b)

Fig. 5-10 Distributions of isotherms when it reaches the steady velocity field at different *Ra* conditions for the permeable solid case (*XLBM* with porosity of 0.1): (a) $Ra = 10^3$, and (b) $Ra = 10^5$.

In detail, Eq. 5-11 compares the difference of velocity field and temperature field between the impermeable and permeable (*XLBM* with porosity of 0.1) cases when $Ra = 10^3$. Compared with the impermeable solid case (the reference base), fluid penetrates into the solid structure and has a velocity distribution inside the permeable solid (Fig. 5-11 (a)). This allows the heat to conduct quickly through the permeable solid with a higher temperature distribution inside (Fig. 5-11 (b)). This further affects the distribution of velocity and temperature in the cavity area as well. In Fig. 5-12, a higher $Ra = 10^5$ condition is also studied. Compared with the above lower *Ra* case, more fluid flow distributes inside the permeable solid (Fig. 5-12 (a)), and the heat conducts even faster than that in the low *Ra* permeable solid case (Fig. 5-12 (b)). This shows that the higher *Ra* condition can speed up the heat transfer through the permeable solid.

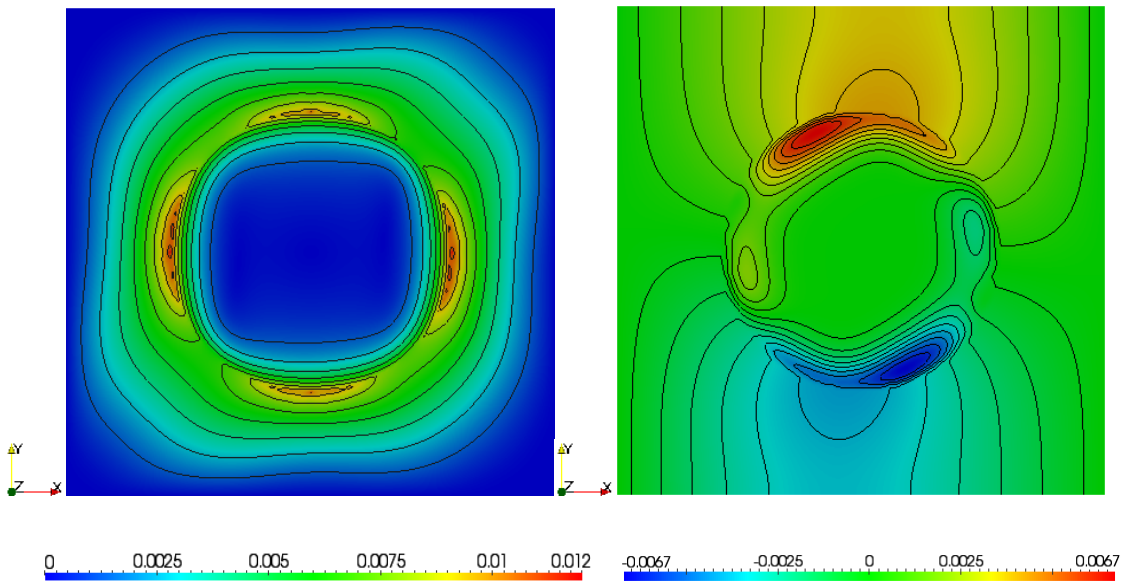

(a) (b)

Fig. 5-11 Difference of (a) velocity field and (b) temperature field between the impermeable and permeable (*XLBM* with porosity of 0.1) cases at $Ra = 10^3$ (the reference base is that in the impermeable case).

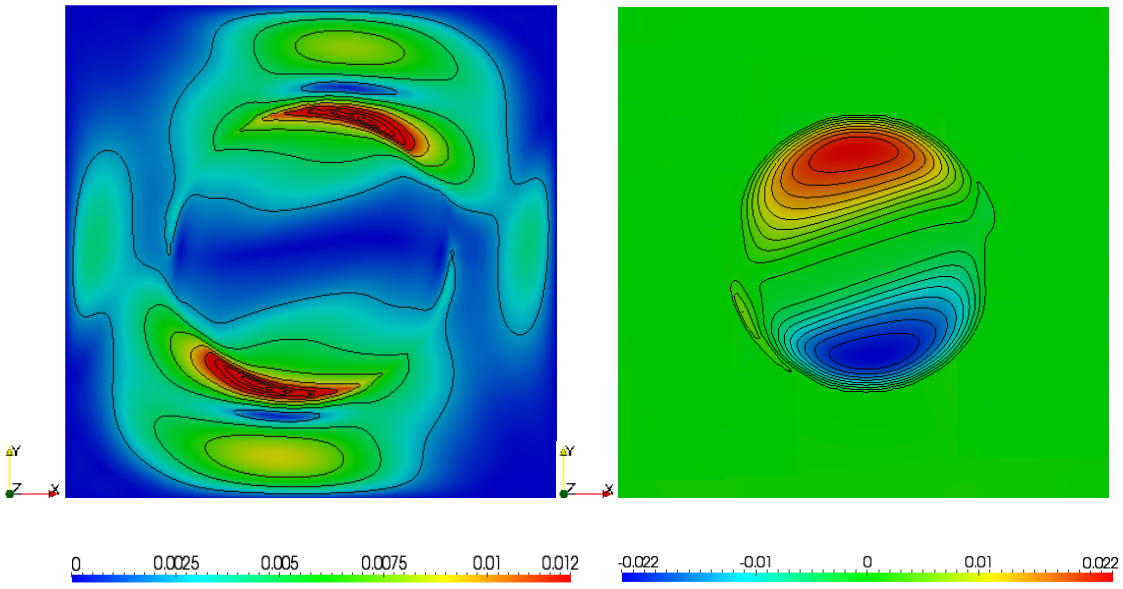

(a) (b)

Fig. 5-12 Difference of (a) velocity field and (b) temperature field between the impermeable and permeable (*XLBM* with porosity of 0.1) cases at $Ra = 10^5$ (the reference base is that in the impermeable case).

The above examples demonstrated the geothermal *XLBM* is capable of simulating heat transfer through both permeable and impermeable solid cases in porous media and has advantages over the conventional *LBM*.

5.4.2 Interactions between the heat transfer and fluid transport

In this application, we compare these two cases for study of the thermal effect on the fluid transport, and fluid transport effect on the heat transfer, respectively. The solids in the medium (lattice grid size of 1000 × 800) have the same solid-phase heat conductivity (Fig. 5-13). The setting of computing parameters is: *Re* is 10^{-1}, *Da* is 10^{-4}, *Ra* is 10^4, and *Pr* is 0.71. Both the top and bottom boundary walls are set as free boundaries, which means the fluid and heat transfer can go out or in freely. In order to analyse interactions between the fluid transport and heat transfer, two cases are compared. Case 1: the left wall at a higher temperature $T_1 = 1.0$ and the right wall at a lower temperature $T_2 = 0.0$ (Section 5.4.2.1); Case 2: the left wall at a higher temperature $T_1 = 1.0$ and a higher pressure $P_1 = 1.0$, and the right wall at a lower temperature $T_2 = 0.0$ and a lower pressure $P_2 = 0.0$ (Section 5.4.2.2). Here, the initial field is set as an average temperature $T_0 = (T_2 + T_1)/2$ in both cases.

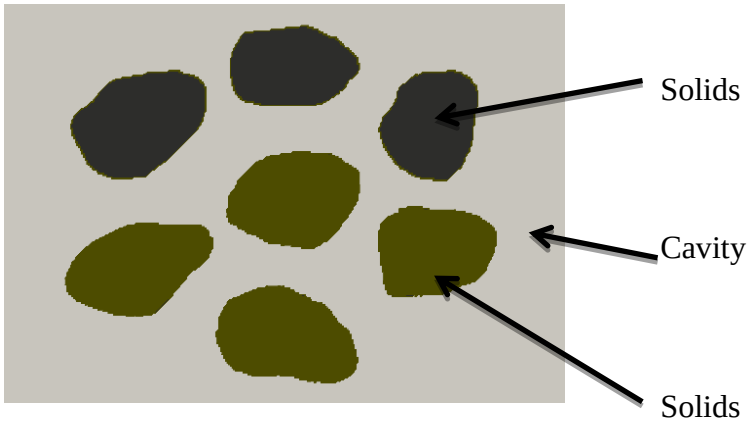

Fig. 5-13 A porous medium with a total lattice size of 1000 ×800.

5.4.2.1 Thermal effect on the fluid transport (Case 1)

In Case 1: the left hot wall and right cold wall is regarded as the heat source. Therefore, the fluid flow is driven under this heat gradient between these two walls. Fig. 5-14 shows the heat distribution and velocity field when the system reaches the velocity equilibrium status.

In Fig. 5-14 (a) and (b), heat transfer occurs in the solids at a slower speed but is faster in the fluids (or pore structures). Thus, the temperature distributions in solids are different from that in fluids: a distribution of a lower temperature inside the solids compared with that in the surrounded fluids. Meanwhile, the heat transfers from the left hot wall to the right cold wall, which results in the fluid flow convection in the whole system (Fig. 5-14 (c) and (d)). The fluid close to the left hot wall is driven up towards the top side due to the heat influence as buoyancy on the left side, whereas the fluid close to the right cold wall is dragged downwards as it cools. Besides, fluid flow is also observed through the pore network between the solids that creates turbulence in a relatively lower velocity distribution. This shows the effect of heat transfer on the fluid transport at the pore scale.

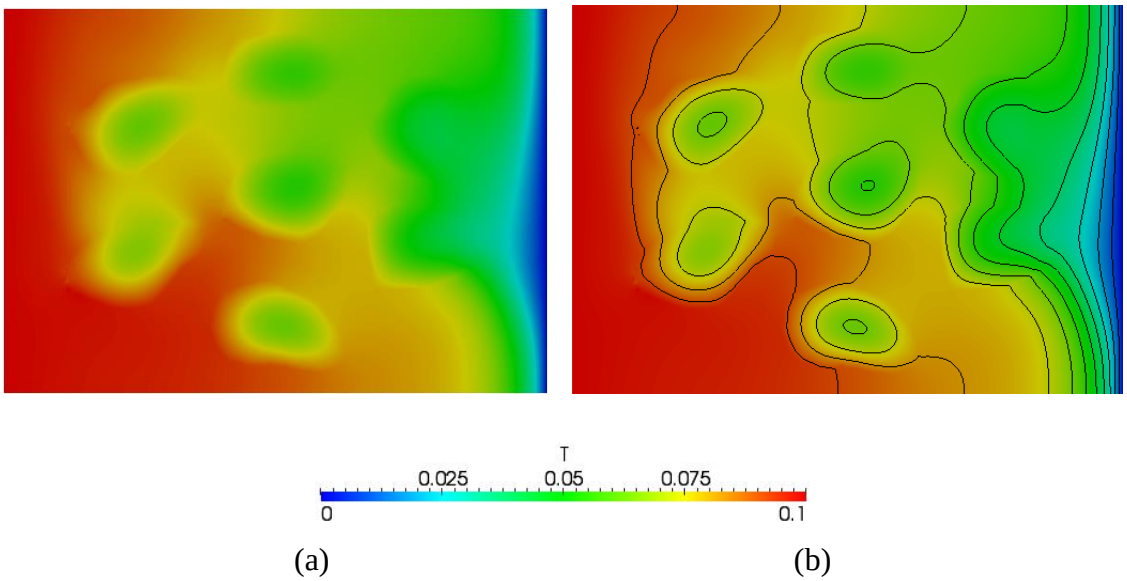

(a) (b)

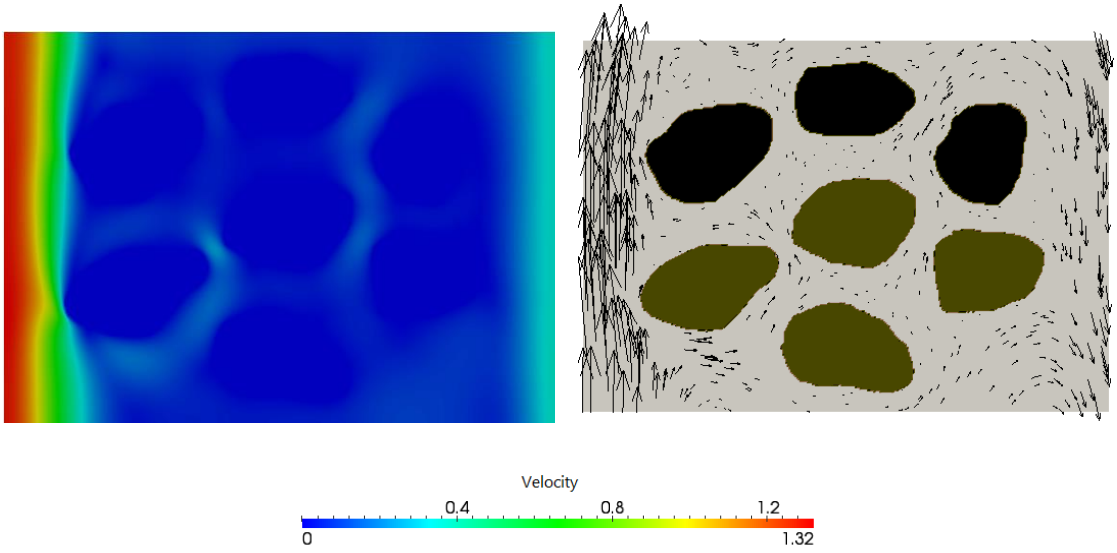

(c) (d)

Fig. 5-14 Distributions of (a) heat distribution and (b) heat distribution with isotherms, and (c) velocity magnitude, (d) velocity (arrow shows the flow direction), at the velocity equilibrium status.

5.4.2.2 Fluid transport effect on the heat transfer process (Case 2)

According to the above analysis, the heat transfer can effectively trigger the fluid flow in the porous media. Considering the coupling of System (**T, H**), the influence of the fluid transport on the heat transfer is also essential. Given the simulation settings and parameters in Cases 2, Fig. 5-15 illustrates the distribution of the velocity field and heat transfer when the whole field reaches the steady velocity status: (1) driven by the pressure gradient, the fluid moves almost straight away through the porous media from the left side to the right side, where the arrow indicates the flow direction as seen in Fig. 5-15 (a) and (b) rather than turbulent flow occurring between the solids as in Fig. 5-14 (c) and (d); and (2) due to the interactions of fluid transport on the heat distribution, the heat transfers quickly from the left hot wall to the right cold wall in a shorter time than that in Fig. 5-14 (a) and (b). Moreover, since the temperature evolution is slower than the fluid transport, it takes a longer time for the temperature distribution inside the solids to diverge from the initial settings (the initial average temperature as 0.5).

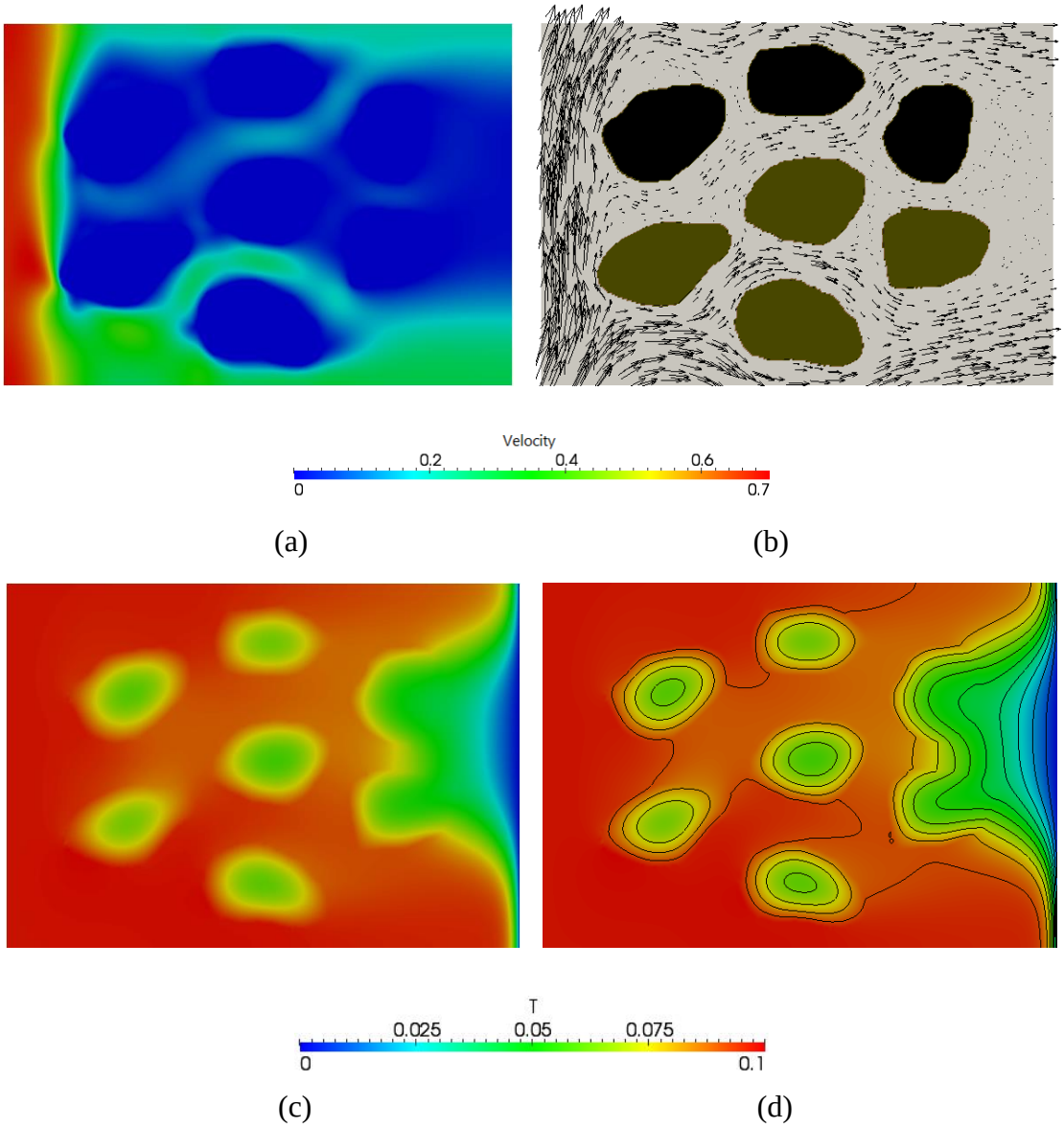

Fig. 5-15 Distributions of (a) velocity magnitude, (b) velocity (arrow shows the flow direction), and (c) heat distribution (d) heat distribution with isotherms, at the velocity equilibrium status.

5.5 Conclusions

This chapter has investigated how the fluid transport and heat transfer interact with each other and how to couple these two processes in the pore scale heterogeneous geomaterials with multiple minerals. An effective pore scale geothermal model was extended and embedded into the proposed parallel *XLBM*. This includes: thermal conduction and convection through pores and multiple solids (or minerals) in the heterogeneous porous media, and the interaction between the fluid transport and heat transfer. After being validated by a natural convection case as a benchmarked test, the *XLBM* model is further used for pore scale coupled **System (T, H)** applications: (1) through a single solid and (2) through a porous medium. Both the heat and velocity distributions have been studied and compared when the whole field reaches the velocity equilibrium status:

1) Increase of Rayleigh (*Ra*) numbers affects the evolution of the heat transfer. The distribution of isotherms changes from the vertical to the tilting orientation (from top right to down left) in the square cavity case. This is the result of natural convection induced by the buoyancy under higher *Ra* numbers. In small *Ra* cases, the heat transfer is mainly shown as conduction; when it gets larger, the heat transfer becomes convection;
2) Temperature gradient results in significant fluid transport, which is also a big impacting factor for creating fluid vortices in a closed cavity. Moreover, temperature can stimulate the seepage in certain permeable geomaterials; and
3) Evolution of temperature inside multiple geomaterials varies significantly due to the influence of different intrinsic geometry and geomaterial distributions. In detail, materials with higher porosity tend to have a higher heat capacity, where heat can conduct and reach the equilibrium status in a relatively shorter time. An extreme condition is the rapid heat transfer through pore structures, whereas it may take more time to transfer through an impermeable solid.

All the studies demonstrated the accuracy and usefulness of the proposed *XLBM* algorithm and the related code in simulating the coupled System (**T, H**) processes. Specially, the *XLBM* allows for the interactions of fluid flow and heat transfer through both permeable and impermeable solid cases that is beyond the capability of the conventional *LBM*. Thus it has advantages over the conventional *LBM* to simulate the diverse porous media where there are no connected pore networks observed at a certain resolution, but the pores are connected at a certain higher resolution.

Chapter 6 Parallel *XLBM* Modelling of Chemical Reactions (C) in Heterogeneous Geomaterials at Pore Scale with Applications in CO_2 Geosequestration

6.1 Introduction

Transport and reactions of fluid occur in many subsurface systems, and bring a wide range of scientific problems, such as simulations of petroleum reservoirs and coal seams, carbon dioxide injection and geological sequestration, environmental contaminant transport, mineral mining and chemical weathering, and cooling magmatic hydrothermal systems.

The coupled transport and reactions have been studied using various approaches. At the macroscale, partial differential equations (e.g. Darcy equation, Brinkman's equation or Finite element method) have been used for modelling fingering (non-complete dissolution in the media forms a narrow but long finger-shaped area), worm-holing (complete dissolved mineral area forms a channel) or mineral precipitation in fault zones in both homogeneous and heterogeneous porous media (Chadam et al., 1986; Ortoleva et al., 1987; Chen et al., 1990; Steefel and Lasaga, 1994; Aharonov et al., 1995; Liu et al., 1997; Ormond and Ortoleva, 2000; Ord et al., 2012). Besides, the thermal effect on geochemical reactions relates to the saturation of chemical components into the in-situ fluid and the pH value; meanwhile chemical reactions also influence the heat consumption (Kissinger, 1957; Hahn and Shiu, 1986; Gupta et al., 1990; Park et al., 1991; Cansell et al., 1993; Hobbs et al., 2000; Valo et al., 2004; Li et al., 2008; Yin et al., 2011). In particular, the program *TOUGHREACT* has applied the integral finite differences for non-isothermal multiphase reactive transport in variably saturated geologic media (Xu et al., 2012). *TOUGHREACT* is able to model both mineral dissolution and precipitation and the reaction-induced changes in mineral surface areas, and has been used in reservoir modelling for single well studies (Xu et al., 2004a; Xu et al., 2004b; Xu et al., 2005; Juanes et al., 2006; Gherardi et al., 2007; Xu, 2008; Alexander and Bryant, 2009).

As a result of chemical reactions, dissolution of solid-phase reactants or precipitation of resolved minerals has a great effect on the porosity. At the pore scale, the dissolution of solid-phase reactants in heterogeneous porous media first occurs as surface reactions. These reactions change the pore scale geo-structures such that wormholes or highly conductive channels are formed, and allow the generation of pore throats and connectivity. Thus, porosity enhancement in these reservoir rocks (Worden, 2006; Strazisar et al., 2009; Farquhar et al., 2013; Farquhar et al., 2014) is then formed; whereas the previously resolved minerals (e.g. ferroan carbonates) can also been precipitated due to chemical reactions. This may occlude the pore throats and eventually lead to the porosity reduction (Wachi and Jones, 1991; Steefel and Lasaga, 1994; Baker et al., 1995; Kinnon et al., 2010). Even a small porosity change at the pore scale induced by the chemical reactions is likely to create obvious

permeability changes due to the generation of pore network. Reasonable modelling of such coupled processes and porosity change at the pore scale are hence essential for the permeability measurement at larger scales.

At the pore scale, the coupled solute transport and chemical reactions have been studied in bulk fluid (Kingdon and Schofield, 1992; Dawson et al., 1993a), at mineral surfaces by using the lattice gas automata method (Wells et al., 1991), lattice Boltzmann simulations (Chen et al., 1995; Kelemen et al., 1995; Kang et al., 2002b) or finite difference schemes (Bekri et al., 1995; Bekri et al., 1997; Adler et al., 2002). In particular, Kang et al. (Kang et al., 2010b) have developed a pore scale model for simulating the injection of CO_2-saturated brine into structured porous media, and focused on the study of the fundamental physics occurring at the pore scale for reactions involved in geologic CO_2 sequestration. However, this work disregarded realistic heterogeneous porous media, used only arbitrary geometries, and did not give thorough consideration of the acidulation process of carbonate reservoirs.

Simulations of such geochemical reactions have become even more complex due to the heterogeneous geometry and multiple minerals involved in many real world situations. This requires consideration of not only the geometry heterogeneity but also the reactive and non-reactive mineralogy distributions, all of which may affect the geochemical reactivity and resultant fluid flow transport. In this chapter, we present a generalized pore scale geochemical reactions computational model based on our previous custom parallel *XLBM*, for studying even more complex geochemical reaction systems (section 6.2). This includes mechanisms of: mutually soluble single-phase acid fluid transport in pore (bulk) structures, acid fluid interactions on reactive and non-reactive mineral surfaces, dissolution/precipitation and mass transfer of the reactive minerals, as well as the temperature impact on the reactivity and potential chemical reactions. The geochemical model has been loosely coupled into the parallel *XLBM* platform.

In section 6.3, a CO_2-water-rock system based upon *CT*-scans of calcite cemented quartzose Hutton Sandstone before and after reaction is used to illustrate the ability of the model to visualise the reactive transport that took place during experiments. The CO_2-water-rock system involves reactive calcite, and non-reactive quartz, feldspar grains or other lithic fragments. The model was setup to mimic the experimental conditions of sample exposure to supercritical CO_2 and water at 60^oC and 12MPa over 18-29 days (including 2-3 days N_2 black pre-reaction at pressure and temperature) and was also extended beyond the experimental timeframe. The proposed model is verified against the laborotary results (section 6.3.2), which serves as a reliable quantitative approach to simulate the reaction transport in heterogeneous porous media involving multiple reactive and non-reactive

minerals. In this case, acid fluid interactions with the frontier non-reactive solid surfaces, acid fluid intrusion along the calcite-cemented cleavages, mass transport due to the calcite dissolution, generation of wormholes and highly conductive channels, and the feedback on porosity change have been discussed at the pore scale. Specially, the focus of this case is on the dissolution reactions that are likely to occur in the immediate wellbore environment. (Massarotto et al., 2010; Bacci et al., 2011). The simulation suggests that the proposed geochemical model may serve as an alternative reliable quantitative approach for studying locally unsteady state reactions, which include both the solute ions transport and the dissolution of solid-phase reactive mineral in heterogeneous porous media with multiple minerals and disparate reactivity.

6.2 Generalized Chemical *XLBM* for Mineral Surface Reactions in *3D* Pore Scale Heterogeneous Porous Media with Multiple Minerals

6.2.1 Comprehensive equilibrium reactions and kinetic rate laws

To simplify the description of the mineral reactions as a general form, the surface reactions are briefly defined as:

$$\text{Reactants } (R) + \text{Minerals } (M) \rightleftharpoons \text{Products } (P) \qquad \text{Eq. 6-1}$$

Here, the Reactants (*R*) stand for liquid or gas reactants, the Minerals (*M*) are reactive inclusions in the heterogeneous porous media and the Products (*P*) are the substances resulting from the chemical reactions. Mineral reactions can be chemically described using kinetic rate laws to predict dissolution or precipitation during the reaction processes. The general reaction rate (r_k) describes the speed at which a chemical reaction occurs, which is a function of the effective reaction-rate constant (k) that is specific to each reaction, mineral reactive surface area (S) exposed to the liquid or gas reactants, concentrations of liquid or gas reactants (C_s) on the mineral reactive surfaces, and the reaction orders (n). Here, the general kinetic rate r_k on the reactive surfaces is described as:

$$r_k = kS\left(\prod_j C_{s_j}^{n_j}\right)\cdot[1 - Q/k_{eq}] \qquad \text{Eq. 6-2}$$

Here, j stands for different species or icons, and Q is the activity products (*IAP*) that relates to the concentrations of species or ions and a measure of the effective concentration of a species under non-ideal conditions. Together with the concentrations, the activities are used to calculate both the

equilibrium constants and reaction rates. k_{eq} is the effective equilibrium constant, which is described as:

$$k_{eq} = \frac{[\text{Products}]^{\text{coefficient}}}{[\text{Reactants}]^{\text{coefficient}}} \quad \text{Eq. 6-3}$$

Square brackets stand for the respective concentrations in molarity, and the coefficients relate to the specific reaction formula in each reaction case.

The general kinetic rate r_k represents the dissolution status if it is positive; if r_k is negative, it represents the precipitation status, and if r_k is zero the system then reaches its equilibrium status. In different reactions, k_r and k_{eq} can be accordingly defined regarding disparate reaction status, which is also effected by the temperature. According to the Arrhenius equation (Arrhenius, 1896), the relationship between the temperature and the effective reaction rate k_r can be described as:

$$k = Ae^{\frac{-E_a}{RT}} \quad \text{Eq. 6-4}$$

Here, A is the pre-exponential factor (also known as the frequency factor for the reaction), E_a is the activation energy per mole (or apparent activation energy, (J/mol), T is the temperature (K), and R is the universal gas constant (8.3144 J/mol·K).

Besides, there are also plenty of non-reactive minerals in acid fluid situations. For these types of minerals, the previously proposed *XLBM* theory is used here for describing the fluid transport and fluid-solid interactions, which has been introduced in Chapter 3.

6.2.2 Reaction Species Model

This section focuses on how to obtain the distribution of reaction species (or ions) in the *XLBM* frame with the chemical reaction process coupled. The distribution of reaction species (or ions) and evolution equations for the species are described as follows:

$$g_{Y_{j,i}}\left(\mathbf{x}+\mathbf{e}_i\Delta t, t+\Delta t\right) - g_{Y_{j,i}}\left(\mathbf{x},t\right) = -\frac{1}{\tau_{Y_j}}\left[g_{Y_{j,i}}\left(\mathbf{x},t\right) - g^{eq}_{Y_{j,i}}\left(Y_j,\mathbf{u}\right)\right] + \omega_i R_s \Delta t \quad \text{Eq. 6-5}$$

Y_j represents the jth species concentration in the bulk fluid, R_s is the species reaction source term that is correlated with the kinetic reaction rate mentioned in the last subsection, and $\boldsymbol{\tau}_{Y_j}$ is the dimensionless relaxation time for species Y_j. $g_{Y_{j,i}}$ is the ith distribution of the species Y_j and $g^{eq}_{Y_{j,i}}$ is the equilibrium distribution function for species Y_j:

$$g_{Y_{j,i}}^{eq}(\mathbf{x},t)=\omega_i Y_j\left[1+\frac{\mathbf{e_i}\cdot\mathbf{u}}{c_s^2}+\frac{(\mathbf{e_i}\cdot\mathbf{u})}{2c_s^4}-\frac{|\mathbf{u}|^2}{2c_s^2}\right] \quad \text{Eq. 6-6}$$

The concentration of species Y_j can be addressed in terms of the distribution function in the *XLBM* framework:

$$Y_j=\sum_i g_{Y_{j,i}} \quad \text{Eq. 6-7}$$

The concentrations of all the reactant species in Eq. 6-2 can be achieved from the above, except the solid phase minerals (e.g. carbonate).

6.2.3 Surface reactions on the reactive minerals

In this section, we discuss the acid reactivity with the reactive minerals and its link with mineral dissolution and mass transfer. In chemistry, the mass action law describes the dissolution of solid minerals in dynamic equilibrium. This process relates to the kinetics of the reactions, such as reaction rates and equilibrium constants. According to the research performed by Guldberg and Waage (Guldberg and Waage, 1867), equilibrium constants were derived by using kinetic data and the rate equation, and. chemical equilibrium is a dynamic process where reaction rates for the forward and backward reactions must be equal at chemical equilibrium. Here, a mass transfer rate equation of solid-phase mass Y_M (reactive minerals) is defined as (Parkhurst and Appelo, 1999; Yin et al., 2011):

$$\frac{\partial Y_M}{\partial t}=M_M R_M \quad \text{Eq. 6-8}$$

M_M is the molecular weight of the reactive mineral, and R_M is the overall reaction rate at the present grid, which is negative to Eq. 6-2. Y_M on the *XLBM* grid can be calculated in the following discrete version:

$$Y_M(\mathbf{x},t+\Delta t)=Y_M(\mathbf{x},t)+M_M R_M \Delta t \quad \text{Eq. 6-9}$$

With the reaction dissolution of solid-phase reactive mineral, the volume of the overall solid-phase matrix becomes less and the porosity then increases. Hence, the mass fraction F_M of the solid-phase reactive mineral is obtained by:

$$F_M(\mathbf{x},t)=\frac{Y_M(\mathbf{x},t)}{Y_{M_0}} \quad \text{Eq. 6-10}$$

Y_{M0} is the initial mass on every mineral grid. The mass is updated after each time step. As the reaction continues, the mass of the reactive mineral at its contact surfaces with acid fluid becomes zero due to the continuous dissolution process.

Using the Chapman-Enskog expansion method, the above chemical reaction model can be proven to derive the convection-diffusion-reaction equation (Dawson et al., 1993a):

$$\frac{\partial Y_j}{\partial t} + (\mathbf{u} \cdot \nabla) Y_j = \nabla \cdot \left(D_j \nabla Y_j \right) + R_s \qquad \text{Eq. 6-11}$$

The species diffusion coefficient D_j can be given by $D_j = (\tau_{Yj} - 0.5) c_s^2 \Delta t$. Here, $c_s^2 = R_g T$ (R_g is the gas constant, and T is the temperature of the acid fluid).

6.3 Computational Model Verification and Simulation Result Discussion

The particular application that motivates the present study is geological sequestration of CO_2 and acid stimulation for increasing production of oil or gas. This involves injection of acid fluid (e.g. CO_2, HCl or SO_2) or mixtures of acid fluid into formation structures, and resultant dissolution of reactive minerals with further impact on the whole system (e.g. deformation or liquid/gas leakage). The proposed model is specified here for an application in CO_2-water-rock system (involving reactive calcite, and non-reactive quartz, feldspars or other lithic fragments), by using reaction kinetics for this special reaction to obtain a reliable outcome. In the real world situations, some lithics may also be reactive, which depends on the mineral composition. For example, some ferroan carbonates can release Iron (Fe), which eventually precipitates as solid-phase minerals due to its low solubility that will locally occlude porosity. In order to describe the reactivity of these lithics, the kinetic rates need to be specified according to different lithics situations. In this chapter, these lithics are described as unreactive for simplicity.

The application is compared with a laboratory experiment carried out by the University of Queensland (section 6.3.1), which is to study the pore scale geometry changes of a Hutton Sandstone sample due to the CO_2 injection into the fresh formation water for sequestration (Farquhar et al., 2013; Farquhar et al., 2014). Regarding this application, the geochemical model is first validated through the experiment, and it is then used for prediction of solute ions transport, dissolution and precipitation of solid-phase reactive mineral (calcite in this case) in carbonic acid until the equilibrium reaction status is achieved.

6.3.1 The laboratory experiment (acid infiltration)

The objective of this experiment is to use the quantified *micro-CT* scanning with *QEMSCAN* mineral mapping to measure geochemical reactivity of the reservoir core material, by comparing the sample before and after the reaction with the carbonic acid.

6.3.1.1 Hutton sandstone and the *3D* digital sample

The Hutton Sandstone is located at a depth of around 800 meters in the Surat Basin, Queensland Australia. Fig. 6-1 (a) and (b) shows the profile of the digital Hutton sample (before the acid infiltration experiment) from different angles, which is an irregular 4 *mm* diameter scale quarter-core. It consists of mostly sub-rounded, poorly sorted framework grains (quartz as the main aggregate). Most of the pore spaces are initially filled with abundant carbonate cements, while highly altered feldspar, some clay and other matrix grains also occur between the main aggregate. In detail, the sample has 76.3% of framework grain content (quartz) and around 5.6% clay and higly altered feldspar grains, 17% calcite cements, and around 1.1% resolved porosity (before the reaction) (Dawsona et al., 2013; Farquhar et al., 2013; Golab et al., 2013b; Dawson et al., 2014; Farquhar et al., 2014).

Fig. 6-1 (a)-(b) show the profile of the digital Hutton sample (before the acid infiltration experiment) from different angles. The *3D* digital sample (with a lattice size of 1400 × 1400 × 350) is reconstructed using the *micro-CT* scans with *QEMSCAN* mapping (around 3 μm voxel size). Fig. 6-1 (c)-(e) shows three different cross-sections from the inside sample: a *XoY* plate along the middle of the vertical *z*-axis (Fig. 6-1 (c)), a *XoY* plate at the bottom of the *z*-axis (Fig. 6-1 (d)), and a *XoZ* plate at the middle of the *y*-axis (Fig. 6-1 (e)). The main quartz aggregate sections (non-reactive) are shown in dark gray, which occupies most of the sample structure (76.3%); cemented calcite sections (reactive with the carbonic acid) are in light blue and also show a large proportion (17%); while most of remaining areas are filled with highly altered feldspar grains, clay and other matrix sections (dark orange) as well as other non-reactive minerals (5.6%). The pore structure only takes up around 1.1% of the whole sample, which can hardly be seen.

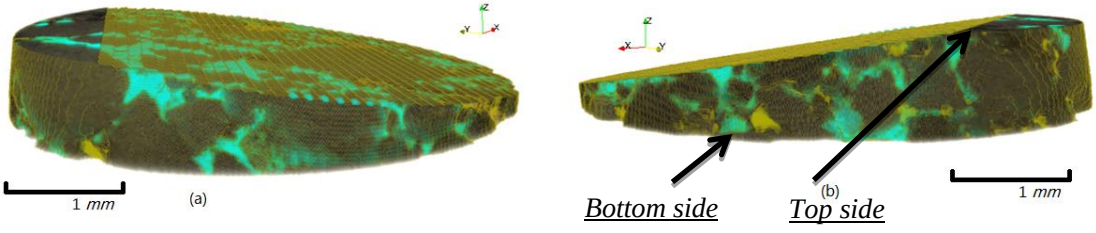

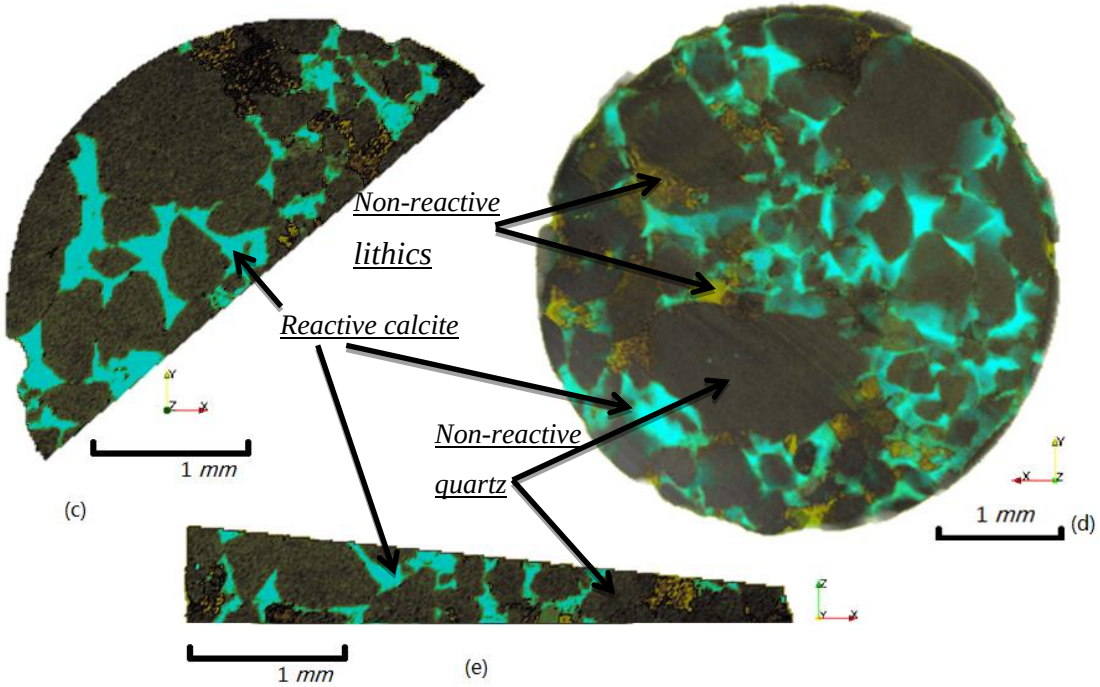

Fig. 6-1 (a)-(b) *3D* digital Hutton Sandstone core, (c) the cross-section (*XoY* plate) at the middle of the vertical direction (*z*-axis), (d) the cross-section (*XoY* plate) at the bottom of the vertical direction (*z*-axis), (e) the cross-section (*XoZ* plate) at the middle of the *y*-axis (quartz-dark gray, cemented calcite-light blue, clay and highly altered feldspar grains and other matrix grains-dark orange).

6.3.1.2 The experiment settings (CO_2 batch-reaction experiment)

The experiment was conducted in a static batch reactor (Fig. 6-2) located at the University of Queensland (Farquhar et al., 2014). The reactor comprises an unstirred 250 mL Parr reactor vessel with corrosion-resistant thermoplastic (PEEK) lining and sampling assembly, equipped with an electronic heating apparatus and fitted to an automatic PC-based temperature and pressure system. Prior to conducting each experiment run, sample holders were acid cleaned and the batch reactor was flushed using two cycles of CO_2 flushes with deoxygenated purified (deionized) water with the rock plug sample suspended in a thermoplastic basket immersed in the water, which is to minimise procedural contamination. Fluid chemistry of effluent from the second clean CO_2 cycle was used as a procedural blank for the subsequent experiment. Then, the vessel was purged of residual air with a low pressure N_2 flush. A syringe pump was used to pressurize vessels to 120 ± 1 bar for CO_2, and this vessel pressure was monitored with pressure transducer. The reactor was connected with pressure and temperature controller monitoring the system, and the vessel was also implemented with a fully contained piped emergency pressure relief system. Vessels were maintained at 60 ± 0.5 ℃ with an external heating jacket with feedback to the control loop, achieved with a thermocouple.

The conditions of 60 ℃ and 12 MPa were used to simulate conditions in part of the Surat Basin, where the sample was exposed to supercritical CO_2 and water at 60 ℃ and 12 MPa over 18-19 days (including 2-3 days N_2 blank at pressure and temperature). The sample was reacted over a period of 384 hours, which parallel studies have shown to be sufficient to simulate reactions likely to take place in the near well-bore environment rapidly after initial CO_2 injection. The sample was oven dried before post-reaction characterisation by *μCT* imaging, *SEM* imaging, and *QEMSCAN* analysis. (Pearce, 2012; Farquhar et al., 2013; Farquhar et al., 2014).

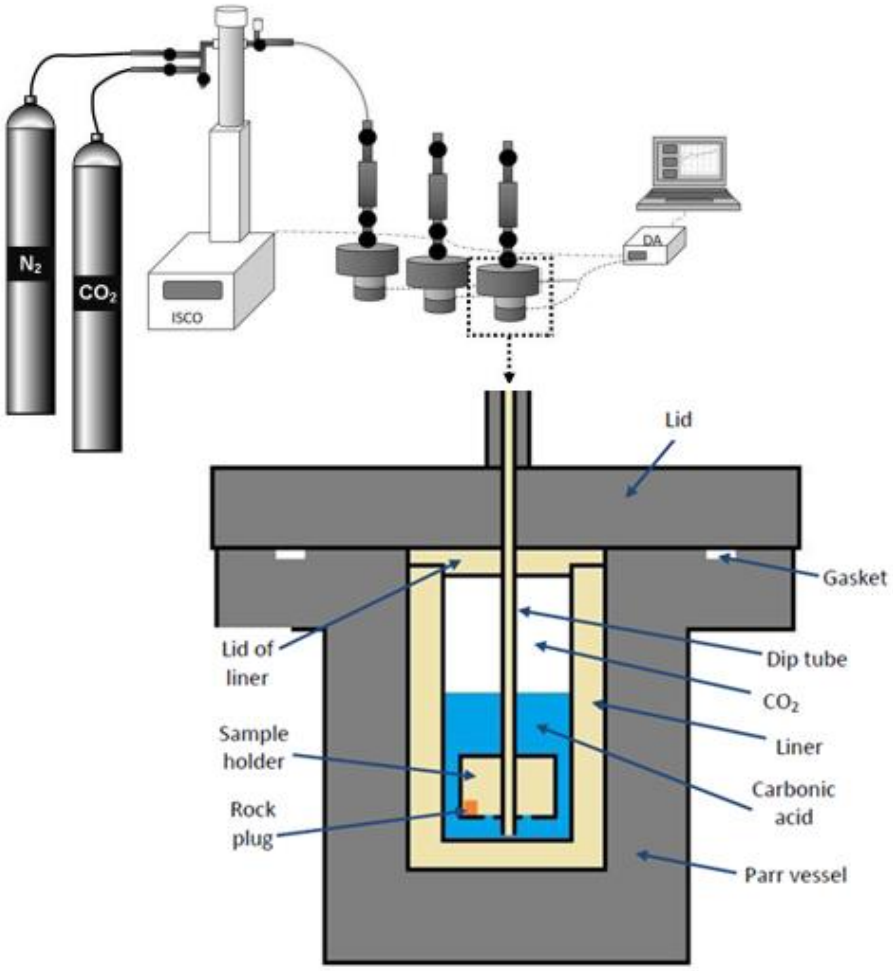

Fig. 6-2 Schematic of Surat Basin batch reactor CO_2-water-rock experiment setup. An internal view of the reaction vessel is provided; a supercritical gas phase head exists above the bulk water phase (shaded) containing saturated core samples (ISCO: injection pump, DA: data acquisition) (Farquhar et al., 2013; Farquhar et al., 2014).

6.3.1.3 The experiment results

The high solubility of CO_2 in water initially generates carbonic acid, and this reacts with the carbonate group in the calcite ($CaCO_3$) and dissolves calcite at the contact surfaces with carbonic acid. Notwithstanding the presence of large pore-filling calcite cements, the majority of the calcite

remains unreacted and only about 2.3% by volume of the calcite was lost during the reactivity experiment (384 hours reaction).

Fig. 6-3 shows the difference of the calcite distribution before (Fig. 6-3 (a)) and after (Fig. 6-3 (b)) the experiment based on the *micro-CT*/*QEMSCAN* images. In particular, Fig. 6-4 demonstrates the calcite that has been dissolved during the experiment (16 days); it is clear that the loss of the calcite cements has been significantly found in the regions at the contact with the carbonic acid (around the edge of the sample).

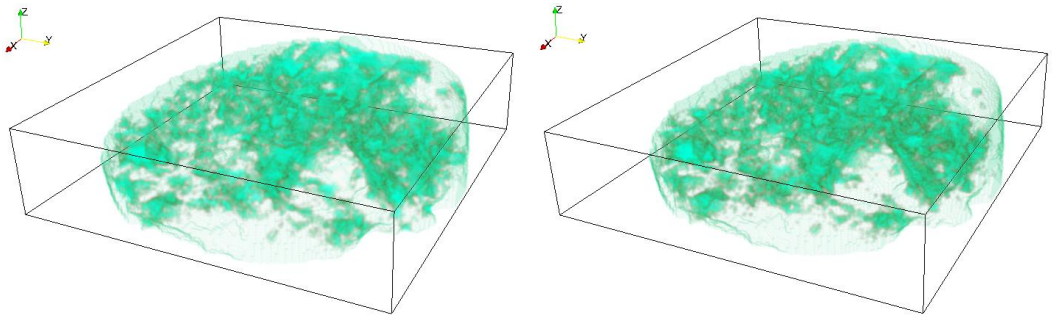

(a) (b)

Fig. 6-3 Comparison of calcite distribution in pre- and post- reaction status (calcite cements in light blue): (a) before the experiment, (b) after the experiment (16 days).

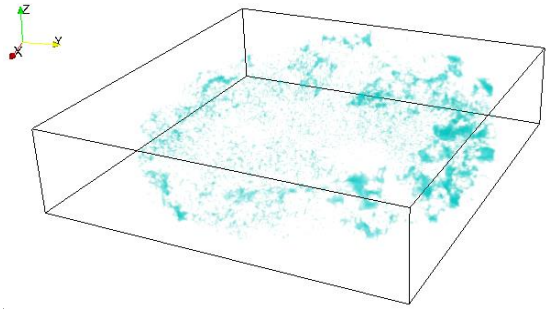

Fig. 6-4 Distribution of the dissolved calcite during the experiment.

For further analysis, Fig. 6-5 compares a thin section before and after the reaction experiment: a cross-section at the *XoY* plate (Fig. 6-5 (a) and (b)) that is at 1/3 height to the bottom side (*z*-negative). Fig. 6-5 (a) shows the mineral distribution before the experiment, where the black is the quartz sections, the dark orange is the matrix of feldspar and other lithics, and calcite is shown as light blue. After the experiment, some cemented calcite has been dissolved (highlighted in red color in Fig. 6-5 (b)). The dissolution occurs mainly around the edge of the sample, where calcite exposures to the carbonic acid and can be easily accessed by the carbonic acid. However, detailed inspection of the tomograms reveals that the majority of the calcite was dissolved along cleavage

planes and at grain/cement contacts, some carbonic acid has penetrated towards the center of the irregular quarter-core sample following the dissolved-calcite induced wormholes, and the total loss of the calcite has created around 2.3% second porosity enhancement.

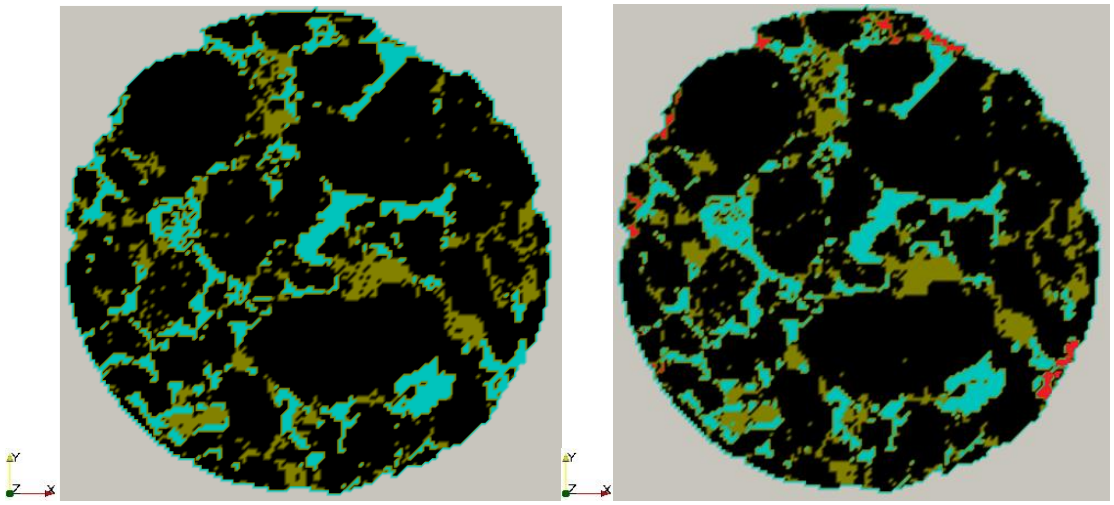

(a) (b)

Fig. 6-5 Comparison of the mineral distribution (a) before the reaction experiment, and (b) after the reaction experiment around 16 days (the dissolved calcite is highlighted in red color).

6.3.2 Simulation results and discussion

Regarding the experiment settings, the sample plug was placed in the sample holder and soaked in the carbonic acid with specific temperature and pressure that describes the Surat Basin conditions. In the numerical simulation, the temperature and pressure are also set as 60 ℃ and 12 MPa for the reaction modelling, respectively.

6.3.2.1 Specialized carbonic acid reaction *XLBM* model

In the CO_2-water-rock application, the reaction *XLBM* model is used to study the transport of bulk CO_2-water mixture (mutually soluble single-phase carbonic acid), carbonic acid interactions on non-reactive solid surfaces, and carbonic acid reactions on reactive minerals surfaces and resultant dissolution of reactive minerals (Gaus et al., 2008; Gaus, 2010).

Generally, pure CO_2 is assumed to be relatively unreactive, once in contact with water or brine, it will form carbonic acid H_2CO_3 and thus leads to the reactions as follows (Gaus et al., 2008; Gaus, 2010; Yin et al., 2011):

$$CO_2 + H_2O \rightleftharpoons H_2CO_3 \rightleftharpoons H^+ + HCO_3^- \qquad \text{Eq. 6-12}$$

Carbonic acid (weak acid) results in a drop in pH of the water or brine and acid attack on the reactive minerals of the host rock. Considering about the heterogeneous porous media, there are always multiple minerals (reactive and non-reactive inclusions). As mentioned in section 6.3.1, the main reactant mineral is defined as pure calcite ($CaCO_3$), which comprises part of the solid skeleton of the host rock. The simplified overall reaction can be described as:

$$CaCO_3 + H^+ \rightleftharpoons Ca^{2+} + HCO_3^- \qquad \text{Eq. 6-13}$$

In modelling geochemical reactions for CO_2 sequestration process, reaction kinetics for this special reaction have to be included in order to obtain a reliable outcome. Many kinetic laws are described in the literature (Plummer et al., 1978; Chou et al., 1989; Pokrovsky et al., 2005; Pokrovsky et al., 2009). The most popular one used in geochemical reaction modelling applied to CO_2 sequestration can be expressed as:

$$R_f = \left(k_1 \alpha_{H^+} + k_2 \alpha_{H_2CO_3} + k_3 \alpha_{H_2O}\right)\left(1 - Q/k_{eq}\right) \qquad \text{Eq. 6-14}$$

Here, R_f is the forward rate of dissolution, k_i (i for difference species or icons) are the reaction rate constants that depend on temperature (Eq. 6-4), α_{H+}, $\alpha_{H_2CO_3}$ and α_{H_2O} refer to the activities of H^+, H_2CO_3 and H_2O, respectively. k_{eq} is the equilibrium constant, and Q is the species or ions activity products (*IAP*) that relates to the concentrations of Ca^{2+} and HCO_3^-, and affects the dynamics of dissolution and precipitation before the system reaches the equilibrium status. The reaction parameters used in Eq. 6-14 are from the typical experimental data of Plummer et al. (Plummer et al., 1978) and Chou et al. (Chou et al., 1989): k_1, k_2 and k_3 are 8.9×10^{-5}, 5.0×10^{-8} and 6.5×10^{-11} (mol/cm^2·s), and k_{eq} is 3.47×10^{-9} (or $\log k_{eq}$ = -8.46).

6.3.2.2 Validation through the experiment

In this case, a fixed volume of carbonic acid reactant is set surrounding the sample to simulate the batch experiment. Fig. 6-6 compares the modelling outputs at the time step of 5×10^3 with the experiment results at the thin section (the *XoY* plate that is at 1/3 height to the bottom side towards the *z*-negative orientation). The dissolved calcite is highlighted in red color. Clearly, the modelling of dissolution (Fig. 6-6 (b)) shows that the majority of calcite matter loss occurs around the edge of the sample, which is largely due to the experimental settings and the intrinsic geometry of the sample. Besides, the carbonic acid starts to penetrate from outside of the sample towards the center along the dissolved channels, which fits the experiment well (Fig. 6-6 (a)).

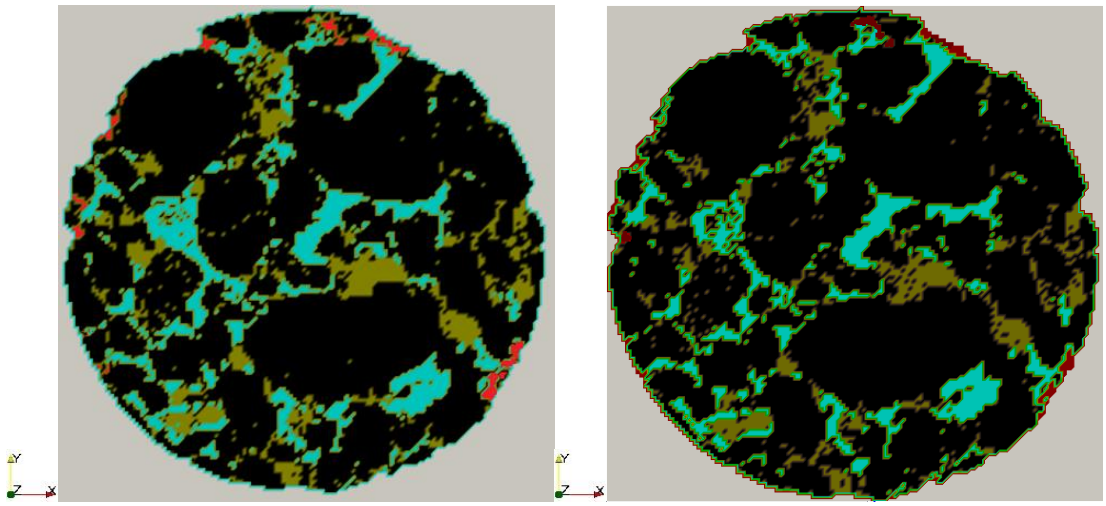

(a) (b)

Fig. 6-6 Comparison of the mineral distribution: (a) the experiment result (16 days outcome), and (b) the modelling result at the time step of 5×10^3 (the dissolved calcite is highlighted in red color).

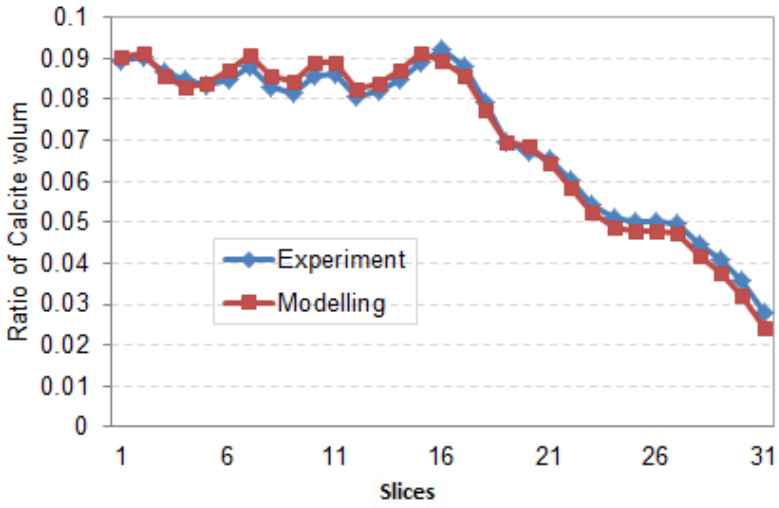

Fig. 6-7 Comparison of the volume percentage of un-dissolved calcite at 30 different cross-sections along the vertical (*z*-axis) direction (sections 1 to 31 are from the bottom side to the top side marked in Fig. 6-1 (b)): the blue line shows the experimental observation (16 days), and the red line shows the modelling results at the time step of 5×10^3.

For comprehensive comparison, Fig. 6-7 also compares the volume percentage of un-dissolved calcite between the experiment and modelling results (at the time step of 5×10^3) for verification: 30 cross-sections along the vertical direction (*z*-axis) are chosen for demonstration, where the blue line shows the experimental observation and the red line shows the modelling results. It is observed that the calcite volume at each cross-section is different due to the sample heterogeneity, and the modelling results fit the experiment observation well as a 16-day reaction outcome.

6.3.2.3 *3D* evolution of CO_2-induced calcite dissolution process

After validation through the laboratory experiment, we model the evolution of calcite dissolution until it reaches the equilibrium status in a long time. To avoid the carbonic acid becomes exhausted, we set up the sample in a sample holder where keeps adding the carbonic acid. This requires more than 16 days, which is beyond the duration of the experiment.

Before the reaction system reaches the equilibrium status, the dissolution proceeds along the cemented area of calcite between the main aggregate (and other non-reactive matrix). The volume of un-dissolved calcite reduces, as the dynamical modelling of the chemical reaction continues. Fig. 6-8 shows the evolution of un-dissolved calcite at these 30 cross-sections from the beginning of the reactions until the reaction equilibrium status is attained. Firstly, it is clearly observed that calcite on both the top (slices 1-6) and bottom sides (slices 26-31) are easily dissolved, since those slices are close to the edge of the sample and can be easily accessed by the carbonic acid; and the closer the slice to the edge, the faster the calcite is dissolved. Secondly, the inside calcite is not quickly dissolved and some is not affected at all because these calcite sections have no connectivity to the outside reactive fluid.

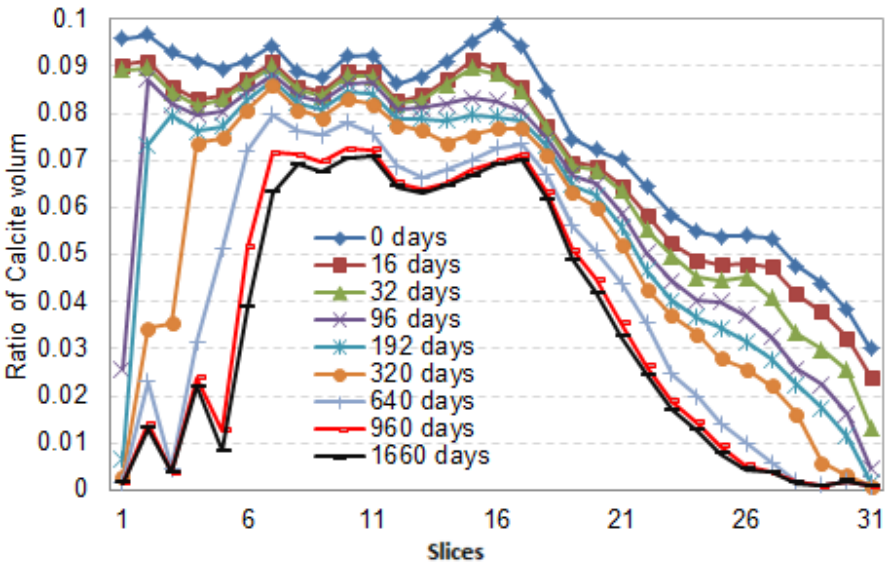

Fig. 6-8 Prediction of calcite volume at these 30 different cross-sections from the beginning of the reactions to the reaction equilibrium status, which indicates the calcite distribution and loss due to the dissolution (sections 1 to 31 are from the bottom side to the top side marked in Fig. 6-1 (b)).

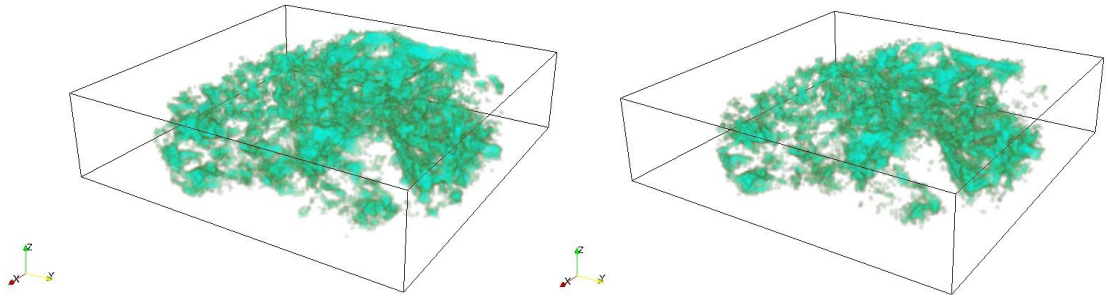

(a) Before the reaction

(b) 16 days

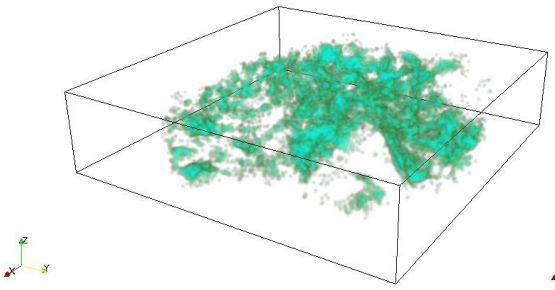

(c) 96 days

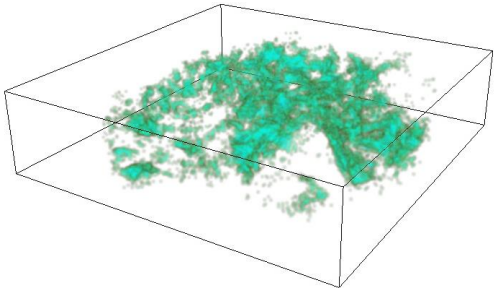

(d) 192 days

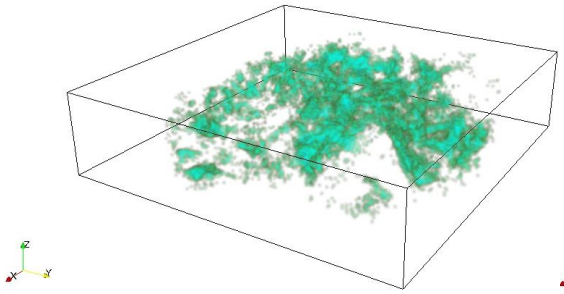

(e) 320 days

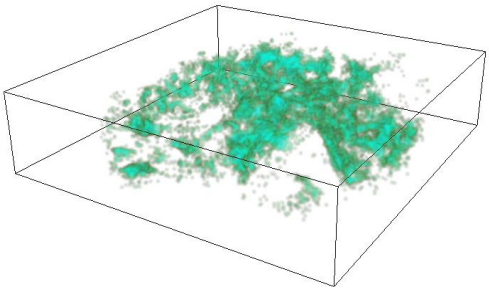

(f) 640 days

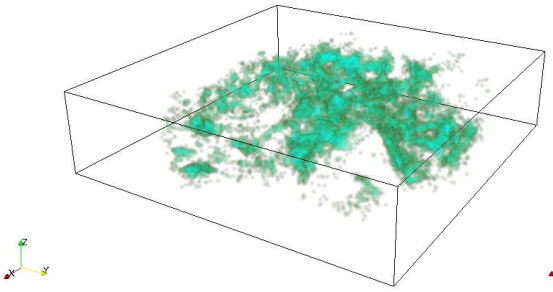

(g) 960 days

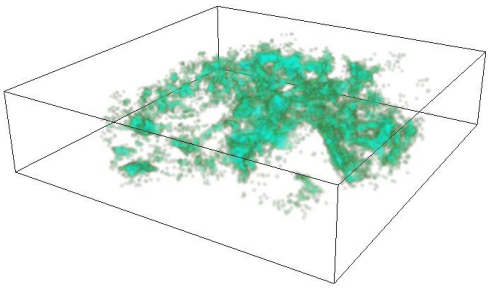

(h) 1600 days

Fig. 6-9 (a-h) Numerical simulation of acid infiltration evolution: blue color indicates the calcite distribution and loss due to the dissolution process.

The total calcite loss from the initial condition until the equilibrium reaction status can be seen from Fig. 6-9, which leads to porosity enhancement in the sample. Due to this secondary porosity improvement, more carbonic acid can penetrate into the sample core following the calcite-dissolved pores, wormholes and channels.

In order to show the calcite dissolution process, a cross-section (Fig. 6-10) right in the middle of *y*-axis is selected for further analysis of carbonic acid penetrating from the edge into the sample core (Fig. 6-11).

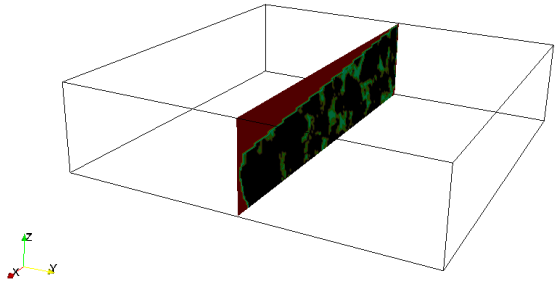

Fig. 6-10 The cross-section selected for the demonstration of the calcite dissolution process.

The dissolution (Fig. 6-11) first occurs around the edge of the sample in immediate contact with the carbonic acid, and then starts to penetrate along the dissolution-induced cleavages. This also confirms the reason why the inside calcite volume is higher than that around the edge area (as shown in Fig. 6-8). The red color represents the carbonic acid and it can be seen that the carbonic acid has reached some places of the inside core following the dissolution channels.

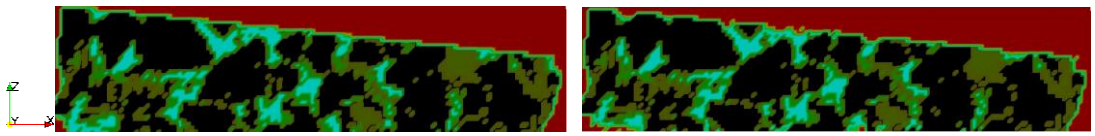

(a) Before the reaction (b) 16 days

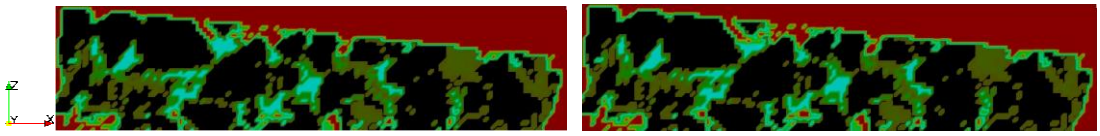

(c) 96 days (d) 192 days

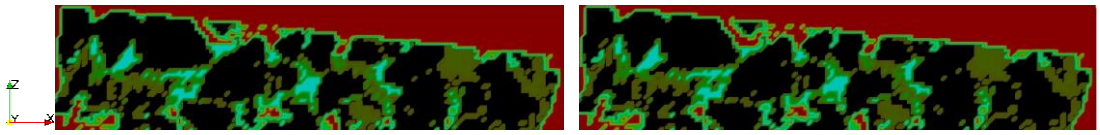

(e) 320 days (f) 640 days

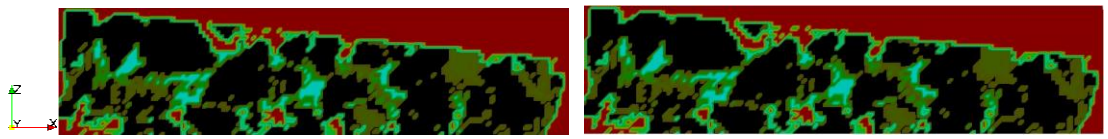

(g) 960 days (h) 1600 days

Fig. 6-11 (a-h) Numerical simulation results of acid infiltration evolution: carbonic acid penetrating from the edge into the sample core due to the calcite dissolution (carbonic acid is highlighted in red color).

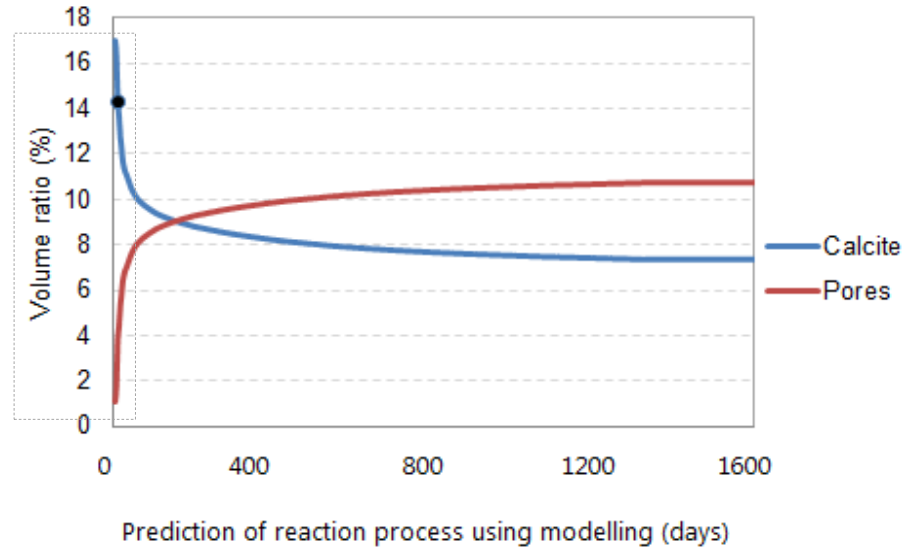

(a)

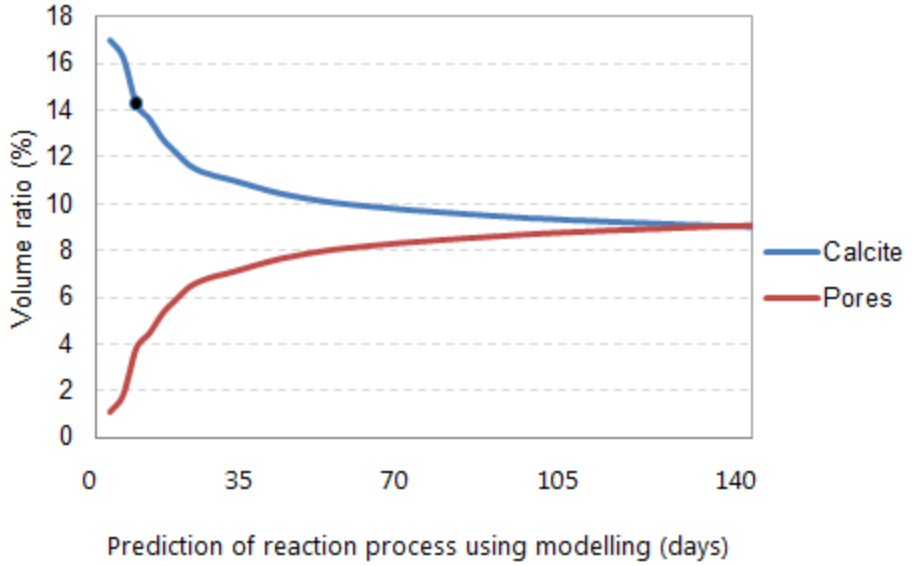

(b)

Fig. 6-12 Total volume change of calcite and pores in the numerical simulation of acid infiltration evolution: the blue line indicates the calcite dissolution process, and red line shows the generation of wormholes (or pore structure).

Fig. 6-12 (a) illustrates the total volume change of calcite and pores from the reaction beginning until the reaction equilibrium status is attained: the blue line shows the dissolution of calcite as the reaction time increases; the red line shows the increase of pore structure and wormholes resulting from the dissolution of cemented calcite along the cleavages planes. For analysis about reaction process in the first few days, Fig. 6-12 (b) has demonstrated the modelling results of calcite and porosity changes in around 140 days.

The calcite has been significantly dissolved in the first 30 days, leading to a calcite volume drop from around 17% to 11%, which has been clearly demonstrated in Fig. 6-12 (b). During this process, around 2.3% of calcite volume has been removed and replaced by the pore in 16 days, marked as a black point in Fig. 6-12 (a) and (b), which has been verified by the experiment. With the ongoing modelling process, the speed of dissolution experiences a gentle drop from 11% to around 8.5% in around 320 days, which largely relates to the presence of small calcite-cemented areas or narrow cleavages that slowed down the dissolution process. The system finally reaches the reaction equilibrium status in around 1440 days, which brings a porosity increase from 1.1% to 10.7%. Around 7.4% of the calcite is unaffected, which indicates the lack of connectivity with the open pores or other dissolved calcite structures, where the carbonic acid cannot access.

6.4 Conclusions

This chapter is towards the coupled flow transport, temperature and geochemical reactions in **System (T, H, C)**. We have developed an effective pore scale reactive transport computational model based on the previous custom parallel *XLBM*, which studies general pore scale reactive transport in three dimensional heterogeneous porous media consisting of both reactive and non-reactive minerals. The work includes the mutually soluble single-phase acid fluid transport in pore (bulk) structures, locally unsteady state reactions and dissolution unstable fronts. In particular, it involves acid fluid interactions on reactive and non-reactive mineral surfaces, solid-phase dissolution and mass transfer, and resultant porosity change.

The following conclusions can be drawn: (1) a general geochemical reaction model is deduced and implemented into the parallel *XLBM* platform, which is to describe coupled processes including the porous media heterogeneity and geometry structures, the species reaction and reactive transport, acid fluid interactions on different solid surfaces, and reactive minerals dissolution and resultant porosity change; (2) the model is specified as a model for carbonic acid reaction with the cemented calcite in the CO_2-water-rock system (involving reactive calcite, and non-reactive quartz, feldspars or other lithic fragments) and verified against results from a laboratory experiment for CO_2

sequestration study (carried out by the University of Queensland); (3) it is shown in the modelling that the reaction concentrates in the region at contact surfaces with the acid fluid (carbonic acid), where most of dissolution occurs at the edge of sample and some carbonic acid penetrates towards the center of sample along the dissolved cleavages between the main aggregate and other non-reactive matrix; (4) the calcite has been dissolved very quickly in the first few weeks and then experiences a gentle dissolution stage, which occurs because of the reaction front meeting numerous small calcite-cemented areas or narrow cleavages that has slowed down the dissolution progress; (5) the modelling system reaches the reaction equilibrium status in around 1440 days (keep adding the carbonic acid in case that the acid fluid is exhausted). This brings a porosity enhancement from 1.1% to 10.7%; while around 7.4% of the calcite is unaffected due to lack of connectivity with the open pores or other dissolved calcite structures, where the carbonic acid hardly can access.

The simulation confirms the capability of the proposed geochemical model for describing the coupled processes of solute reaction transport, fluid interaction with the frontier solid surfaces, and solid skeleton dissolution linking with the porosity change. In the real world situation, it is commonly more complex than these modelling conditions. For example, lithics like reactive silicates may release Fe and Mg during the reactions, leading eventually to the precipitation of ferroan carbonates that will locally occlude porosity. Moreover, disparate kinetic rates of multiple minerals need to be specified under different chemical reaction cases. Notwithstanding, it is feasible to extend the proposed *XLBM* model to study multiple reactive minerals with disparate reactivity rates, and provide predictive simulations beyond the duration of the experiment.

Chapter 7 From Pore Scale to REV Scale: A Permeability Study of the Coupled System (T, H, C)

7.1 Introduction

Reservoir rocks commonly have strong *3D* anisotropy that can be described by the directional permeability along three orientations at the macroscale (as *3D* permeability). This *3D* permeability depends on the intrinsic features (e.g. anisotropy) of the targeted reservoir rocks. Meanwhile, an insight gained from the nonlinear coupled **System** (**T**, **H**, **C**) studies the impacting factors that ultimately determine dynamic and directional effects on the pore scale geo-structures and flow dynamics over the temporal scale (fourth scale). The study demonstrates capability in modelling porosity change in heterogeneous geomaterial structures when the whole system reaches a relatively 'stable' or 'static' status after passing through a dynamic or 'unsteady' phase. Thus, the term - *4D* permeability rather than the *3D* permeability is essential to determine the changes in these systems.

Moreover, the permeability is sensitive to the sample scale (size). Representative Elementary Volume (*REV*) has been widely selected in the laboratory research or reservoir engineering (Kanit et al., 2003; Gitman et al., 2007) as the smallest sample size that provides reliable and representative transport calculations (e.g. directional permeability and connectivity) for upscaling reference. These *REV* scales are larger than the pore scale but much smaller than the field scale. The characteristic features at the *REV* scale represent the basic but essential inputs for macroscale analysis.

This chapter introduces a reference study from the pore scale coupled process to the evaluation of the *REV* scale parameters. Two applications are studied for the pore scale coupled **System (T, H, C)** in natural, fractured reservoir rocks and the resultant impact on the permeability measurement: (1) analysis of the dynamic permeability change and evaluation of the *4D* permeability change (section 7.2); and (2) sample size (scale) effect on the permeability evaluation for the *REV* scale (section 7.3).

7.2 *4D* Permeability Evaluation

Cleats represent the primary flow conduits in coal and the detrimental effect of cleat mineralization on coal permeability is well known (Gamson et al., 1993; Levine, 1993; Yee et al., 1993; Turner et al., 2013). In general, minerals occur as finely disseminated particles throughout the coal matrix, in distinct non-coal interbeds and as infill in fractures and cleats. Acids are traditionally selected as dissolution treatments in carbonates or sandstone reservoirs, particularly after mud treatments where formation damage may occur. In particular, hydrochloric acid (HCl) has been widely used.

However, the extent that demineralization techniques may enhance coal permeability is yet to be fully realized. This present study investigates the use of HCl to enhance coal permeability via cleat de-mineralization. The acid flooding modelling is meant to evaluate the *4D* permeability as the acid flooding proceeds.

7.2.1 Brief information about the coal sample and core flooding

The cropped coal sample (Fig. 7-1 (a)) for analysis is a cuboid (5.3 cm × 5.3 cm × 1.3 cm) and includes a significant carbonate component (mainly calcite) that infills the cleats (Turner, 2014). The reconstructed digital coal core has a lattice size of $1000 \times 1000 \times 250$ at the voxel size of 53 μm (Fig. 7-1 (a)). At least one calcite filled cleat is clearly observed aligned with the *z*-axis orientation (bottom left image in Fig. 7-1 (a)). For clear demonstration, the inner calcite distribution (dark blue) is displayed in Fig. 7-1 (b). Two wider calcite filled cleats (marked as C1 and C2) are aligned with the *z*-axis orientation. Besides, there are also some narrow calcite filled cleats found aligned with the *z*-axis orientation (marked as C3 and C4). In addition, these calcite filled cleats are not connected along both the *x*-axis and *y*-axis directions, as it is observed from the *XoY* plane (Fig. 7-1 (c)). In particular, the distribution of the calcite reflects some degree of alignment along the *x*-axis compared with that along the *y*-axis.

The core flooding test uses 1% hydrochloric acid (HCl) to study the calcite dissolution, as it is known that 1% HCl can effectively dissolve carbonates such as calcite and apatite mineralisation. Here, the calcite dissolution in HCl is as follows:

$$CaCO_3 + 2HCl \rightarrow CaCl_2 + CO_2 + H_2O \qquad \text{Eq. 7-1}$$

In modelling chemical reactions for the coal core acid stimulation process, the reaction kinetics for this specific reaction have to be included in order to obtain a reliable outcome. The reaction rate of hydrochloric acid with carbonate minerals is very rapid, which results in poor etched fracture lengths and high corrosion rates, particularly in high temperature formations. The rate of the reaction of HCl with calcite can be described using the power-law model from the literature (Lund et al., 1975; Plummer et al., 1978; Mumallah, 1991; Alkattan et al., 1998; Fredd and Fogler, 1998; Fredd and Scott Fogler, 1998; Alkattan et al., 2002; Buijse et al., 2004; Santschi and Rossi, 2006). These studies provide the reaction kinetics parameters, which are essential in designing different stimulation treatments. The most popular one used in the chemical reaction modelling applied to the dissolution of calcite in hydrochloric acid is:

$$R_f = k(\alpha_{H^+})^n = k(\alpha_{HCl})^n \qquad \text{Eq. 7-2}$$

R_f is the forward rate of dissolution, k is the reaction rate constant dependent on temperature (Eq. 6-4), n is the reaction order, and α_{H+} and α_{HCl} refer to the activity of H^+ and HCl, respectively. Here, we set n is 1.0 and k is 7.5×10^{-5} mol/cm^2·s.

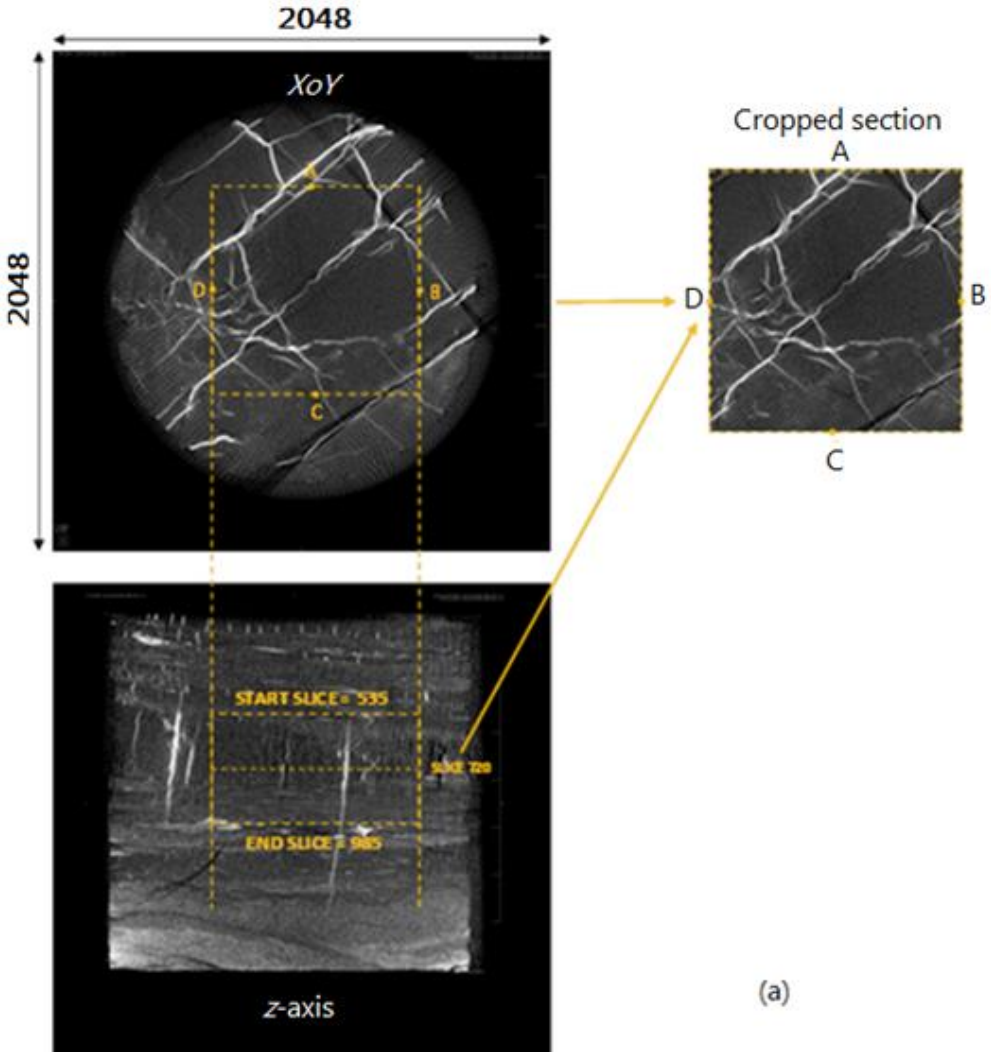

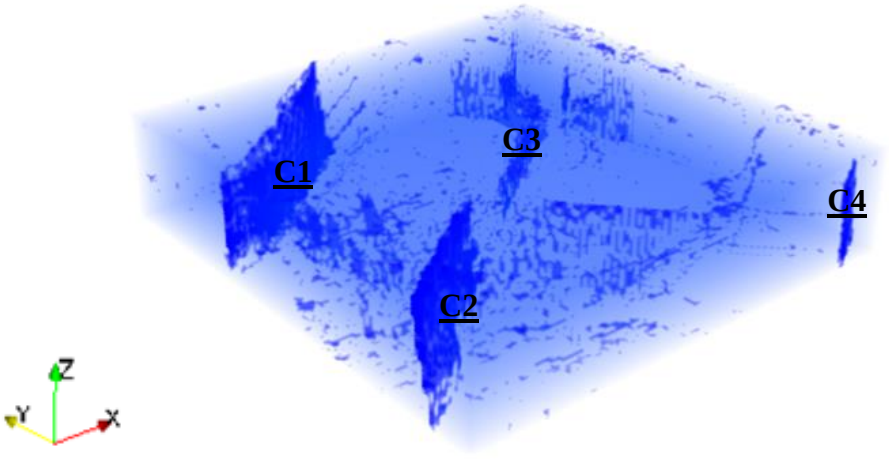

(b)

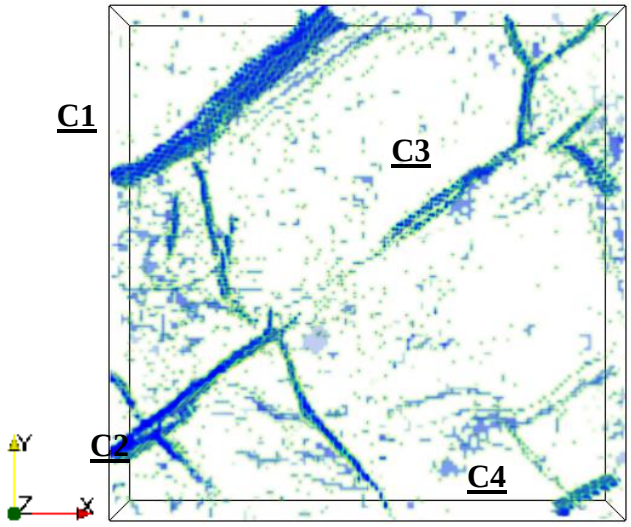

(c)

Fig. 7-1 (a) Selection of the cropped coal core for *4D* permeability modelling (Turner, 2014), (b) the coal matrix (light blue) and the calcite distribution (dark blue) after the digital coal core reconstruction, and (c) the distribution of calcite filled cleats (dark blue) observed at the *XoY* (axial) plane.

7.2.2 Simulation results and discussion

In the modelling, we analyse the reaction process at the temperature of 40^{o}C that is representative of the subsurface in a coal bed methane (CBM) field. The reaction rates can be obtained according to Eq. 6-3. The HCl viscosity is 0.7225×10^{-3} Pa·s and is flooded through the coal core in three different cases: along the positive *x*-axis (sagittal plane), *y*-axis (coronal plane), and *z*-axis (axial plane) respectively for the *4D* permeability study (Fig. 7-1 (b)). The coal matrix commonly has some intrinsic permeability, which is also determined by the forces acting on the coal in the subsurface. At deeper levels, the coal matrix can have a much lower permeability. According to the literature (Somerton et al., 1975; McKee et al., 1988; Seidle et al., 1992), the intrinsic permeability of coal matrix varies over a wide range from 0.01 *mD* to 100 *mD* at the lowest stress level. In this case, this intrinsic coal permeability excluding the cleats is set as 0.2 *mD* and the flooding pressure gradient is 10 *bar*/*mm*. Other side walls are set as closed boundaries without fluid inlet and outlet.

According to Chapter 6, the coupled **System (T, H, C)** significantly affects the porosity over the temporal scale, which relates to the connectivity and tortuosity of the pore network for fluid flow. Here, we illustrate the distribution of the calcite dissolution (Fig. 7-2) and porosity increase (Fig. 7-3) in these three flooding cases.

It is firstly seen that the calcite has been dissolved as the acid was flooded through the coal core in all three cases. The coal matrix has an intrinsic permeability so the HCl penetrated through the matrix and eventually dissolved all the calcite in the cleats. Secondly, in detail, the calcite dissolution in the *z*-axis flooding case was finished in a shorter time (around 20 minutes, Fig. 7-2 (b)), whereas the dissolution process in the other two cases has taken a relatively longer duration: around 6.5 hours in the *y*-axis flooding and 7 hours in the *x*-axis flooding (Fig. 7-2 (a)). In particular, the calcite dissolution in the *x*-axis flooding case is faster than the dissolution in the *y*-axis flooding case in the first two and half hours. This confirms the observation in Fig. 7-1 (c) that the distribution of the calcite reflects some degree of alignment along the *x*-axis. Moreover, the lengths of the sample in the *x*-axis and *y*-axis flooding are 4 times of that in the *z*-axis case. This is the reason for the difference of the dissolution durations in three cases. The other cause, more importantly, is due to the intrinsic anisotropy related to the calcite filled cleats, where the sharp slope of the calcite dissolution along the *z*-axis indicates more calcite was exposed to HCl and was accessed by the acid. In detail, we compared the inner information (e.g. the reaction induced calcite dissolution and fluid dynamics) during the acid stimulation in these three cases: the *z*-axis (Fig. 7-4), *x*-axis (Fig. 7-5) and *y*-axis flooding (Fig. 7-6).

Here, we chose some representative reaction durations (marked with black spots in Fig. 7-2 and Fig. 7-3) to illustrate the inner calcite distribution and the fluid dynamics. For the *z*-axis flooding: 2.5 minutes, 5 minutes, 10 minutes, and 20 minutes (Fig. 7-4); for the *x*-axis (Fig. 7-5) flooding: 0.5 hours, 2.5 hours, 5 hours, and 6.5 hours; and for the *y*-axis (Fig. 7-6) flooding: 0.5 hours, 2.5 hours, 5 hours, and 7 hours.

In Fig. 7-4 (a)-(d), HCl was flooded through the coal core along the positive *z*-axis (axial plane). The calcite was dissolved quickly as the HCl was flooded through, where the unaffected calcite is marked in dark blue, the dissolved calcite is in red and the coal matrix is in light blue. At the 20 minutes, all the calcite has been dissolved, which is consistent with the results shown in Fig. 7-2. During this process, a *z*-axis connected pore network for free fluid flow has been generated at the 20 minutes and the volume percentage of the cleats has reached to the largest 2.84% (also observed in Fig. 7-3). Fluid dynamics was compared in Fig. 7-4 (e)-(h). These illustrations have clearly demonstrated the velocity field, where the fluid velocity through the cleats induced by dissolution of calcite has become significantly larger than that through the coal matrix. Particularly in Fig. 7-4 (h), a clear free fluid flow network along the *z*-axis direction was found through the connected cleats induced by the calcite dissolution, once a high connectivity of pore network (open cleats) along the *z*-axis was generated.

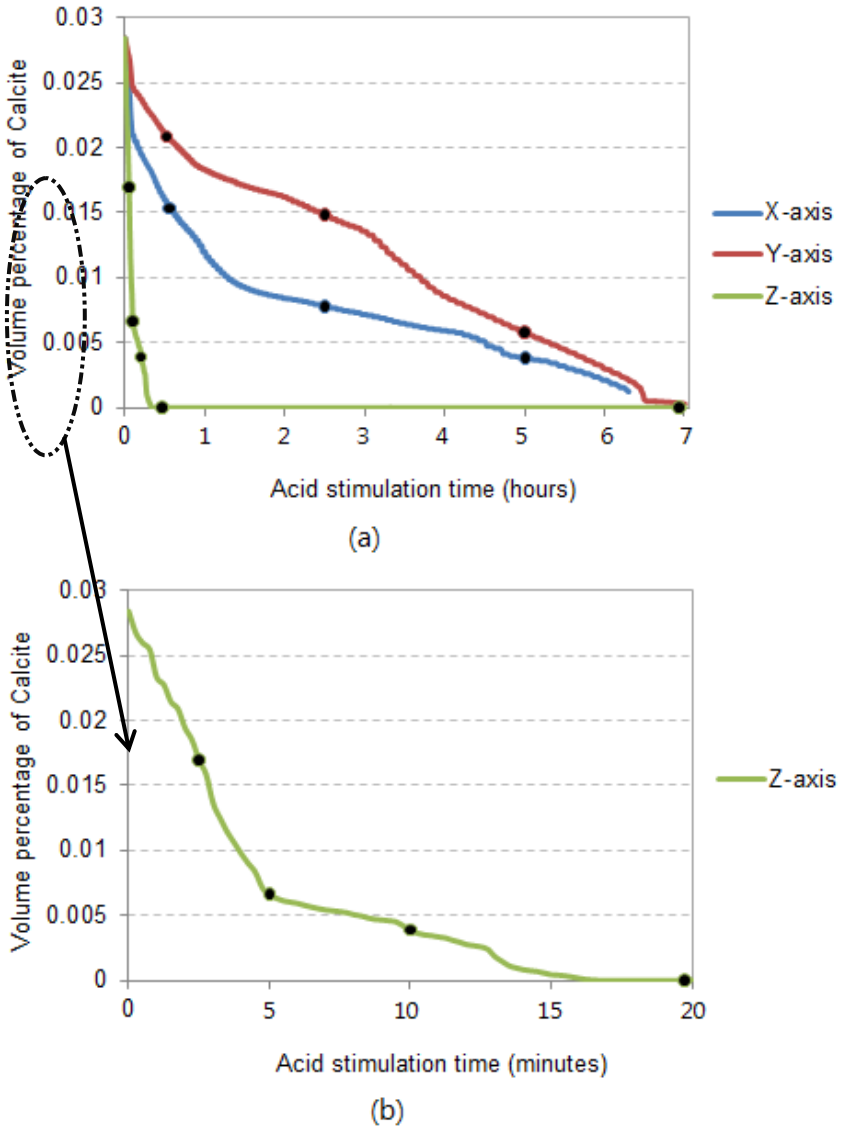

Fig. 7-2 Trend of the calcite dissolution in three flooding cases: the axial (*z*-axis), coronal (*y*-axis) and sagittal (*x*-axis) flooding.

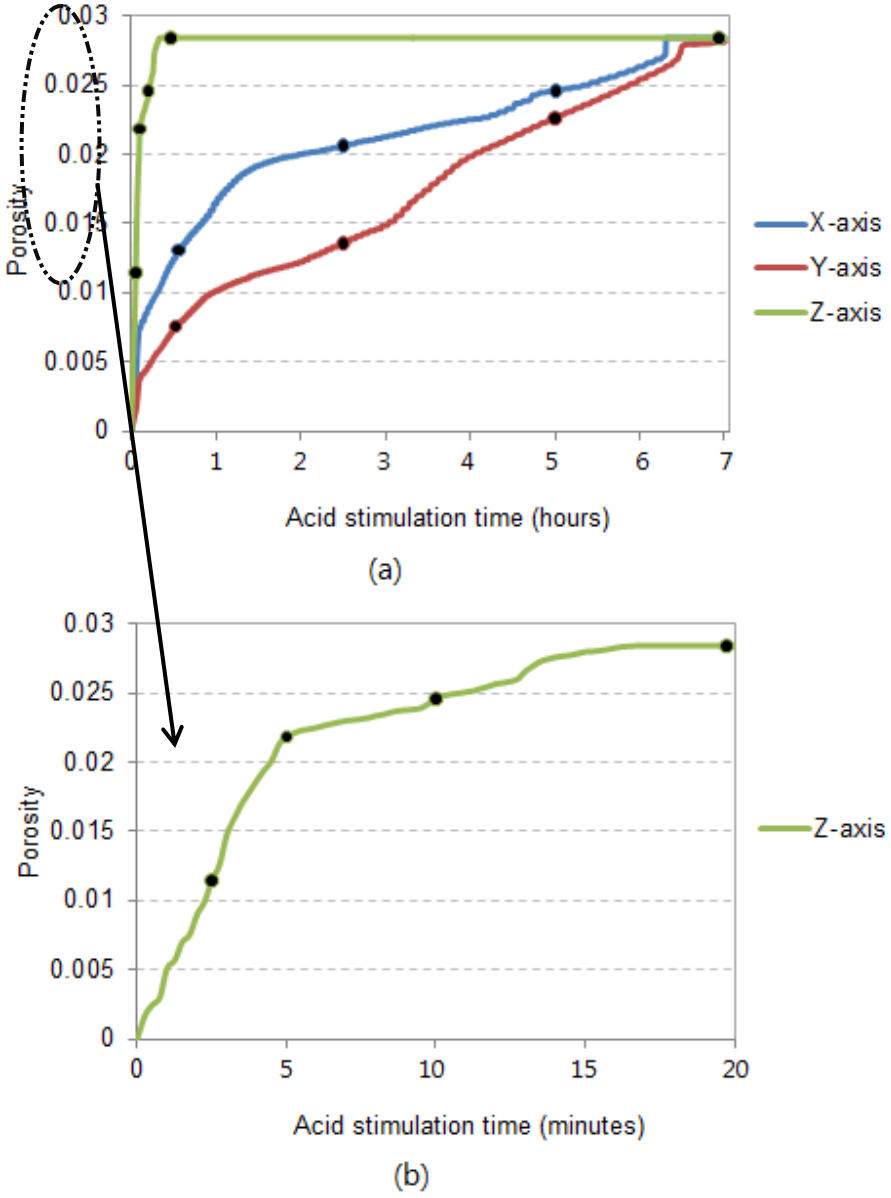

Fig. 7-3 Porosity change in three flooding cases: the axial (*z*-axis), coronal (*y*-axis) and sagittal (*x*-axis) flooding.

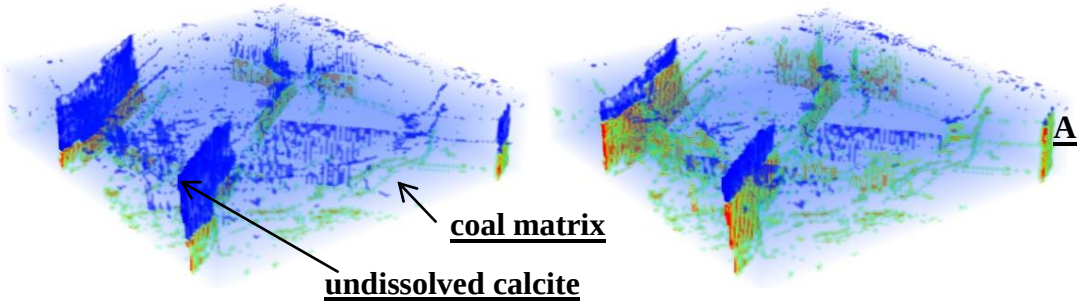

(a) at the 2.5 minutes (b) at the 5 minutes

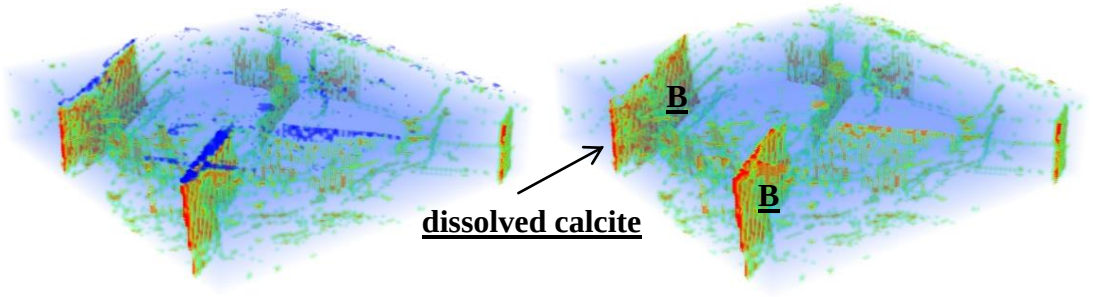

(c) at the 10 minutes (d) at the 20 minutes

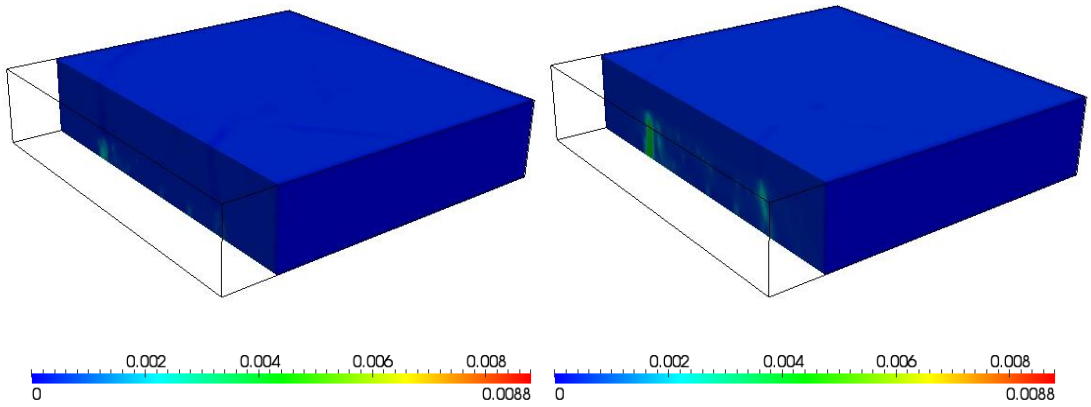

(e) at the 2.5 minutes (f) at the 5 minutes

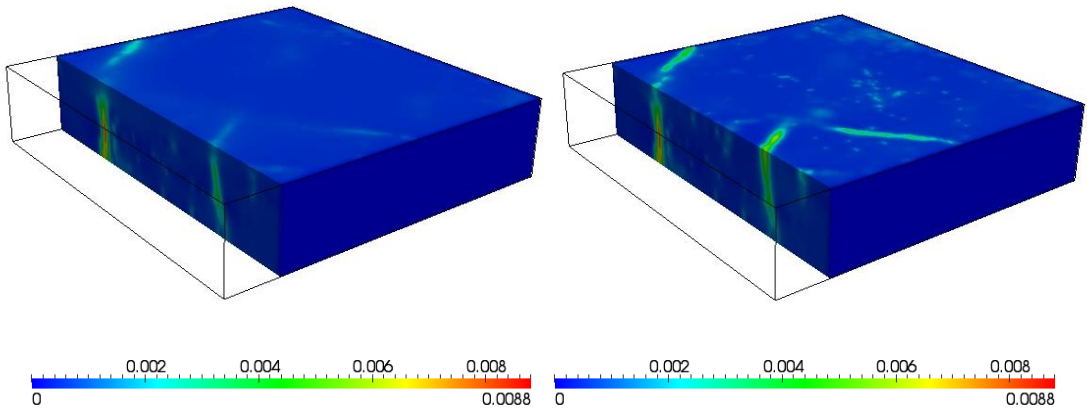

(g) at the 10 minutes (h) at the 20 minutes

Fig. 7-4 The *z*-axis acid flooding: (a)-(d) calcite distribution, and (e)-(h) fluid dynamics in different flooding durations (the velocity unit is 10^{-5} m/s).

Similarly in the *x*-axis acid flooding (Fig. 7-5 (a)-(d)), calcite was dissolved along the positive *x*-axis orientation and finally gone after 6.5 hours. According to the fluid dynamics in Fig. 7-5 (e)-(h),

the velocity reached to the peak value when all the calcite was dissolved after 6.5 hours, which was around 1/6 of that in the above z-axis flooding case. This is largely related to that there was no generation of an *x*-axis connected pore network for free fluid flow. Thus, large portion of the fluid transport was seepage through the coal matrix.

In the *y*-axis flooding case (Fig. 7-6), the dissolution was the slowest one, which has taken around 7 hours before the calcite was totally dissolved. This reflects a relatively poorer alignment of calcite filled cleats with the *y*-axis. The peak velocity then was observed to be around 1/8 of that in the *z*-axis flooding case. Also, there was no *y*-axis connected pore network for free fluid flow but only fluid flow as seepage through the coal matrix.

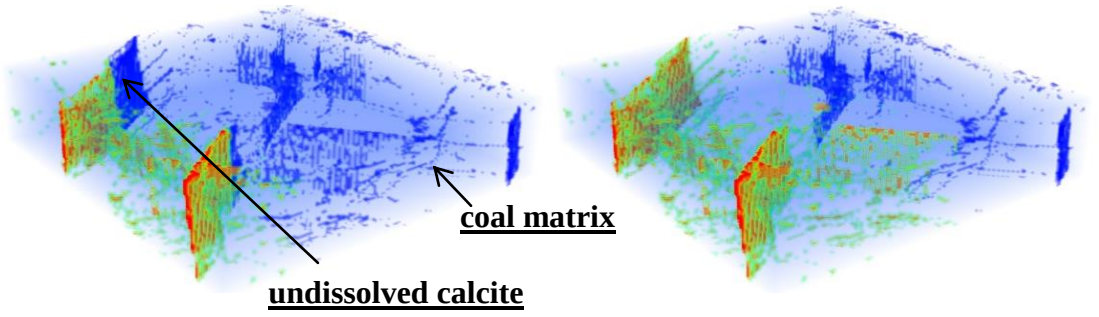

(a) at the 0.5 hours (b) at the 2.5 hours

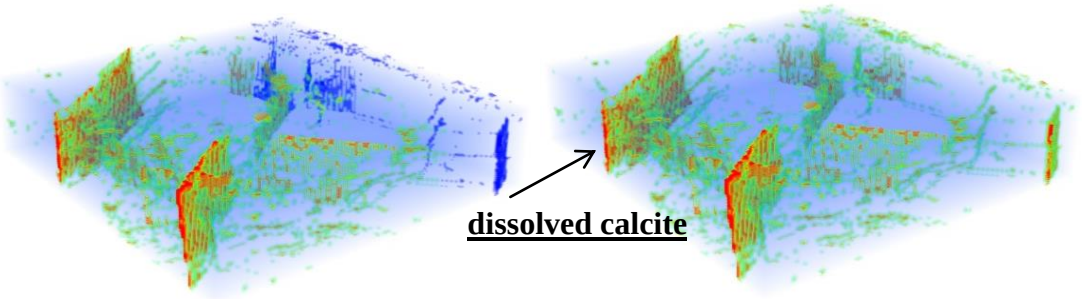

(c) at the 5 hours (d) at the 6.5 hours

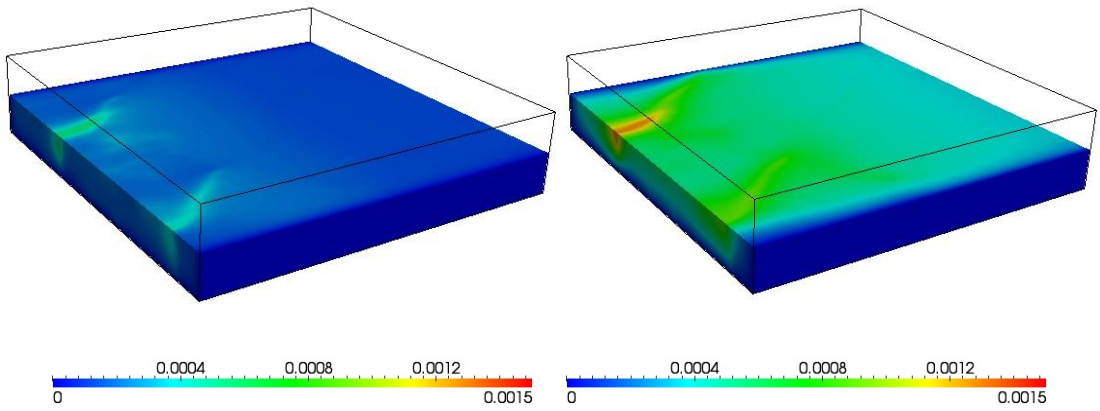

(e) at the 0.5 hours (f) at the 2.5 hours

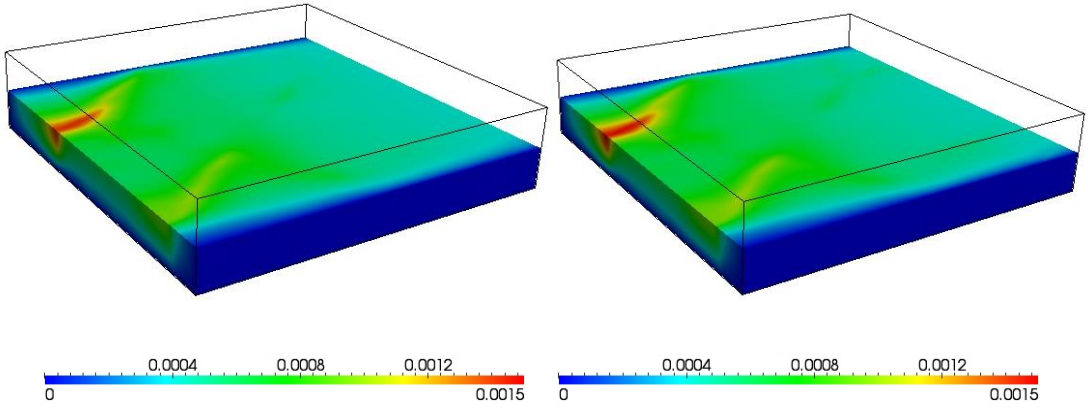

(g) at the 5 hours (h) at the 6.5 hours

Fig. 7-5 The *x*-axis acid flooding: (a)-(d) calcite distribution, and (e)-(h) fluid dynamics in different flooding durations (the velocity unit is 10^{-5} m/s)..

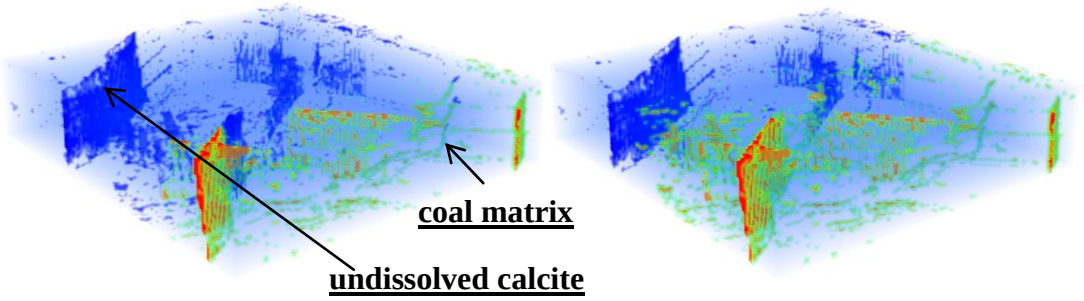

(a) at the 0.5 hours (b) at the 2.5 hours

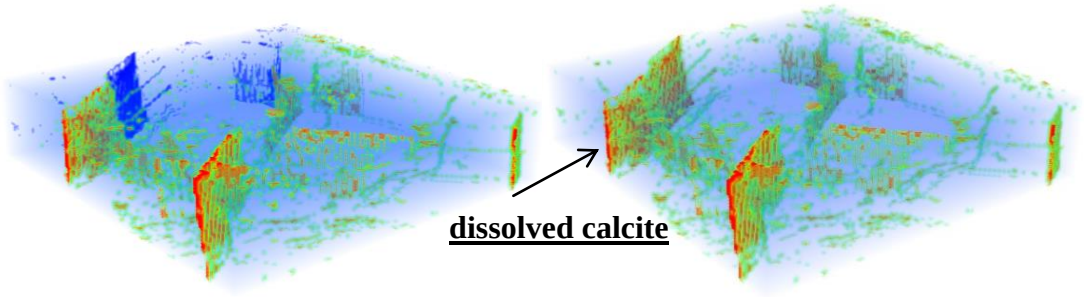

(c) at the 5 hours (d) at the 7 hours

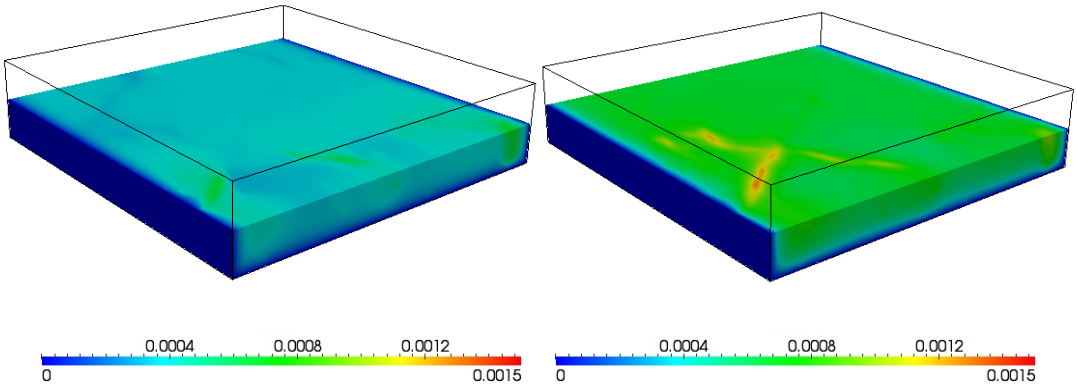

(e) at the 0.5 hours (f) at the 2.5 hours

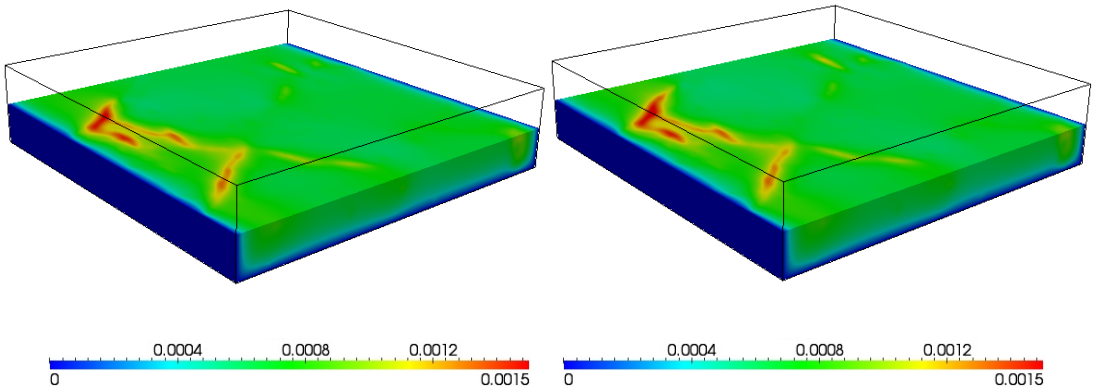

(g) at the 5 hours (h) at the 7 hours

Fig. 7-6 The *y*-axis acid flooding: (a)-(d) calcite distribution, and (e)-(h) fluid dynamics in different flooding durations (the velocity unit is 10^{-5} m/s).

These above analysis have demonstrated the changes of porosity and fluid dynamics over the temporal scale regarding the intrinsic *3D* anisotropy of the selected sample. This consequently results in the permeability change because the permeability is functionally dependent on these important intrinsic features of reservoir rocks. Here is the *4D* permeability analysis based on the above simulations (Fig. 7-7).

1) According to Fig. 7-7, the *4D* permeability has experienced an increase as the acid stimulation proceeds. In detail, the *x*-axis (Fig. 7-7 (a)) permeability remained around 0.2 *mD* reflecting the intrinsic permeability of the coal matrix. Then, after 6 hours, the calcite has been dissolved, which results in another relatively sharp permeability increment by 1.79 *mD* (from 0.2 *mD* to

1.99 *mD*) Similar conditions were found in the *y*-axis case, the permeability enhancement after the acid stimulation was from 0.2 *mD* to around 0.96 *mD* (an increment of 0.76 *mD*); and

2) along the *z*-axis orientation (Fig. 7-7 (b)), the coal sample experienced a sharp permeability increment from of 2.7 *mD* (from 0.2 *mD* to 2.9 *mD*) at the 5 minutes, the direct reason is the opening of a cleat through the *z*-axis orientation for free fluid flow as a result of calcite dissolution (marked as '**A'** in Fig. 7-4 (b)). Then, the permeability remained relatively constant for some 20 minutes when another two cleats were opened (marked as '**B'** in Fig. 7-4 (b)). This resulted in another permeability increment of 2.53 *mD* (from 2.9 *mD* to 5.43 *mD*).

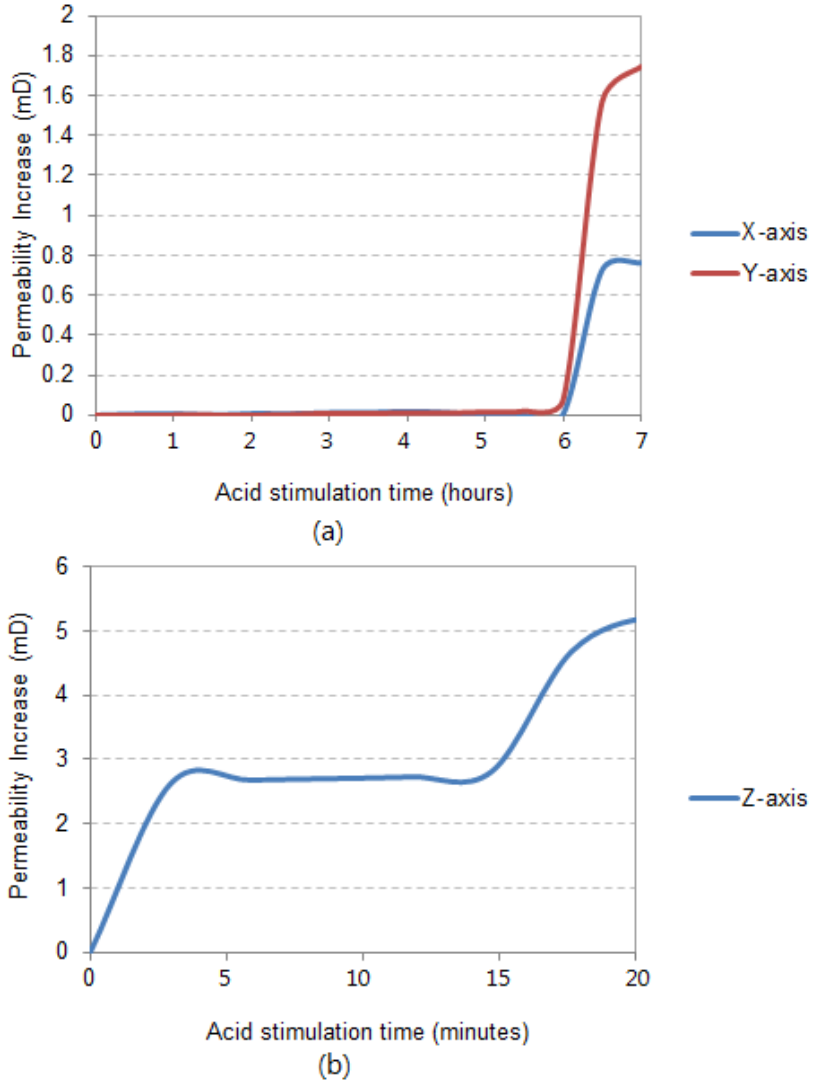

Fig. 7-7 The *4D* permeability evaluation of the coal sample in the three acid stimulation cases.

The HCl reaction occurs at the surface of the carbonate minerals, which induces generation of pore structure until a connected pore network is achieved. Accordingly, the conclusion can be drawn:

1) the calcite inside the coal core has been dissolved gradually, but this is directly dependent on the strong intrinsic anisotropy of the coal core at different orientations. This results in different

distributions of inner fluid dynamics, which hence dynamically changes the directional permeability;

2) the calcite-filled cleats were dissolved into connected open pore networks along the *z*-axis for the free fluid flow, while there is no connected pore network generated along the other two orientations so that only seepage of fluid flow in the coal matrix was found. This occurs because the alignment of the *x*-axis and *y*-axis with the calcite filled cleats directions is poorly observed, whereas these cleats are more alignment with the *z*-axis. Therefore, the permeability enhancement at the *z*-axis orientation occurred significantly when the calcite was dissolved; and
3) the above discussion about the strong anisotropy of the sample is proven by the fact that the calcite-filled cleats are mostly connected along the *z*-axis orientation (Fig. 7-1).

According to the application, the *4D* permeability is explored by studying the coupled **System (T, H, C)** at the pore scale and these permeability changes are largely dependent on the intrinsic anisotropy of different reservoir rocks. The analysis and evaluation of the *4D* permeability is conducted as a contribution of the thesis work for the fluid flow modelling in the subsurface petrophysical conditions, at the micron to centimeter scales.

7.3 Sample Size (Scale) and the Permeability

The permeability measured in lab experiments is at the plug scale but will be amplified at larger scales. For engineering purposes, permeability used for reservoir engineering is meant to be sample size independent. Hence, the study of sample size (scale) effect on the permeability measurement is essential. Then, a question is raised as to the sample size effect on the permeability evaluation? In this section, a pore scale permeability study is conducted to deal with this question: how to measure the *REV* scale permeability and also investigate the voxel size effect on the evaluation of the *REV* scale size in the numerical modelling.

7.3.1 Sample information

These plugs (Table.7-1) for lab experiment tests were collected from different depths of the Chinchilla 4 well in the Surat Basin, Queensland, Australia, which is a potential target for CO_2 geosequestration. They are identified as coming from the Evergreen Formation that is the proposed seal unit and the Precipice Sandstone that is the proposed reservoir unit (Golab, 2012; Farquhar et al., 2013; Gao et al., 2014b).

Name	*Depth (m)*	*Whole-rock mineralogy*		
		Major	Moderate	Minor / ± trace
Evergreen Formation	980.1	Quartz, albite	K-feldspar, kaolinite, chlorite	Muscovite ± carbonate, anatase
Precipice Sandstone	1207.6	Quartz	N/A	Kaolinite

Table.7-1 Mineralogy analysis of the two rock samples.

7.3.1.1 Evergreen Formation

The Evergreen Formation sample is a 4.164 *mm* diameter and 7.26 *mm* length core at the plug scale (Fig. 7-8). The composition of the sample is demonstrated within segmented *micro-CT* slices along different orientations at a voxel size of 3 *μm* to show the pore scale structure (Fig. 7-9). Most structures are filled with quartz grains (light gray), pores (black) and clay (dark gray), some small portion of high density minerals (white). This sample is from the Lower Evergreen Formation rather than the overlying low permeability siltstones and fine grained sandstones that are the seal rocks sensu stricto. The reconstructed digital Evergreen Formation sample involves a lattice grid of 1388 × 1388 × 2420 (around 4.67 billion grids) as the architectural input for the later dynamical modelling.

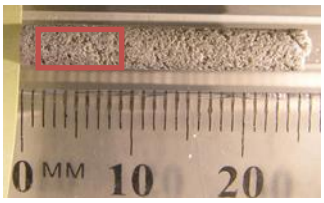

Fig. 7-8 Core photography of an Evergreen Formation sub-plug selected for high resolution *micro-CT* imaging (marked in red, 4.164 *mm* × 4.164 *mm* × 7.26 *mm*) (Golab, 2012; Farquhar et al., 2013; Gao et al., 2014b).

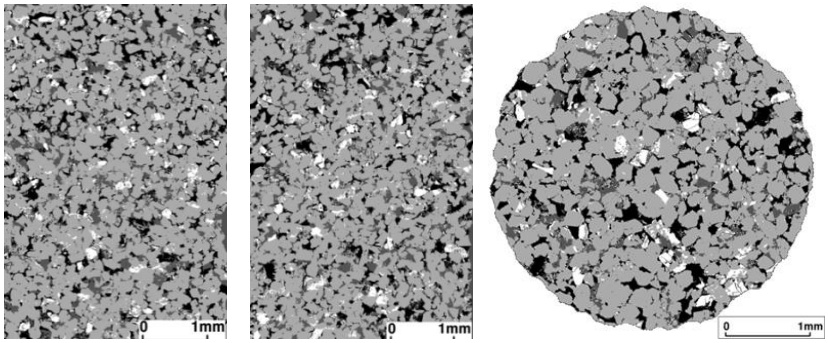

(a) (b) (c)

Fig. 7-9 Segmented *micro-CT* images of the Evergreen Formation sub-plug with composition distribution along three different orientations: (a) *x*-orientation, (b) *y*-orientation, and (c) *z*-orientation (voxel size as 3 μm): quartz grains (light gray), pores (black), clay (dark gray) and some small portion of high density minerals (white) (Golab, 2012; Farquhar et al., 2013; Gao et al., 2014b).

7.3.1.2 Precipice Sandstone

The Precipice Sandstone has been introduced in Chapter 4 as an application example (section 4.3). The sample has a size of 10.14 mm × 9.636 mm × 12.276 mm and is a typical core varying from coarse to medium-grained sandstone with laminations and a clear boundary between coarse-grained and medium grained sandstone (Fig. 7-10). The composition of the sample is demonstrated within segmented *micro-CT* slices along different orientations at voxel size of 6.6 μm (Fig. 7-11). Similar to the Evergreen Formation sub-plug, quartz grains (light gray) constitute the framework of the Precipice Sandstone, and some pores (black), clays (dark gray) and high density minerals (white) are also observed. Besides, clear anisotropy along the vertical orientation is seen through these *micro-CT* images. Moreover, the reconstructed digital sample has a lattice grid size of 1536 × 1460 × 1860 (around 4.17 billion grids).

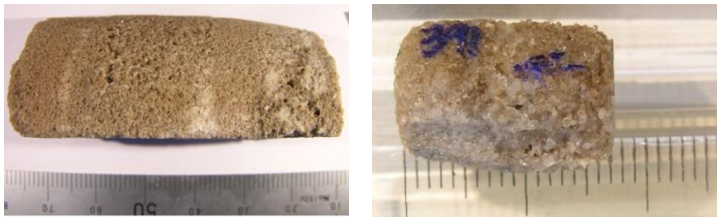

(a) (b)

Fig. 7-10 (a) Image of the original Precipice Sandstone sample as received state, (b) Core photography of the sub-plug retrieved for high resolution *micro-CT* imaging (the plug size is 10.14 *mm* ×9.636 *mm* ×12.276 *mm*) (Golab, 2012; Farquhar et al., 2013; Gao et al., 2014b).

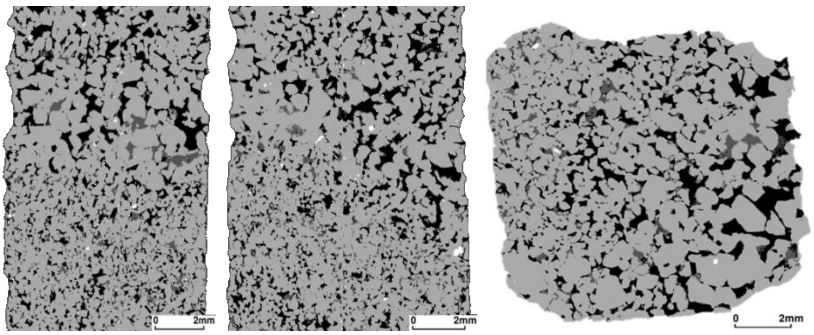

(a) (b) (c)

Fig. 7-11 Segmented *micro-CT* cross-sections of the Precipice Sandstone sub-plug with composition distribution along three different orientations: (a) *x*-orientation, (b) *y*-orientation, and (c) *z*-orientation (voxel size as 6.6 *μm*): quartz grains (light gray), pores (black), clay (dark gray) and some small portion of high density minerals (white) (Golab, 2012; Farquhar et al., 2013; Gao et al., 2014b).

7.3.1.3 Analysis of the pore connectivity

Notwithstanding that seepage occurs through some permeable geomaterials, pore connectivity is essential for fluid transport networks, which significantly affect the fluid dynamics and permeability measurement. Thus, the pore connectivity in these two rock samples is studied in this section.

These two samples have a highly connected pore network with an isometric view of the inner pore connectivity. Features clearly observed in the *micro-CT* images include that the pore radius of the Evergreen plug is around 15.7 ± 5.4 *μm* and the radius of pore network throats is around 7.6 ± 3.8 *μm*; the pore radius of the Precipice plug is around 40.5 ± 22.6 *μm* and the radius of pore network throats is around 25.3 ± 20.7 *μm*. These two plugs both have high pore networks with an isometric view of the inside pore connectivity in Fig. 7-12: the pore connectivity of the Evergreen plug reaches 94% and that of the Precipice plug reaches 97.7%; regarding the pore connectivity, the Evergreen plug shows weak anisotropy at the vertical orientation (Fig. 7-12 (a)), but the Precipice plug shows strong vertical anisotropy (Fig. 7-12 (b)).

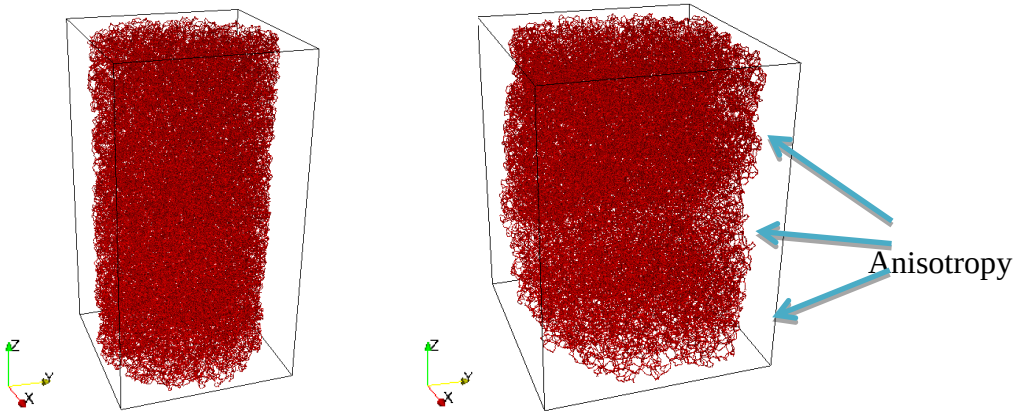

(a) (b)

Fig. 7-12 Pore connectivity of the two samples: (a) the Evergreen Formation sample and (b) the Precipice Sandstone sample.

The directional permeability tested in this case is along the vertical orientation (*z*-axis), thus, the pore connectivity along the vertical orientation is first studied in this section. Meanwhile, due to the high pore connectivity in these two samples, the porosity that is similar to the pore connectivity distribution is employed to compare the pore connectivity at each vertical cross-section (Fig. 7-13). It is observed that:

1) the Evergreen sample (Fig. 7-13 (a)) shows slight cross-sectional porosity fluctuation around 0.14 ± 0.02 as the sample length increases until it reaches the 4 *mm* scale; and then it experiences a decline of cross-sectional porosity to 0.089 at the sample length between 4.6 *mm* and 4.8 *mm*, which relates to the narrow pore connectivity in this area. Then, from 4.8 *mm* to 7.26 *mm*, it shows a porosity fluctuation in the range of 0.09 to 0.15. This confirms the anisotropy of the Evergreen sample along the vertical orientation that will affect the directional permeability measurement; and
2) the Precipice sample exhibits a significant cross-sectional porosity change along the vertical orientation. In the first 4 *mm* length, the porosity remains at a high level around 0.2, but from the 4 *mm* to 6 *mm* length it experiences a decrease and fluctuates around 0.16. Then from the 6 *mm* to 10 *mm* length, the cross-sectional porosity decreases and fluctuates around 0.115. This confirms the existence of a clear observed anisotropy from the coarse to medium grained region along the vertical orientation, and also less pore connectivity around 6–10 mm length, which confirms the observation in Fig. 7-12 (b).

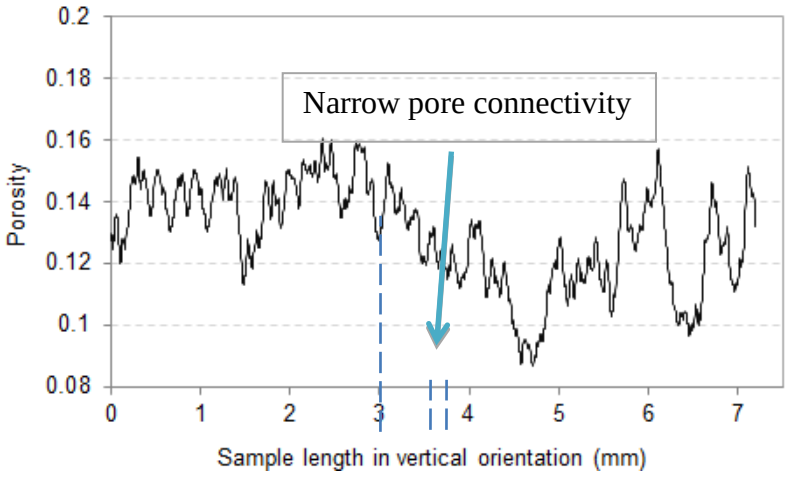

(a)

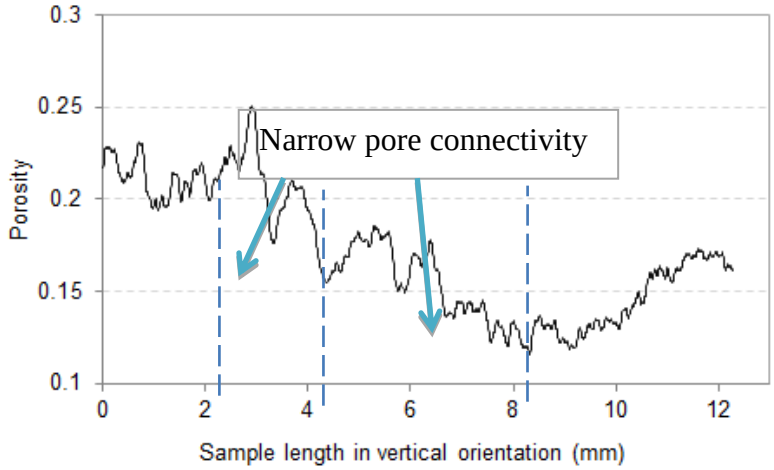

(b)

Fig. 7-13 Porosity distribution at each cross-section along the vertical orientation of the sample (sample length): (a) the Evergreen Formation sample and (b) the Precipice Sandstone sample.

7.3.2 Simulation results and discussion

7.3.2.1 Sample size effect on the permeability measurement

When referring to sample size or scale effect on the permeability, for the vertical permeability measurement in this case, both the horizontal cross-sectional area and the vertical length of the sample are required for consideration.

We first compare the sample length effect on the vertical permeability (Fig. 7-14). As shown, countable tests are chosen for different sample lengths:

1) the permeability decreases as the sample length increases in both cases, with a slight drop in the Evergreen sample (Fig. 7-14 (a)) and a sharp drop in the Precipice sample (Fig. 7-14 (b)). In detail, the vertical permeability of the Evergreen sample reduces by around 8% as the sample

length increases from 1.8 *mm* to 7.26 *mm*. Specifically, there is a 6% permeability drop when the sample length reaches 4.6 to 4.8 *mm*, which is likely due to the narrow pore connectivity observed in Fig. 7-13 (a); and

2) the vertical permeability of the Precipice sample reduces by around 38% as the sample length increases from 2 *mm* to around 12 *mm* (Fig. 7-14 (b)). The first 2 *mm* to 4 *mm* section results in around 5% permeability drop due to the cross-sectional porosity decrease from 0.2 to 0.16 in this area; while a sharp decrease of about 33% of the vertical permeability is observed as the sample length is larger than 6 *mm*, which is due to this sub-plug having narrow pore throats and a less connected pore network from 6 *mm* to 10 *mm* length scale.

Regarding the permeability analysis, it also indicates the anisotropy in these two samples: the Evergreen sample shows weak anisotropy along the vertical orientation. In particular, from the 1.8 *mm* to 4 *mm* length, the permeability maintains a stable value. In contrast, the sharp vertical permeability change represents the strong anisotropy of the Precipice plug along the vertical orientation.

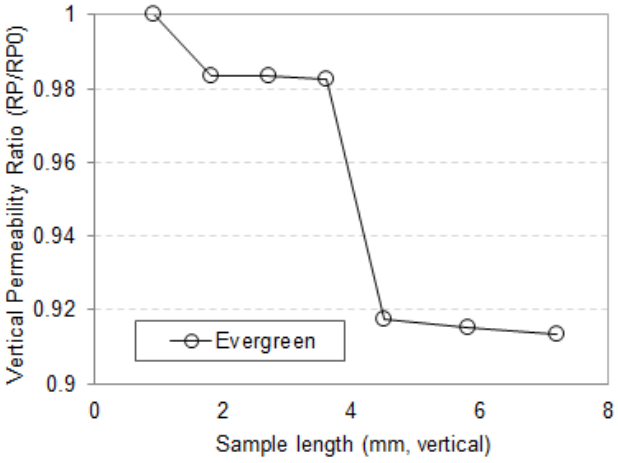

(a)

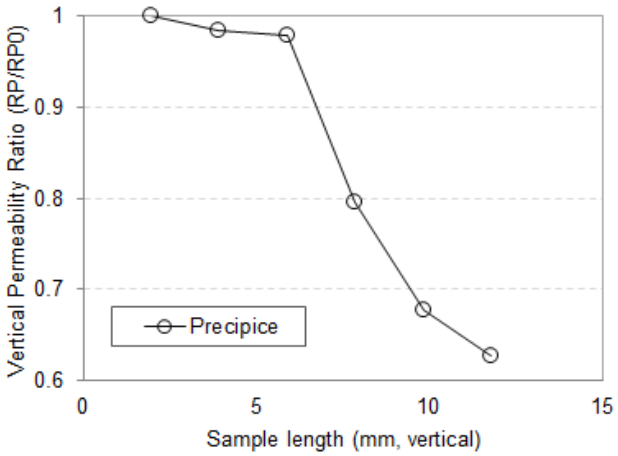

(b)

Fig. 7-14 Vertical permeability tested under different sample lengths: (a) the Evergreen sample, and (b) the Precipice sample.

Besides, we studied the effect of the horizontal cross-sectional area on the vertical permeability. If the permeability fluctuates sharply with large amplitude as the sample cross-sectional area changes, it indicates strong anisotropy at the horizontal orientation, and vice versa. In Fig. 7-15 (a), the dashed line shows the permeability distribution when the Evergreen sample has a horizontal cross-sectional area of 0.81 mm^2. For the 9 cases tested, the permeability fluctuates in a small range from 0.12 *Da* to 0.16 *Da*. The solid line shows the measured permeability when the cross-sectional area is increased to 2.43 mm^2 (6 cases tested) where the amplitude of the permeability fluctuation is somewhat weak varying from 0.13 *Da* to 0.145 *Da*. When the larger cross-sectional area of 7.29 mm^2 is chosen, the permeability measured is 0.145 *Da*. The test results largely depend on the intrinsic features of different samples, and shows the permeability results converge as the cross-sectional area gets larger, which means the Evergreen subsamples have only weak horizontal anisotropy.

In the Precipice sample case, the permeability tested in the cross-sectional area of 3.86 mm^2 (9 subsamples) varies from 0.3 to 0.38 *Da*. When the area is increased to 11.59 mm^2, the permeability fluctuates between 0.33 and 0.36 *Da* with slight convergence. With a larger cross-sectional area of 34.76 mm^2, the permeability is 0.35 *Da*. Similarly to the Evergreen sample, the Precipice subsamples also show weak horizontal anisotropy.

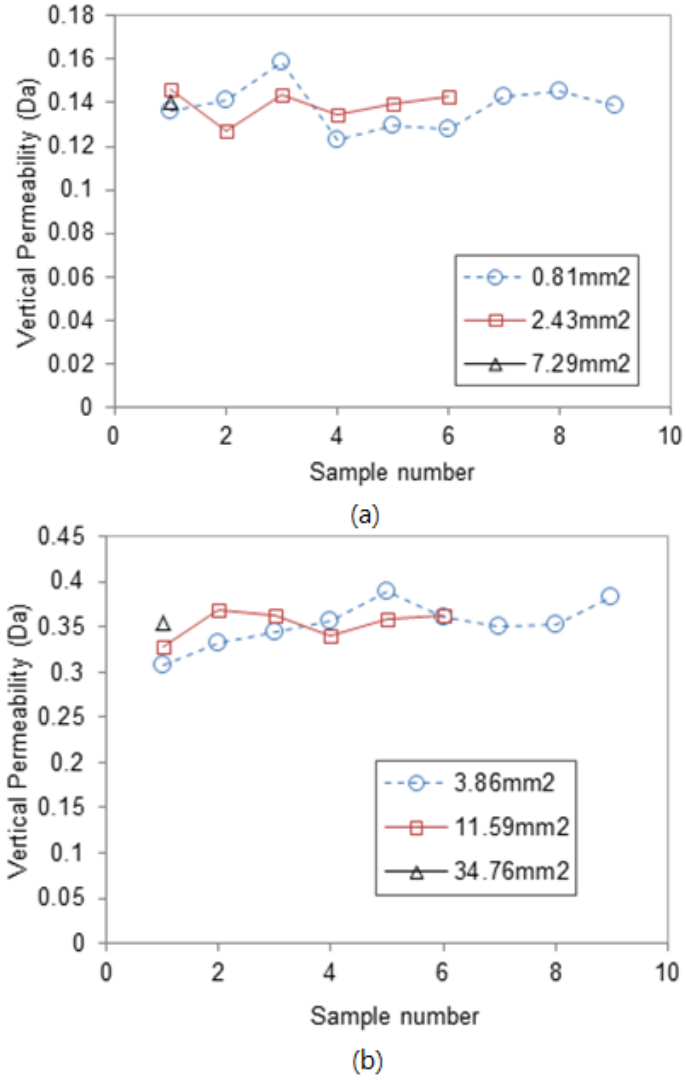

Fig. 7-15 Effect of horizontal cross-sectional area on the vertical permeability: (a) the Evergreen Formation sample and (b) the Precipice Sandstone sample.

The test results for both these samples show that the *3D* permeability tends to decrease when the sample length increases, which is consistent with the process of the *REV* scale measurement. As the sample size increases, the *3D* permeability experiences a decline; once the sample length reaches the *REV* size, the permeability will approach a relatively constant value due to that the resistance force reaches steady. Compared with these two samples, the *REV* scale evaluation requires even larger samples for a full view.

7.3.2.2 Evaluation of the *REV* scale permeability

There is currently limited capacity for upscaling from the pore scale (which is physically where changes occur) to the laboratory scale (where measurements of properties are typically done), and to the field scale (simulations that are operationally important).

Analysis at the *REV* scale aims to investigate the characteristic value of the geometric information and fluid transport, so that it can further represent the macroscopic dynamic pattern. Hence the characteristic information at the *REV* scale is an essential input for correct macroscopic depiction in reservoir or field scale engineering. In order to measure the *REV* scale permeability for different reservoir rocks, the sizes of samples used for the lab experiments are normally around a length scale of several tens of millimetres or more. This raises an important question as to what minimum sample scale (size) is necessary to retain physical structure fidelity (e.g. pore size and tortuosity) and provide representative transport calculations (e.g. directional permeability) for comparison and validation against laboratory characterizations. Here, we study the effect of sample size (vertical length in this case) on the flow character – permeability, and then define how to measure the effective *REV* size (using the Precipice sample as an application). Besides, in consideration of the *micro-CT* voxel resolutions effect on the numerical simulations, we also compare the simulation results under three *micro-CT* voxel sizes: 6.6 μm, 13.2 μm and 33μm for the Precipice sample case.

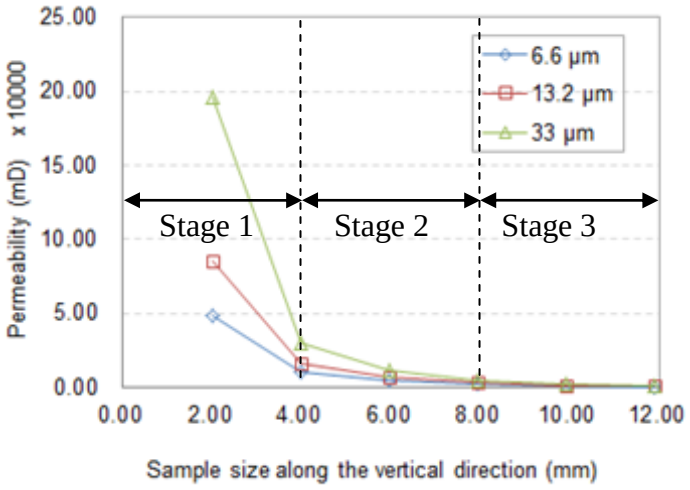

Fig. 7-16 Trend of permeability change at different sample scales (effect of different *micro-CT* voxel sizes at 6.6 μm, 13.2 μm and 33 μm is considered)

Directional permeability values of the Precipice sample when different sample sizes are selected for the measurement are shown in Fig. 7-16:

1) In the 6.6 μm case, the vertical permeability drops sharply from 48.2 to 10.4 *Da* when the sample size is smaller than 6 *mm*, and approaches around 0.82 *Da* as the sample size reaches 10 *mm*. Similar permeability increase are obtained when voxel size is coarsened, where the directional permeability is somewhat higher when it reaches the stable value (1.22 *Da* for 13.2 μm case and 1.90 *Da* for 33 μm case). Therefore, we conclude that 10 *mm* is an appropriate size for the *REV* scale of this sandstone material; and

2) Large sample scales (e.g., >10 *mm REV*) can be used for simulations in *REV* or larger scales with the usage of representative parameters (directional permeability). When the sample size is smaller than 5 *mm*, especially around 1 or 2 *mm*, the directional permeability in 13.2 and 33 μm cases are around 85.5 and 196.2 *Da* respectively. These values are much higher than that in the 6.6 μm case (48.2 *Da*). Coarsened voxel size cases can provide similar *REV* scale size as the small voxel size case (6.6 μm) does, but affect the directional permeability value due to the loss of microstructures fidelity. However, when the sample size is significantly smaller than the *REV* size, even higher voxel resolution (smaller voxel size) cannot retain the representative physical structure fidelity (e.g., pore size, grains of matrices and connectivity).

We conclude that 10 *mm* is an appropriate size for the *REV* scale of this sandstone material. On one hand, larger sample scales (e.g. > 10 *mm* representative) can be used for simulations at the *REV* scale or larger scales with the usage of *REV* scale parameters (directional permeability). In this case, the voxel resolution affects the permeability value but not the trend. Coarsened voxel resolution cases (13.2 μm and 33 μm) can provide similar *REV* scale size as the small voxel size case (6.6 μm) does, but they affect the directional permeability value due to the loss of microstructures information. However, this depends on the intrinsic character of the sample. For instance in some cases, excessively coarsened voxel resolution in small sample cases has resulted in severe loss of the internal structure information in the porous medium, such as information of pore throats. This affects the distribution of pore networks and consequently the fluid dynamics and resultant permeability evaluation. The study confirms the importance of the higher resolutions of *micro-CT* scans in pore scale studies. On the other hand, when the sample size is rather smaller than the *REV* size, even higher voxel resolution cannot retain the representative physical structure fidelity (e.g. pore size, grains of matrices and connectivity).

7.4 Conclusions

Upscaling from pore scale to laboratory scale and to field scale remains a challenging and unsolved area of research. Conventionally, geomaterial parameters (e.g., porosity and permeability) at the representative scale are defined based on the experiments as well as statistical correlations, and then averaged and upscaled to the grid blocks used in field scale or reservoir scale simulations. This chapter provides an integrated study from the pore scale coupled processes to the representative scale (*REV)* permeability, which provides a possible averaging method for upscaling the flow physics from pore scale to laboratory scale and even field scale. It uses the proposed parallel *XLBM* in two applications with sedimentary rocks and coals for: *4D* permeability evaluation, sample scale

(size) effect and *REV* scale permeability measurement. Through these studies, a link between the pore scale and the *REV* scale has been established:

1) It is confirmed that the measured permeability gradually approaches a constant value when the sample size reaches the *REV* scale or larger;
2) the critical sample size (the smallest size providing reliable and representative transport calculations) is defined as the corresponding *REV* sample size for upscaling purpose;
3) the *REV* scale is larger than the pore scale but much smaller the field or reservoir scales;
4) characterization of effective *REV* scale permeability largely relies on the geometry information, thus he relationship between the anisotropy and the permeability is also studied, where sharp permeability changes represent strong anisotropy, and vice versa. For some similar rocks with weakly anisotropy, it is possible to use the *REV* scale parameters for upscaling reference; However for highly anisotropic and heterogeneous rocks, lower-scale modelling is compulsory to find reasonable *REV* scale parameters.

Chapter 8 Conclusions and Recommendations

8.1 Conclusions

The study of fluid dynamics in subsurface systems is an essential aspect of reservoir engineering (e.g. gas or oil, carbon geosequestration, geothermal electricity and heating), mining engineering and environmental science issues related to underground water. In this context, the nonlinear flow behavior has been recognized as a crucial factor in fluid flow through porous and fractured reservoir rocks that may be influenced by the heat transfer and chemical reactions.

To fundamentally address these coupled **System (T, H, C)** problems and develop insight into seemingly differing geological problems at the pore scale, this thesis work proposes a multi-disciplinary approach by applying and extending the lattice Boltzmann method for the solutions. It provides a unified and expandable framework (a numerical parallel *XLBM* model) that covers a range of topics spinning from the modern imaging technology, numerical algorithms and equations, and advanced parallel computing. It is applied to three geological processes in heterogeneous porous media at the pore scale: namely, fluid transport (**H**), heat transfer (**T**), and chemical reactions (**C**).

8.1.1 Fluid transport (H)

In chapter 3, an *eXtended LBM* (*XLBM*) model was introduced and developed in *C++* as a starting framework. In the numerical algorithm, the generalized Bhatnagar-Gross-Krook (BGK) *LBM* equation was employed for the evolution of basic fluid transport. The Kozeny-Carmon (k-C) equation was used to describe the pore scale parameters (e.g. the geometric function related to geomaterial features). Then, the model was extended and furthered by adding the material localization method, multiple contact boundaries and the statistics theory. This custom extended model enables more advanced study of fluid transport in diverse heterogeneous geomaterials, where each constituent has its own hydraulic properties. Both *2D* and *3D* equations were introduced in Chapter 3, and the model was verified through benchmarking.

According to these studies, the effect of geometric information and geomaterial properties on the pore fluid flow detail was concluded as: (1) the external force was the main reason for leading flow dynamics, and the flow dynamics were also significantly affected by geomaterial properties; (2) no fluid flow was observed through the impermeable aggregate, whereas fluid flowed faster through pores due to the zero resistance force in these areas; and (3) a lower-speed fluid flow was observed in permeable geomaterials compared with that in pores, which may significantly change the flow

pattern in the whole domain. This level of investigation of pore fluid flow is beyond the capability of the conventional *LBM*. The simulation results demonstrate a possible approach for quantitatively describing complex fluid flow through multiple-matrix constructed heterogeneous porous media. This can be applied to scientific issues for the fundamental fluid transport (**H**) and complex fluid-matrix contacts at the pore scale. The work serves as the basis for more advanced study of the coupled **System (T, H, C)** problems as below.

8.1.2 Heat transfer (T)

In Chapter 5, the numerical *XLBM* platform was updated by embedding the extended double-distribution function governing equations for the pore scale coupled **System (T, H)** modelling. The generalized macroscopic governing equation for heat transfer in incompressible fluids and solids are specified, where the heat capacity and the effective thermal diffusivity depend on the intrinsic features (e.g. geometry and geomaterials) of the porous media. The thermal equations are capable of determining the evolution of heat transfer through multiple geomaterials involving pore structures and materials with respective intrinsic permeability. Similar to that in the fluid flow (**H**) field, each lattice node also has its own thermal property due to the description of material localization. This thermal module is firstly validated by a benchmarked test (natural convection in a square cavity), and then applied in two pore scale geothermal cases.

These application examples were studied for: (1) the effect of intrinsic pore scale geometry and geomaterials on the heat distribution; and (2) the heat transfer and fluid transport interactions with each other at the pore scale. Prandtl and Rayleigh numbers were employed here to describe the relationship between the fluid transport (momentum transport) and the heat transport. Based on the simulation results, the following conclusions were drawn: (1) the free convection or natural convection induced by the buoyancy under higher Rayleigh (*Ra*) numbers affected the heat transfer process. In small *Ra* cases, the heat transfer was mainly shown as conduction; when it got larger, the heat transfer became convection; (2) the presence of a temperature gradient resulted in significant fluid transport, such as fluid vortices in a closed cavity. Moreover, temperature can stimulate the seepage phenomena in certain permeable geomaterials; and (3) the evolution of temperature inside multiple geomaterials occurred very differently because of the influence of different intrinsic geometry and geomaterial distributions. In detail, materials with higher porosity tend to have a higher heat capacity, where heat can conduct and reaches the equilibrium status in a relatively shorter time. An extreme condition is the very rapid heat transfer through pore structures, whereas it may take more time to transfer through an impermeable solid.

These studies demonstrated the geothermal *XLBM* is capable of simulating heat transfer and its interactions with fluid dynamics through both permeable and impermeable matrix cases in diverse porous media, where there may be no connected pore networks observed at a certain resolution but connected at a higher resolution.

8.1.3 Chemical reactions (C)

A generalized geochemical *XLBM* Model for surface reactions in both *2D* and *3D* pore scale heterogeneous porous media with multiple minerals was developed in Chapter 6. This includes studies of: (1) comprehensive equilibrium reactions and kinetic reaction rate laws for describing the reaction status (e.g. equilibrium, dissolution or precipitation); (2) reaction species for setting up a reaction distribution function for different species, which also was coupled with the fluid transport and heat transfer functions; (3) surface reactions on the reactive minerals that correlates the kinetic reaction rates with the reactive solid-phase mass transfer. The model was firstly verified against results from a CO_2-water-rock interaction experiment carried out by the University of Queensland (Farquhar et al., 2014), and then for a possible prediction of long-time reactions.

According to the simulation results, it is shown in the modelling that: (1) the reaction concentrated in the region at contact surfaces with the acidic fluid (carbonic acid), where most of dissolution occurred at the edge of sample and some carbonic acid penetrated towards the center of the sample along the dissolved cleavages between the main aggregate and other non-reactive minerals; (2) the calcite has been dissolved very quickly in the first few weeks and then experiences a gentle dissolution stage, which was largely related to the reaction front meeting numerous small calcite-cemented areas or narrow cleavages that has slowed down the dissolution progress; and (3) the modelling system reached the reaction equilibrium status in around 1440 days, and brought a porosity enhancement from 1.1% to 10.7%. Around 7.4% of the calcite is un-affected due to the lack of connectivity with the open pores or other dissolved calcite structures, where the carbonic acid hardly can access.

The simulation shows the capability of the proposed geochemical model for describing the coupled processes of solute reaction transport, fluid interaction with the frontier solid surfaces, and solid skeleton dissolution at the pore scale linking with the porosity change. Based on the studies, the model can be applied in analyzing the acid fluid interactions on reactive and non-reactive mineral surfaces, solid-phase dissolution and mass transfer, and resultant porosity change. Moreover, it can be extended to study the simultaneous presence of chemical reactions with reactive minerals, multiple reactive minerals with disparate reactivity rates, and to provide predictive simulations

beyond the limitation of experiment duration. More importantly, it has provided thermal and chemical reaction (dissolution/precipitation) effects in ways that honor subsurface petrophysical conditions at the temporal scale.

8.1.4 Parallel *XLBM* and massive data sets processing

All the modelling work in this thesis was implemented on the custom *XLBM* platform (see Appendix-B for detail) for compatible parallel computing on supercomputers (introduced in Chapter 4). This was to address the key issues including massive *3D* data sets processing and its large scale simulations with respect to high-resolution digital samples. In detail, a special Input Preparation module as pre-processing was designed for reconstructing and re-decomposing massive data sets into required blocks; an effective parallel computing and data communication scheme as Run-time Control; and a memory-saving scheme for effective data management and visualization. Through various benchmarks and practical applications, the effective implementation of parallel computational platform *XLBM* has achieved a nearly-linear speedup and nearly-orthogonal extensibility (scalability), and it is effective to handle massive data sets from *Gigabytes* to *Terabytes* or even more as an initial input in high-resolution or large scale computational analysis. The computing efficiency still reaches around 93.8% when 512 processors are used, which confirms the high scalability of the custom *XLBM* and provides capability for massive data sets analysis.

The studies have shown that the proposed computational *XLBM* model and algorithm is a powerful tool for modelling coupled nonlinear processes of fluid flow, heat transfer and chemical reactions in the heterogeneous and anisotropic porous media. Besides, the model also strengthens the capability of determining reliable permeability values in seemingly different geological problems.

8.1.5 Applications of the coupled (T, H, C) problem

Notwithstanding the thesis has focused more on the pore scale coupled issues, we also provided a possible link between the pore scale and the macroscale. To investigate and describe the resultant effect of pore scale coupled (**T**, **H**, **C**) processes on the macroscale, a permeability study has been conducted in Chapter 7 for the solutions through practical applications in *4D* permeability measurement and analysis of the sample scale (size) effect on the evaluation of the *REV* scale permeability.

8.1.5.1 *4D* permeability measurement

This was an integrated permeability study based on the pore scale coupled **System (T, H, C)**. The term, *4D* permeability, considers the coupled **System** (**T**, **H**, **C**) effect on the dynamical *3D*

permeability (relates to the *3D* anisotropy in the reservoir rocks) over the temporal scale (fourth scale). A practical coal core acid stimulation was modelled for the *4D* permeability study. Through the application, it was concluded that: (1) the reaction first occurred at the contact surface of calcite with the carbonic acid, where the calcite inside the coal core was dissolved gradually and resulted in the generation of pore structure until a connected pore network was achieved; (2) the reaction was directly dependent on the strong intrinsic *3D* anisotropy of the coal core. In detail, the calcite-filled cleats were dissolved into connected open pore networks along the *z*-axis for the free fluid flow, whereas there was no connected pore network generated along the *x*-axis and *y*-axis where only fluid flow seepage in the coal matrix was found; and (4) the permeability enhancement at the *z*-axis orientation consequently occurred significantly when the calcite was dissolved.

Notwithstanding the case was specified as a coal acid stimulation case, this can be extended to seemingly different issues, where *4D* permeability in the heterogeneous porous media with diverse geomaterials, complex geometry and tortuosity, can be modelled and evaluated at the pore scale through the *XLBM* model.

8.1.5.2 Sample scale (size) effect and the *REV* scale permeability

For the sample size effect, we investigated whether the permeability is dependent on the sample scale and how to determine the *REV* size effectively. Both the horizontal cross-sectional area and the vertical length of the sample were taken into consideration. This study looked at the relationship between the anisotropy and the permeability and showed that sharp permeability changes with different sample sizes represent the strong anisotropy of the targeted samples, and vice versa. The work confirms the assumption that the measured permeability gradually approaches a constant value when the sample size reaches the *REV* scale or larger; and the critical sample size that provides the *REV* scale permeability is defined as the corresponding *REV* sample size. This provides a possible averaging method for upscaling the flow physics from pore scale to Representative Elementary Volume (*REV*) scale. According to these studies, a link between the pore scale and the *REV* scale has been established.

8.2 Future Work

Future work for coupled problems is to extend the numerical algorithm by adding more complex parameters (e.g. different fluid properties or kinetic reaction rates) to the coupled **System (T, H, C)** problem, and multiple chemical reactions for various practical scenarios, which would advance simulations of realistic reservoir behavior in nature. Besides, a relative permeability study regarding

multicomponent and multiphase problems, and desorption and adsorption in the porous media are also essential for building a robust numerical model for realistic pore scale modelling.

Notwithstanding the correlations between my results and experimental results have been discussed in this thesis work, the ongoing work on this topic will bring more complexity to the current model including comprehensive direct observation and validations at the pore scale. Integrating more sophisticated mathematical equations and controlling parameters in my models will enable to faithfully simulate the coupled issues that control petrophysical features.

Appendices

Appendix-A: Summary of Samples and Their Origins

All the sandstone samples used in this thesis were collected from the GSQ Chinchilla 4 stratigraphic fully-cored borehole. The well site is situated in the Surat Basin (Queensland, Australia), which extends from southeast Queensland into northern New South Wales. Fig. A.1 has illustrated the geological setting of the Surat Basin, well locations and subcrop map. The Surat Basin exhibits diverse mineralogy and has been an important target for hydrocarbon exploration in the past century. Nowadays, the Surat Basin is a potential site for CO_2 sequestration. It is located in southeast Queensland and extending into northern New South Wales (Australia), and exhibits considerably different mineralogy. Significant bodies of units in the Surat Basin have been identified as potential reservoirs for CO2 storage, especially the Precipice Sandstone. It is a relatively clean primary reservoir and geochemically poorly reactive with a clean, quartzose mineralogy dominated by quartz and kaolinitic clays. These clays coat grains and partially fill pores, having formed from the extensive leaching of unstable feldspars and lithics, and are commonly associated with Fe-oxide/hydroxide (Farquhar et al., 2014).

The Precipice Sandstone has been identified as a potential reservoir for CO_2 storage, with the overlying Evergreen Formation acting as a primary seal, and Hutton Sandstone acting as either a secondary seal or else another reservoir in its own right, depending upon local lithology (Fig. A.2).

This study focused on three units in the Surat Basin system: the Precipice Sandstone, Evergreen Formation and Hutton Sandstone. In detail (see Fig. A.2), the Precipice Sandstone is a relatively clean primary reservoir for CO_2 storage, which is overlain by a variably fine-grained, low-permeability Evergreen Formation as a seal cap-rock. The Hutton Sandstone is a heterogeneous, internally baffled reservoir that serves as a secondary seal over the Evergreen Formation. Here, we briefly summarize the features of these three units (see Table A.1) and three sandstone samples used in this thesis (see Table A.2).

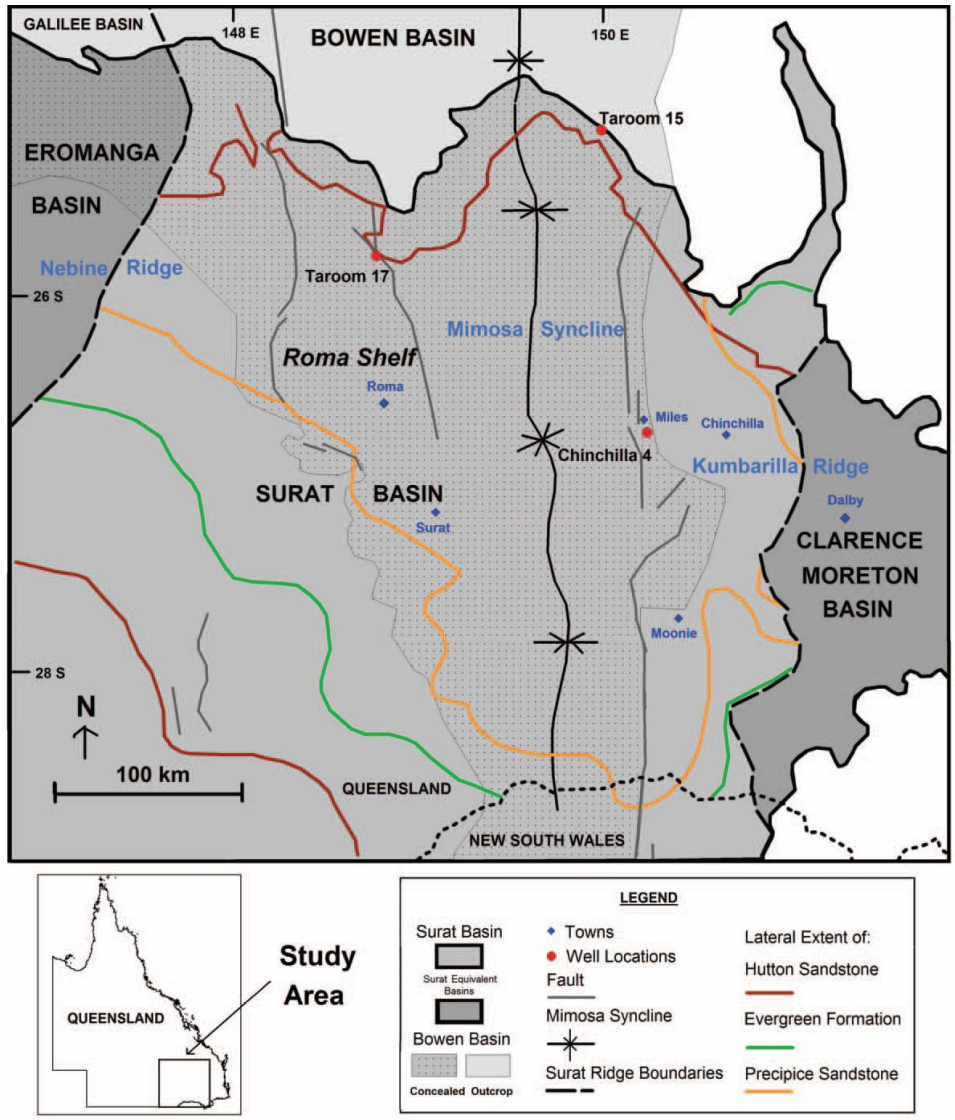

Fig. A.1 Geological setting of the Surat Basin, well locations and subcrop map of the Precipice Sandstone, Evergreen Formation and Hutton Sandstone within the Surat Basin, Queensland (Farquhar et al., 2013).

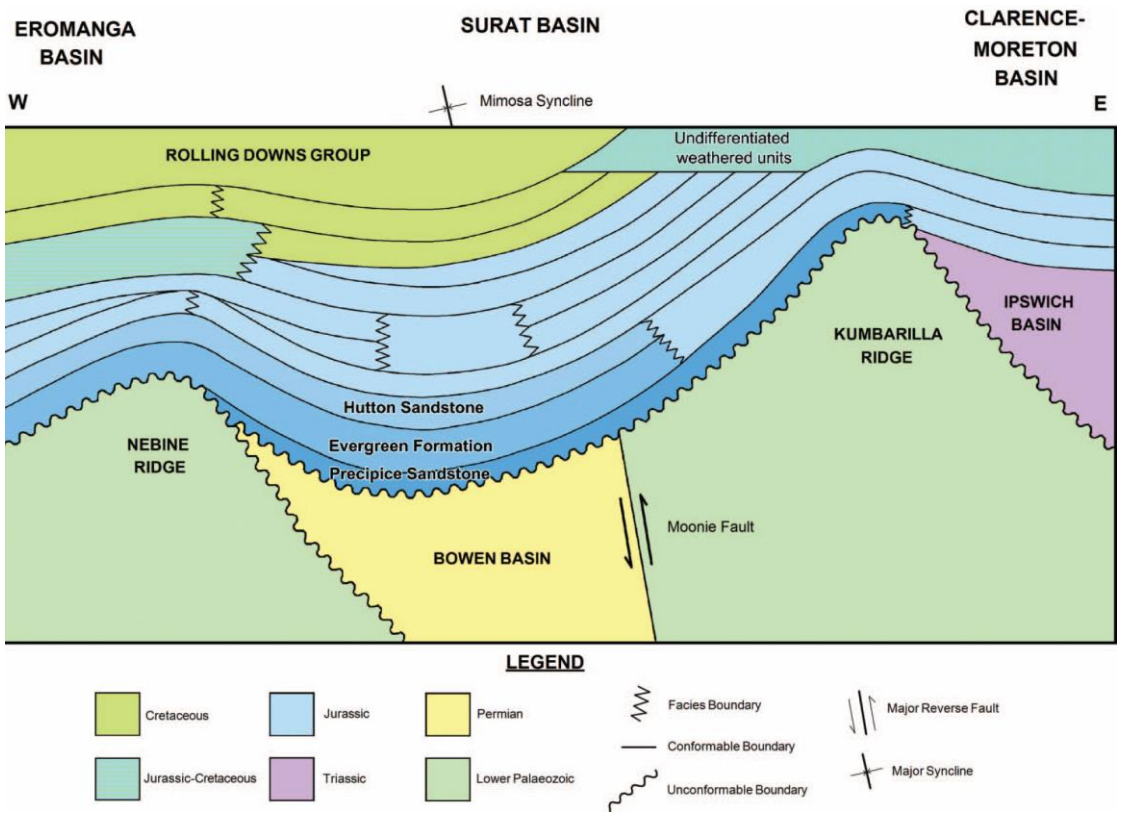

Fig. A.2 Schematic section through Surat Basin to show general stratigraphic relationships (Farquhar et al., 2013).

Units	*Features*
Precipice Sandstone	Geochemically poorly reactive with a clean, quartzose mineralogy dominated by quartz with some kaolin clays. These clays coat grains and partially fill pores, and are sometimes associated with Fe-oxide/hydroxide.
Evergreen Formation	Fairly geochemically reactive. Contains quartz and abundant plagioclase feldspar, K-feldspar, smectite, chlorite, biotite, phlogopite, carbonate and kaolinite, and should therefore serve as an effective intra-formational seal. Low permeability is attributed to extensive porosity loss following burial compaction, which is evident from the formation of pressure-dissolution features and a lithic-derived clay-rich pseudo matrix in several samples (Farquhar et al., 2013).
Hutton Sandstone	A heterogeneous potential reservoir, with geochemically reactive intervals containing smectite, chlorite and Fe-Mn-Mg-Ca carbonates, feldspars and lithics. Variable clay matrix content, porosity and locally significant cementation within the Hutton Sandstone indicate a mineralogically heterogeneous unit that is capable of buffering pH due to possible emplacement of CO_2. This potentially provides an additional vertical component of capture and storage to the potential reservoir system, in addition to the traditional regional seal provided by the Evergreen Formation.

Table A.1 Features of units related to the CO_2 sequestration sites in Surat Basin (Farquhar et al., 2013).

Sample Number	*Chapters Mentioned, and Functions*	*Features*
Hutton Sandstone sample	6 for studies in chemical reactions, a nd *4D* permeability evaluation	Poorly sorted medium to very coarse-grained calcite-cemented sandstone; anisotropic
Evergreen Formation sample	7 for studies in permeability evaluation and sample size (scale) effect	Parallel to cross-bedded fine sandstone; significant open and connected porosity; anisotropic
Precipice Sandstone sample	4 & 7 for massive data sets analysis, and *REV* scale evaluation	Medium to coarse grained, laminated to cross-bedded sandstone; significant open and connected porosity; severely anisotropic

Table A.2 Sample information and the application in the thesis.

Appendix-B: The Parallel *XLBM* Software Code

1. What is the code?

The thesis has involved a significant body of computational developments spanning from **THC** problems to parallel computing with high efficiency. These simulations works were all conducted on our parallel *XLBM* software, while the codes developed in these studies have also now become part of this software. Overall, *XLBM* has implemented a number of methods and techniques introduced in the previous chapters in this thesis. In addition to the parallel modelling for **THC** problems in heterogeneous porous media, this software also provides code interface for extending more complex issues in geological field and engineering as a practical tool with high efficiency and accuracy. Development of this software was also part of this PhD work.

2. What is the code capability?

This software is based on the extended lattice Boltzmann method, which focuses on providing solutions for complex **THC** issues in seemingly different porous media systems (complex grain contacts and multiple geomaterial features). This provides applications and references for petrophysical, hydraulic, thermal and chemical processes studies from pore scale to the *REV* scale.

3. The functional program structure

The scalable parallel *XLBM* code was written in *C++* language and designed to maintain portability on different computing architectures, compilers, and *MPI* libraries. A portable *Makefile* is programmed to enable easy compilation and installation across different multiprocessors or multicores platforms. For instance, the parallel *XLBM* software code has been installed and planted on the supercomputer infrastructures *Raijin* and *Savanna* (mentioned in Chapter 4). For special transplanting on these two supercomputers, the compiler was chosen as ***intel-mpi/4.1.2.040***. Once the users run the *makefile*, the main source file was compiled as the execution file ***xlbm***:

/intel-mpi/4.1.2.040/mpicxx -o xlbm.o -mcmodel=large -lstdc++ -c -O0 -g -fpic -DXFL_MPI_PARALLEL -DXFL_USE_POSIX ***xlbm.cpp***
ar rc lib.xlbm.a xlbm.o
/intel-mpi/4.1.2.040/mpicxx –o ***xlbm*** *xlbm.o lib.xlbm.a*

Due to the design of compatible code interface, the software can be further transplanted onto different supercomputer infrastructures for high performance computing. The parallelism

implementation of the custom *XLBM* has been introduced in Chapter 4 (see Fig. 4-1). Here we briefly introduced the functional program structure of the parallel *XLBM* code (Fig. B.1).

In this thesis, computational code has been developed and employed for conducting analysis for different samples including sandstones and coal cores. The code comprises three functional modules, namely: the pre-processing for initial data sets preparation; the main run-time parallel computing for **THC** simulations; and the post-processing for data outputs, visualization and analysis.

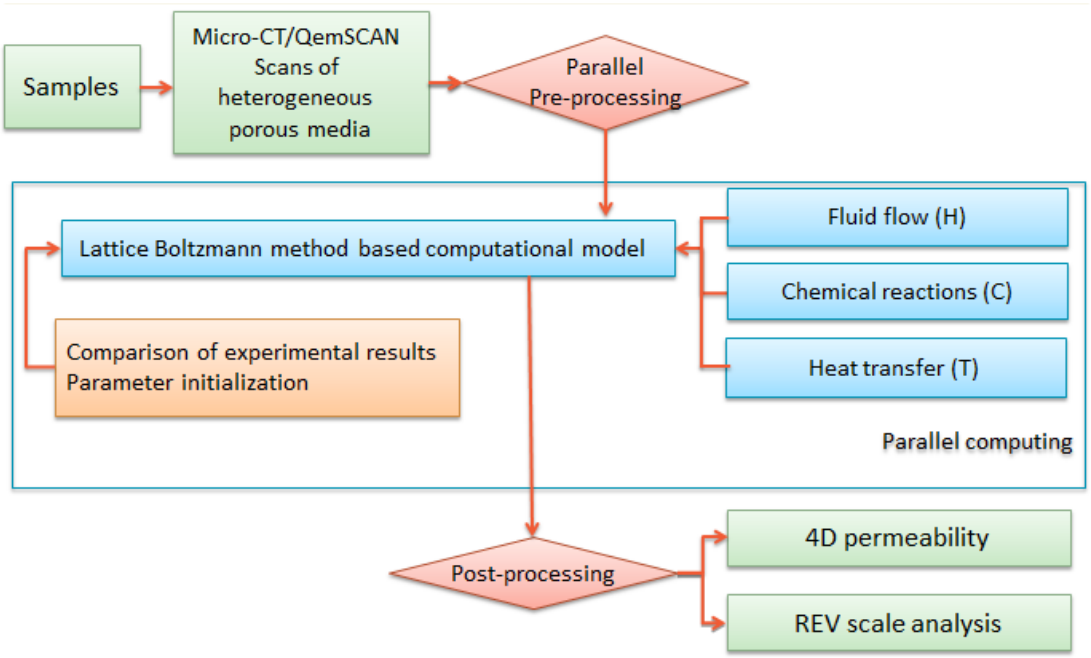

Fig. B.1 Functional program structure of the parallel *XLBM* software code.

How to use this software?

The software provides a friendly user interface. For users, firstly, there are only two files which are required to be modified and uploaded onto the supercomputers before the execution: the initial parameter file (***PARA.DAT***) for computing and the micro-CT images of the samples (as ***SAMPLE.DAT***) for petrophysical information. Secondly, users can run the execution script ***run.script***. Thirdly, output files for visualization or further data analysis can be obtained in the designated directory.

Here we give a brief introduction on the software code usage, including: how to prepare the initial data files, how to execute the program, and how to visualize the output files.

1) Data preparation

The ***PARA.DAT*** file for some main parameters is listed as follows.

PARA.DAT

LB paras:

Tau;	*// the dimensionless relaxation time*
Boundary;	*//1: for bounce-back; 2: for free slip; 3: periodic;*

Sample paras:

Viscosity;	*//the fluid viscosity*
Materials;	*//number of materials*
Permeability;	*//permeability of different materials*
Reaction;	*/1: run Reaction module; 0: disable*
Reactive icons;	*//number of reactive icons, eg.* H^+, Ca^{2+}
Reaction para;	*//* reaction parameters for different icons, eg. H^+, Ca^{2+}
Temperature;	*//1: run Temperature module; 0: disable*
Temperature para;	*//temperature settings*
Pressure;	*// pressure gradient*
Re;	*//Reynolds number*
Pr;	*//Prandtl number*
Ra;	*//Rayleigh number*

2) Run the program

For users, the main body of the software is a black box. To run the program, users need to download the ***run.script*** template and set parameters as required.

The ***run.script*** is listed as follows.

run.script

#!/bin/sh

#PBS -S /bin/sh

#PBS -q job_queue

#PBS -l nodes=m:ppn=n

#PBS -l walltime=hh:mm:ss

#PBS -l mem=xxxG

. /usr/share/modules/init/sh

module load intel-mpi/4.1.2.040

module load intel-cc-13/14.0.1

mpirun -perhost n -np m×n ./xlbm 3D NX NY NZ VX VY VZ OUTFILE_NO SAMPLE.DAT PARA.DAT DIROUT

Here, *job_queue* is the job queue related to the PBS system on the supercomputer used in your case; *m* is the used node number of supercomputers; *n* is the processor number on each node. *NX*, *NY*, and *NZ* are the lattice grid size (digital resolution of the sample), *VX*, *VY*, and *VZ* are the voxel size of the original sample. *OUTFILE_NO* means file number of the output results, and the *DIROUT* is the designated directory for output files.

4. A case demonstration

For a usage demonstration, we applied the software to simulate the application case (chemical reactions) mentioned in Chapter 6. Fig. B.2 shows the working flow of the case. First, the users need to download the ***PARA.DAT*** template (introduced as above) to provide essential parameters for the calculations, and upload the high resolution micro-CT images of the Hutton Sandstone sample as ***SAMPLE.DAT***.

In this case, the ***PARA.DAT*** was set as:

PARA.DAT

LB paras:

1.25; *// the dimensionless relaxation time*

3; *//1: for bounce-back; 2: for free slip; 3: periodic;*

Sample paras:

10^{-4}; *//the fluid viscosity, unit: Pa·s*

3; *//number of materials, 1: calcite, 2: quartz, 3: unreactive lithics*

0; *//permeability of different materials*

1; */1: run Reaction module; 0: disable*

3; // reaction parameters for different icons, including: H^+, Ca^{2+},

8.9×10^{-5}; //reaction parameter k_1 for H^+, unit: mol/cm^2·s

5.0×10^{-8}; //reaction parameter k_2 for H_2CO_3, unit: mol/cm^2·s

6.5×10^{-11}; // reaction parameter k_2 for H_2O, unit: mol/cm^2·s

1; *//1: run Temperature module; 0: disable*

60^{o}C *//temperature settings*

10; *// pressure gradient, unit: bar/mm*

0.1; *//Reynolds number*

0.71; *//Prandtl number*

1000; *//Rayleigh number*

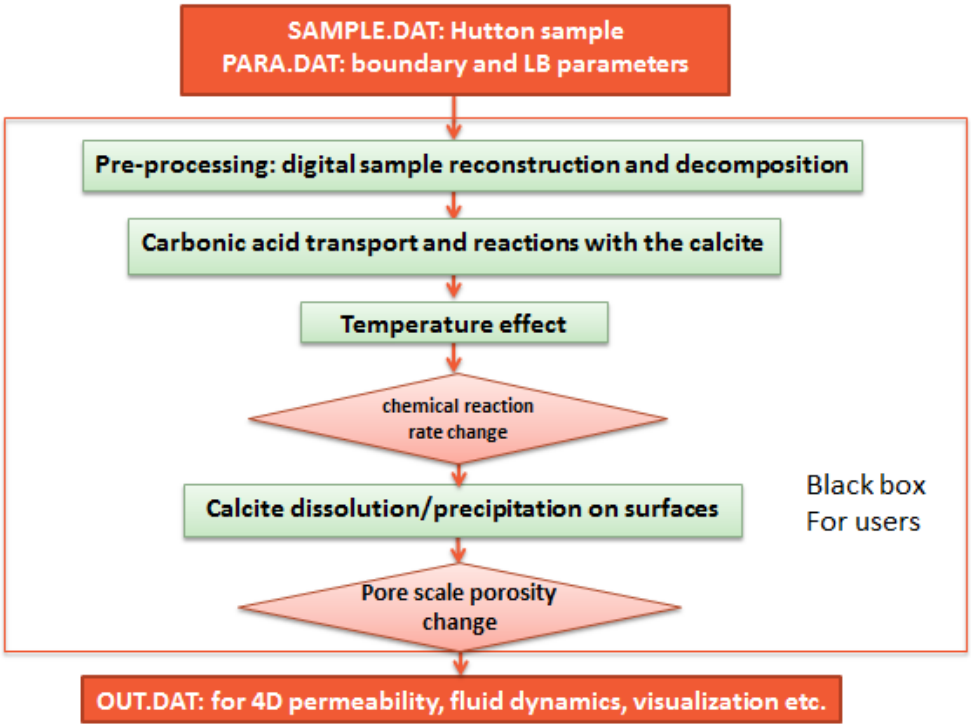

Fig. B.2 Functional program structure of the parallel *XLBM* software code.

Users need to download the ***run.script*** template and modify as required. For users, the main body of the software is a black box (see Fig. B.2). The execution was set as:

qsub run.script

Here is the ***run.script*** for this demonstration case.

#!/bin/sh

#PBS -S /bin/sh

#PBS -q workq

#PBS -l nodes=16:ppn=8

#PBS -l walltime=50:00:00

#PBS -l mem=31g

. /usr/share/modules/init/sh

module load intel-mpi/4.1.2.040

module load intel-cc-13/14.0.1

mpirun -perhost 8 -np 128 ./xlbm 3D 1400 1400 300 3 3 3 64 PARA.DAT SAMPLE.DAT /chemical_reaction/chapter_6/OUT.DAT.

After the simulation, the output files were generated as */chemical_reaction/chapter_6/OUT.DAT00xx* (*xx* means 00 to 63) for visualization and analysis. The head of these data files were stored in the standard *vtk* format (as follows) and can be visualized by a variety of visualization software (e.g. *Paraview*).

vtk output

ASCII

DATASET STRUCTURED_POINTS

DIMENSIONS 375 375 75

SPACING 1 1 1

ORIGIN 0 0 0

POINT_DATA 10546875

SCALARS pixel_value int

LOOKUP_TABLE default

…

Bibliography

AALTOSALMI U., 2005. Fluid flow in porous media with the lattice-Boltzmann method. University of Jyv äskyl ä

ADLER P., THOVERT J.-F., BEKRI S. & YOUSEFIAN F. 2002. Real porous media: local geometry and transports. *Journal of engineering mechanics*, **128,** 829-839.

AGARWAL R., CARTER R. & POLLOCK C. 1979. Evaluation and performance prediction of low-permeability gas wells stimulated by massive hydraulic fracturing. *Journal of petroleum Technology*, **31,** 362-372.

AGHIGHI M.A. & RAHMAN S.S. 2010. Horizontal permeability anisotropy: Effect upon the evaluation and design of primary and secondary hydraulic fracture treatments in tight gas reservoirs. *Journal of Petroleum Science and Engineering*, **74,** 4-13.

AHARONOV E. & ROTHMAN D.H. 1993. Non ‐ Newtonian flow (through porous media): A lattice ‐ Boltzmann method. *Geophysical Research Letters*, **20,** 679-682.

AHARONOV E., WHITEHEAD J., KELEMEN P. & SPIEGELMAN M. 1995. Channeling instability of upwelling melt in the mantle. *Journal of Geophysical Research: Solid Earth (1978–2012)*, **100,** 20433-20450.

AHMED M., RAHIM Z., AL-ANAZI H., AL-KANAAN A. & MOHIUDDIN M., 2012. Development of Low Permeability Reservoir Utilizing Multi-stage Fracture Completion in the Minimum Stress Direction, SPE Saudi Arabia Section Technical Symposium and Exhibition. Society of Petroleum Engineers.

AIDUN C.K. & CLAUSEN J.R. 2010. Lattice-Boltzmann method for complex flows. *Annual Review of Fluid Mechanics*, **42,** 439-472.

AIDUN C.K. & LU Y. 1995. Lattice Boltzmann simulation of solid particles suspended in fluid. *Journal of Statistical Physics*, **81,** 49-61.

AL-HADRAMI H. & TEUFEL L., 2000. Influence of Permeability Anisotropy and Reservoir Heterogeneity on Optimization of Infill Drilling in Naturally Fractured Tight-Gas Mesaverde Sandstone Reservoirs San Juan Basin, SPE Rocky Mountain Regional/Low-Permeability Reservoirs Symposium and Exhibition. Society of Petroleum Engineers.

ALEXANDER D. & BRYANT S.L. 2009. Evaluating storage and leakage scenarios for carbo n dioxide sequestration in Trinidad and Tobago. *Energy Procedia*, **1,** 2761-2768.

ALI A. 2011. Correlations between the effective permeability and seismic anisotropy of fractured reservoirs.

ALKATTAN M., OELKERS E.H., DANDURAND J.-L. & SCHOTT J. 1998. An experimental study of calcite and limestone dissolution rates as a function of pH from− 1 to 3 and temperature from 25 to 80 C. *Chemical geology*, **151,** 199-214.

ALKATTAN M., OELKERS E.H., DANDURAND J.-L. & SCHOTT J. 2002. An experimental study of calcite dissolution rates at acidic conditions and 25 ° C in the presence of NaPO< sub> 3</sub> and MgCl< sub> 2</sub>. *Chemical Geology*, **190,** 291-302.

ALLEN J.L., JOHNSON C.L., HEUMANN M.J., GOOLEY J. & GALLIN W. 2012. New technology and methodology for assessing sandstone composition: A preliminary case study using a quantitative electron microscope scanner (QEMScan). *Geological Society of America Special Papers*, **487,** 177-194.

ALMASI G.S. & GOTTLIEB A., 1989. Highly parallel computing. Benjamin-Cummings Publishing Co., Inc.

ALVAREZ-RAM REZ J., NIEVES-MENDOZA S. & GONZ LEZ-TREJO J. 1996. Calculation of the effective diffusivity of heterogeneous media using the lattice-Boltzmann method. *Physical Review E*, **53,** 2298.

AMDAHL G.M., 1967. Validity of the single processor approach to achieving large scale computing capabilities, Proceedings of the April 18-20, 1967, spring joint computer conference. ACM, pp. 483-485.

AMERI S., MOLNAR D., MOHAGHEGH S. & AMINIAN K., 1993. Permeability Evaluation in Heterogeneous Formations Using Geophysical Well Logs and Geological Interpretations, SPE Western Regional Meeting. Society of Petroleum Engineers.

ANDERSSON L., JONES A.C., KNACKSTEDT M.A. & BERGSTR M L. 2011. Permeability, pore connectivity and critical pore throat control of expandable polymeric sphere templated macroporous alumina. *Acta Materialia*, **59,** 1239-1248.

ANDR L., AZAROUAL M. & MENJOZ A. 2010. Numerical simulations of the thermal impact of supercritical CO2 injection on chemical reactivity in a carbonate saline reservoir. *Transport in porous media*, **82,** 247-274.

ANDREANI M., LUQUOT L., GOUZE P., GODARD M., HOISE E. & GIBERT B. 2009. Experimental study of carbon sequestration reactions controlled by the percolation of CO2-rich brine through peridotites. *Environmental Science & Technology*, **43,** 1226-1231.

ANSUMALI S. & KARLIN I.V. 2002. Single relaxation time model for entropic lattice Boltzmann methods. *PHYSICAL REVIEW-SERIES E-*, **65,** 56312-56312.

ARMITAGE P., FAULKNER D., WORDEN R., APLIN A., BUTCHER A. & ILIFFE J. 2011. Experimental measurement of, and controls on, permeability and permeability anisotropy of caprocks from the CO2 storage project at the Krechba Field, Algeria. *Journal of Geophysical Research: Solid Earth (1978–2012)*, **116,**

ARNS C., BAUGET F., GHOUS A., SAKELLARIOU A., SENDEN T., SHEPPARD A., SOK R., PINCZEWSKI W., KELLY J. & KNACKSTEDT M. 2005a. Digital core laboratory: Petrophysical analysis from 3D imaging of reservoir core fragments. *Petrophysics*, **46,** 260-277.

ARNS C.H., BAUGET F., LIMAYE A., SAKELLARIOU A., SENDEN T., SHEPPARD A., SOK R.M., PINCZEWSKI W., BAKKE S. & BERGE L.I. 2005b. Pore-scale characterization of carbonates using X-ray microtomography. *SPE JOURNAL-RICHARDSON-*, **10,** 475.

ARNS J.-Y., ARNS C.H., SHEPPARD A.P., SOK R.M., KNACKSTEDT M.A. & VAL PINCZEWSKI W. 2003. Relative permeability from tomographic images; effect of correlated heterogeneity. *Journal of Petroleum Science and Engineering*, **39,** 247-259.

ARRHENIUS S. 1896. XXXI. On the influence of carbonic acid in the air upon the temperature of the ground. *The London, Edinburgh, and Dublin Philosophical Magazine and Journal of Science*, **41,** 237-276.

ASANOVIC K., BODIK R., DEMMEL J., KEAVENY T., KEUTZER K., KUBIATOWICZ J., MORGAN N., PATTERSON D., SEN K. & WAWRZYNEK J. 2009. A view of the parallel computing landscape. *Communications of the ACM*, **52,** 56-67.

AXNER L., BERNSDORF J., ZEISER T., LAMMERS P., LINXWEILER J. & HOEKSTRA A.G. 2008. Performance evaluation of a parallel sparse lattice Boltzmann solver. *Journal of Computational Physics*, **227,** 4895-4911.

AYAN C., COLLEY N., COWAN G., EZEKWE E., WANNELL M., GOODE P., HALFORD F., JOSEPH J., MONGINI A. & POP J. 1994. Measuring permeability anisotropy: The latest approach. *Oilfield Review*, **6,** 24-35.

AYRES D.L., DARLING A., ZWICKL D.J., BEERLI P., HOLDER M.T., LEWIS P.O., HUELSENBECK J.P., RONQUIST F., SWOFFORD D.L. & CUMMINGS M.P. 2012. BEAGLE: an application programming interface and high-performance computing library for statistical phylogenetics. *Systematic biology*, **61,** 170-173.

BACCI G., KORRE A. & DURUCAN S. 2011. An experimental and numerical investigation into the impact of dissolution/precipitation mechanisms on CO< sub> 2</sub> injectivity in the wellbore and far field regions. *International Journal of Greenhouse Gas Control*, **5,** 579-588.

BAKER J.C., BAI G.P., HAMILTON P.J., GOLDING S.D. & KEENE J.B. 1995. Continental-scale magmatic carbon dioxide seepage recorded by dawsonite in the Bowen-Gunnedah-Sydney Basin system, eastern Australia. *Journal of Sedimentary research*, **65,**

BAO H., BIELAK J., GHATTAS O., KALLIVOKAS L.F., O'HALLARON D.R., SHEWCHUK J.R. & XU J., 1996. Earthquake ground motion modeling on parallel computers, Proceedings of the 1996 ACM/IEEE conference on Supercomputing. IEEE Computer Society, pp. 13.

BARAKOS G., MITSOULIS E. & ASSIMACOPOULOS D. 1994. Natural convection flow in a square cavity revisited: laminar and turbulent models with wall functions. *International Journal for Numerical Methods in Fluids*, **18,** 695-719.

BARNEY B. 2010. Introduction to parallel computing. *Lawrence Livermore National Laboratory*, **6,** 10.

BARTON C.A., MOOS D., PESKA P. & ZOBACK M.D. 1997. Utilizing wellbore image data to determine the complete stress tensor: application to permeability anisotropy and wellbore stability. *The log analyst*, **38,**

BARTON C.A. & ZOBACK M.D. 2002. Discrimination of natural fractures from drilling-induced wellbore failures in wellbore image data-implications for reservoir permeability. *SPE Reservoir Evaluation & Engineering*, **5,** 249-254.

BAUGET F., ARNS C.H., SAADATFAR M., SHEPPARD A., SOK R., TURNER M., PINCZEWSKI W.V. & KNACKSTEDT M.A., 2005. What is the Characteristic Length Scale for Permeability? Direct Analysis From Microtomographic Data, SPE Annual Technical Conference and Exhibition. Society of Petroleum Engineers.

BEAR J., 2013. Dynamics of fluids in porous media. Courier Dover Publications.

BEDIENT P.B., RIFAI H.S. & NEWELL C.J., 1994. Ground water contamination: transport and remediation. Prentice-Hall International, Inc.

BEDRIKOVETSKI P. 2006. Exact solutions for non-linear problems of reactive flows in rocks.

BEDRIKOVETSKI P., PAIVA R. & FONSECA D. 2005. Effects of Cold Water Injection on Injectivity Impairment.

BEDRIKOVETSKI P., PIRES A.P. & SHAPIRO A., 2004. Conservation law system for two-phase n-component flow in porous media: splitting between thermodynamics and hydrodynamics, International Congress on Hyperbolic Problems Theory (10th: 2004: Osaka, Japan).

BEKKERMAN R., BILENKO M. & LANGFORD J., 2012. Scaling up machine learning: Parallel and distributed approaches. Cambridge University Press.

BEKRI S., THOVERT J.-F. & ADLER P. 1997. Dissolution and deposition in fractures. *Engineering geology*, **48,** 283-308.

BEKRI S., THOVERT J. & ADLER P. 1995. Dissolution of porous media. *Chemical engineering science*, **50,** 2765-2791.

BELL J.B., COLELLA P. & GLAZ H.M. 1989. A second-order projection method for the incompressible Navier-Stokes equations. *Journal of Computational Physics*, **85,** 257-283.

BENNETT S.P., 2003. Designing a compiler for a distributed memory parallel computing system, Citeseer.

BENNION B. & BACHU S. 2008. Drainage and Imbibition Relative Permeability Relationships for Supercritical CO2/Brine and H2S/Brine Systems in Intergranular Sandstone Carbonate Shale and Anhydrite Rocks. *SPE Reservoir Evaluation & Engineering*, **11,** 487-496.

BENSON S.M. & COLE D.R. 2008. CO2 sequestration in deep sedimentary formations. *Elements*, **4,** 325-331.

BENZI R., SUCCI S. & VERGASSOLA M. 1992. The lattice Boltzmann equation: theory and applications. *Physics Reports*, **222,** 145-197.

BERA B., MITRA S.K. & VICK D. 2011. Understanding the micro structure of Berea Sandstone by the simultaneous use of micro-computed tomography (micro-CT) and focused ion beam-scanning electron microscopy (FIB-SEM). *Micron*, **42,** 412-418.

BERNASCHI M., FATICA M., MELCHIONNA S., SUCCI S. & KAXIRAS E. 2010. A flexible high‐performance Lattice Boltzmann GPU code for the simulations of fluid flows in complex geometries. *Concurrency and Computation: Practice and Experience*, **22,** 1-14.

BERNER R.A. 1970. Sedimentary pyrite formation. *American Journal of Science*, **268,** 1-23.

BICKLE M. 1978. Heat loss from the earth: a constraint on Archaean tectonics from the relation between geothermal gradients and the rate of plate production. *Earth and Planetary Science Letters*, **40,** 301-315.

BIELAK J., GRAVES R.W., OLSEN K.B., TABORDA R., RAM REZ ‐ GUZM N L., DAY S.M., ELY G.P., ROTEN D., JORDAN T.H. & MAECHLING P.J. 2010. The ShakeOut earthquake scenario: Verification of three simulation sets. *Geophysical Journal International*, **180,** 375-404.

BIELICKI J., FITTS J., PETERS C. & WILSON E., 2013. Monetizing Leakage Risk of Geologic CO2 Storage using Wellbore Permeability Frequency Distributions, EGU General Assembly Conference Abstracts, pp. 10924.

BIRKHOLZER J. & TSANG Y. 2000. Modeling the thermal ‐ hydrologic processes in a large ‐ scale underground heater test in partially saturated fractured tuff. *Water Resources Research*, **36,** 1431-1447.

BLUNT M. & KING P. 1990. Macroscopic parameters from simulations of pore scale flow. *Physical Review A*, **42,** 4780.

BLUNT M.J. 2001. Flow in porous media--pore-network models and multiphase flow. *Current opinion in colloid & interface science*, **6,** 197-207.

BLUNT M.J., JACKSON M.D., PIRI M. & VALVATNE P.H. 2002. Detailed physics, predictive capabilities and macroscopic consequences for pore-network models of multiphase flow. *Advances in water resources*, **25,** 1069-1089.

BOGGS S., 1995. Principles of sedimentology and stratigraphy, 23117923. Prentice Hall New Jersey.

BOMANS L., ROOSE D. & HEMPEL R. 1990. The Argonne/GMD macros in FORTRAN for portable parallel programming and their implementation on the Intel iPSC/2. *Parallel Computing*, **15,** 119-132.

BORNERT M. 2010. X-ray micro CT for studying strain localization in clay rocks under triaxial compression. *Advances in X-ray Tomography for Geomaterials*, **118,** 35.

BROWNLEE R., GORBAN A.N. & LEVESLEY J. 2007. Stability and stabilization of the lattice Boltzmann method. *Physical Review E*, **75,** 036711.

BUGNION E., AMARASINGHE S., ANDERSON J., LIAO S.-W., MURPHY B., HALL M. & LAM M.S. 1996. Maximizing multiprocessor performance with the SUIF compiler. *Computer*, **29,** 84-84.

BUIJSE M., DE BOER P., BREUKEL B. & BURGOS G. 2004. Organic acids in carbonate acidizing. *SPE Production & Facilities*, **19,** 128-134.

BURMEISTER L.C., 1993. Convective heat transfer. John Wiley & Sons.

CANSELL F., FABRE D. & PETITET J.P. 1993. Phase transitions and chemical transformations of benzene up to 550 C and 30 GPa. *The Journal of chemical physics*, **99,** 7300-7304.

CAO T.-K., DUAN Y.-G., YU B.-M., FANG Q.-T. & WANG R. 2014. Pore-scale simulation of gas-water flow in low permeability gas reservoirs. *Journal of Central South University*, **21,** 2793-2800.

CARLSON W., ROWE T., KETCHAM R. & COLBERT M. 2003. Applications of high-resolution X-ray computed tomography in petrology, meteoritics and palaeontology. *Geological Society, London, Special Publications*, **215,** 7-22.

CARMAN P.C., 1956. Flow of gases through porous media. Butterworths Scientific Publications London.

CARTER J. & OLIKER L., 2006. Performance evaluation of Lattice-Boltzmann magnetohydrodynamics simulations on modern parallel vector systems. Springer.

CHADAM J., HOFF D., MERINO E., ORTOLEVA P. & SEN A. 1986. Reactive infiltration instabilities. *IMA Journal of Applied Mathematics*, **36,** 207-221.

CHAIANANSUTCHARIT T., CHEN H.-Y. & TEUFEL L.W., 2001. Impacts of permeability anisotropy and pressure interference on coalbed methane (CBM) production, SPE Rocky Mountain Petroleum Technology Conference. Society of Petroleum Engineers.

CHANDESRIS M. & JAMET D. 2006. Boundary conditions at a planar fluid–porous interface for a Poiseuille flow. *International journal of heat and mass transfer*, **49,** 2137-2150.

CHEN H., CHEN S. & MATTHAEUS W.H. 1992. Recovery of the Navier-Stokes equations using a lattice-gas Boltzmann method. *Physical Review A*, **45,** 5339-5342.

CHEN S., DAWSON S., DOOLEN G., JANECKY D. & LAWNICZAK A. 1995. Lattice methods and their applications to reacting systems. *Computers & chemical engineering*, **19,** 617-646.

CHEN S. & DOOLEN G.D. 1998. Lattice Boltzmann method for fluid flows. *Annual review of fluid mechanics*, **30,** 329-364.

CHEN W., GHAITH A., PARK A. & ORTOLEVA P. 1990. Diagenesis through coupled processes: modeling approach, self-organization, and implications for exploration.

CHEN Y., DURLOFSKY L.J., GERRITSEN M. & WEN X.H. 2003. A coupled local-global upscaling approach for simulating flow in highly heterogeneous formations. *Advances in water resources*, **26,** 1041-1060.

CHENG P., BESTEHORN M. & FIROOZABADI A. 2012. Effect of permeability anisotropy on buoyancy ‐ driven flow for CO2 sequestration in saline aquifers. *Water Resources Research*, **48,**

CHEPURNIY N. 1984. Kinetic theories for granular flow: inelastic particles in Couette flow and slightly inelastic particles in a general flow field. *Journal of fluid mechanics*, **140,** 256.

CHILAKAPATI A., YABUSAKI S., SZECSODY J. & MACEVOY W. 2000. Groundwater flow, multicomponent transport and biogeochemistry: development and application of a coupled process model. *Journal of Contaminant Hydrology*, **43,** 303-325.

CHOU L., GARRELS R.M. & WOLLAST R. 1989. Comparative study of the kinetics and mechanisms of dissolution of carbonate minerals. *Chemical geology*, **78,** 269-282.

CHRISTEN M., SCHENK O. & BURKHART H., 2011. Patus: A code generation and autotuning framework for parallel iterative stencil computations on modern microarchitectures, Parallel & Distributed Processing Symposium (IPDPS), 2011 IEEE International. IEEE, pp. 676-687.

CINAR Y., BUKHTEEVA O., NEAL P.R., ALLINSON W.G. & PATERSON L., 2008. CO2 Storage in low permeability formations, SPE Symposium on Improved Oil Recovery. Society of Petroleum Engineers.

CLARKSON C.R., PAN Z., PALMER I.D. & HARPALANI S. 2010. Predicting sorption-induced strain and permeability increase with depletion for coalbed-methane reservoirs. *SPE Journal*, **15,** 152-159.

CLAUSEN J.R., REASOR JR D.A. & AIDUN C.K. 2010. Parallel performance of a lattice-Boltzmann/finite element cellular blood flow solver on the IBM Blue Gene/P architecture. *Computer Physics Communications*, **181,** 1013-1020.

CLAVAUD J.B., MAINEULT A., ZAMORA M., RASOLOFOSAON P. & SCHLITTER C. 2008. Permeability anisotropy and its relations with porous medium structure. *Journal of Geophysical Research: Solid Earth (1978–2012)*, **113,**

CLINE S. & TIAB D., 2001. Studies in Vertical and Horizontal Well-Flow Behavior in Cases of Permeability Anisotropy, SPE Rocky Mountain Petroleum Technology Conference. Society of Petroleum Engineers.

CLOSE J.C. 1993. Natural Fractures in Coal: Chapter 5.

COCHOCKI A. & UNBEHAUEN R., 1993. Neural networks for optimization and signal processing. John Wiley & Sons, Inc.

COHEN D.S. & ROSENBLAT S. 1979. Multi-species interactions with hereditary effects and spatial diffusion. *Journal of Mathematical Biology*, **7,** 231-241.

CONNOR J.J. & BREBBIA C.A. 1976. Finite element techniques for fluid flow. *London, Newnes-Butterworths, 1976. 317 p.*, **1,**

CORCORAN J., 1989. The use of SEM/EDS techniques in studies of coal and associated mineral matter, Proceedings of the mineralogy-petrology symposium, Sydney, Australia, 6-8 February 1989.

CUI Y., MOORE R., OLSEN K., CHOURASIA A., MAECHLING P., MINSTER B., DAY S., HU Y., ZHU J. & JORDAN T. 2009. Toward petascale earthquake simulations. *Acta Geotechnica*, **4,** 79-93.

CUI Y., OLSEN K.B., JORDAN T.H., LEE K., ZHOU J., SMALL P., ROTEN D., ELY G., PANDA D.K. & CHOURASIA A., 2010. Scalable earthquake simulation on petascale supercomputers, High Performance Computing, Networking, Storage and Analysis (SC), 2010 International Conference for. IEEE, pp. 1-20.

D'HUMI RES D. 2002. Multiple–relaxation–time lattice Boltzmann models in three dimensions. *Philosophical Transactions of the Royal Society of London. Series A: Mathematical, Physical and Engineering Sciences*, **360,** 437-451.

DAKE L.P., 1983. Fundamentals of reservoir engineering. Elsevier.

DANESI P., HORWITZ E., VANDEGRIFT G. & CHIARIZIA R. 1981. Mass transfer rate through liquid membranes: interfacial chemical reactions and diffusion as simultaneous permeability controlling factors. *Separation science and Technology*, **16,** 201-211.

DARRIBA D., TABOADA G.L., DOALLO R. & POSADA D. 2012. jModelTest 2: more models, new heuristics and parallel computing. *Nature Methods*, **9,** 772-772.

DAUNGTHONGSUK W. & WONGWISES S. 2007. A critical review of convective heat transfer of nanofluids. *Renewable and Sustainable Energy Reviews*, **11,** 797-817.

DAWSON G. & ESTERLE J. 2010. Controls on coal cleat spacing. *International Journal of Coal Geology*, **82,** 213-218.

DAWSON G., GOLDING S., MASSAROTTO P. & ESTERLE J. 2011. Experimental supercritical CO< sub> 2</sub> and water interactions with coal under simulated in situ conditions. *Energy Procedia*, **4,** 3139-3146.

DAWSON G.K.W., BIDDLE D., FARQUHAR S.M., GAO J., GOLDING S.D., JIANG X., KECK R., KHAN C., LAW A.C.K., LI Q., PEARCE J.K., RUDOLPH V., WATSON A. & XING H. 2014. ANLEC Project 7-1110-0101: Achieving Risk and Cost Reductions in CO2 Geosequestration through 4D Characterisation of Host Formations. . Final Report. ANLEC R&D, Manuka, ACT, Australia, p. 140. (Peer reviewed research report).

DAWSON S.P., CHEN S. & DOOLEN G. 1993a. Lattice Boltzmann computations for reaction‐diffusion equations. *The Journal of chemical physics*, **98,** 1514-1523.

DAWSON S.P., CHEN S. & DOOLEN G. 1993b. Lattice Boltzmann computations for reaction‐diffusion equations. *The Journal of chemical physics*, **98,** 1514.

DAWSONA G.K.W., SIDIQB H., PEARCEA J., GAO J., GOLDING S.D., RUDOLPHB V., LI Q. & XING H.L. 2013. ANLEC Project 3-1110-0101: Review of laboratory-scale geochemical and geomechanical experiments simulating geosequestration of CO2 in sandstone, and associated modelling studies.

DE VAHL DAVIS G. 1983. Natural convection of air in a square cavity: a bench mark numerical solution. *International Journal for Numerical Methods in Fluids*, **3,** 249-264.

DEGOND P. & DIMARCO G. 2012. Fluid simulations with localized Boltzmann upscaling by direct simulation Monte-Carlo. *Journal of Computational Physics*, **231,** 2414-2437.

DESBOIS G., URAI J.L., KUKLA P.A., KONSTANTY J. & BAERLE C. 2011. High-resolution 3D fabric and porosity model in a tight gas sandstone reservoir: a new approach to investigate microstructures from mm-to nm-scale combining argon beam cross-sectioning and SEM imaging. *Journal of Petroleum Science and Engineering*, **78,** 243-257.

DESPLAT J.-C., PAGONABARRAGA I. & BLADON P. 2001. LUDWIG: A parallel Lattice-Boltzmann code for complex fluids. *Computer Physics Communications*, **134,** 273-290.

DESRUES J., VIGGIANI G. & BESUELLE P., 2010. Advances in X-ray Tomography for Geomaterials, 118. John Wiley & Sons.

DIODATO D. 1994. A compendium of fracture flow models—1994. *Work sponsored by US Department of Defense, United States Army, Europe, Combat Maneuver Training Center, Hohenfels, Germany*

DOMENICO P.A. & SCHWARTZ F.W., 1998. Physical and chemical hydrogeology, 44. Wiley New York.

DONATH S., IGLBERGER K., WELLEIN G., ZEISER T., NITSURE A. & RUDE U. 2008. Performance comparison of different parallel lattice Boltzmann implementations on multi-

core multi-socket systems. *International Journal of Computational Science and Engineering*, **4,** 3-11.

DONG H., TOUATI M. & BLUNT M.J., 2007. Pore network modeling: analysis of pore size distribution of Arabian core samples, SPE Middle East Oil and Gas Show and Conference. Society of Petroleum Engineers.

DONGARRA J.J., FOSTER I., FOX G., GROPP W., KENNEDY K., TORCZON L. & WHITE A., 2003. Sourcebook of parallel computing, 3003. Morgan Kaufmann Publishers San Francisco.

DUBOS-SALL E N. & RASOLOFOSAON P.N. 2011. Estimation of permeability anisotropy using seismic inversion for the CO2 geological storage site of Sleipner (North Sea). *Geophysics*, **76,** WA63-WA69.

DUGUID J.O. & LEE P. 1977. Flow in fractured porous media. *Water Resources Research*, **13,** 558-566.

DUSSEAULT M.B. 2004a. Coupled processes and petroleum geomechanics. *Elsevier Geo-Engineering Book Series*, **2,** 49-62.

DUSSEAULT M.B. 2004b. Coupled thermo-mechano-chemical processes in shales: the petroleum borehole. *Elsevier Geo-Engineering Book Series*, **2,** 573-580.

DZWINEL W. & YUEN D.A. 2000. Matching macroscopic properties of binary fluids to the interactions of dissipative particle dynamics. *International Journal of Modern Physics C-Physics and Computer*, **11,** 1-26.

ECKERT E.R.G. & DRAKE JR R.M. 1987. Analysis of heat and mass transfer.

EDMUNDS W., ANDREWS J., BURGESS W., KAY R. & LEE D. 1984. The evolution of saline and thermal groundwaters in the Carnmenellis granite. *Mineralogical Magazine*, **48,** 407-424.

EKANAYAKE J. & FOX G. 2010. High performance parallel computing with clouds and cloud technologies. In: *Cloud Computing*, pp. 20-38. Springer,

EMERY A., CHESLER S. & MACCREHAN W. 1992. Recovery of diesel fuel from clays by supercritical fluid extraction—gas chromatography. *Journal of Chromatography A*, **606,** 221-228.

ERGUN S. 1955. Flow Experiments in Studying Kinetics. *Industrial & Engineering Chemistry*, **47,** 2075-2080.

ESMAEILZADEH H., BLEM E., ST AMANT R., SANKARALINGAM K. & BURGER D., 2011. Dark silicon and the end of multicore scaling, Computer Architecture (ISCA), 2011 38th Annual International Symposium on. IEEE, pp. 365-376.

ESSCC. http://www.uq.edu.au/esscc/index.html?page=55390.

FARQUHAR S.M., DAWSON G.K.W., ESTERLE J.S. & GOLDING S.D. 2013. Mineralogical characterisation of a potential reservoir system for CO2 sequestration in the Surat Basin. *Australian Journal of Earth Sciences*, **60,** 91-110.

FARQUHAR S.M., PEARCE J.K., DAWSON G.K.W., GOLAB A., SOMMACAL A., KIRSTE D., BIDDLE D. & GOLDING S.D. 2014. A fresh approach to investigating CO2 storage: Experimental CO2-water-rock interactions in a low-salinity reservoir system. *Chemical Geology*.

FATT I. 1956. The network model of porous media I. Capillary pressure characteristics. *Trans. AIME*, **207,** 144-159.

FEALI M., PINCZEWSKI W., CINAR Y., ARNS C.H., ARNS J.-Y., FRANCOIS N., TURNER M.L., SENDEN T. & KNACKSTEDT M.A. 2012. Qualitative and Quantitative Analyses of the Three-Phase Distribution of Oil Water and Gas in Bentheimer Sandstone by Use of Micro-CT Imaging. *SPE Reservoir Evaluation & Engineering*, **15,** 706-711.

FENWICK D.H. & BLUNT M.J. 1998. Three-dimensional modeling of three phase imbibition and drainage. *Advances in water resources*, **21,** 121-143.

FERER M., BROMHAL G.S. & SMITH D.H. 2003. Pore-level modeling of immiscible drainage: validation in the invasion percolation and DLA limits. *Physica A: Statistical Mechanics and its Applications*, **319,** 11-35.

FERZIGER J.H. & PERIĆ M., 1996. Computational methods for fluid dynamics, 3. Springer Berlin.

FERZIGER J.H. & PERIĆ M., 1999. Computational methods for fluid dynamics, 3. Springer Berlin etc.

FIELD B. & ATKINS C., 2012. Characterization of Fine Grained Sediment in the AND-2A Drillhole Core (southern McMurdo Sound, Antarctica) Using QEMSCAN®. GNS Science.

FOX G.C., WILLIAMS R.D. & MESSINA P.C. 1994. Parallel computing works!

FREDD C.N. & FOGLER H.S. 1998. The influence of chelating agents on the kinetics of calcite dissolution. *Journal of colloid and interface science*, **204,** 187-197.

FREDD C.N. & SCOTT FOGLER H. 1998. The kinetics of calcite dissolution in acetic acid solutions. *Chemical Engineering Science*, **53,** 3863-3874.

FRENCH D., WARD C. & BUTCHER A., 2008. QEMSCAN for characterisation of coal and coal utilisation by-products, Co-operative Research Centre for Coal in Sustainable Development, Brisbane, Australia, Research Report, 93, 20088.

FU X., QIN Y., WANG G.G. & RUDOLPH V. 2009. Evaluation of coal structure and permeability with the aid of geophysical logging technology. *Fuel*, **88,** 2278-2285.

FULLER S.H. & MILLETT L.I., 2011. The Future of Computing Performance: Game Over or Next Level? National Academies Press.

GALPERIN B. & ORSZAG S.A., 1993. Large eddy simulation of complex engineering and geophysical flows. Cambridge University Press.

GAMSON P.D., BEAMISH B. & JOHNSON D.P. 1993. Coal microstructure and micropermeability and their effects on natural gas recovery. *Fuel*, **72,** 87-99.

GAO J. & XING H. 2013. High Performance Simulation of Complicated Fluid Flow in 3D Fractured Porous Media with Permeable Material Matrix Using LBM. In: *High Performance Computing for Computational Science-VECPAR 2012*, pp. 93-104. Springer,

GAO J., XING H., TIAN Z. & MUHLHAUS H. 2014a. Lattice Boltzmann modeling and evaluation of fluid flow in heterogeneous porous media involving multiple matrix constituents. *Computers & Geosciences*, **62,** 198-207.

GAO J., XING H.L., RUDOLPH V., LI Q. & GOLDING S.D. 2014b. Parallel Lattice Boltzmann Computing and Applications in Core Sample Feature Evaluation. *Transport in porous media*. Under revision.

GASDA S.E., CELIA M.A., WANG J.Z. & DUGUID A. 2013. Wellbore permeability estimates from vertical interference testing of existing wells. *Energy Procedia*, **37,** 5673-5680.

GATENS J., LEE W., HOPKINS C. & LANCASTER D., 1991. The effect of permeability anisotropy on the evaluation and design of hydraulic fracture treatments and well performance, SPE Gas Technology Symposium. Society of Petroleum Engineers.

GAUS I. 2010. Role and impact of CO< sub> 2</sub>–rock interactions during CO< sub> 2</sub> storage in sedimentary rocks. *International Journal of Greenhouse Gas Control*, **4,** 73-89.

GAUS I., AUDIGANE P., ANDR L., LIONS J., JACQUEMET N., DURST P., CZERNICHOWSKI-LAURIOL I. & AZAROUAL M. 2008. Geochemical and solute transport modelling for CO< sub> 2</sub> storage, what to expect from it? *International Journal of Greenhouse Gas Control*, **2,** 605-625.

GERRITSEN M.G. & DURLOFSKY L.J. 2005. Modeling fluid flow in oil reservoirs. *Annu. Rev. Fluid Mech.*, **37,** 211-238.

GHASSEMI A. & PAK A. 2011. Pore scale study of permeability and tortuosity for flow through particulate media using Lattice Boltzmann method. *International Journal for Numerical and Analytical Methods in Geomechanics*, **35,** 886-901.

GHERARDI F., AUDIGANE P. & GAUCHER E.C. 2012. Predicting long-term geochemical alteration of wellbore cement in a generic geological CO< sub> 2</sub> confinement site: Tackling a difficult reactive transport modeling challenge. *Journal of Hydrology*, **420,** 340-359.

GHERARDI F., XU T. & PRUESS K. 2007. Numerical modeling of self-limiting and self-enhancing caprock alteration induced by CO< sub> 2</sub> storage in a depleted gas reservoir. *Chemical Geology*, **244,** 103-129.

GHEZZEHEI T.A. 2012. Linking sub-pore scale heterogeneity of biological and geochemical deposits with changes in permeability. *Advances in Water Resources*, **39,** 1-6.

GINZBURG I. 2008. Consistent Lattice Boltzmann schemes for the Brinkman model of porous flow and infinite Chapman-Enskog expansion. *Physical Review E*, **77,** 066704.

GITMAN I., ASKES H. & SLUYS L. 2007. Representative volume: existence and size determination. *Engineering Fracture Mechanics*, **74,** 2518-2534.

GOLAB A. 2012. Chinchilla & Burunga Wells Report & Overview. ANLEC Report.

GOLAB A., ROMEYN R., AVERDUNK H., KNACKSTEDT M. & SENDEN T. 2013a. 3D characterisation of potential CO2 reservoir and seal rocks. *Australian Journal of Earth Sciences*, **60,** 111-123.

GOLAB A., SOMMACAL S., GOODWIN C., KHOR J., CARNERUP A., DODD N., DAWSON G. & GOLDING S.D. 2013b. Technical report for Sub-project 5: Undertake time series (4D) imaging and conventional experimental studies to measure geochemical reactivity and dissolution trapping capacity of core material using supercritical CO_2. ANLEC R&D report.

GOLAB A., WARD C.R., PERMANA A., LENNOX P. & BOTHA P. 2013c. High-resolution three-dimensional imaging of coal using microfocus X-ray computed tomography, with special reference to modes of mineral occurrence. *International Journal of Coal Geology*, **113,** 97-108.

GOLAB A.N., KNACKSTEDT M.A., AVERDUNK H., SENDEN T., BUTCHER A.R. & JAIME P. 2010. 3D porosity and mineralogy characterization in tight gas sandstones. *The Leading Edge*, **29,** 1476-1483.

GOODALL W.R. 2008. Characterisation of mineralogy and gold deportment for complex tailings deposits using QEMSCAN< sup>®</sup>. *Minerals Engineering*, **21,** 518-523.

GORMAN A.R. & SENGER K. 2010. Defining the updip extent of the gas hydrate stability zone on continental margins with low geothermal gradients. *Journal of Geophysical Research: Solid Earth (1978–2012)*, **115,**

GRAMA A., 2003. Introduction to parallel computing. Pearson Education.

GRAUE D.J., 2001. Upgrading and recovery of heavy crude oils and natural bitumens by in situ hydrovisbreaking. Google Patents.

GRAY I. 1987. Reservoir engineering in coal seams: Part 1-The physical process of gas storage and movement in coal seams. *SPE Reservoir Engineering*, **2,** 28-34.

GREEN W.J., LEE G.F. & JONES R.A. 1981. Clay-soils permeability and hazardous waste storage. *Journal (Water Pollution Control Federation)*1347-1354.

GRIMSHAW A.S. 1993. Easy-to-use object-oriented parallel processing with Mentat. *Computer*, **26,** 39-51.

GROPP W., LUSK E. & SKJELLUM A., 1999. Using MPI: portable parallel programming with the message-passing interface, 1. MIT press.

GUGGENHEIM S. & MARTIN R. 1995. Definition of clay and clay mineral: joint report of the AIPEA nomenclature and CMS nomenclature committees. *Clays and Clay Minerals*, **43,** 255-256.

GULDBERG C.M. & WAAGE P., 1867. Etudes sur les affinités chimiques. Brøgger & Christie.

GUO Z., SHI B. & ZHENG C. 2002. A coupled lattice BGK model for the Boussinesq equations. *International Journal for Numerical Methods in Fluids*, **39,** 325-342.

GUO Z. & ZHAO T. 2002. Lattice Boltzmann model for incompressible flows through porous media. *Physical Review E*, **66,** 036304.

GUO Z. & ZHAO T. 2005. A lattice Boltzmann model for convection heat transfer in porous media. *Numerical Heat Transfer, Part B*, **47,** 157-177.

GUPTA R.N., YOS J.M., THOMPSON R.A. & LEE K.-P. 1990. A review of reaction rates and thermodynamic and transport properties for an 11-species air model for chemical and

thermal nonequilibrium calculations to 30000 K. *NASA STI/Recon Technical Report N*, **90,** 27064.

GUSTAFSON J.L. 1988. Reevaluating Amdahl's law. *Communications of the ACM*, **31,** 532-533.

HAHN G.M. & SHIU E.C. 1986. Adaptation to low pH modifies thermal and thermo-chemical responses of mammalian cells. *International journal of hyperthermia*, **2,** 379-387.

HALL S., BORNERT M., DESRUES J., PANNIER Y., LENOIR N., VIGGIANI G. & B SUELLE P. 2010. Discrete and continuum analysis of localised deformation in sand using X-ray μCT and volumetric digital image correlation. *Géotechnique*, **60,** 315-322.

HAN F., BUSCH A., KROOSS B.M., LIU Z., VAN WAGENINGEN N. & YANG J. 2010. Experimental study on fluid transport processes in the cleat and matrix systems of coal. *Energy & Fuels*, **24,** 6653-6661.

HART R. & ST JOHN C., 1986. Formulation of a fully-coupled thermal—mechanical—fluid flow model for non-linear geologic systems, International Journal of Rock Mechanics and Mining Sciences & Geomechanics Abstracts. Elsevier, pp. 213-224.

HART R.D. 1981. A fully coupled thermal-mechanical-fluid flow model for nonlinear geologic systems.

HE X., CHEN S. & DOOLEN G.D. 1998. A novel thermal model for the lattice Boltzmann method in incompressible limit. *Journal of Computational Physics*, **146,** 282-300.

HE X., ZOU Q., LUO L.-S. & DEMBO M. 1997. Analytic solutions of simple flows and analysis of nonslip boundary conditions for the lattice Boltzmann BGK model. *Journal of Statistical Physics*, **87,** 115-136.

HIRANANDANI S., KENNEDY K. & TSENG C.-W. 1991. Compiler support for machine-independent parallel programming in Fortran D.

HIRONO T., TAKAHASHI M. & NAKASHIMA S. 2003. In situ visualization of fluid flow image within deformed rock by X-ray CT. *Engineering Geology*, **70,** 37-46.

HIRSHFELD D. & RAPAPORT D. 1998. Molecular dynamics simulation of Taylor-Couette vortex formation. *Physical Review Letters*, **80,** 5337-5340.

HITCHON B. 1984. Geothermal gradients, hydrodynamics, and hydrocarbon occurrences, Alberta, Canada. *AAPG Bulletin*, **68,** 713-743.

HOBBS B., ZHANG Y., ORD A. & ZHAO C. 2000. Application of coupled deformation, fluid flow, thermal and chemical modelling to predictive mineral exploration. *Journal of Geochemical Exploration*, **69,** 505-509.

HOCKNEY R.W. & JESSHOPE C.R., 1988. Parallel Computers 2: architecture, programming and algorithms, 2. CRC Press.

HOOGERBRUGGE P. & KOELMAN J. 1992. Simulating microscopic hydrodynamic phenomena with dissipative particle dynamics. *EPL (Europhysics Letters)*, **19,** 155.

HORTMANN M., PERIĆ M. & SCHEUERER G. 1990. Finite volume multigrid prediction of laminar natural convection: Bench‐mark solutions. *International Journal for Numerical Methods in Fluids*, **11,** 189-207.

HOU J., LI Z., ZHANG S., CAO X., DU Q. & SONG X. 2009. Computerized tomography study of the microscopic flow mechanism of polymer flooding. *Transport in porous media*, **79,** 407-418.

HUERTA N.J., HESSE M.A., BRYANT S.L., STRAZISAR B.R. & LOPANO C.L. 2012. Experimental evidence for self-limiting reactive flow through a fractured cement core: Implications for time-dependent wellbore leakage. *Environmental science & technology*, **47,** 269-275.

HUYAKORN P.S., 1983. Computational methods in subsurface flow. Academic Press.

HUYAKORN P.S. & PINDER G.F. 1986. Computational methods in subsurface flow.

INCROPERA F.P., 2011. Introduction to heat transfer. John Wiley & Sons.

INGHAM D.B. & POP I., 2005. Transport phenomena in porous media III, 3. Elsevier.

ITOI E., LEE S.-B., AMRAMI K.K., WENGER D.E. & AN K.-N. 2003. Quantitative assessment of classic anteroinferior bony Bankart lesions by radiography and computed tomography. *The American journal of sports medicine*, **31,** 112-118.

JACKSON M., GALLAGHER K., PETFORD N. & CHEADLE M. 2005. Towards a coupled physical and chemical model for tonalite–trondhjemite–granodiorite magma formation. *Lithos*, **79,** 43-60.

JIANG X. 2011. A review of physical modelling and numerical simulation of long-term geological storage of CO< sub> 2</sub>. *Applied Energy*, **88,** 3557-3566.

JING L. 2003. A review of techniques, advances and outstanding issues in numerical modelling for rock mechanics and rock engineering. *International Journal of Rock Mechanics and Mining Sciences*, **40,** 283-353.

JOEKAR NIASAR V., HASSANIZADEH S., PYRAK ‐ NOLTE L. & BERENTSEN C. 2009. Simulating drainage and imbibition experiments in a high ‐ porosity micromodel using an unstructured pore network model. *Water resources research*, **45,**

JOSEPH D., NIELD D. & PAPANICOLAOU G. 1982. Nonlinear equation governing flow in a saturated porous medium. *Water Resources Research*, **18,** 1049-1052.

JOSEPH D., NIELD D., PAPANICOLAOU G., ENGINEERING M.U.M.D.O.A. & MECHANICS., 1981. Nonlinear equation governing flow in a saturated porous medium. Defense Technical Information Center.

JUANES R., MACMINN C.W. & SZULCZEWSKI M.L. 2010. The footprint of the CO2 plume during carbon dioxide storage in saline aquifers: storage efficiency for capillary trapping at the basin scale. *Transport in porous media*, **82,** 19-30.

JUANES R., SPITERI E., ORR F. & BLUNT M. 2006. Impact of relative permeability hysteresis on geological CO2 storage. *Water Resources Research*, **42,**

KALENDER W.A. 2006. X-ray computed tomography. *Physics in medicine and biology*, **51,** R29.

KANDHAI D., KOPONEN A., HOEKSTRA A.G., KATAJA M., TIMONEN J. & SLOOT P.M. 1998. Lattice-Boltzmann hydrodynamics on parallel systems. *Computer Physics Communications*, **111,** 14-26.

KANG Q., LICHTNER P.C. & JANECKY D.R., 2010a. Lattice Boltzmann method for reacting flows in porous media, The 3rd USGS Modeling Conference.

KANG Q., LICHTNER P.C., VISWANATHAN H.S. & ABDEL-FATTAH A.I. 2010b. Pore scale modeling of reactive transport involved in geologic CO2 sequestration. *Transport in porous media*, **82,** 197-213.

KANG Q., LICHTNER P.C. & ZHANG D. 2007. An improved lattice Boltzmann model for multicomponent reactive transport in porous media at the pore scale. *Water Resources Research*, **43,**

KANG Q., ZHANG D. & CHEN S. 2002a. Unified lattice Boltzmann method for flow in multiscale porous media. *Physical Review E*, **66,** 056307.

KANG Q., ZHANG D., CHEN S. & HE X. 2002b. Lattice Boltzmann simulation of chemical dissolution in porous media. *Physical Review E*, **65,** 036318.

KANIT T., FOREST S., GALLIET I., MOUNOURY V. & JEULIN D. 2003. Determination of the size of the representative volume element for random composites: statistical and numerical approach. *International Journal of solids and structures*, **40,** 3647-3679.

KARACAN C.Ö. 2007. Swelling-induced volumetric strains internal to a stressed coal associated with CO< sub> 2</sub> sorption. *International Journal of Coal Geology*, **72,** 209-220.

KARACAN C.Ö. 2009. Reservoir rock properties of coal measure strata of the Lower Monongahela Group, Greene County (Southwestern Pennsylvania), from methane control and production perspectives. *International Journal of Coal Geology*, **78,** 47-64.

KARAJ S. & M LLER J. 2011. Optimizing mechanical oil extraction of< i> Jatropha curcas</i> L. seeds with respect to press capacity, oil recovery and energy efficiency. *Industrial Crops and Products*, **34,** 1010-1016.

KARLSSON S. & BRORSSON M., 2004. A free OpenMP compiler and run-time library infrastructure for research on shared memory parallel computing, Proceedings of the 16th IASTED International Conference on Parallel and Distributed Computing and Systems, pp. 354-361.

KASZUBA J.P., JANECKY D.R. & SNOW M.G. 2003. Carbon dioxide reaction processes in a model brine aquifer at 200 C and 200 bars: implications for geologic sequestration of carbon. *Applied Geochemistry*, **18,** 1065-1080.

KAUFMAN W.J. & ORLOB G.T. 1956. Measuring ground water movement with radioactive and chemical tracers. *Journal (American Water Works Association)*559-572.

KEATING E.H., NEWELL D.L., VISWANATHAN H., CAREY J., ZYVOLOSKI G. & PAWAR R. 2012. CO2/brine transport into shallow aquifers along fault zones. *Environmental science & technology*, **47,** 290-297.

KEBLINSKI P., PHILLPOT S., CHOI S. & EASTMAN J. 2002. Mechanisms of heat flow in suspensions of nano-sized particles (nanofluids). *International journal of heat and mass transfer*, **45,** 855-863.

KELEMEN P.B., WHITEHEAD J., AHARONOV E. & JORDAHL K.A. 1995. Experiments on flow focusing in soluble porous media, with applications to melt extraction from the mantle. *Journal of Geophysical Research: Solid Earth (1978–2012)*, **100,** 475-496.

KHALILI A.D., ARNS C.H., ARNS J.-Y., HUSSAIN F., CINAR Y., PINCZEWSKI W.V., LATHAM S. & FUNK J., 2012. Permeability upscaling for carbonates from the pore-scale using multi-scale Xray-CT images, SPE/EAGE European Unconventional Resources Conference & Exhibition-From Potential to Production.

KHAN M. & TEUFEL L. 2000. The effect of geological and geomechanical parameters on reservoir stress path and its importance in studying permeability anisotropy. *SPE Reservoir Evaluation & Engineering*, **3,** 394-400.

KINGDON R. & SCHOFIELD P. 1992. A reaction-flow lattice Boltzmann model. *Journal of Physics A: Mathematical and General*, **25,** L907.

KINNON E., GOLDING S., BOREHAM C., BAUBLYS K. & ESTERLE J. 2010. Stable isotope and water quality analysis of coal bed methane production waters and gases from the Bowen Basin, Australia. *International Journal of Coal Geology*, **82,** 219-231.

KIRK D.B. & WEN-MEI W.H., 2012. Programming massively parallel processors: a hands-on approach. Newnes.

KISH L.B. 2002. End of Moore's law: thermal (noise) death of integration in micro and nano electronics. *Physics Letters A*, **305,** 144-149.

KISSINGER H.E. 1957. Reaction kinetics in differential thermal analysis. *Analytical chemistry*, **29,** 1702-1706.

KNACKSTEDT M., ARNS C., GHOUS A., SAKELLARIOU A., SENDEN T., SHEPPARD A., SOK R., AVERDUNK H., PINCZEWSKI W.V. & PADHY G.S. 2006. 3D imaging and flow characterization of the pore space of carbonate core samples.

KNACKSTEDT M., GOLAB A. & RIEPE L., 2012. Petrophysical characterization of unconventional reservoir core at multiple scales, SPWLA 53rd Annual Logging Symposium. Society of Petrophysicists and Well-Log Analysts.

KNACKSTEDT M.A., LATHAM S., MADADI M., SHEPPARD A., VARSLOT T. & ARNS C. 2009. Digital rock physics: 3D imaging of core material and correlations to acoustic and flow properties. *The Leading Edge*, **28,** 28-33.

KOELBEL C. & MEHROTRA P. 1991. Compiling global name-space parallel loops for distributed execution. *Parallel and Distributed Systems, IEEE Transactions on*, **2,** 440-451.

KOH J., ROSHAN H. & RAHMAN S.S. 2011. A numerical study on the long term thermo-poroelastic effects of cold water injection into naturally fractured geothermal reservoirs. *Computers and Geotechnics*, **38,** 669-682.

KOPANIDIS A., THEODORAKAKOS A., GAVAISES E. & BOURIS D. 2010. 3D numerical simulation of flow and conjugate heat transfer through a pore scale model of high porosity open cell metal foam. *International Journal of Heat and Mass Transfer*, **53,** 2539-2550.

KOPLIK J., BANAVAR J.R. & WILLEMSEN J.F. 1988. Molecular dynamics of Poiseuille flow and moving contact lines. *Physical Review Letters*, **60,** 1282-1285.

KOUZNETSOVA V., GEERS M. & BREKELMANS W. 2004. Multi-scale second-order computational homogenization of multi-phase materials: a nested finite element solution strategy. *Computer methods in applied mechanics and engineering*, **193,** 5525-5550.

KUMAR V., GRAMA A., GUPTA A. & KARYPIS G., 1994. Introduction to parallel computing: design and analysis of algorithms. Benjamin/Cummings Publishing Company Redwood City, CA.

KUZNETSOV A. 1998. Analytical investigation of Couette flow in a composite channel partially filled with a porous medium and partially with a clear fluid. *International journal of heat and mass transfer*, **41,** 2556-2560.

LAPWOOD E. 1948. Convection of a fluid in a porous medium. *Proceedings of the Cambridge*

LARSON B., YANG W., ICE G., BUDAI J. & TISCHLER J. 2002. Three-dimensional X-ray structural microscopy with submicrometre resolution. *Nature*, **415,** 887-890.

LATHAM S., VARSLOT T. & SHEPPARD A., 2008. Image registration: Enhancing and calibrating X-ray micro-CT imaging, Proceedings of the International Symposium of the Society of Core Analysts. SCA2008-35. Abu Dhabi, United Arab Emirates.

LEIGHTON F.T., 1992. Introduction to parallel algorithms and architectures. Kaufmann.

LERMAN A., 1979. Geochemical processes. Water and sediment environments. John Wiley and Sons, Inc.

LEVENSPIEL O., 1972. Chemical reaction engineering, 2. Wiley New York etc.

LEVENSPIEL O. 1999. Chemical reaction engineering. *Industrial & engineering chemistry research*, **38,** 4140-4143.

LEVINE J.R. 1993. Coalification: The Evolution of Coal as Source Rock and Reservoir Rock for Oil and Gas: Chapter 3.

LEWIS R.W., NITHIARASU P., SEETHARAMU K.N., WILEY J. & SONS I., 2004. Fundamentals of the finite element method for heat and fluid flow. Wiley Online Library.

LI K., 1988. IVY: A Shared Virtual Memory System for Parallel Computing, ICPP (2), pp. 94-101.

LI Q., HE Y., TANG G. & TAO W. 2011. Lattice Boltzmann modeling of microchannel flows in the transition flow regime. *Microfluidics and nanofluidics*, **10,** 607-618.

LI X., LIN C.-L., MILLER J.D. & JOHNSON W.P. 2006. Pore-scale observation of microsphere deposition at grain-to-grain contacts over assemblage-scale porous media domains using X-ray microtomography. *Environmental science & technology*, **40,** 3762-3768.

LI X., ZHU D., WANG X., WANG N., GAO J. & LI H. 2008. Thermal conductivity enhancement dependent pH and chemical surfactant for Cu-H< sub> 2</sub> O nanofluids. *Thermochimica Acta*, **469,** 98-103.

LINGARD P., PHILLIPS H. & DOIG I., 1984. Laboratory studies of the sorption characteristics and permeability of triaxially stressed coal samples, Proceeding 3rd Int. congress on mine ventilation, Harrogate, pp. 143-150.

LISHMAN J. 1970. Core permeability anisotropy. *Journal of Canadian Petroleum Technology*, **9,**

LIU C., WANG G., SANG S. & RUDOLPH V. 2010. Changes in pore structure of anthracite coal associated with CO< sub> 2</sub> sequestration process. *Fuel*, **89,** 2665-2672.

LIU X., ORMOND A., BARTKO K., YING L. & ORTOLEVA P. 1997. A geochemical reaction-transport simulator for matrix acidizing analysis and design. *Journal of Petroleum Science and Engineering*, **17,** 181-196.

LOUCKS R.G., REED R.M., RUPPEL S.C. & JARVIE D.M. 2009. Morphology, genesis, and distribution of nanometer-scale pores in siliceous mudstones of the Mississippian Barnett Shale. *Journal of Sedimentary Research*, **79,** 848-861.

LUHMANN A., DING K., SAAR M. & SEYFRIED W., 2011. Effects of small-scale chemical reactions between supercritical CO2 and arkosic sandstone on large-scale permeability fields: An experimental study with implications for geologic carbon sequestration, AGU Fall Meeting Abstracts, pp. 1261.

LUND K., FOGLER H.S., MCCUNE C. & AULT J. 1975. Acidizationā€" II. The dissolution of calcite in hydrochloric acid. *Chemical Engineering Science*, **30,** 825-835.

LUO L.-S., LIAO W., CHEN X., PENG Y. & ZHANG W. 2011. Numerics of the lattice Boltzmann method: Effects of collision models on the lattice Boltzmann simulations. *Physical Review E,* **83,** 056710.

M HEUST Y. & SCHMITTBUHL J. 2001. Geometrical heterogeneities and permeability anisotropy of rough fractures. *Journal of Geophysical Research: Solid Earth (1978–2012)*, **106,** 2089-2102.

MAGNICO P. 2009. Pore‐scale simulations of unsteady flow and heat transfer in tubular fixed beds. *AIChE journal*, **55,** 849-867.

MANN C.C. 2000. The End of Moores Law. *Technology Review*, **103,** 42-48.

MARSHALL J., ADCROFT A., HILL C., PERELMAN L. & HEISEY C. 1997. A finite‐volume, incompressible Navier Stokes model for studies of the ocean on parallel computers. *Journal of Geophysical Research: Oceans (1978–2012)*, **102,** 5753-5766.

MARTYS N., BENTZ D. & GARBOCZI E. 1994. Computer simulation study of the effective viscosity in Brinkman's equation. *Physics of Fluids*, **6,** 1434.

MASSAROTTO P., GOLDING S., BAE J.-S., IYER R. & RUDOLPH V. 2010. Changes in reservoir properties from injection of supercritical CO< sub> 2</sub> into coal seams—A laboratory study. *International Journal of Coal Geology*, **82,** 269-279.

MASSAROTTO P., GOLDING S.D. & RUDOLPH V., 2009a. Constant volume CBM reservoirs: an important principle, 2009 International Coalbed and Shale Gas Symposium/RPSEA Forum. University of Alabama.

MASSAROTTO P., GOLDING S.D. & RUDOLPH V., 2009b. Dynamic 4D coal permeability: Benefits of a constant volume reservoir, 2009 Asia Pacific Coalbed Methane Symposium and 2009 China Coalbed Symposium. China University of Mining and Technology Press, pp. 271-286.

MASSAROTTO P., IYER R.S., ELMA M. & NICHOLSON T. 2014. An Experimental Study on Characterizing Coal Bed Methane (CBM) Fines Production and Migration of Mineral Matter in Coal Beds. *Energy & Fuels*, **28,** 766-773.

MASSAROTTO P., RUDOLPH V. & GOLDING S., 2001. 4-D Permeability Characterisation of Coal Enhances Exploration & Production of CBM, 2001 International Coalbed Methane Symposium. University of Alabama, pp. 1-11.

MASSAROTTO P., RUDOLPH V. & GOLDING S., 2003a. Anisotropic permeability characterisation of Permian coals, Proceedings of the International CBM Symposium, University of Alabama, Tuscaloosa, USA.

MASSAROTTO P., RUDOLPH V., GOLDING S. & IYER R. 2003b. The effect of directional net stresses on the directional permeability of coal. *paper*, **358,** 7-8.

MAZUMDER S., WOLF K.-H., ELEWAUT K. & EPHRAIM R. 2006. Application of X-ray computed tomography for analyzing cleat spacing and cleat aperture in coal samples. *International Journal of Coal Geology*, **68,** 205-222.

MAZZEO M.D. & COVENEY P.V. 2008. HemeLB: A high performance parallel lattice-Boltzmann code for large scale fluid flow in complex geometries. *Computer Physics Communications*, **178,** 894-914.

MCCRACKEN M.E. & ABRAHAM J. 2005. Multiple-relaxation-time lattice-Boltzmann model for multiphase flow. *Physical Review E*, **71,** 036701.

MCKEE C., BUMB A. & KOENIG R. 1988. Stress-dependent permeability and porosity of coal and other geologic formations. *SPE formation evaluation*, **3,** 81-91.

MEAKIN P. & TARTAKOVSKY A.M. 2009. Modeling and simulation of pore-scale multiphase fluid flow and reactive transport in fractured and porous media. *Reviews of Geophysics*, **47,** RG3002.

MEINZER O.E. 1923. Outline of ground-water hydrology. *US Geology Survey Water Supply*, **8,**

MICHAEL K., GOLAB A., SHULAKOVA V., ENNIS-KING J., ALLINSON G., SHARMA S. & AIKEN T. 2010. Geological storage of CO< sub> 2</sub> in saline aquifers—A review of the experience from existing storage operations. *International Journal of Greenhouse Gas Control*, **4,** 659-667.

MIGDALAS A., PARDALOS P.M. & STORY S., 2012. Parallel computing in optimization. Springer Publishing Company, Incorporated.

MITCHELL J.K., HOOPER D.R. & CAMPANELLA R.G. 1900. Permeability of compacted clay. *Journal of Soil Mechanics & Foundations Div*, **92,**

MOKHATAB S. & POE W.A., 2012. Handbook of natural gas transmission and processing. Gulf Professional Publishing.

MOLERO G MEZ A., PEREYRA L PEZ C. & MARTINEZ DE LA OSSA E. 1996. Recovery of grape seed oil by liquid and supercritical carbon dioxide extraction: a comparison with conventional solvent extraction. *The Chemical Engineering Journal and the Biochemical Engineering Journal*, **61,** 227-231.

MOONEY S., PRIDMORE T., HELLIWELL J. & BENNETT M. 2012. Developing X-ray Computed Tomography to non-invasively image 3-D root systems architecture in soil. *Plant and soil*, **352,** 1-22.

MOORE G.E., 1965. Cramming more components onto integrated circuits. McGraw-Hill New York, NY, USA.

MORANDI CECCHI M. & FORNASIER M. 2005. Fast homogenization algorithm based on asymptotic theory and multiscale schemes. *Numerical Algorithms*, **40,** 171-186.

MUMALLAH N., 1991. Factors influencing the reaction rate of hydrochloric acid and carbonate rock, SPE International Symposium on Oilfield Chemistry. Society of Petroleum Engineers.

MYRE J., WALSH S.D., LILJA D. & SAAR M.O. 2011. Performance analysis of single ‐ phase, multiphase, and multicomponent lattice ‐ Boltzmann fluid flow simulations on GPU clusters. *Concurrency and Computation: Practice and Experience*, **23,** 332-350.

NAKAJIMA K. 2002. Parallel multilevel iterative linear solvers with unstructured adaptive grids for simulations in earth science. *Concurrency and Computation: Practice and Experience*, **14,** 483-498.

NAKAJIMA K., 2003. Parallel iterative solvers of geofem with selective blocking preconditioning for nonlinear contact problems on the earth simulator, Supercomputing, 2003 ACM/IEEE Conference. IEEE, pp. 13-13.

NCI. http://nci.org.au/nci-systems/national-facility/peak-system/raijin/.

NEDKVITNE T., KARLSEN D.A., BJ RLYKKE K. & LARTER S.R. 1993. Relationship between reservoir diagenetic evolution and petroleum emplacement in the Ula Field, North Sea. *Marine and Petroleum Geology*, **10,** 255-270.

NESIĆ S., POSTLETHWAITE J. & VRHOVAC M., 1997. CO2 corrosion of carbon steel-from mechanistic to empirical modelling.

NEUZIL C. 1994. How permeable are clays and shales? *Water resources research*, **30,** 145-150.

NIELD D.A. & BEJAN A., 2006. Convection in porous media. springer.

NITHIARASU P., SEETHARAMU K. & SUNDARARAJAN T. 1997. Natural convective heat transfer in a fluid saturated variable porosity medium. *International Journal of Heat and Mass Transfer*, **40,** 3955-3967.

OGAWA M. 1994. Effects of chemical fractionation of heat-producing elements on mantle evolution inferred from a numerical model of coupled magmatism-mantle convection system. *Physics of the earth and planetary interiors*, **83,** 101-127.

OKABE H. & BLUNT M.J. 2005. Pore space reconstruction using multiple-point statistics. *Journal of Petroleum Science and Engineering*, **46,** 121-137.

OLSON C.F. 1995. Parallel algorithms for hierarchical clustering. *Parallel computing*, **21,** 1313-1325.

OR D. & TULLER M. 2000. Flow in unsaturated fractured porous media: Hydraulic conductivity of rough surfaces. *Water Resources Research*, **36,** 1165-1177.

ORD A., HOBBS B.E. & LESTER D.R. 2012. The mechanics of hydrothermal systems: I. Ore systems as chemical reactors. *Ore geology reviews*, **49,** 1-44.

OREN P.E., BAKKE S. & ARNTZEN O.J. 1998. Extending predictive capabilities to network models. *SPE Journal*, **3,** 324-336.

ORMOND A. & ORTOLEVA P. 2000. Numerical modeling of reaction‐induced cavities in a porous rock. *Journal of Geophysical Research: Solid Earth (1978–2012)*, **105,** 16737-16747.

ORTOLEVA P., CHADAM J., MERINO E. & SEN A. 1987. Geochemical self-organization II: the reactive-infiltration instability. *Am. J. Sci*, **287,** 1008-1040.

PALMER C.D., BLOWES D.W., FRIND E.O. & MOLSON J.W. 1992. Thermal energy storage in an unconfined aquifer: 1. Field injection experiment. *Water Resources Research*, **28,** 2845-2856.

PALMER I. 2010. Coalbed methane completions: a world view. *International Journal of Coal Geology*, **82,** 184-195.

PAN C., LUO L.-S. & MILLER C.T. 2006. An evaluation of lattice Boltzmann schemes for porous medium flow simulation. *Computers & fluids*, **35,** 898-909.

PAN C., PRINS J.F. & MILLER C.T. 2004. A high-performance lattice Boltzmann implementation to model flow in porous media. *Computer Physics Communications*, **158,** 89-105.

PAN Z. & CONNELL L.D. 2007. A theoretical model for gas adsorption-induced coal swelling. *International Journal of Coal Geology*, **69,** 243-252.

PAN Z. & CONNELL L.D. 2009. Comparison of adsorption models in reservoir simulation of enhanced coalbed methane recovery and CO< sub> 2</sub> sequestration in coal. *International journal of greenhouse gas control*, **3,** 77-89.

PAN Z. & CONNELL L.D. 2011a. Impact of coal seam as interlayer on CO< sub> 2</sub> storage in saline aquifers: A reservoir simulation study. *International Journal of Greenhouse Gas Control*, **5,** 99-114.

PAN Z. & CONNELL L.D. 2011b. Modelling of anisotropic coal swelling and its impact on permeability behaviour for primary and enhanced coalbed methane recovery. *International Journal of Coal Geology*, **85,** 257-267.

PAN Z. & CONNELL L.D. 2012. Modelling permeability for coal reservoirs: a review of analytical models and testing data. *International Journal of Coal Geology*, **92,** 1-44.

PAN Z., CONNELL L.D. & CAMILLERI M. 2010. Laboratory characterisation of coal reservoir permeability for primary and enhanced coalbed methane recovery. *International Journal of Coal Geology*, **82,** 252-261.

PANT L.M., MITRA S.K. & SECANELL M. 2012. Absolute permeability and Knudsen diffusivity measurements in PEMFC gas diffusion layers and micro porous layers. *Journal of power sources*, **206,** 153-160.

PARK Y., DEANS H. & TEZDUYAR T. 1991. Thermal Effects on Single-Well Chemical-Tracer Tests for Measuring Residual Oil Saturation. *SPE Formation Evaluation*, **6,** 401-408.

PARKHURST D.L. & APPELO C. 1999. User's guide to PHREEQC (Version 2): A computer program for speciation, batch-reaction, one-dimensional transport, and inverse geochemical calculations.

PARRA J.O. 2000. Poroelastic model to relate seismic wave attenuation and dispersion to permeability anisotropy. *Geophysics*, **65,** 202-210.

PASTERNAK E. & M HLHAUS H.B. 2005. Generalised homogenisation procedures for granular materials. *Mathematics and Mechanics of Granular Materials*199-229.

PATERSON L. 1984. Diffusion-limited aggregation and two-fluid displacements in porous media. *Physical Review Letters*, **52,** 1621-1624.

PATRICK R., FORD E. & QUARLES J., 1987. Groundwater contamination in the United States. University of Pennsylvania Press.

PATZEK T. 2001. Verification of a complete pore network simulator of drainage and imbibition. *SPE Journal*, **6,** 144-156.

PEARCE J., BIDDLE D., GOLDING S., RUDOLPH V. & KIRSTE D. 2012. Mineral, fluid and gas interactions under CO2 storage conditions–the role of SO2, NOX, and O2. *Mineralogical Magazine*, **76,** 2214-2214.

PEARCE J., DAWSON G., FARQUHAR S. & GOLDING S., 2013. SO2 and O2 co-injection with potential carbon storage target sandstone from a fresh-water aquifer, Mineralogical Magazine. Mineralogical Society, pp. 1942-1942.

PEARCE J.K., GOLDING S.D., FRANK A. & KIRSTE D. 2014. SOX and O2 co-contaminant impacts in geological carbon storage. *CO2CRC Report RPT13-4173*

PEARCE J.K., GOLDING, S. D., BIDDLE, D. AND RUDOLPH, V. 2012. CO2CRC Report RPT12-3804:Implementation of a reaction rig for CO2-SOx-O2-brine-rock interaction experiments St Lucia, QLD Australia: The University of Queensland, School of Chemistry and Molecular Biosciences

PEREA-REEVES S.J. & STOCKMAN H.W. 1997. A lattice-gas study of dispersion in alveolated channels. *Chemical engineering science*, **52,** 3277-3286.

PERRIN J.-C. & BENSON S. 2010. An experimental study on the influence of sub-core scale heterogeneities on CO2 distribution in reservoir rocks. *Transport in porous media*, **82,** 93-109.

PEYRET R. & TAYLOR T.D. 1985. Computational methods for fluid flow. *Shock and Vibration*, **1,**

PIRRIE D., BUTCHER A.R., POWER M.R., GOTTLIEB P. & MILLER G.L. 2004. Rapid quantitative mineral and phase analysis using automated scanning electron microscopy (QemSCAN); potential applications in forensic geoscience. *Geological Society, London, Special Publications*, **232,** 123-136.

PLIMPTON S. 1995. Fast parallel algorithms for short-range molecular dynamics. *Journal of Computational Physics*, **117,** 1-19.

PLUMMER L., WIGLEY T. & PARKHURST D. 1978. The kinetics of calcite dissolution in CO 2-water systems at 5 degrees to 60 degrees C and 0.0 to 1.0 atm CO 2. *American Journal of Science*, **278,** 179-216.

POHL T., DESERNO F., THUREY N., RUDE U., LAMMERS P., WELLEIN G. & ZEISER T., 2004. Performance evaluation of parallel large-scale lattice Boltzmann applications on three supercomputing architectures, Proceedings of the 2004 ACM/IEEE conference on Supercomputing. IEEE Computer Society, pp. 21.

POHL T., KOWARSCHIK M., WILKE J., IGLBERGER K. & R DE U. 2003. Optimization and profiling of the cache performance of parallel lattice Boltzmann codes. *Parallel Processing Letters*, **13,** 549-560.

POKROVSKY O.S., GOLUBEV S.V. & SCHOTT J. 2005. Dissolution kinetics of calcite, dolomite and magnesite at 25 °C and 0 to 50 atm< i> p</i> CO< sub> 2</sub>. *Chemical geology*, **217,** 239-255.

POKROVSKY O.S., GOLUBEV S.V., SCHOTT J. & CASTILLO A. 2009. Calcite, dolomite and magnesite dissolution kinetics in aqueous solutions at acid to circumneutral pH, 25 to 150 ° C and 1 to 55 atm< i> p</i> CO< sub> 2</sub>: New constraints on CO< sub> 2</sub> sequestration in sedimentary basins. *Chemical geology*, **265,** 20-32.

PONE J.D.N., HALLECK P.M. & MATHEWS J.P. 2010. 3D characterization of coal strains induced by compression, carbon dioxide sorption, and desorption at in-situ stress conditions. *International Journal of Coal Geology*, **82,** 262-268.

PONE J.D.N., HILE M., HALLECK P.M. & MATHEWS J.P. 2009. Three-dimensional carbon dioxide-induced strain distribution within a confined bituminous coal. *International Journal of Coal Geology*, **77,** 103-108.

PRAT M. 2002. Recent advances in pore-scale models for drying of porous media. *Chemical engineering journal*, **86,** 153-164.

PREMNATH K.N. & ABRAHAM J. 2007. Three-dimensional multi-relaxation time (MRT) lattice-Boltzmann models for multiphase flow. *Journal of Computational Physics*, **224,** 539-559.

QIAN Y., D'HUMIERES D. & LALLEMAND P. 1992. Lattice BGK models for Navier-Stokes equation. *EPL (Europhysics Letters)*, **17,** 479.

QU H., LIU J., CHEN Z., WANG J., PAN Z., CONNELL L. & ELSWORTH D. 2012. Complex evolution of coal permeability during CO< sub> 2</sub> injection under variable temperatures. *International Journal of Greenhouse Gas Control*, **9,** 281-293.

RAABE D. 2004. Overview of the lattice Boltzmann method for nano-and microscale fluid dynamics in materials science and engineering. *Modelling and Simulation in Materials Science and Engineering*, **12,** R13.

RAHMAN S.S., 2000. A 3-D Numerical Model for Designing and Planning of Matrix Acid Stimulation in Low-Permeability Rocks, SPE Asia Pacific Oil and Gas Conference and Exhibition. Society of Petroleum Engineers.

RASOLOFOSAON P.N. & ZINSZNER B.E. 2002. Comparison between permeability anisotropy and elasticity anisotropy of reservoir rocks. *Geophysics*, **67,** 230-240.

RAYNAUD S., FABRE D., MAZEROLLE F., GERAUD Y. & LATI RE H.J. 1989. Analysis of the internal structure of rocks and characterization of mechanical deformation by a non-destructive method: X-ray tomodensitometry. *Tectonophysics*, **159,** 149-159.

REDDY J.N. & GARTLING D.K., 2010. The finite element method in heat transfer and fluid dynamics. CRC.

REICHENBERGER V., JAKOBS H., BASTIAN P. & HELMIG R. 2006. A mixed-dimensional finite volume method for two-phase flow in fractured porous media. *Advances in Water Resources*, **29,** 1020-1036.

ROBERTSON E.P., 2005. Measurement and modeling of sorption-induced strain and permeability changes in coal. United States. Department of Energy.

RODGERS D.P., 1985. Improvements in multiprocessor system design, ACM SIGARCH Computer Architecture News. IEEE Computer Society Press, pp. 225-231.

ROSE W., 1982. Permeability anisotropy in low permeability formations, SPE Unconventional Gas Recovery Symposium. Society of Petroleum Engineers.

ROSHAN H. & RAHMAN S. 2013. Effects of Ion Advection and Thermal Convection on Pore Pressure Changes in High Permeable Chemically Active Shale Formations. *Petroleum Science and Technology*, **31,** 727-737.

S EZ A. & TOLEDO M. 2009. Thermal effect of the adsorption heat on an adsorbed natural gas storage and transportation systems. *Applied Thermal Engineering*, **29,** 2617-2623.

SAHIMI M., 2011. Flow and transport in porous media and fractured rock: From classical methods to modern approaches. Wiley-VCH.

SANTSCHI C. & ROSSI M. 2006. Uptake of CO2, SO2, HNO3 and HCl on calcite (CaCO3) at 300 K: Mechanism and the role of adsorbed water. *The Journal of Physical Chemistry A*, **110,** 6789-6802.

SAPTORO A., VUTHALURU H. & TAD M., 2006. A comparative study of prediction of elemental composition of coal using empirical modelling, Proceedings of the IFAC Symposium on Advanced Control of Chemical Processes.

SCHALLER R.R. 1997. Moore's law: past, present and future. *Spectrum, IEEE*, **34,** 52-59.

SCHERER M.M., RICHTER S., VALENTINE R.L. & ALVAREZ P.J. 2000. Chemistry and microbiology of permeable reactive barriers for in situ groundwater clean up. *Critical reviews in microbiology*, **26,** 221-264.

SEETHARAM S., THOMAS H. & CLEALL P. 2007. Coupled thermo/hydro/chemical/mechanical model for unsaturated soils—numerical algorithm. *International journal for numerical methods in engineering*, **70,** 1480-1511.

SEIDLE J., JEANSONNE M. & ERICKSON D., 1992. Application of matchstick geometry to stress dependent permeability in coals, SPE rocky mountain regional meeting. Society of Petroleum Engineers.

SHAIK A.R., RAHMAN S.S., TRAN N.H. & TRAN T. 2011. Numerical simulation of fluid-rock coupling heat transfer in naturally fractured geothermal system. *Applied Thermal Engineering*, **31,** 1600-1606.

SHIPTON Z.K., EVANS J.P., KIRSCHNER D., KOLESAR P.T., WILLIAMS A.P. & HEATH J. 2004. Analysis of CO2 leakage through 'low-permeability'faults from natural reservoirs in the Colorado Plateau, east-central Utah. *Geological Society, London, Special Publications*, **233,** 43-58.

SHOKOUHMAND H., JAM F. & SALIMPOUR M. 2009. Simulation of laminar flow and convective heat transfer in conduits filled with porous media using Lattice Boltzmann Method. *International Communications in Heat and Mass Transfer*, **36,** 378-384.

SINHA P.K., HALLECK P. & WANG C.-Y. 2006. Quantification of liquid water saturation in a PEM fuel cell diffusion medium using X-ray microtomography. *Electrochemical and Solid-State Letters*, **9,** A344-A348.

SINHA P.K. & WANG C.-Y. 2007. Pore-network modeling of liquid water transport in gas diffusion layer of a polymer electrolyte fuel cell. *Electrochimica Acta*, **52,** 7936-7945.

SLOAN E.D. 2003. Fundamental principles and applications of natural gas hydrates. *Nature*, **426,** 353-363.

SNOW D.T. 1969. Anisotropie permeability of fractured media. *Water Resources Research*, **5,** 1273-1289.

SOK R.M., VARSLOT T., GHOUS A., LATHAM S., SHEPPARD A.P. & KNACKSTEDT M.A. 2010. Pore Scale Characterization of Carbonates at Multiple Scales: Integration of Micro-CT, BSEM, FIBSEM. *Petrophysics*, **51,** 379.

SOMERTON W.H., S YLEMEZOĞLU I. & DUDLEY R., 1975. Effect of stress on permeability of coal, International journal of rock mechanics and mining sciences & geomechanics abstracts. Elsevier, pp. 129-145.

SPAID M.A. & PHELAN JR F.R. 1997. Lattice Boltzmann methods for modeling microscale flow in fibrous porous media. *Physics of Fluids*, **9,** 2468.

SPERA F.J., YUEN D.A. & KIRSCHVINK S.J. 1982. Thermal boundary layer convection in silicic magma chambers: Effects of temperature‐dependent rheology and implications for thermogravitational chemical fractionation. *Journal of Geophysical Research: Solid Earth (1978–2012)*, **87,** 8755-8767.

SPITERI E., JUANES R., BLUNT M.J. & ORR F.M., 2005. Relative-Permeability Hysteresis: Trapping Models and Application to Geological CO2 Sequestration, SPE Annual Technical Conference and Exhibition. Society of Petroleum Engineers.

STEEFEL C.I. & LASAGA A.C. 1994. A coupled model for transport of multiple chemical species and kinetic precipitation/dissolution reactions with application to reactive flow in single phase hydrothermal systems. *American Journal of Science*, **294,** 529-592.

STOCKMAN H.W. 1997. A lattice gas study of retardation and dispersion in fractures: Assessment of errors from desorption kinetics and buoyancy. *Water Resources Research*, **33,** 1823-1831.

STRAZISAR B., KUTCHKO B. & HUERTA N. 2009. Chemical Reactions of Wellbore Cement Under CO< sub> 2</sub> Storage Conditions: Effects of Cement Additives. *Energy Procedia*, **1,** 3603-3607.

SUCCI S., 2001. The lattice Boltzmann equation: for fluid dynamics and beyond. Oxford university press.

SUGITA F., GILLHAM R.W. & MASE C. 1995. Pore scale variation in retardation factor as a cause of nonideal reactive breakthrough curves: 2. Pore network analysis. *Water Resources Research*, **31,** 113-119.

SUGITA T., SATO T., HIRABAYASHI S., NAGAO J., JIN Y., KIYONO F., EBINUMA T. & NARITA H. 2012. A pore-scale numerical simulation method for estimating the permeability of sand sediment. *Transport in porous media*, **94,** 1-17.

SUKOP M.C. & OR D. 2004. Lattice Boltzmann method for modeling liquid ‐ vapor interface configurations in porous media. *Water Resources Research*, **40,**

SUKOP M.C. & THORNE D.T., 2007. Lattice Boltzmann modeling: an introduction for geoscientists and engineers. Springer.

SUKOP M.C. & THORNE JR D.T., 2007. Lattice Boltzmann modeling: an introduction for geoscientists and engineers. Springer Publishing Company, Incorporated.

SWIFT M.R., ORLANDINI E., OSBORN W. & YEOMANS J. 1996. Lattice Boltzmann simulations of liquid-gas and binary fluid systems. *Physical Review E*, **54,** 5041.

SYED A., SHI J.-Q. & DURUCAN S. 2011. Permeability and injectivity improvement in CO< sub> 2</sub> enhanced coalbed methane recovery: Thermal stimulation of the near wellbore region. *Energy Procedia*, **4,** 2137-2143.

TAHERI P., TORRILHON M. & STRUCHTRUP H. 2009. Couette and Poiseuille microflows: analytical solutions for regularized 13-moment equations. *Physics of Fluids (1994-present)*, **21,** 017102.

TAINA I., HECK R. & ELLIOT T. 2008. Application of X-ray computed tomography to soil science: A literature review. *Canadian Journal of Soil Science*, **88,** 1-19.

TAVENAS F., JEAN P., LEBLOND P. & LEROUEIL S. 1983. The permeability of natural soft clays. Part II: Permeability characteristics. *Canadian Geotechnical Journal*, **20,** 645-660.

TEIMOORI A., CHEN Z., RAHMAN S.S. & TRAN T. 2005. Effective permeability calculation using boundary element method in naturally fractured reservoirs. *Petroleum science and technology*, **23,** 693-709.

TIAN Z.-W., ZOU C., LIU Z.-H., GUO Z.-L., LIU H.-J. & ZHENG C.-G. 2006. Lattice Boltzmann method in simulation of thermal micro-flow with temperature jump. *International Journal of Modern Physics C*, **17,** 603-614.

TIAN Z., XING H., TAN Y. & GAO J. 2014. A coupled lattice Boltzmann model for simulating reactive transport in CO< sub> 2</sub> injection. *Physica A: Statistical Mechanics and its Applications*, **403,** 155-164.

TOP 500 WEBSITE. http://www.top500.org/lists/2013/11/#.U3wMc4GSywQ.

TRACY S.R., ROBERTS J.A., BLACK C.R., MCNEILL A., DAVIDSON R. & MOONEY S.J. 2010. The X-factor: visualizing undisturbed root architecture in soils using X-ray computed tomography. *Journal of experimental botany*, **61,** 311-313.

TUOMI I. 2002. The lives and death of Moore's Law. *First Monday*, **7,**

TURNER L.G. 2014. Permeability modelling using computed tomography scans of mineralised coal cores. *The Department of Chemical Engineering, The University of Queensland.* Project description.

TURNER L.G., STEEL K.M. & PELL S., 2013. Novel chemical stimulation techniques to enhance coal permeability for coal seam gas extraction, SPE 13URCE: Unconventional Resources Conference and Exhibition-Asia Pacific 2013. Society of Petroleum Engineers (SPE), pp. 1-10.

TURNER M., KN FING L., ARNS C., SAKELLARIOU A., SENDEN T., SHEPPARD A., SOK R., LIMAYE A., PINCZEWSKI W. & KNACKSTEDT M. 2004. Three-dimensional imaging of multiphase flow in porous media. *Physica A: Statistical mechanics and its applications*, **339,** 166-172.

UYSAL I.T., GLIKSON M., GOLDING S.D. & AUDSLEY F. 2000. The thermal history of the Bowen Basin, Queensland, Australia: vitrinite reflectance and clay mineralogy of Late Permian coal measures. *Tectonophysics*, **323,** 105-129.

UYSAL I.T., GOLDING S.D., BOLHAR R., ZHAO J.-X., FENG Y.-X., BAUBLYS K.A. & GREIG A. 2011. CO< sub> 2</sub> degassing and trapping during hydrothermal cycles

related to Gondwana rifting in eastern Australia. *Geochimica et Cosmochimica Acta,* **75,** 5444-5466.

VAFAI K., 2010. Handbook of porous media. Crc Press.

VAFAI K. & TIEN C. 1981. Boundary and inertia effects on flow and heat transfer in porous media. *International Journal of Heat and Mass Transfer,* **24,** 195-203.

VALO A., CARR RE H. & DELGEN S J.P. 2004. Thermal, chemical and thermo‐chemical pre‐treatment of waste activated sludge for anaerobic digestion. *Journal of Chemical Technology and Biotechnology,* **79,** 1197-1203.

VAN GEET M. & SWENNEN R. 2001. Quantitative 3D‐fracture analysis by means of microfocus X‐Ray Computer Tomography (μCT): An example from coal. *Geophysical Research Letters,* **28,** 3333-3336.

VAN GENUCHTEN M.T. 1980. A closed-form equation for predicting the hydraulic conductivity of unsaturated soils. *Soil Science Society of America Journal,* **44,** 892-898.

VASCO D., SEONGSIK Y. & DATTA-GUPTA A. 1999. Integrating dynamic data into high-resolution reservoir models using streamline-based analytic sensitivity coefficients. *SPE journal,* **4,** 389-399.

VEDVIK A., WAGNER G., OXAAL U., FEDER J., MEAKIN P. & J SSANG T. 1998. Fragmentation transition for invasion percolation in hydraulic gradients. *Physical Review Letters,* **80,** 3065-3068.

VELIVELLI A. & BRYDEN K. 2006. Parallel performance and accuracy of lattice Boltzmann and traditional finite difference methods for solving the unsteady two-dimensional Burger's equation. *Physica A: Statistical Mechanics and its Applications,* **362,** 139-145.

VENGOSH A., JACKSON R.B., WARNER N., DARRAH T.H. & KONDASH A. 2014. A critical review of the risks to water resources from unconventional shale gas development and hydraulic fracturing in the United States. *Environmental science & technology*

VETTER J.S., GLASSBROOK R., DONGARRA J., SCHWAN K., LOFTIS B., MCNALLY S., MEREDITH J., ROGERS J., ROTH P. & SPAFFORD K. 2011. Keeneland: Bringing heterogeneous GPU computing to the computational science community. *Computing in Science and Engineering,* **13,** 90-95.

VIDAL D., ROY R. & BERTRAND F. 2010. On improving the performance of large parallel lattice Boltzmann flow simulations in heterogeneous porous media. *Computers & Fluids,* **39,** 324-337.

VISWANATHAN H.S., PAWAR R.J., STAUFFER P.H., KASZUBA J.P., CAREY J.W., OLSEN S.C., KEATING G.N., KAVETSKI D. & GUTHRIE G.D. 2008. Development of a hybrid process and system model for the assessment of wellbore leakage at a geologic CO2 sequestration site. *Environmental science & technology,* **42,** 7280-7286.

WACHI S. & JONES A.G. 1991. Mass transfer with chemical reaction and precipitation. *Chemical Engineering Science,* **46,** 1027-1033.

WAGNER W. 1992. A convergence proof for Bird's direct simulation Monte Carlo method for the Boltzmann equation. *Journal of Statistical Physics,* **66,** 1011-1044.

WANG F., ZHU Z., MASSAROTTO P. & RUDOLPH V. 2007a. Mass transfer in coal seams for CO2 sequestration. *AIChE journal,* **53,** 1028-1049.

WANG F., ZHU Z., MASSAROTTO P. & RUDOLPH V. 2007b. A simplified dynamic model for accelerated methane residual recovery from coals. *Chemical engineering science,* **62,** 3268-3275.

WANG G., MASSAROTTO P. & RUDOLPH V. 2009. An improved permeability model of coal for coalbed methane recovery and CO< sub> 2</sub> geosequestration. *International Journal of Coal Geology,* **77,** 127-136.

WANG J., WANG M. & LI Z. 2007c. A lattice Boltzmann algorithm for fluid–solid conjugate heat transfer. *International journal of thermal sciences,* **46,** 228-234.

WANG J., ZHANG X., BENGOUGH A.G. & CRAWFORD J.W. 2005. Domain-decomposition method for parallel lattice Boltzmann simulation of incompressible flow in porous media. *Physical Review E*, **72,** 016706.

WANG M., HE J., YU J. & PAN N. 2007d. Lattice Boltzmann modeling of the effective thermal conductivity for fibrous materials. *International Journal of Thermal Sciences*, **46,** 848-855.

WANG X.-Q. & MUJUMDAR A.S. 2007. Heat transfer characteristics of nanofluids: a review. *International journal of thermal sciences*, **46,** 1-19.

WANG X., XU X. & S. CHOI S.U. 1999. Thermal conductivity of nanoparticle-fluid mixture. *Journal of thermophysics and heat transfer*, **13,** 474-480.

WEI X., MASSAROTTO P., WANG G., RUDOLPH V. & GOLDING S.D. 2010. CO< sub> 2</sub> sequestration in coals and enhanced coalbed methane recovery: New numerical approach. *Fuel*, **89,** 1110-1118.

WEI X.R., WANG G.X., MASSAROTTO P., GOLDING S.D. & RUDOLPH V. 2007. A review on recent advances in the numerical simulation for coalbed-methane-recovery process. *SPE Reservoir Evaluation & Engineering*, **10,** 657-666.

WELLINGTON S. & VINEGAR H. 1987. X-ray computerized tomography. *Journal of Petroleum Technology*, **39,** 885-898.

WELLS J., JANECKY D. & TRAVIS B. 1991. A lattice gas automata model for heterogeneous chemical reactions at mineral surfaces and in pore networks. *Physica D: Nonlinear Phenomena*, **47,** 115-123.

WHITAKER S. 1977. Simultaneous heat, mass, and momentum transfer in porous media: a theory of drying. *Advances in heat transfer*, **13,** 119-203.

WHITAKER S. 1986. Flow in porous media I: A theoretical derivation of Darcy's law. *Transport in porous media*, **1,** 3-25.

WILDENSCHILD D. & SHEPPARD A.P. 2013. X-ray imaging and analysis techniques for quantifying pore-scale structure and processes in subsurface porous medium systems. *Advances in Water Resources*, **51,** 217-246.

WILKE J., POHL T., KOWARSCHIK M. & R DE U. 2003. Cache performance optimizations for parallel lattice Boltzmann codes. In: *Euro-Par 2003 Parallel Processing*, pp. 441-450. Springer,

WILKINSON D. & WILLEMSEN J.F. 1983. Invasion percolation: a new form of percolation theory. *Journal of physics A: Mathematical and general*, **16,** 3365.

WITTEN JR T. & SANDER L.M. 1981. Diffusion-limited aggregation, a kinetic critical phenomenon. *Physical Review Letters*, **47,** 1400-1403.

WOLF K.-H.A., VAN BERGEN F., EPHRAIM R. & PAGNIER H. 2008. Determination of the cleat angle distribution of the RECOPOL coal seams, using CT-scans and image analysis on drilling cuttings and coal blocks. *International Journal of Coal Geology*, **73,** 259-272.

WORDEN R. & MORAD S. 2000. Quartz cementation in oil field sandstones: a review of the key controversies. *Quartz cementation in sandstones, Special publications of international association of sedimentologists*, **29,** 1-20.

WORDEN R.H. 2006. Dawsonite cement in the Triassic Lam Formation, Shabwa basin, Yemen: A natural analogue for a potential mineral product of subsurface CO2 storage for greenhouse gas reduction. *Marine and Petroleum Geology*, **23,** 61-77.

XING H., LI Q., RUDOLPH V., GAO J. & GOLDING S.D., 2013. Scale Effect of 3D Heterogeneous Porous Media on Geo-Fluid Characteristics: Insight from Massively Parallel Lattice Boltzmann Computing, SPE Unconventional Resources Conference and Exhibition-Asia Pacific. Society of Petroleum Engineers.

XU T. 2008. TOUGHREACT testing in high ionic strength brine sandstone systems. *Lawrence Berkeley National Laboratory*

XU T., APPS J.A. & PRUESS K. 2004a. Numerical simulation of CO< sub> 2</sub> disposal by mineral trapping in deep aquifers. *Applied geochemistry*, **19,** 917-936.

XU T., APPS J.A. & PRUESS K. 2005. Mineral sequestration of carbon dioxide in a sandstone–shale system. *Chemical geology*, **217,** 295-318.

XU T., APPS J.A., PRUESS K. & YAMAMOTO H. 2004b. Injection of CO2 with H2S and SO2 and subsequent mineral trapping in Sandstone-Shale Formation. *Lawrence Berkeley National Laboratory*

XU T., SPYCHER N., SONNENTHAL E., ZHENG L. & PRUESS K. 2012. TOUGHREACT User's Guid: A Simulation Program for Non-isothermal Multiphase Reactive Transport in Variable Saturated Geologic Media, Version 2.0. Tutorial document.

YAO Y., LIU D., CHE Y., TANG D., TANG S. & HUANG W. 2009. Non-destructive characterization of coal samples from China using microfocus X-ray computed tomography. *International Journal of Coal Geology*, **80,** 113-123.

YEE D., SEIDLE J.P. & HANSON W.B. 1993. Gas sorption on coal and measurement of gas content. *Hydrocarbons from coal: AAPG Studies in Geology*, **38,** 203-218.

YETKIN C., RAMIREZ B., AL-KOBAISI M., KAZEMI H. & OZKAN E., 2009. A Simple Method to Account for Permeability Anisotropy in Reservoir Models and Multi-Well Pressure Interference Tests, SPE Rocky Mountain Petroleum Technology Conference. Society of Petroleum Engineers.

YIN S., DUSSEAULT M.B. & ROTHENBURG L. 2011. Coupled THMC modeling of CO< sub> 2</sub> injection by finite element methods. *Journal of Petroleum Science and Engineering*, **80,** 53-60.

YIN X.-C., CHEN X.-Z., SONG Z.-P. & YIN C. 1995. A new approach to earthquake prediction: The Load/Unload Response Ratio (LURR) theory. *Pure and Applied Geophysics*, **145,** 701-715.

YIOTIS A.G., TSIMPANOGIANNIS I.N., STUBOS A.K. & YORTSOS Y.C. 2006. Pore-network study of the characteristic periods in the drying of porous materials. *Journal of colloid and interface science*, **297,** 738-748.

YONG R.N., MOHAMED A.-M.O. & WARKENTIN B.P., 1992. Principles of contaminant transport in soils. Elsevier Science Publishers.

YOSHINO M., MURAYAMA T., MATSUZAKI A. & HITOMI T. 2009. Simulation of Mass Transfer of Calcium in Concrete by the Lattice Kinetic Scheme for a Binary Miscible Fluid Mixture. *Journal of Fluid Science and Technology*, **4,** 13-24.

YU D., MEI R., LUO L.-S. & SHYY W. 2003. Viscous flow computations with the method of lattice Boltzmann equation. *Progress in Aerospace Sciences*, **39,** 329-367.

YU H., MA K.-L. & WELLING J., 2004. A parallel visualization pipeline for terascale earthquake simulations, Proceedings of the 2004 ACM/IEEE conference on Supercomputing. IEEE Computer Society, pp. 49.

YU Q. & FISH J. 2002. Multiscale asymptotic homogenization for multiphysics problems with multiple spatial and temporal scales: a coupled thermo-viscoelastic example problem. *International journal of solids and structures*, **39,** 6429-6452.

ZALBA B., MARíN J.M., CABEZA L.F. & MEHLING H. 2003. Review on thermal energy storage with phase change: materials, heat transfer analysis and applications. *Applied thermal engineering*, **23,** 251-283.

ZHANG H., ZHANG S., BI J. & SCHREFLER B. 2007. Thermo‐mechanical analysis of periodic multiphase materials by a multiscale asymptotic homogenization approach. *International journal for numerical methods in engineering*, **69,** 87-113.

ZHANG S., TULLIS T.E. & SCRUGGS V.J. 1999. Permeability anisotropy and pressure dependency of permeability in experimentally sheared gouge materials. *Journal of structural geology*, **21,** 795-806.

ZHANG S., TULLIS T.E. & SCRUGGS V.J. 2001. Implications of permeability and its anisotropy in a mica gouge for pore pressures in fault zones. *Tectonophysics*, **335,** 37-50.

ZHANG Y. 2008. Online-coupled meteorology and chemistry models: history, current status, and outlook. *Atmospheric Chemistry and Physics*, **8,** 2895-2932.

ZHAO C., XU T. & VALLIAPPAN S. 1994. Numerical modelling of mass transport problems in porous media: A review. *Computers & structures*, **53,** 849-860.

ZHAO J., YAN Z.-P., SHAO J.-L., CUI Y.-L., LIU X.-H. & TIAN L.-H. 2009. Impact of pumping and injection modes on groundwater temperature in energy extraction area with regional flow [J]. *Journal of Hunan University of Science & Technology (Natural Science Edition)*, **2,** 007.

ZOU Q. & HE X. 1997. On pressure and velocity boundary conditions for the lattice Boltzmann BGK model. *Physics of Fluids (1994-present)*, **9,** 1591-1598.

ZULKARNAIN I., 2005. Simulation study of the effect of well spacing, effect of permeability anisotropy, and effect of Palmer and Mansoori model on coalbed methane production, Texas A&M University.